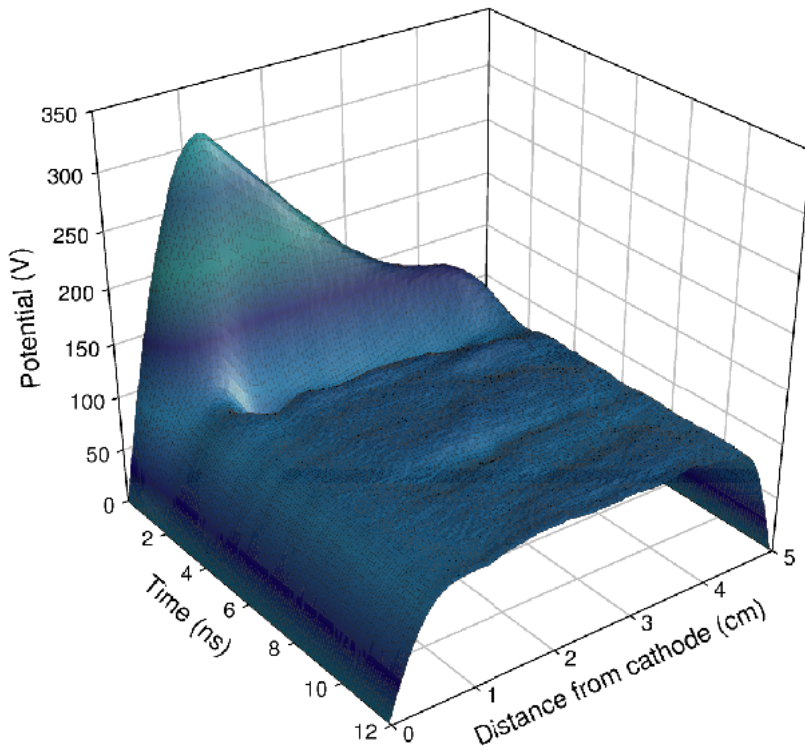


---

# Studies of Electrical Plasma Discharges

---



**Casper V Budtz-Jørgensen**

phd thesis





This thesis has been submitted to the  
Faculty of Science, Aarhus University,  
Denmark, to meet the requirements for  
the degree of Doctor of Philosophy.



Submitted on January 11<sup>th</sup> 2001

Public defence held on April 27<sup>th</sup> 2001

This document has been typeset using pdf $\TeX$  and (apart from a few typos) is identical to the submitted version.

Electronic versions may be obtained at <[www.budtz.net/phd](http://www.budtz.net/phd)> or by contacting the author at [casper.work@budtz.net](mailto:casper.work@budtz.net).

***Front cover.** The collapsing plasma. Computer simulation showing the temporal evolution of the potential distribution between the cathode and anode of an argon glow-discharge right after the cathode has been grounded. The existence of this potential causes the anode to be bombarded by energetic ions during the collapse of the plasma, which can lead to anode material sputtering. See Chap. 5 for more information.*

---

# CONTENTS

---

<b>Preface</b>	<b>v</b>
<b>Introduction</b>	<b>1</b>
<b>1 Basic Plasma Physics</b>	<b>5</b>
1.1 Introduction and Basic Concepts	5
1.2 Collisions in Plasmas	9
1.3 The Direct-Current Glow-Discharge	11
Plasma ignition / 11 • Sheath formation / 13 • Basic characteristics / 15	
1.4 The Collisional Child Law	16
1.5 The Davis and Vanderslice Model	20
1.6 Plasma Simulations	23
Introduction / 23 • The Ar glow-discharge / 25 • Plasma profiles / 27 • Ion energy and angular distributions / 29	
<b>2 Experimental</b>	<b>33</b>
2.1 Introduction	33
2.2 The Plasma Chamber	35
The electrodes / 35 • The orifice / 37 • The gas supply system / 39 • Voltage control and data acquisition / 40	
2.3 The Hiden EQP	42
Main characteristics / 42 • Angular acceptance / 46	
2.4 Rutherford Backscattering Spectrometry	52
Theory / 52 • Apparatus / 53	
<b>3 The Argon Discharge: some fundamental studies</b>	<b>55</b>
3.1 Introduction	55
Attacking the Davis and Vanderslice model / 57 • Comparison with experiments in the literature / 59 • Energetic neutrals / 62	
3.2 Ar <sup>+</sup> Ion Energy-Distribution Measurements	64
Experimental / 64 • Theoretical model / 65	

---

3.3	Results	66
	Dependence on discharge voltage / 66 • Dependence on pressure / 68	
3.4	Discussion	68
3.5	Conclusions and Summary	70
	Practical applications / 71	
<b>4</b>	<b>The Ar-H<sub>2</sub> Discharge: sputtering of Au and Al<sub>2</sub>O<sub>3</sub></b>	<b>73</b>
4.1	Introduction and Basic Concepts	73
	Findings in the literature / 73 • Physical sputtering / 76 • Chemical sputtering / 79	
4.2	Measurements of the Ar-H <sub>2</sub> Discharge	82
	Plasma intensity / 82 • Ion energy-distributions / 86	
4.3	Sputtering Experiments — Methods	91
4.4	Gold — Physical Sputtering	92
	Introduction / 92 • Experimental / 93 • Results / 95 • Discussion / 100 • Summary / 101 • Further notes (thesis only) / 102	
4.5	Oxidation of Metals — Al and Fe	103
	Sputtering yield as a function of partial oxygen pressure / 103 • Summary / 105	
4.6	Alumina — Chemically Enhanced Sputtering	107
	Introduction / 107 • Experimental / 110 • Results / 112 • Discussion / 115 • Conclusions / 117	
4.7	Sputtering Experiments — Summary	118
<b>5</b>	<b>Energetic Ion Bombardment of the Anode</b>	<b>121</b>
5.1	Introduction	122
5.2	The DC Discharge	123
5.3	Experimental	124
5.4	Experimental Results	125
5.5	Plasma Simulations	129
5.6	Anode Sputtering	133
5.7	Discussion and Concluding Remarks	135
5.8	Summary (thesis only)	135
<b>6</b>	<b>The N<sub>2</sub> and N<sub>2</sub>-H<sub>2</sub> Discharges: characterization and nitriding</b>	<b>137</b>
6.1	Introduction	137

---

6.2	The N <sub>2</sub> discharge	138
	N <sub>2</sub> <sup>+</sup> (I) / 139 • N <sup>+</sup> / 141 • N <sub>2</sub> <sup>+</sup> (II) / 142 • Dependence on Voltage and Pressure / 143	
6.3	The N <sub>2</sub> -H <sub>2</sub> discharge	144
	N <sup>+</sup> , N <sub>2</sub> <sup>+</sup> and N <sub>2</sub> H <sup>+</sup> / 145 • NH <sub>4</sub> <sup>+</sup> / 145 • H <sub>2</sub> <sup>+</sup> and H <sub>3</sub> <sup>+</sup> / 149	
6.4	Nitriding Experiments	149
	Introduction / 149 • The nitriding process / 150 • Hardness depth-profiles / 151 • Hiden measurements — ion energy doses / 153	
	• Discussion / 155	
6.5	Summary	157
	<b>Summary</b>	<b>159</b>
	<b>A Experimental Notes</b>	<b>163</b>
	A.1 Hiden EQP Data Acquisition	163
	A.2 Changing the Electrode Material	164
	A.3 Sample Attachment	166
	<b>References</b>	<b>167</b>
	Author Index	175



# Preface

What a joy! The thesis you hold in your hands is out of mine, and has been submitted to the Faculty of Science, Aarhus University, Denmark, in partial fulfilment of the requirements for the degree of Doctor of Philosophy (PhD). The work presented here has been carried out under the supervision of Prof. Jørgen Bøttiger between August 1997 and September 2000 at the Institute of Physics and Astronomy, Aarhus University and the Tribology Centre at the Danish Technological Institute (Aarhus).

The purpose of this work has been study glow-discharges used for plasma-assisted surface processing techniques by energy and mass analysis of the ions impinging on the cathode of such discharges, and correlate these studies with a number practical applications.

## Acknowledgements

Financial support from the Centre for Industrial Materials Physics and Tribology (CIMT) and The Danish Research Council is gratefully acknowledged.

Let me express my gratitude to all the people who, in each their own way, have helped me during the 3 years of this project. First of all, I am indebted to my supervisor Jørgen Bøttiger, for his very kind and skilled guidance during the progress of my work. Warm thanks are also due to Per Kringhøj, with whom I have been collaborating for around 5 years, both in the Semiconductor Group at Aarhus University and, during the past 3 years, here in the Plasma Group. The fruitful and often very joyful discussions we have had, both on and off topic, have been invaluable. I thank Jacques Chevallier for the preparation of the thin films used during my work, and keeping the “basics” of my french vocabulary up to date. From the Tribology Centre I would like to thank Claus Mathiasen for his help with the equipment there and Christen A. Stræde for acknowledging the importance of the collaboration between universities and the industry — a collaboration which is embodied in CIMT and has made this project possible.

More thanks are due to a number of people, but these are best given over a bottle of wine (or the likes of it)...

## Publications

The present work has so far resulted in the following publications:

- [I] *The Critical Role of Hydrogen for Physical Sputtering with Ar-H<sub>2</sub> Glow Discharges.*  
C. V. Budtz-Jørgensen, P. Kringhøj, and J. Bøttiger.  
*Surf. Coat. Tech.*, **116–119**, 1999, p. 938.
- [II] *Energy Spectra of Particles Bombarding the Cathode in glow discharges.*  
C. V. Budtz-Jørgensen, J. Bøttiger, and P. Kringhøj.  
*Vacuum*, **56**, 2000, p. 9.
- [III] *Chemical and Physical Sputtering of Aluminium and Gold Samples Using Ar-H<sub>2</sub> DC-Glow Discharges.*  
C. V. Budtz-Jørgensen, P. Kringhøj, J. F. Nielsen, and J. Bøttiger.  
*Surf. Coat. Tech.*, **135**, 2000, p. 299.
- [IV] *Energetic Ion Bombardment of the Grounded Anode in Pulsed DC-Glow Discharges.*  
C. V. Budtz-Jørgensen, J. Bøttiger, and P. Kringhøj.  
*Surf. Coat. Tech.*, **137**, 2001, p. 104.
- [V] *On Nitriding of Steels.*  
M. Berg, C. V. Budtz-Jørgensen, H. Reitz, K. O. Schweitz, J. Chevallier, P. Kringhøj, and J. Bøttiger.  
*Surf. Coat. Tech.*, **124**, 2000, p. 25.
- [VI] *On Glow-Discharge Sputtering of Iron and Steels in a Commercial Deposition Plant.*  
P. Kringhøj, C. V. Budtz-Jørgensen, J. F. Nielsen, J. Bøttiger, S. S. Eskildsen, and C. Mathiasen.  
*Surf. Coat. Tech.*, 2001.

Articles I–IV encompass the major part of the work presented in this thesis. Besides the preparation of thin films by Jacques Chevallier and the RBS measurements which were performed by Per Kringhøj, all the experimental work and analysis and the subsequent writing of the articles was performed by the author of this thesis. Relevant parts of Articles V and VI, to which I have contributed, are also presented in this thesis (Sects. 4.5 and 6.4).

---

# INTRODUCTION

---

The highly beneficial application of plasmas for surface processing techniques is well-established. The role of the plasma in this respect is two-fold; firstly, through the formation of reactive species at lower temperatures than is possible with conventional surface processing techniques (e.g., chemical vapor deposition (CVD)), and, secondly, the creation of ionic species within the plasma, which can be made to bombard the processed surface with high energies (typically in the 10–1 000 eV range). The advantage of minimizing the process temperature is obvious, since a large number of materials are not able to withstand the elevated temperatures which are needed in many conventional surface processing techniques. For instance, the creation of TiN coatings from hydrogen, nitrogen and titanium-tetra-chloride ( $\text{TiCl}_4$ ) gases requires temperatures of 1 000°C — a temperature which would change the properties of a typical (temperature-hardened) tool steel. Irrespective of temperature, however, the simultaneous ion-irradiation during surface processing has in many cases been shown to give the surface processing engineer an array of new opportunities for tailoring the deposited film and surface properties [1, 2].

## The importance of ion energies

The most straightforward way to take advantage of the possibilities of ion-irradiation, is to combine a small ion accelerator with a conventional surface processing facility, i.e., ion-beam assisted deposition (IBAD). For example, using IBAD, Ensinger [2, 3] has shown that the preferred crystal orientation of a TiN film grown by Ti evaporation under nitrogen ion bombardment correlates directly with the  $\text{N}^+$  ion energy, changing from the (1 1 1) to the (1 0 0) orientation in the 100–500 eV range. In experiments by Schweitz *et al.* [4], also using IBAD, the stress of Ni films, grown using e-gun deposition of Ni during argon ion bombardment, was shown to reverse from tensile to compressive in the 0–200 eV range. A similar effect was observed by Huang *et al.* [5, ref'd in [1]], using argon ion bombardment during the growth of Ag films at room temperature, showing a reversion of stress at an  $\text{Ar}^+$  energy of 42 eV. Other changes in film properties with increasing  $\text{Ar}^+$  energy reported here include a decrease in average grain size and an increase in dislocation number density. At elevated growth temperatures, however, ion-irradiation can have the opposite effects, since ion-irradiation induced intrinsic defects can be annealed out during deposition. This, for example, was shown to be the case for epitaxial TiN films grown

on MgO(001) substrates by reactive magnetron sputtering in pure nitrogen discharges (Hultman *et al.* [6, 7, ref'd in [1]]). At a fixed deposition temperature of 650°C, the dislocation number density was observed to drop by more than a decade if the substrate was simultaneously bombarded with  $\sim 150$  eV nitrogen ions originating from the plasma.

### Plasma-assisted ion-irradiation

In this last example, a radio-frequency magnetron discharge was used as a source of energetic ions. Using plasmas instead of ion beams originating from miniature ion accelerators gives one, apart from the temperature minimization previously mentioned, a number of improved practical applicabilities. When using a plasma, the reaction or processing atmosphere itself contains ionic species. These can be accelerated towards the substrate surfaces simply by applying a negative voltage to the substrate. This drastically increases the ease with which more complex 3D bodies may be treated, as compared to for example IBAD or similar techniques, which are limited by the line-of-sight of the ion beam. In effect, plasma-assisted techniques combine ion-irradiation with the chemically reactive qualities of e.g., CVD, in one relatively simple and versatile environment. One such environment is plasma-assisted chemical vapor deposition (PA-CVD), which is well-established as a suitable technique for nitriding (i.e., metal surface hardening by nitrogen intake) and the growth of TiN coatings at low temperatures.

Since radio-frequency plasmas are usually driven at low pressures, the ions which are extracted from it and accelerated towards the substrate undergo relatively few collisions, and hence bombard the substrate with a well-defined energy. This, for example, was the case for the experiments by Hultman *et al.* just mentioned, where the energy of the  $N^+$  ions bombarding the growing TiN film was about 150 eV. In many cases a DC plasma or DC *glow-discharge* is used, which is normally driven at much higher gas pressure. This, for example, is the case for the PA-CVD technique used at the Tribology Centre at the Danish Technological Institute in Århus, for the deposition of TiN films and the nitriding of steels. At these higher pressures, the ions which are attracted towards the cathodic surfaces of the discharge undergo numerous collisions on their way, thus ending up with some final energy-distribution upon impinging on the substrate surfaces.

### The aim of this work

Clearly, in any plasma-assisted surface processing technique where ion-irradiation is of importance, knowledge of the energy-distributions of the ions hitting the substrate surfaces is pertinent to the understanding of the processes taking place at the surface and hence the further development of the technique

itself. As opposed to e.g., IBAD, where the energy of the ions is in principle externally and arbitrarily adjustable, the energies of the ions originating from a plasma are an intrinsic property of the plasma itself, and hence defined by the process parameters used (i.e., voltage, pressure, gas composition, etc.).<sup>1</sup> Therefore, one has to have a good knowledge of the basic physics of the plasma itself, and how its properties depend on the parameters which define it. This, of course, a plasma physicist knows “all” about. However, this knowledge must then be combined with the knowledge of the surface scientist, in order to achieve a full picture of the plasma-surface interactions, which are essential to the techniques described here.

During my, relatively short experience in this field, it seems to me that there has been a reluctance for the plasma and the surface physicist to meet. This is not saying that no literature of this kind exists — far from it! But, for example, the conferences which I have attended have either been totally dominated by either the surface processing perspective (PSE, E-MRS) or the “pure” interest in the physics of plasmas (GEC).<sup>2</sup> The work presented in this thesis may be viewed upon as an attempt of combining these two worlds. At the center of the experiments presented here is an ion energy and mass analyzer which is connected to an experimental DC glow-discharge chamber, allowing high-sensitivity measurement of the ions impinging on the cathode of such a discharge. Thus, for a given set of plasma parameters, the ionic species at the cathode and their energy-distribution can be determined. The aim of this is both to correlate these measurements with actual surface processes and to gain a deeper understanding of what defines these energy-distributions, and, to some extent, what the physics behind all this is. The thesis has the following structure:

**Chapter 1.** Here, the basic plasma physics of the glow-discharge will be reviewed to the extent which is necessary to understand the results of this thesis. Also, towards the end of the chapter, a series of computer simulations of a glow-discharge equivalent to the ones being experimentally studied here will be presented.

**Chapter 2.** This chapter is an account of the experimental setup and techniques used. This is mainly concerned with the equipment surrounding the mass and energy analyzer and an assessment of its sensitivity, on the basis the glow-discharge simulations and a simulation of the beam-optics of the analyzer. Furthermore Rutherford backscattering spectrometry (RBS) is briefly reviewed.

**Chapter 3.** Here a more thorough investigation of the pure argon glow-dis-

---

<sup>1</sup>This is, of course, to a lesser extent the case for low-pressure plasmas, where the ion energies are well-defined and more or less proportional to the substrate voltage.

<sup>2</sup>PSE: Plasma Surface Engineering, E-MRS: European Materials Research Society, GEC: Gaseous Electronics Conference.

charge is given, with emphasis on the energetic particles bombarding the cathode. This will be partly substantiated by experimental measurements. The results of this chapter are contained in **Article II**.

**Chapter 4.** The Ar-H<sub>2</sub> glow-discharge was extensively examined with its practical applicability as a pre-deposition surface cleaning process in mind. The efficiency of the Ar-H<sub>2</sub> discharge in this respect is due to its physical and chemical sputtering properties. These two types of sputtering mechanism are briefly reviewed, and sputtering experiments performed on Au and Al samples are presented. Furthermore, the fundamentals of the Ar-H<sub>2</sub> discharge are discussed. The results of this chapter are contained in **Articles I, III and VI**.

**Chapter 5.** The voltage of most DC glow-discharges used for practical surface processing techniques is pulsed. This allows one to control the power of the discharge, by varying the pulse times, without changing the basic parameters of the discharge (i.e., the voltage). A side effect of this pulsing, however, is that the anode of the discharge is bombarded with energetic ions during at the onset of the off-pulse (i.e., the collapse of the discharge), which may result in anode material sputtering. In this chapter, experimental evidence of this will be presented and explained with the aid of computer simulations of the discharge. The results of this chapter are contained in **Article IV**.

**Chapter 6.** The N<sub>2</sub> and N<sub>2</sub>-H<sub>2</sub> discharges were also investigated. In this chapter, measured ion energy-distributions of these two discharges are presented and discussed. As an example of a practical application some nitriding experiments are presented and discussed on the basis of the measured energy-distributions. The results of this chapter are contained in **Article V**.

# 1

---

## BASIC PLASMA PHYSICS

---

*A plasma, sometimes also referred to as the fourth state of matter, is an electrically conducting medium in which there are roughly equal numbers of positively and negatively charged particles, produced when the atoms in a gas become ionized (Encyclopædia Britannica Online [8]). Plasmas can be divided into two main categories: those which are in thermal equilibrium (i.e., thermal plasmas) and those which are not. The type of plasma used in this work is the latter — more specifically, a so-called direct-current glow-discharge, which is an electrically induced plasma. After a short introduction to plasmas in general, this chapter will deal with the basic physics of such a glow-discharge.*

### 1.1 Introduction and Basic Concepts

The term “plasma” was first introduced by Irving Langmuir (1881–1957) in 1923 to describe the jellylike behaviour of those regions of an electrical discharge capable of showing a certain periodic variation or movement of the free electrons (the so-called *plasma-oscillations*). It was not until the early 50’ies however, that the concept of a plasma as a distinct state of a gas was fully appreciated. Of the many types of plasmas which exist, the most commonly known to people in general are probably those observed in neon lamps and sparks of lightning (although probably only few recognize them as a plasmas at all). The plasma formed in these cases is an electrically induced plasma, called a *discharge* (the type of plasma Irving Langmuir was studying). Discharges are relatively easy to produce, and they are also, in the form of lightning, the only types of plasma which occur naturally on or near the surface of the Earth. Most naturally occurring plasmas are only formed in extreme environments such as the Sun, where

	THERMAL	ELECTRICAL
Temperature	$T_i \simeq T_e \simeq T_g$ 4 000–20 000 K	$T_e \gg T_g, T_e > T_i > T_g$ $T_e \sim 1\text{--}10\text{ V } (10^4\text{--}10^5\text{ K})$
Density/ionization	$n_i \simeq n_e, x_{iz} \leq 1$	$n_i \simeq n_e \lesssim 10^{-4} n_g$
Thermal equilibrium	yes	no
Popular examples	stars, fusion reactors	lightning, neon lights

**Table 1.1** Comparison between thermal and electrical plasmas. The indices denote ion (i), electron (e) and gas (g) quantities. In thermal plasmas, the gas is heated to a temperature sufficient for partly or full ionization to occur ( $x_{iz} = n_i/[n_g + n_i]$  defines the fractional ionization of the plasma). In electrically induced plasmas the electrons are heated preferentially, keeping the gas at a low temperature (e.g., room temperature).

temperatures easily reach the 4 000–20 000 K needed to thermally ionize a sufficient amount of gas atoms to produce the plasma state.

### *Thermal plasmas*

A plasma consists of neutral gas atoms/molecules (g), ions (i) and electrons (e). As mentioned, in thermal plasmas, the gas is “simply” heated to a temperature high enough to partly or fully ionize it. Hence, all the species are in thermal equilibrium with each other, i.e.,

$$T_i \simeq T_e \simeq T_g \quad (1.1)$$

and the electron and ion densities ( $n_e$  and  $n_i$  respectively) can, if the temperature is high enough, be comparable with or even exceed the neutral gas density,  $n_g$  (see Tab. 1.1). No matter the degree of ionization, there will (per definition) always be a roughly equal number of electrons and ions in the plasma (i.e.,  $n_e \simeq n_i$ ). Hence, on a significantly large scale, the plasma in itself will exhibit charge neutrality, since any localized non-zero space-charge would result in an electric field, causing an immediate redistribution of the electrons until the electric field is cancelled (*electron shielding*). Nevertheless, because of the thermal kinetic energy of the electrons,  $T_e$ , significant charge densities can spontaneously exist in the plasma, if the energy of a localized charge-perturbation is lower than  $T_e$ .<sup>1</sup> The characteristic length scale below which this can occur is called the *electron Debye length*, and, thus, signifies the scale above which the plasma exhibits *quasi-neutrality*. The Debye length is given by (e.g., see Lieberman and Lichten-

<sup>1</sup>In plasma physics it is a custom to denote particle temperatures in volts, i.e., an electron temperature of  $T_e = 1\text{ V}$  is equivalent to an energy of 1 eV and a thermal temperature of  $(1\text{ eV})/k \sim 10^4\text{ K}$ , where  $k$  is the Boltzmann constant.

berg [9, p. 40] for a derivation):

$$\lambda_{De} = \left( \frac{\varepsilon_0 T_e}{en_e} \right)^{1/2}, \quad (1.2)$$

where  $\varepsilon_0$  is the permittivity of free space and  $e$  is the unit charge. If the electron temperature increases, localized charge-densities can be sustained over larger distances, hence  $\lambda_{De}$  increases. An increase in the electron density  $n_e$ , however, decreases the length needed to sustain a given electric field (consider the Poisson equation), effectively decreasing  $\lambda_{De}$ .

Dealing with the temperatures of thermal plasmas is of course a cumbersome and costly matter, which greatly restricts the practical applications of such plasmas. And, needless to say, the high temperature in itself would be highly destructive for any material which would come in contact with the plasma gas. Nonetheless, thermal plasmas in the form of very hot combustion flames are actually used in some plasma chambers to enhance electrical plasmas used for surface processing. Another example of “earthly” thermal plasmas are plasmas used in (the still experimental) fusion reactors

### Electrical plasmas

One way of circumventing the necessity of high gas temperatures is by exploiting the electrical properties of a plasma. Because the electrons and ions are charged, these particles can be preferentially heated by applying an electric or magnetic field to the plasma, keeping the neutral gas atoms at a low temperature (e.g., room temperature). Most notably, because of their low mass, electrons are easily accelerated to energies which are sufficient to ionize the gas atoms, with typical values of  $T_e$  in the 1–10 V range,<sup>2</sup> which is equivalent to  $10^4$ – $10^5$  K. Electrically induced plasmas are called *discharges* and, because of their low gas temperatures, are sometimes also referred to as *cold plasmas*. Obviously, discharge plasmas are not in thermal equilibrium, since

$$T_e \gg T_g \quad \text{and} \quad T_e > T_i > T_g. \quad (1.3)$$

Note, that the ion temperature,  $T_i$ , can lie anywhere between  $T_e$  and  $T_g$ , depending on the type of plasma. Furthermore, the degree of ionization in electrical plasmas is usually much lower than is the case for thermal plasmas, with  $n_e, n_i \lesssim 10^{-4}n_g$  for the typical plasmas considered in this thesis. The two most common types of electrically induced plasmas are the *direct-current glow-discharge*, created by applying a DC voltage over a gas, and the *rf-discharge*,

<sup>2</sup>Although most electron-impact ionization thresholds are above 10 eV, a small amount of electrons will have an energy above  $T_e$ , so that significant degree of ionization can occur. More on this in the next section.

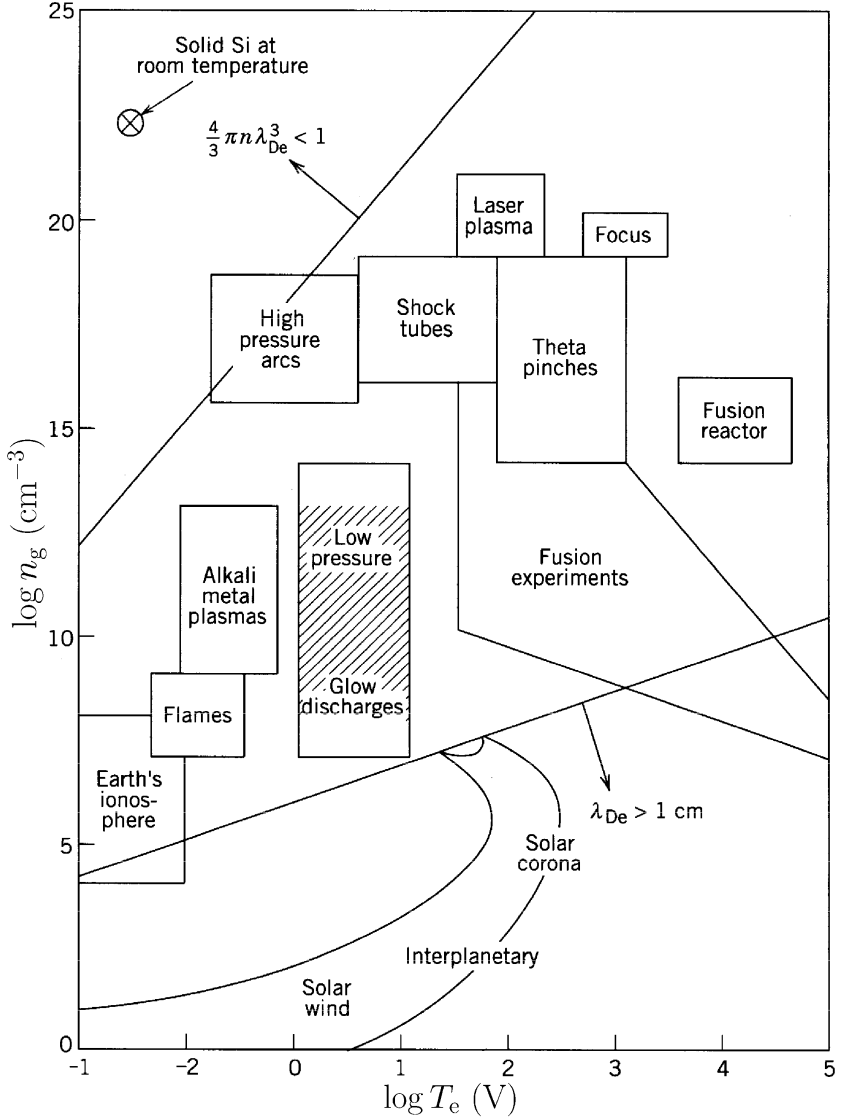


**Figure 1.1** Space and laboratory plasmas on a  $\log n_g$  versus  $\log T_e$  diagram. The *Debye length*, given by Eq. (1.2), signifies the scale on which quasi-neutrality is exhibited by the plasma. Naturally, this length cannot be lower than the average distance between individual particles in the (fully ionized) plasma. The plasmas considered in this thesis are *low-pressure glow-discharges* (hatched area). Taken from Ref. 9.

where a radio-frequency (usually 13.56 MHz) electric field is coupled either capacitively or inductively to the electrons of the discharge. Sometimes, magnetic fields are used in conjunction with rf-discharges, either to enhance the plasma or to achieve some degree of spatial control of the plasma intensity.

Tab. 1.1 briefly summarizes the basic qualities of thermal and electrical plasmas with respect to the temperature and density of the species involved. Furthermore, in Fig. 1.1, a diagram is shown containing laboratory and space plasmas on a  $\log n_g$  vs.  $\log T_e$  plot. As is clear from the figure, plasmas cover a very wide range of densities and temperatures. The type of plasma we will be looking at in this thesis is the low-pressure, direct-current glow-discharge (hatched area). Typical gas pressures of such discharges are in the range  $10^{-3}$ –1 mbar. In this work, the pressure range is somewhat narrower: 0.1–1 mbar. One other important characteristic of the glow-discharge is that the ions are more or less thermalized by the neutral gas atoms, so the particle temperatures obey the more restricted range

$$T_e \gg T_i \simeq T_g, \quad (1.4)$$

rather than Eq. (1.3). While  $T_e$  is in the 1–10 V range, both  $T_i$  and  $T_g$  are kept at room temperature (i.e.,  $T_i, T_g \sim 0.026$  V). Using a gas pressure of  $p = 0.5$  mbar, we get a neutral gas density of

$$n_g = p/kT_g \sim 10^{16} \text{ cm}^{-3}, \quad (1.5)$$

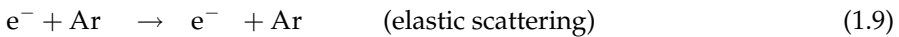
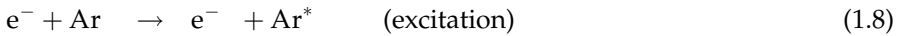
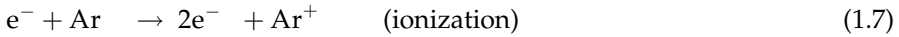
which, using a fractional ionization of  $10^{-4}$ , yields:

$$n_e, n_i \sim 10^{12} \text{ cm}^{-3} \quad \text{and} \quad \lambda_{De} \sim 0.01 \text{ mm}. \quad (1.6)$$

The remainder of this chapter — and thesis — will deal with the physics of direct-current glow-discharges, within the parameter ranges given by Eqs. (1.4)–(1.6). Before igniting the glow-discharge, however, let us first have a look at some of the important collisional processes taking place in the plasma.

## 1.2 Collisions in Plasmas

Naturally, collisions between species are of great importance in plasmas. Foremost, it is electron-impact ionization of neutral gas atoms that creates the ions which are necessary to sustain the discharge. Let us look at the argon discharge as a simple and relevant example. The most abundant species in low-pressure glow-discharges are the neutral gas atoms (i.e., Ar atoms). Hence the dominant collisional process are those involving atoms and electrons:



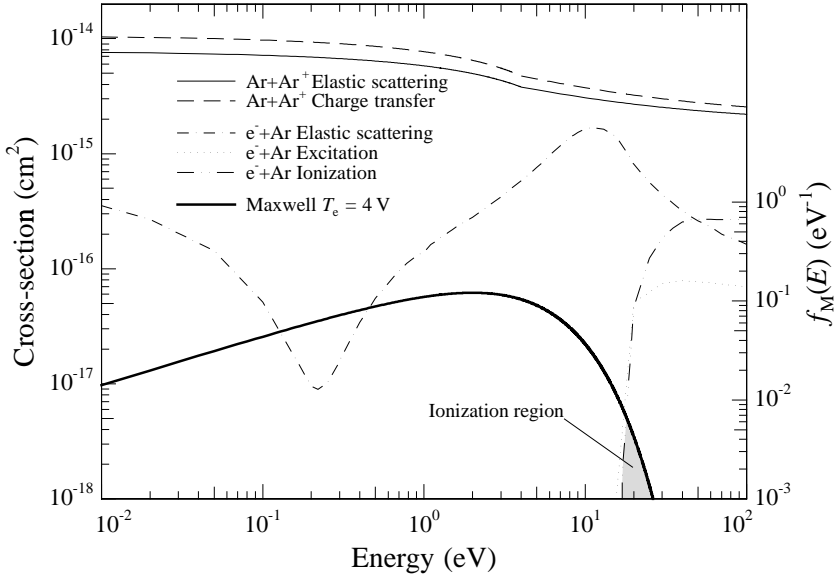
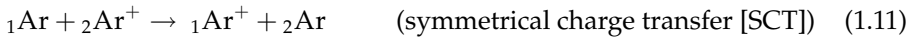
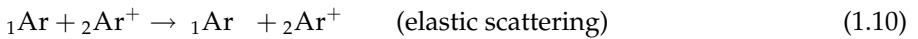


**Figure 1.2** Collisional cross-sections relevant for an argon plasma (left axis) and the Maxwell distribution function,  $f_M(E)$ , for  $T_e = 4$  eV electrons (right axis). Electron impact ionization of argon atoms is due to the high-energy “tail” of the Maxwell distribution (shaded area). See for example Phelps [10, 11].

and those involving atoms and ions (the indices “1” and “2” provide nuclei identification):



The cross-sections for these processes are shown in Fig. 1.2. As is evident from the figure, the threshold for electron-impact ionization and excitation lies above the typical electron temperature,  $T_e$ . Also shown in the figure, however, is the Maxwell distribution function,  $f_M(E)$ , for  $T_e = 4$  V electrons:<sup>3</sup>

$$f_M(E) = \frac{2(E/\pi)^{1/2} \exp(-E/eT_e)}{(eT_e)^{3/2}}. \quad (1.12)$$

Although the actual electron energy-distribution of the plasma might well not be exactly Maxwellian, its qualitative features are applicable for comparison.

<sup>3</sup>Note that our convention for temperature units requires us to make the exchange  $kT \rightarrow eT$ . See footnote 1 on page 6.

As can be seen from the figure, although the majority of the electrons have energies which are lower than the threshold for Ar-atom ionization, a small fraction (shaded area) will in fact be energetic enough for electron-impact ionization to occur. It is this small overlap between the electron energy-distribution function and the ionization cross-section which supplies the feedstock ions of the discharge. The cross-section for elastic scattering between electrons and Ar atoms gives one an indication of the dominant electron cooling mechanism. As can be seen, this cross-section has a sharp peak around 10 eV, effectively keeping the electron temperature below this level.

Neutral-atom collisions are also the major cooling factor for ions — especially in our case, with the neutral gas density being so much higher than the ion density. This, and the fact that the inert ions are much more weakly coupled to an external electric field than the electrons, effectively keeps the ion temperature,  $T_i$ , close to the neutral gas temperature,  $T_g$ . Notably, the symmetric charge transfer (SCT) process, which has a very large cross-section because of its resonant character, is a major cooling factor, since it immediately slows the ions down to  $T_g$ : fast ions which undergo SCT instantly switch “identity” to fast Ar atoms, which are very quickly thermalized by the surrounding gas atoms. The original Ar atom, which has now become an ion, of course also has a thermal energy of  $\sim T_g$ . As we shall see later (Sect. 1.5), the SCT process is also of great importance in defining the energy-distribution of the ions hitting the cathodic surfaces in glow-discharges.

## 1.3 The Direct-Current Glow-Discharge

### Plasma ignition

Consider two parallel plates separated by a distance  $d$ , and with a potential difference  $V_0$ . Between the plates a gas at pressure  $p$  is introduced. Because of the electric field between the plates, electrons emitted from the cathode ( $z = 0$ ) will be drawn towards the anode ( $z = d$ ), creating electron-ion pairs on their way through collisions with neutrals. The ions generated in this way will travel in the opposite direction, bombarding the cathode and thereby causing new electrons to be emitted. The number of electrons emitted per bombarding ion is called the *secondary electron emission coefficient*,  $\gamma_{se}$ , and, besides the type of ion, depends on the cathode material (in the energy region relevant for our case,  $\gamma_{se}$  can be considered energy independent).

If the degree of ionization achieved via this process is high enough, a plasma is formed between the electrodes.<sup>4</sup> However, in order for the plasma to be self-sustainable, the generation of electron-ion pairs must be sufficient to make up

<sup>4</sup>To ignite the plasma in the first place, there of course must be some free electrons present in the gas to start an ionization avalanche. Even at room temperature, this will always be the case.

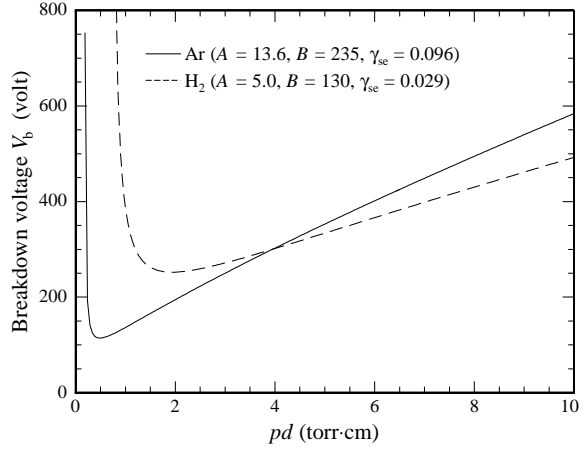


**Figure 1.3** The Paschen curve for Ar and H<sub>2</sub>, showing the breakdown voltage as a function of  $pd$  for a tungsten cathode, calculated using Eq. (1.13). An optimum arises because of the counterbalance between ionization rates and loss rates with changing gas pressure,  $p$ , and cathode-anode spacing,  $d$ .

for the loss of charged particles to the electrodes and chamber walls (i.e., in the direction perpendicular to the anode-cathode axis). At low pressures the ionization process becomes ineffective because the probability for electron-neutral collisions is too small, whereas at high pressures elastic collisions prevent the electrons from reaching energies which are high enough for ionization to occur and ion-neutral collisions increase the ion loss to the walls. Hence, for fixed  $d$ , an optimum pressure for plasma breakdown exists. Fig. 1.3 shows the breakdown voltage,  $V_b$ , for Ar and H<sub>2</sub> as a function of  $pd$ , called the *Paschen curve*, which can be expressed using the formula [9, p. 459]:

$$V_b = \frac{Bpd}{\ln(Apd) - \ln(\ln[1 + 1/\gamma_{se}])}, \quad (1.13)$$

where  $A$  and  $B$  are empirically determined coefficients expressing the ionization rate. Eq. (1.13) is quite easily derived by solving the rate equations for the electron and the ion fluxes.

Once the plasma has ignited it quickly ( $\sim \mu\text{s}$ 's) settles to a steady state configuration. It is the physics of this configuration which is the scope of this chapter. In Fig. 1.4 the qualitative characteristics of a DC glow-discharge are shown. As is apparent from the figure, the detailed features of a glow-discharge are not a simple matter, it exhibiting a large number of dark and light emitting (glowing) regions. In Sect. 1.6 we will have a closer look at these different regions of the glow-discharge and how they are formed. For now, it is not of importance to understand the full complexity revealed in the figure. Hence, I will concentrate on some of the basic and relevant features. The most important of these is the positively<sup>5</sup> charged *sheath region*, which forms adjacent to any electrode in

<sup>5</sup>Considering electropositive plasmas, as will be done throughout this thesis.

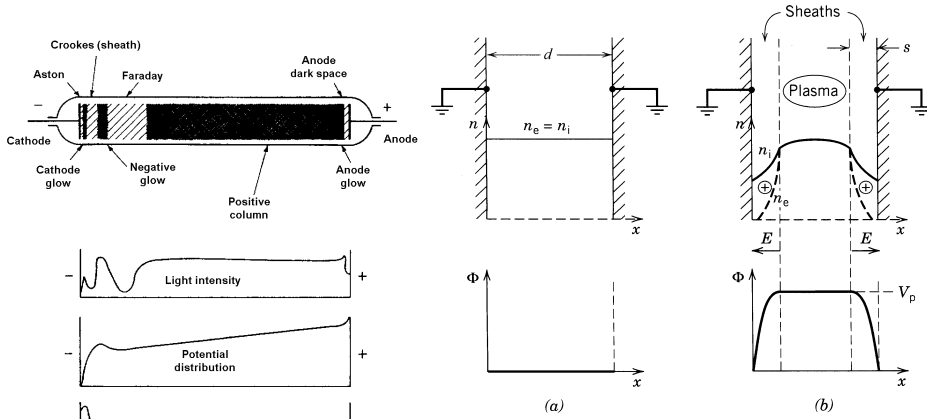


**Figure 1.4 (left)** Qualitative characteristics of a DC glow-discharge. The highly asymmetric features are a consequence of the difference in mass and hence mobility between the ions and electrons, resulting in the formation of a positively charged *sheath* region or *Crookes space* adjacent to the electrodes. Taken from Ref. 9.

**Figure 1.5 (above)** The formation of plasma sheaths: ion and electron densities (a) before and (b) after formation. Taken from Ref. 9.

contact with the plasma. The formation of this region is a consequence of the difference in mass and hence mobility between the electrons and the ions.

### Sheath formation

The basic principles leading to the formation of plasma sheaths can be understood from Fig. 1.5. Consider first the situation depicted in Fig. 1.5a, of a plasma of width  $d$  confined between two grounded ( $\Phi = 0$ ) absorbing walls. Since, on a whole, we have charge neutrality (i.e.,  $n_e \simeq n_i$ ) the electric potential,  $\Phi$ , and the electric field,  $E_x$ , is zero everywhere. Hence, the fast-moving electrons are not confined to the plasma and will rapidly be lost to the walls. On a short<sup>6</sup> timescale (Fig. 1.5b), this will lead to the formation of a net positive space-charge region ( $s \ll d$ ) near the walls, due to the presence of the more inert ions (i.e.,  $n_e \ll n_i$ ). This net positive space-charge leads to a potential profile,  $\Phi(x)$ , with a positive value,  $V_p$ , within the plasma, and rapidly falling to zero near

<sup>6</sup>By “short” we mean shorter than the timescale of ion motion but longer than that of electron motion. The thermal velocities of the electrons and the ions are  $(eT_e/m_e)^{1/2}$  and  $(eT_i/M)^{1/2}$  respectively, where  $m_e \ll M$  and  $T_e \gg T_i$ .

both walls (as dictated by the boundary conditions). Since the electric fields of this potential profile are directed from the plasma towards the walls, the negatively charged electrons are confined within the plasma while the positively charged ions entering the sheath-region are attracted towards the walls, bombarding them with an energy of  $\sim eV_p$ . As long as the ionization processes taking place within the bulk plasma can produce a sufficient supply of ions, the potential profile of Fig. 1.5b will remain steady, also on a longer timescale.

Typical values of the *plasma potential*,  $V_p$ , are around a few  $T_e$  (i.e., 1–10 V), which is needed to confine most of the electrons. The sheath thickness,  $s$ , as we shall see later, is of some importance. In principle, determining it is just a question of solving the Poisson equation in the sheath region, using the sheath charge density,  $n_s$ . If  $V_p$  and  $n_s$  are given,  $s$  has to be large enough to sustain the potential difference between the plasma and the grounded wall. Using the simplest approximation, known as a *matrix sheath*, we assume a uniform ion density in the sheath, which gives us (since  $n_e \ll n_i$ ):

$$n_s = n_i = \text{const.} \quad (1.14)$$

In this case, the Poisson equation is easily solved, choosing  $x = 0$  at the grounded wall:

$$\frac{d^2\Phi}{dx^2} = -\frac{en_i}{\epsilon_0}, \quad (1.15)$$

which yields, setting  $\Phi(x = s) = V_p$ , the matrix sheath thickness

$$s = \left( \frac{2\epsilon_0 V_p}{en_i} \right)^{1/2}. \quad (1.16)$$

In terms of the electron Debye length  $\lambda_{De} = (\epsilon_0 T_e / en_s)^{1/2}$  at the sheath edge, we get:

$$s = \lambda_{De} \left( \frac{2V_p}{T_e} \right)^{1/2}. \quad (1.17)$$

Hence, the sheath thickness at a grounded electrode is of the order of the electron Debye length (i.e.,  $\sim 0.01$  mm). Now, the case of a plasma confined between two grounded electrodes is not quite the situation we want to describe.<sup>7</sup> For a direct-current glow-discharge, one of the electrodes (the cathode) will have a large negative bias (usually between  $-200$  and  $-1000$  volts). The increased potential difference between the plasma and the cathode will of course, assuming  $n_s$  to be unaltered, lead to an increased sheath thickness. Within the matrix

<sup>7</sup>This would be the case if, for example, we were considering an rf-frequency discharge, where the electrons in the bulk plasma are *externally* heated by an oscillating electric field.

sheath approximation, we can simply make the substitution  $V_p \rightarrow |V_0|$ , where  $V_0$  is the cathode voltage. Taking  $V_0 = -400$  V for a typical plasma, we get  $s \simeq 0.1$  mm.

Although the approximations made here are somewhat crude, they serve well to give the reader a qualitative understanding of how the plasma sheath builds up, and what aspects are important in defining its thickness. The thicknesses derived here, however, are largely underestimated. In a moment, we will expand a bit on our theory for the sheath thickness, by introduction of the *collisional Child law*. Before doing this, however, let us first establish the basic characteristics of an actual steady-state, low-pressure, direct-current glow-discharge.

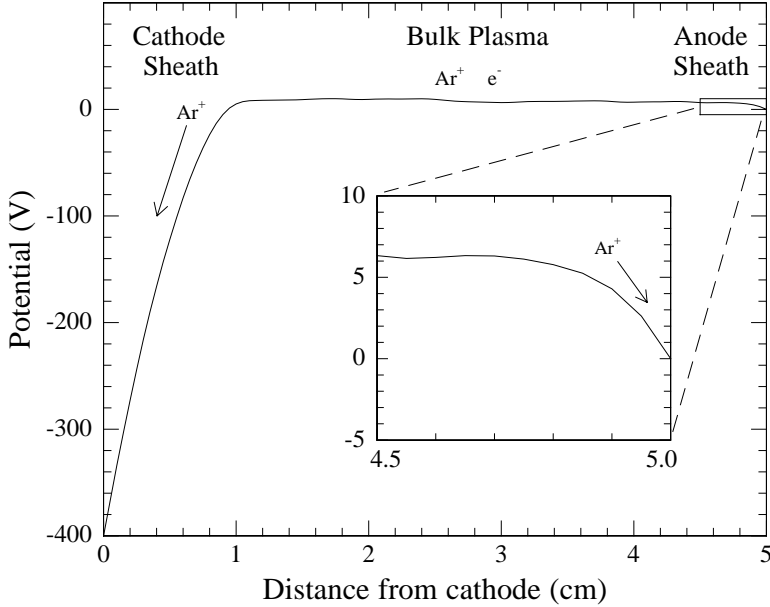
### Basic characteristics

Fig. 1.6 shows the steady-state plasma potential between the cathode and the anode of a computer-simulated argon glow-discharge, driven at a discharge voltage of  $V_0 = -400$  V and a pressure of 0.5 mbar. The figure reveals the three major regions of such a discharge:

- **The cathode sheath**, carrying all of the potential difference,  $V_0$ , between the cathode and the anode. Ions entering this region are drawn towards the cathode, bombarding it with high energies. However, because of collisions with neutral atoms, the ions do not gain the full potential energy  $eV_0$ , but end up with some energy-distribution. More on this in Sect. 1.5.
- **The bulk plasma**, with a slightly elevated potential,  $V_p \sim 8$  V in this case (clearly seen in subplot), which confines the electrons to this region. In principle, this region is the “actual” plasma, since it is here that the condition of quasi-neutrality is met (cf. the definition of a plasma).
- **The anode sheath** (subplot), is similar to the cathode sheath, but carrying a potential difference of only  $V_p$ . As at the cathode, ions are accelerated towards the anode, bombarding it with energies of  $\sim V_p$ .

Clearly, the sheath thickness values derived in the previous section are largely underestimated, suggesting that the matrix sheath assumption (Eq. (1.14)) does not hold, with  $n_s$  being too large. To elaborate on our sheath theory, we have to consider two important aspects of the sheath charge-density which were previously ignored:

1. As indicated in Fig. 1.6, ions entering the sheath are accelerated towards the cathode. This will lead to a gradual thinning of the ion density in the sheath as we approach the cathode.
2. As we saw in Sect. 1.2, the cross-section for ion-atom collisions for argon is quite high, with values of  $\sigma_i \sim 5 \times 10^{-15}$  cm<sup>2</sup>, which is equivalent to an



**Figure 1.6** Potential distribution of an argon DC glow-discharge. The curve stems from a simulation of an argon discharge, driven at a discharge voltage of  $-400$  V, a pressure of  $0.5$  mbar and a cathode-anode spacing of  $5$  cm.

ion collision mean-free-path of:

$$\lambda_i = \frac{1}{n_g \sigma_i} \sim 0.2 \text{ mm}, \quad (1.18)$$

at a gas density of  $n_g \sim 10^{16} \text{ cm}^{-3}$  (considering an ideal gas at pressure  $p = 0.5$  mbar and temperature  $T = 300$  K). Since the cathode sheath in Fig. 1.6 can be seen to be of the order of  $1$  cm, the kinetics of the ions in the cathode sheath must be expected to be collision-limited.

These two points must be included in the functionality of the sheath charge distribution,  $n_s$ .

## 1.4 The Collisional Child Law

Let us thus return to the problem of estimating the thickness of the cathode sheath. The problem with the matrix sheath approximation (Eq. (1.14)) is as

already mentioned, that the ion density,  $n_i$ , is overestimated and not uniform throughout the sheath. First of all, since the ions accelerate when they transverse the sheath, this will have an thinning-out effect on the ion density, leading to a sheath density function,  $n_s(x) = n_i(x)$ .<sup>8</sup> Furthermore, since the sheath thickness may well be significantly larger than the mean-free-path (mpf) for symmetrical charge exchange, we must expect the ions to undergo quite a number of collisions on their way through the sheath. This also, must be included in defining  $n_s(x)$ .

Instead of trying to figure out the exact functionality of  $n_s(x)$ , and solving the Poisson equation with it, let us take a more “experimentalist” approach to the problem. Although we cannot easily determine  $n_s(x)$ , measuring the discharge current,  $J_0$ , is straightforward. With this in mind, and assuming that we have no ionization in the sheath,<sup>9</sup> let us thus write:

$$n_s(x) = n_i(x) \quad \text{and} \quad u_s(x) = u_i(x) \quad (1.19)$$

$$n_i(x)u_i(x) = n_s(x)u_s(x) = j_0, \quad (1.20)$$

where  $u(x)$  denotes the velocity, and the discharge current-density,  $j_0$ , is a constant which we can assume that we know. Eq. (1.19) states the fact that the sheath charge density is equivalent to the ion density. Therefore, let us choose the ion-index “i” hence forward. Eq. (1.20) is merely the continuity of current-density, which must hold if we disregard ionization in the sheath. The ion velocity,  $u_i$ , can be connected to the electric field in sheath,  $E$ , through the relation  $u_i = \mu_i E$ , where  $\mu_i$  is the ion mobility. For the low pressure collisional case, which we are considering here, the ion mobility is approximately given by [9, p. 137].<sup>10</sup>

$$\mu_i \simeq \frac{2e\lambda_i}{\pi M |\mathbf{u}_i(x)|}, \quad (1.21)$$

where  $M$  is the ion mass and  $\lambda_i$  is the ion mean-free-path. Hence, the ion velocity can be expressed by:

$$u_i(x) = \mu_i E(x) \simeq \frac{2e\lambda_i}{\pi M |\mathbf{u}_i(x)|} E(x). \quad (1.22)$$

Eq. (1.22) embraces the two points mentioned at the end of the previous section, and which are neglected in the matrix sheath approximation: the acceleration of

<sup>8</sup>The assumption of  $n_s(x) = n_i(x)$  resides, since we still have  $n_i(x) \gg n_e$ . In other words, the sheath charge density is the ion density.

<sup>9</sup>Which we can readily justified. See for example Chapman [12, Chap. 4].

<sup>10</sup>In doing this, we are assuming that we have a constant uniform electric field,  $E(x) = E_0$ . Although this is clearly not the case, the approximate relation of Eq. (1.21) suffices for the calculations made here.

the ions in the sheath and its collision-limited nature. Inserting this in Eq. (1.20), gives us what we are looking for, namely an expression for the ion density which contemplates ion sheath kinetics:

$$n_i(x) = \frac{j_0}{[2e\lambda_i E(x)/\pi M]^{1/2}}. \quad (1.23)$$

Using Gauss' law we can solve for  $E$ :

$$\frac{dE}{dx} = \frac{ej_0}{\varepsilon_0[2e\lambda_i E(x)/\pi M]^{1/2}}, \quad (1.24)$$

which gives us

$$E(x) = \left[ \frac{3ej_0}{2\varepsilon_0(2e\lambda_i/\pi M)^{1/2}} \right]^{2/3} x^{2/3}, \quad (1.25)$$

where we have set  $E(0) \simeq 0$  at the sheath-bulk plasma interface. A second integration gives us the sheath potential function:

$$\Phi(x) = -\frac{3}{5} \left( \frac{3}{2\varepsilon_0} \right)^{2/3} \frac{(ej_0)^{2/3}}{(2e\lambda_i/\pi M)^{1/3}} x^{5/3}, \quad (1.26)$$

where we have set  $\Phi(0) = 0$ .<sup>11</sup> Taking  $\Phi(x = s) = -V_0$  we obtain:

$$\boxed{j_0 = \left( \frac{2}{3} \right) \left( \frac{5}{3} \right)^{3/2} \varepsilon_0 \left( \frac{2e\lambda_i}{\pi M} \right)^{1/2} \frac{V_0^{3/2}}{s^{5/2}}}. \quad (1.27)$$

(collisional Child law)

Eq. (1.27) is the *collisional Child law* for a low-pressure glow-discharge. Noting that the ion mean-free-path,  $\lambda_i$ , depends on the gas pressure,  $p$ :

$$\lambda_i = 1/(n_g \sigma_i) \quad \text{where} \quad n_g = p/(kT_g), \quad (1.28)$$

and where we have  $T_g \simeq 300$  K, we see that the Child law encompasses the balance which must exist between the basic discharge parameters; the current-density,  $j_0$ , the cathode voltage,  $V_0$ , and the pressure,  $p$ , by defining the sheath thickness,  $s$ . It is important to understand, that Eq. (1.27) is not a theoretical expression for the sheath thickness, in the sense that it *predicts* the thickness for a given set of parameters, since the discharge current-density,  $j_0$ , should also be an outcome of such a full theory. To make a complete theory, however, we need

<sup>11</sup>Thus disregarding the plasma potential,  $V_p \ll V_0$ .

a detailed knowledge of particle-loss rates, secondary electron emission coefficients, ionization rates and so on, for all regions of the discharge. By using the current-density as an input parameter, we avoid this, making quite a shortcut. And as mentioned before, from an experimental point of view, Eq. (1.27) is quite adequate as a tool, since the current-density is easily measured.

The basic assumption in the derivation of Eq. (1.27) is that the ion mobility is given by Eq. (1.21). If we change the pressure regime, this will not be the case. For completeness, and to clear the picture with any previous knowledge the reader might have, let us briefly look at some of these cases. For example, in the very-low pressure regime, the ions will not undergo any collisions in the sheath, and their velocity will therefore not be collision-limited, but space-charge-limited. In this case, we end up with an alternate Child law [9, p. 165]:

$$j_0 = \frac{4}{9} \epsilon_0 \left( \frac{2e}{M} \right)^{1/2} \frac{V_0^{3/2}}{s^2}. \quad (1.29)$$

(space-charge-limited Child law)

As can be seen, this expression has a slightly different interdependence of the discharge parameters, and does not depend on  $\lambda_i$ . Moving now to the high pressure regime, and hence highly collisional case, the ion mobility becomes diffusion-limited and hence independent of the ion velocity. In this case, the Child law becomes [9, p. 171]:

$$j_0 = \frac{9}{8} \epsilon_0 \mu_i \frac{V_0^2}{s^3}. \quad (1.30)$$

(diffusion-limited Child law)

For even more alternative Child laws see for example Vahedi *et al.* [13] or Jelić *et al.* [14], who also devise a theory for independent prediction of the current-density.

So, did we choose the right Child law in Eq. (1.27)? Let us compare with the simulated potential profile shown in Fig. 1.6. According to Eq. (1.26), the potential in the sheath should have a  $x^{5/3}$ -dependence. Writing  $\Phi(x)$  in a generalized form:

$$\Phi(x) = -V_0 \left( 1 - \frac{x}{b} \right)^a, \quad (1.31)$$

where  $a$  is the power and  $b$  the sheath thickness, we can make a numerical fit to the simulated data. Note, that we have written Eq. (1.31) on a form which puts the cathode at  $x = 0$ , and not at  $x = s$  as was done in the derivation of the Child law. Setting  $V_0 = 400$  V the fit shown in Fig. 1.7 yields:

$$\begin{aligned} a &\rightarrow 1.67(2) && \text{(power)} \\ b &\rightarrow 0.980(7) && \text{(sheath thickness [cm])} \end{aligned}$$

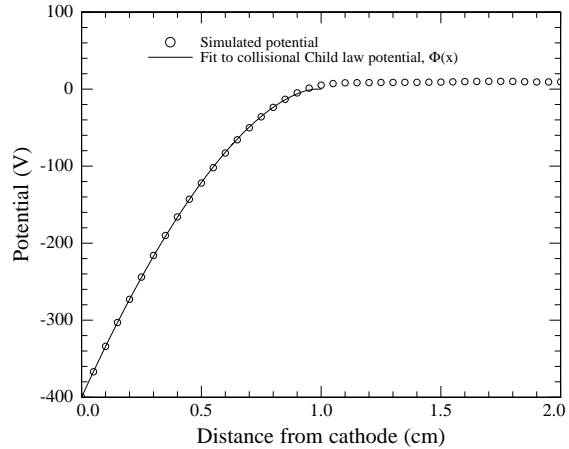


**Figure 1.7** A fit of the power law potential function given by Eq. (1.31) (solid line) to the computer simulated potential profile of Fig. 1.6 (open circles) in the range  $[0.0 \rightarrow 1.0]$ . See text for details.

which is in good agreement with the collisional Child law, which predicts a power of  $5/3 \simeq 1.67$ . The other Child laws have powers of 1.33 and 1.5 for the space-charge-limited and diffusion-limited cases respectively. Now what about the sheath thickness, which according to the fit is around 1 cm? From direct measurements of a glow-discharge with the same parameters as those used in the simulation, we can put  $j_0 \sim 0.05 \text{ mA/cm}^2$ . Inserting this in Eq. (1.27) yields  $s \simeq 0.6 \text{ cm}$ . Although this estimate is still somewhat lower than that of the simulation, it is a vast improvement over the matrix sheath thickness of  $\sim 0.01 \text{ cm}$ .

## 1.5 The Davis and Vanderslice Model

Now that we have established the discharge and understand the basic mechanisms leading to the formation of sheaths, let us have a closer look at the kinetics of the sheath ions. As mentioned earlier, because of collisions with neutrals (remember that  $\lambda_i \ll s$ ), ions transversing the sheath do not gain the full potential energy  $eV_0$ , but will end up with some final energy-distribution,  $f(E)$ , at the cathode. We shall use a slightly generalized version of the model proposed by Davis and Vanderslice [15] in 1963 to describe this distribution for the case of a mono-atomic discharge. This version was first proposed by Rickards [16] in 1984 and is an extension to a potential distribution of the form  $x^m$ . Just like Davis and Vanderslice's original function, the Rickards extension has a couple of built-in inconsistencies, the importance of which we shall have a look at in Chap. 3. For now, let us concentrate on the derivation of the distribution function. There are four basic assumptions to the model:

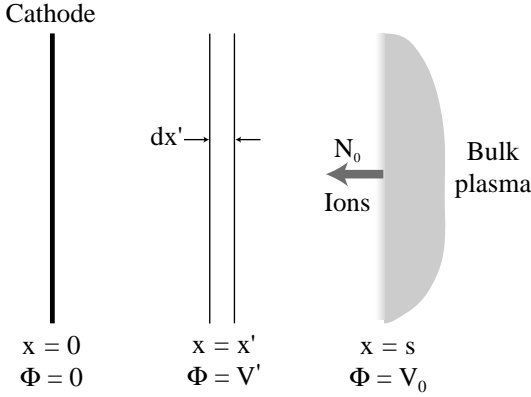


**Figure 1.8** The Davis and Vanderslice model for cathode ion energy-distributions. See text for details.

1. All the ions originate in the bulk plasma region (i.e., no ionization in the sheath).
2. In those collisions responsible for the energy-distribution, the ions lose all their energy in the process. This is the case for symmetric charge transfer (Sect. 1.2).
3. The ion-collision cross section,  $\sigma_i$ , is energy independent (see Fig. 1.2). This is a reasonable approximation over the energy range in consideration, since, as we shall see later, a vast majority of the ions will have energies below 10–20 eV.
4. The sheath potential has the form:

$$\Phi(x) = -V_0 \left(1 - \frac{x}{s}\right)^m + V_0, \quad (1.32)$$

where  $m$  is a constant and, for convenience, we have chosen ground potential at the cathode ( $x=0$ ). In the original paper Davis and Vanderslice assume a linear electric field, i.e.,  $m=2$ . On the basis of the discussion of Sect. 1.4 we choose  $m=5/3$ . The exact choice of  $m$ , however, is not of great importance for the conclusions and practical uses of the model we will be making.

The model used in the derivation of the energy-distribution is illustrated in Fig. 1.8. Obviously, the only way for an ion to reach the cathode with an energy of  $eV'$ , would be for it to undergo charge transfer at a point  $x'$  and then travel the way to the cathode without further collision. Since we assume not to have ionization in the sheath, the number of ions entering from the bulk plasma,  $N_0$ ,

will remain constant throughout the sheath.<sup>12</sup> Hence, the number of collisions occurring in the region  $dx'$  is given by  $N_0(dx'/\lambda_i)$ , where  $\lambda_i$  is the ion mean-free-path. The probability for any of these ions to reach the cathode without further charge transfer is given by  $e^{-x'/\lambda_i}$ , and, thus, the number of ions of energy  $eV'$  at the cathode is given by:

$$dN' = (N_0/\lambda_i)e^{-x'/\lambda_i}dx'. \quad (1.33)$$

Using Eq. (1.32) and setting  $\Phi(x') = V'$  we get the relationships

$$x' = s[1 - (1 - V'/V_0)^{1/m}] \quad (1.34)$$

and

$$dx' = \frac{s}{m}[1 - (V'/V_0)]^{(1/m)-1}d(V'/V_0). \quad (1.35)$$

Letting  $E = V'/V_0$  denote the ion energy normalized to the discharge voltage, we find the ion energy-distribution function by substituting Eqs. (1.34) and (1.35) into Eq. (1.33):<sup>13</sup>

$$\boxed{f(E) = \frac{1}{m} \frac{s}{\lambda_i} (1 - E)^{(1/m)-1} \exp \left[ -\frac{s}{\lambda_i} (1 - [1 - E]^{1/m}) \right]} \quad (1.36)$$

(cathode ion energy-distribution)

Eq. (1.36) is the Davis and Vanderslice distribution function generalized to an arbitrary potential distribution of the form given by Eq. (1.32). Note, that the (usually very small) fraction of ions that transverse the entire sheath *without any* collisions,  $e^{-s/\lambda_i}$ , is not included in Eq. (1.36). Hence, strictly speaking,  $f(E)$  is not normalized.<sup>14</sup>

The controlling parameter of the distribution function can be seen to be  $s/\lambda_i$ , which is the mean number of collisions an ion undergoes on its way through the sheath. Fig. 1.9 shows a number of distribution curves for  $s/\lambda_i$ -values between 0.5 and 70. For high values, i.e., many collisions, the cathode ions naturally have relatively low energies. Furthermore, the energy-distribution is clearly exponential, which can be seen by approximating Eq. (1.36) in the limit  $E \ll 1$  (which is valid for high values of  $s/\lambda_i$ ):

$$f(E) \simeq \frac{s}{m\lambda_i} \exp \left[ -\frac{s}{m\lambda_i} E \right]. \quad (E \ll 1) \quad (1.37)$$

<sup>12</sup>This is essentially only true for  $m = 2$ , since only a quadratic potential is equivalent to a constant charge density in the sheath. See for example Wroński [17] for more on this.

<sup>13</sup>Note the change of parameter  $dx' \rightarrow dV'$ , leading to the definition  $f(V'/V_0)dE = (V'/N_0)(dN'/dV')dE$ .

<sup>14</sup>This is easily seen by integration of  $f(E)$ , yielding:  $\int_0^1 f(E)dE = 1 - e^{-s/\lambda_i}$ .

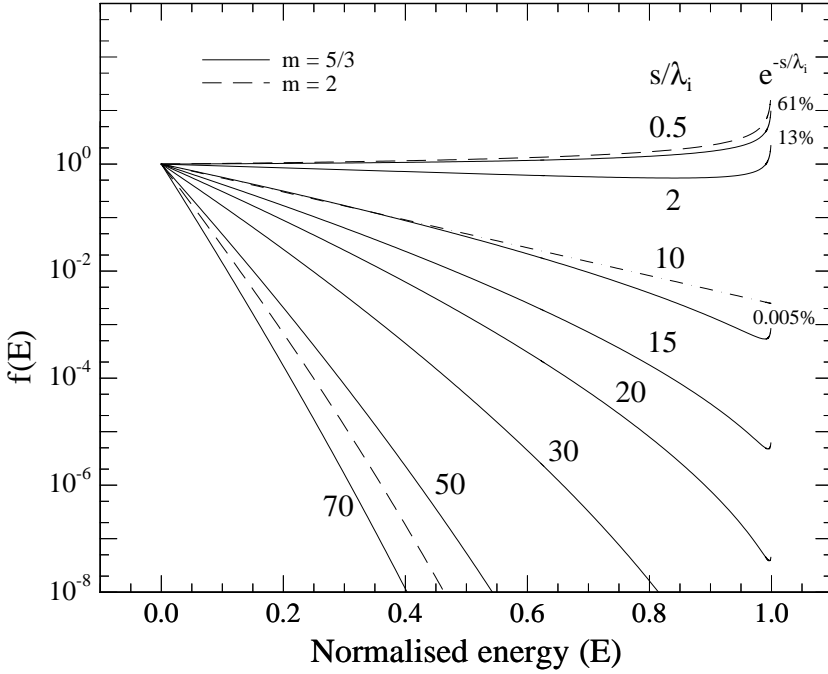


**Figure 1.9** Theoretical cathode ion energy-distributions (Eq. (1.36)) for values of  $s/\lambda_i$  between 0.5 and 70, using  $m = 5/3$  (solid lines) and  $m = 2$  (dashed lines,  $s/\lambda_i = 0.5$  and 70). The collisionless fraction,  $e^{-s/\lambda_i}$ , is shown for low  $s/\lambda_i$ -values. Also shown for the  $s/\lambda = 10$  case is the exponential approximation given by Eq. (1.37). For clarity, the origin of all the curves has been fixed at  $(0,10^0)$ .

As the number of collisions decreases, the distribution function starts to deviate from a clean exponential in the high-energy region. Furthermore, an increase in the high-energy peak is observed, corresponding to ions with a near-to maximum kinetic energy. Also shown (for  $s/\lambda_i = 10, 2, 0.5$ ) is the collisionless fraction,  $e^{-s/\lambda_i}$ .

## 1.6 Plasma Simulations

### Introduction

Even in the relatively simple case of a pure argon discharge, the collisional processes taking place between the three major species (electrons, neutrals and ions) are quite complicated. Hence, rather than trying to describe the plasma through analytical means, it can often be more fruitful to use computer simulation tech-

niques to gain information on some of the plasma properties. The problem that arises here, of course, is the vast amount of particles that make up a plasma. There are basically two computational methods which are used to deal with this problem. In the *fluid* approach, the ions and electrons are treated as a fluid rather than individual particles, thus allowing the use of fluid equations to calculate their kinetics. In the *Particle-in-Cell* (PIC) approach, it is assumed that the plasma can be described by a number of *computer particles*, each with charge and mass corresponding to a large amount of real particles, thus minimizing the amount of particles to be simulated. The neutral background gas can, in most cases, be treated as having a uniform and constant density. Collisions between the different species is treated as a separate problem, usually using a Monte-Carlo collision (MCC) model. See Lister [18] for a review on the subject of low-pressure discharge modeling.

A series of plasma simulations of an argon glow-discharge were performed in connection with the work presented in this thesis. These were performed with the *xpdp1* plasma simulation software [19, 20, 21, 22] developed by the *Plasma Theory and Simulation Group* at University of California, Berkeley [23]. The simulation methods of the program are based on the PIC and MCC models for particle kinetics and collisions respectively. A brief outline of the methods is given in the following. For more information and references see the PhD thesis of Mogensen [24] or the book of Birdsall and Langdon [22] from the Plasma Theory and Simulation Group, which is a thorough review of the techniques used.

### *The Particle-in-Cell method*

The program uses the *Particle-in-Cell* [22] method to simulate the electrons and ions, while the neutral gas is regarded as having a uniform and constant density. As already mentioned, instead of modeling the vast amount of particles which form a typical plasma discharge, the PIC method uses computer particles having the same mass-to-charge ratio as the real particles, but with absolute values corresponding to  $\sim 10^9$  particles. In this way only a corresponding fraction of particles have to be handled (typically around 6000 computer particles). Because of the cylindrical symmetry of the discharge, only one spatial dimension is considered, it being the one between the anode and the cathode, while the velocity of the particles is treated in all three dimension (1d3v model).

In the model, a spatial grid is defined between the electrodes of the discharge. For each grid segment, the charge- and current-densities of the computer particles within it are used to calculate the electric and magnetic fields at the grid points, taking into account the boundary conditions imposed by the electrodes. These fields are in turn used to calculate the forces acting on the computer particles by interpolation of the field values of the two grid points surrounding a segment. In this way the charge- and current-densities of the

computer particles are readjusted, thus closing the flow of the particle kinetics simulation.

### *The Monte-Carlo collision model*

The collisions in the plasma are accounted for using a Monte-Carlo collision model [21]. At the foundation of any Monte-Carlo simulation is the use of random numbers, which decide whether or not a particle is subjected to a collision, and what type of collision is to occur. Depending on the type of collision, random numbers are used to decide the angular and kinetic distribution of the product particles. Hence, in this type of Monte-Carlo simulation, each particle is characterized by some (energy dependent) collision probability, against which the random numbers are compared. This means that every computer particle must be evaluated in every time-step of the simulation.

A computationally more efficient approach is the *null-collision* method, which assumes that all the particles can be modeled by one, energy independent, collision probability. To do this, a new collision is introduced – the null-collision – which has a collision probability equal to the assumed constant probability minus the true collision probability for each particle. Hence, a null-collision is a collision which does not introduce any change to the particle involved. The simulation program can now randomly select a number of particles based on the (constant) collision probability, valid for all particles, and concentrate on evaluating this selected fraction particles, deciding which collision (including the null-collision) they are to undergo. Hence, by introducing the null-collision, the program must only evaluate a fraction of the computer particles for every time step.

The *xpdp1* v. 3.5 code can simulate He, Ar, O<sub>2</sub> and Cl<sub>2</sub> glow-discharges. While the anode is always grounded, the cathode can be given any time varying voltage dependence. For example, in this work a pulsed-DC voltage was applied. Because only one collision is considered in each time step the upper limit of the time step is around 10<sup>-11</sup> seconds.

## **The Ar glow-discharge**

A series of simulations of argon DC-pulsed glow-discharges were performed, mainly to gain some insight on the ion kinetics near the electrodes (energy and angular distributions). The results of these simulations will be presented in the following. Before doing this, however, let us have a look at some of the various plasma profiles which were extracted from the simulations. In Fig. 1.6 the plasma potential profile was shown, clearly indicating the existence of the cathode and anode sheath regions. However, as was revealed in Fig 1.4, the sheath

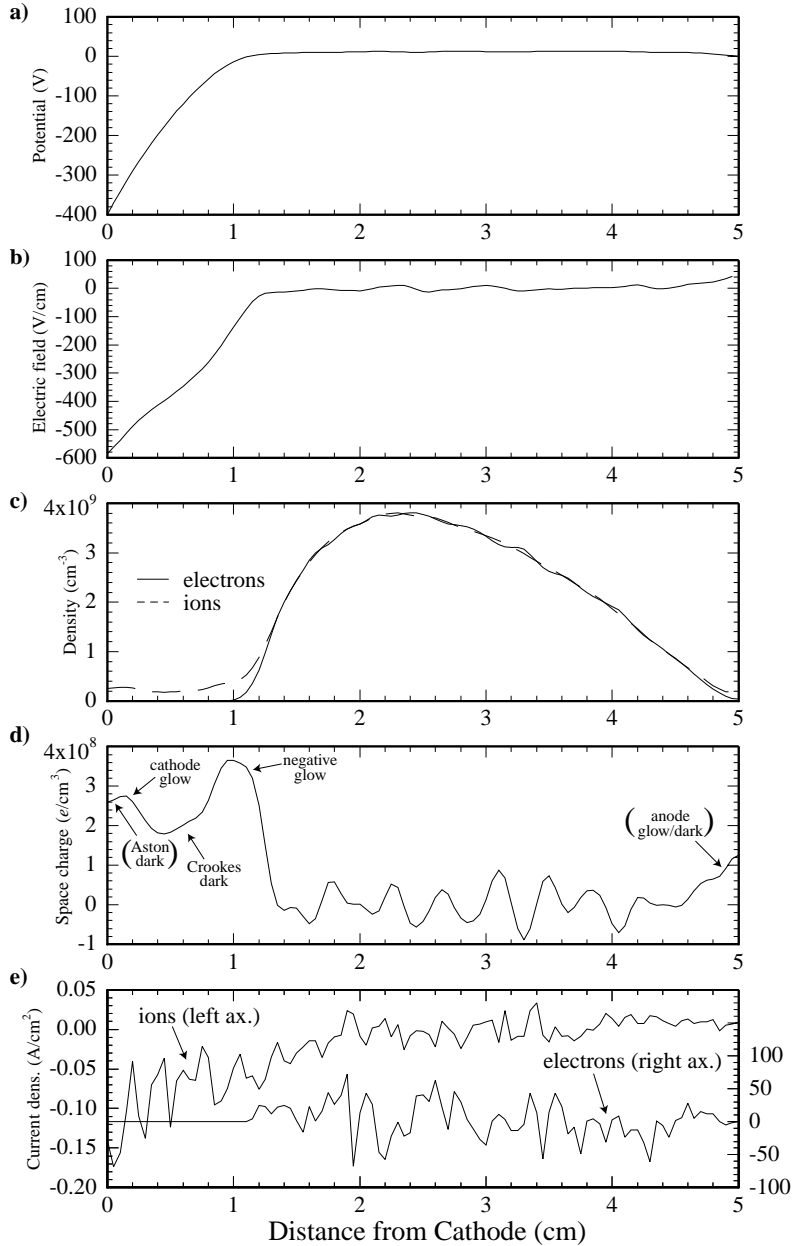


**Figure 1.10** Spatial profiles of **a)** the plasma potential, **b)** electric field, **c)** ion- and electron-density, **d)** space-charge density and **e)** ion and electron current-density. Simulated data for a 0.5 mbar, -400 V argon glow-discharge. See text for details.

regions contain a number of dark and light-emitting (glow) regions, the existence of which we are now able to understand on the basis of these simulations.

The simulation parameters were similar to those used in the experiments performed. When simulating Ar discharges, the collisional processes given in (1.7)–(1.11) are considered by the *xpdp1* code, with the collision cross-sections shown in Fig. 1.2. Another important, and somewhat crucial parameter is the secondary electron emission coefficient,  $\gamma_{se}$ , which is assumed here to have a value of 0.03. Since, essentially, it is the emission of secondary electrons from the cathode by ion impact which keeps the plasma “alive”, the exact value of  $\gamma_{se}$  must be expected to have a large influence on the steady state of the discharge. However, its exact value is not very well known, and, apart from the electrode material, also depends on the “dirtiness” of the metal. See, for example, Phelps and Petrović [25] for a review on this subject. Nevertheless, although a change in  $\gamma_{se}$  will have an effect on, e.g., the absolute value of the discharge current, the fundamental characteristics of the profiles are not expected to be influenced.

## Plasma profiles

Fig 1.10 shows the spatial profiles of the plasma potential, electric field, ion- and electron-density, space-charge density and ion and electron current-density. The curves stem from a simulation of an argon discharge with a pressure of 0.5 mbar and a cathode voltage of  $-400$  V. The discharge voltage was pulsed with on- and off-times of  $200 \mu\text{s}$ , and the profiles shown were extracted during the end of an on-pulse, thus eliminating any transient effects (as mentioned in Sect. 1.3, the steady state of a glow-discharge is reached within some  $\mu\text{s}$ 's).

The potential profile in Fig. 1.10a is equivalent to the one shown in Figs. 1.6 and 1.7, where the  $x^{5/3}$ -dependence of the sheath potential predicted by the collisional Child law was verified. As the potential profile dictates, the electric fields (Fig. 1.10b) are large in the sheath areas near the electrodes and virtually zero in the bulk plasma region. The origin of these electric fields is clearly seen in Fig. 1.10c, showing the ion- and electron-density. As expected, the ion and electron densities are more or less the same in the bulk plasma region, while the sheaths are depleted of electrons, thus resulting in a net positive space-charge from the ions.

If we subtract the electron density curve from that of the ions, we get the net space-charge profile shown in Fig. 1.10d. Comparing with the discharge image of Fig. 1.4, we can now begin to identify the different dark and glow regions of the cathode sheath. As is clear from Fig. 1.10d, two regions of relative high ion density exist in the cathode sheath (denoted “cathode glow” and “negative glow”), indicating that some degree of argon atom ionization is occurring in these regions. Now, as we saw in Fig. 1.2, the cross-sections for electron impact ionization and excitation of argon atoms have almost the same envelope, hence one would expect that regions with high degrees of ionization and excita-

tion are coincident. Since it is excitation of atoms which leads to light emission, these are also the optically visible regions of the discharge. As electrons are emitted from the cathode, they are accelerated towards the bulk plasma region. Since the threshold for ionization/excitation is  $\sim 20$  eV a thin region adjacent to the cathode exists, called the *Aston dark space*, where little ionization/excitation takes place (since the electrons have not yet been accelerated to energies which are sufficient for ionization). This thin region is barely visible in the charge density profile, and is in principle narrower than the spatial resolution of the plot — hence the parentheses. The first region of high intensity is the *cathode glow*, where the electrons have the optimum energy for ionization/excitation. As the electrons are accelerated even further by the strong electric field, the ionization/excitation rates decrease, resulting in yet another dark region called *Crookes dark space*. Upon entering the bulk plasma region, the electric field becomes too weak to accelerate the electrons, which are constantly being attenuated through elastic scattering with the neutral gas atoms. This effect creates a region of high intensity, called the *cathode glow*, since the electrons now again gain energies which are optimal for ionization/excitation. It is this region of the discharge which has the highest degree of light emission. At the anode similar effects create the *anode glow* and *anode dark space* regions (not discernable in the space-charge profile curve).

Although sheath ionization hence *does* occur, the main constituent ions of the sheath are nonetheless those originating from the bulk plasma. The seemingly highly irregular space-charge profile of Fig. 1.10d does in fact, upon integration, yield the electric field and potential curves shown in Figs. 1.10b and 1.10a respectively — the latter of which we have shown to have the  $x^{5/3}$ -dependence predicted by the collisional Child law (which ignores sheath ionization).

Finally, some interesting facts can be observed in Fig. 1.10e, showing the electron and ion current-densities. Firstly, near the cathode, the ion current-density attains relatively large negative values. These are the ions which are being accelerated towards the cathode — the ones which are the main scope of this thesis. The highly irregular shape in this region is probably because of the limited statistics of the curve.<sup>15</sup> Again, the depletion of electrons from the sheath is evident. Secondly, in the bulk plasma region, both the ion and electron current-densities are characteristic to that of thermal equilibrium, although not with each other. The mean kinetic energy of the ions and electrons is given by:

$$\langle E_{i,e} \rangle = \frac{1}{2} m_{i,e} \langle v_{i,e}^2 \rangle, \quad (1.38)$$

where  $m_{i,e}$  and  $v_{i,e}$  denote the ion and electron masses and velocities respectively. Since the ion and electron densities in the bulk plasma are the same, we

<sup>15</sup>The time-step of the simulation was  $2 \times 10^{-10}$  s, while the average time-separation between two cathode computer-ion *events* (i.e., a computer ion impinging on the cathode) was  $6 \times 10^{-8}$  s, over 300 times longer.

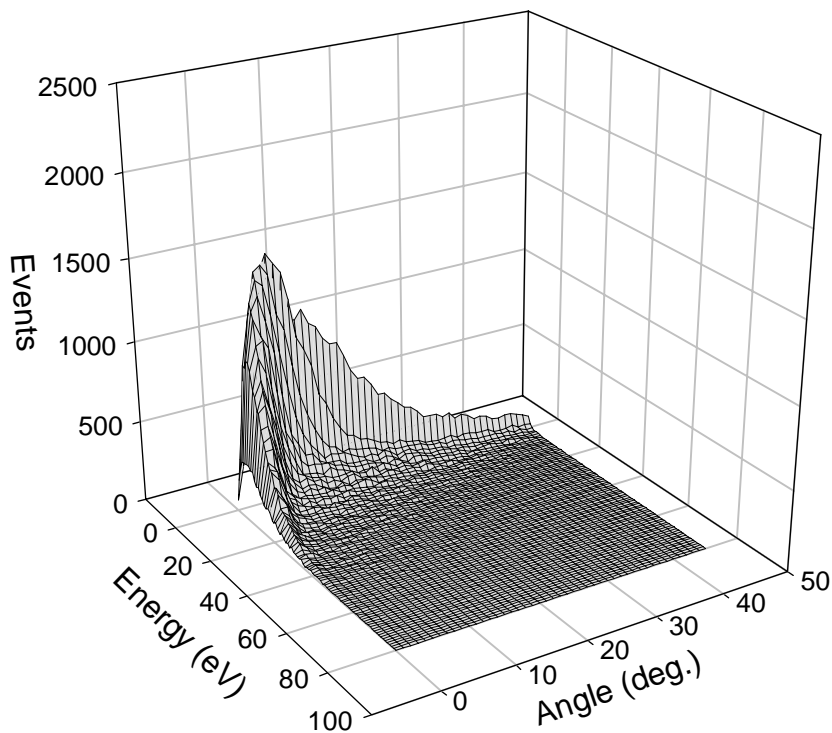


**Figure 1.11** Surface plot of the energy and incident angle distribution of  $\text{Ar}^+$  ions impinging on the cathode of an Ar glow-discharge (0.5 mbar,  $-340$  V). Simulated data.

can directly calculate  $\langle E_i \rangle / \langle E_e \rangle$  by computing the ratio of the mean squared ion and electron current-densities in Fig. 1.10e. Doing this in the region  $\{2 \rightarrow 4\}$  cm yields  $\langle E_i \rangle / \langle E_e \rangle \sim 0.015$ . Since the ions are close to room-temperature,  $T_i \sim 0.026$  eV, we can derive an electron temperature of  $T_e \equiv \langle E_e \rangle \sim 2$  eV, which is a very reasonable result.

### Ion energy and angular distributions

Every time a particle hits the cathode of the simulated discharge, its kinetic energy and incident angle is recorded. Fig. 1.11 shows a 3D plot of these data, as the total number of such events as a function of energy and incident angle. The data stems from a simulation of an argon discharge with a pressure of 0.5 mbar and discharge voltage of  $-340$  V. The discharge voltage was pulsed with on- and off-times of  $200 \mu\text{s}$ , and the simulation ran for 14 ms of discharge-time (around a

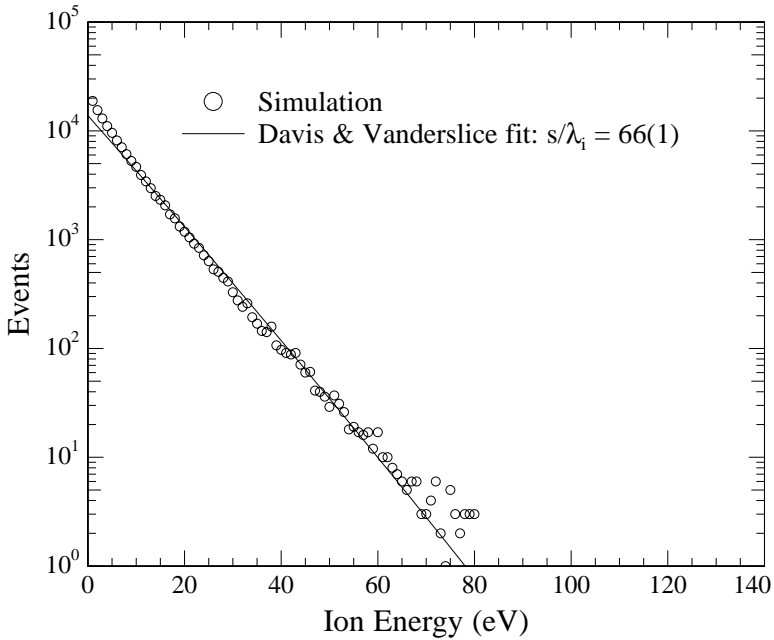


**Figure 1.12** Simulated  $\text{Ar}^+$  energy-distribution ( $\circ$ ) and a fit of the Davis and Vanderslice model to the data ( $—$ ). Extracted from the data shown in Fig. 1.11.

couple of days worth of computer-time), equivalent to 35 voltage cycles. As the figure shows, the ion energies are relatively low. This, as explained in Sect. 1.5, is because of the symmetrical charge transfer (SCT) process between  $\text{Ar}^+$  and  $\text{Ar}$ , which effectively slows down the ions on their way through the cathode sheath.

Fig. 1.12 shows the *energy* distribution of the simulated events ( $\circ$ ), obtained by “collapsing” the *angle*-axis of Fig. 1.11, so to speak. Also shown in the figure is a fit to the data ( $—$ ) of the Davis and Vanderslice model, given by Eq. (1.36), yielding a ratio of  $s/\lambda_i = 66(1)$  between the sheath thickness and the mean-free-path (mfp) for ion-neutral collisions. Since the sheath thickness is around 1 cm,<sup>16</sup> this gives us a simulated/theoretical mfp of  $(\lambda_i)_{\text{sim}} \sim 0.15$  mm. Now, since the mean number of collisions per ion transversing the sheath is  $s/\lambda_i \sim 66$ , it is safe to assume that the energy of the *average* ion at its *last* collision before hitting the cathode is around  $340 \text{ eV}/66 \sim 5 \text{ eV}$ . The SCT-scattering cross-section for 5 eV

<sup>16</sup>Probably even slightly larger, since this simulation had a discharge voltage of  $-340 \text{ V}$ , and not the  $-400 \text{ V}$  of Fig. 1.10, thus slightly underestimating the simulated value of  $\lambda_i$  derived here.

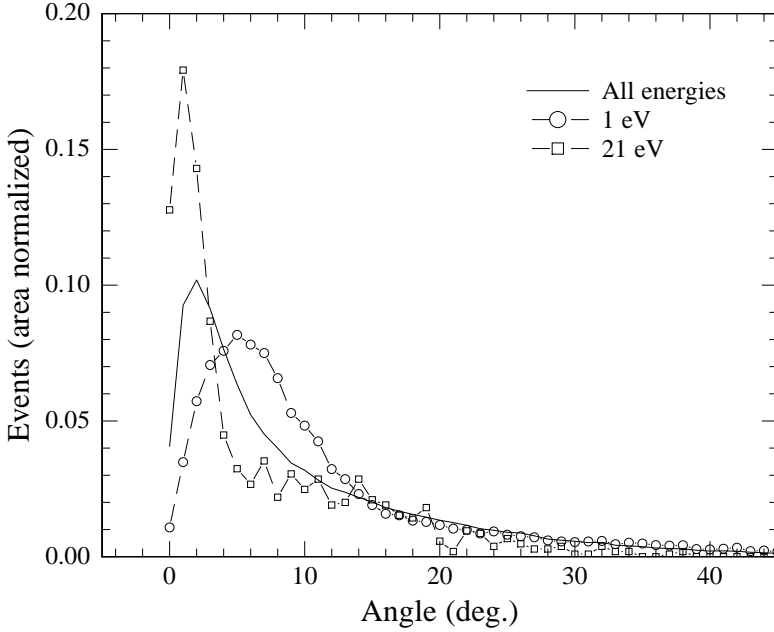


**Figure 1.13** Simulated  $\text{Ar}^+$  angular distribution for all ion energies (—) and for 1 eV (○) and 21 eV ions (□). Extracted from the data shown in Fig. 1.11.

ions is  $\sigma_i \sim 5.4 \times 10^{-15} \text{ cm}^2$  (see Fig. 1.2 on page 10), and this value thus serves well as an overall average. From this we can calculate the expected mfp:

$$(\lambda_i)_{\text{exp}} = \frac{1}{n_g \sigma_i} \sim 0.19 \text{ mm}, \quad (1.39)$$

where we have used the gas density  $n_g \sim 10^{16} \text{ cm}^{-3}$  (0.5 mbar, 300 K). Hence, the value of  $(\lambda_i)_{\text{sim}}$  derived from the theoretical fit to the simulated data is in good agreement with the known scattering cross-section for SCT. This, in itself, is of course not very ground breaking, since the simulation is directly based on these same scattering cross-sections. It does, however, give credit to the simulation code and, most importantly, to the adequacy of the Davis and Vanderslice model in this respect.

Although the simulated energy-distribution is well described by the Davis and Vanderslice model, one can see, most notably at very low energies, a discrepancy between the two. One probable reason for this is that elastic scattering is not included in the Davis and Vanderslice model. As is evident from Fig. 1.11,

the low-energy ions have quite a wide angular distribution, with incident angles of up to several tens of degrees. Fig. 1.13 shows the incident-angle distribution of the simulated events (—) in Fig. 1.11 (once again, obtained by “collapsing” the *energy*-axis of the 3D plot). Also shown in the figure, is the incident-angle distribution for 1 eV (○) and 21 eV (□) ions, clearly showing that whereas the low-energy ions have a quite wide distribution, the distribution narrows down rather quickly with increasing ion energy. Although the simulation presented here is valid only for the mono-atomic argon discharge, the fact that only the low-energy ions can have a wide energy-distribution will always be the case. If a high-energy ion is to have a large incident angle, it must undergo some collision(s), giving it an equally large momentum (i.e., equivalent to several hundred eV) in a direction perpendicular to the discharge axis. Since no strong electric fields exist on this axis, no conceivable collision process can do this. Ions that *do* have a large incident angle, must have this because of numerous collisions on their way through the sheath, and hence, they will also have a small energy.

---

# 2

---

## EXPERIMENTAL

---

*This chapter deals with the experimental set-up and techniques which have been used during this project. The set-up itself consists of two main sections: the plasma chamber, where the plasma itself formed, and the Hidden EQP, which is the mass and energy analysis device used for studying the plasma. Apart from these two sections, there are of course a number of “buts’n’bolts”, peripheral equipment, and so on, that goes with the set-up. All this will be described in some detail in the following sections. Finally, the Rutherford backscattering spectrometry (RBS) technique will be briefly described.*

### 2.1 Introduction

Fig. 2.1 shows a photograph of the set-up, as it stands at the *Tribology Centre* at the *Danish Technological Institute* (TI) in Århus.<sup>1</sup> On the left-hand side one sees the plasma chamber: a stainless steel cylindrical vacuum chamber with a length and diameter of 30 cm each. Basically, the inside of the chamber consists of two electrodes between which the glow-discharge is formed. One of the electrodes has an orifice (30-300  $\mu\text{m}$  in diameter) at the center, through which the different plasma species (ions, atoms or molecules) can enter into the Hidden EQP. This segment, which is seen on the right-hand side in the picture, consists of an ion/atom extraction device, a 45° electrostatic deflector section used for energy analysis, a quadrupole mass spectrometer (QMS) and finally a secondary electron multiplier (SEM) for ion detection. The entire analysis segment is mounted within a two-stage differentially pumped system, driven by two turbo-pumps.

---

<sup>1</sup><http://www.uk.teknologisk.dk>



**Figure 2.1** A photograph of the main experimental set-up used in this work. On the left-hand side one sees (1) the plasma chamber, and on the right-hand-side (2) the ion/atom extraction and analysis segment, consisting of (3) a 45° deflector field energy analyser, (4) a quadrupole mass spectrometer, (5) a secondary electron multiplier and finally (6) the RF-head which supplies the beam-optics electrode voltages and the RF-voltage for the quadrupole mass spectrometer. Also seen in the photograph is (7) the trigger-box, (8) the current-probe, (9) a gas-flow meter, and (10) the membrane valve leading to (12) the Edwards rotary pump. Down in the left corner one sees (11) the MSIU control unit.

In this way, the operating pressure of the EQP ( $10^{-6}$  mbar) can be maintained whilst having pressures in the mbar-range within the plasma chamber. The Hiden EQP is fully computer controlled, both when it comes to operation of the plasma chamber, the EQP itself, and, of course, data acquisition.

The apparatus was purchased at *Hiden Analytical Ltd.* (Warrington, England) for about D. Kr. 1 mill. and arrived at TI in June 1997, some months before I entered the project. As is usually the case with new equipment, quite some time is spent figuring out how to use it — *properly*. Reading manuals does take you quite a bit down the road, but far from all the way. Actually, manuals might even lead you down the wrong path! It is important to devise some kind of routine in using this kind of equipment, to assure both physically sensible and reproducible results, and this takes time. About one year in this case — a time filled with *EUREKA!*'s — and their subsequent retraction. Ultimately, however, a good and quite straightforward routine was conceived. I will not tire the reader with all the details hereof; the practical procedures I propose one to use when working with the Hiden EQP set-up are described in App. A, which is intended as a *practical* user's manual.

## 2.2 The Plasma Chamber

Fig. 2.2 shows a schematic diagram of the plasma chamber and part of the ion/atom extraction segment of the Hiden EQP. The plasma chamber itself is a cylindrical stainless steel (SS) vacuum chamber with length and diameter of 30 cm. Within it, there are two circular electrodes, one of which has an orifice at the center, serving as the “eye” of the Hiden EQP. The feedstock gas is supplied through a gas shower and kept at a preset pressure by a membrane valve leading to a rotary pump.

### The electrodes

Both the movable electrode (denoted “Anode” in Fig. 2.2) and the fixed electrode (denoted “Cathode”) are circular and have a diameter of 12 cm. Both are made of stainless steel and have exterior high-voltage connections. A front view image of the fixed electrode is shown in Fig. 2.3. A thin grounded shield, also made of stainless steel, encircles each of the electrodes at a 1-mm distance, so as to ensure a well-defined electrode region. Essentially, this prevents the plasma from igniting anywhere else than directly in front of the electrodes, and the cylindrical space-region they form. Apart from the shield, the fixed electrode consists of an outer and removable inner electrode, which are in electrical contact with each other. The orifice, through which the atoms/ions can enter the Hiden EQP, is located at the center of the inner electrode. Hence, by changing this electrode, different orifice sizes could be used (30, 100, 200 and 300  $\mu\text{m}$

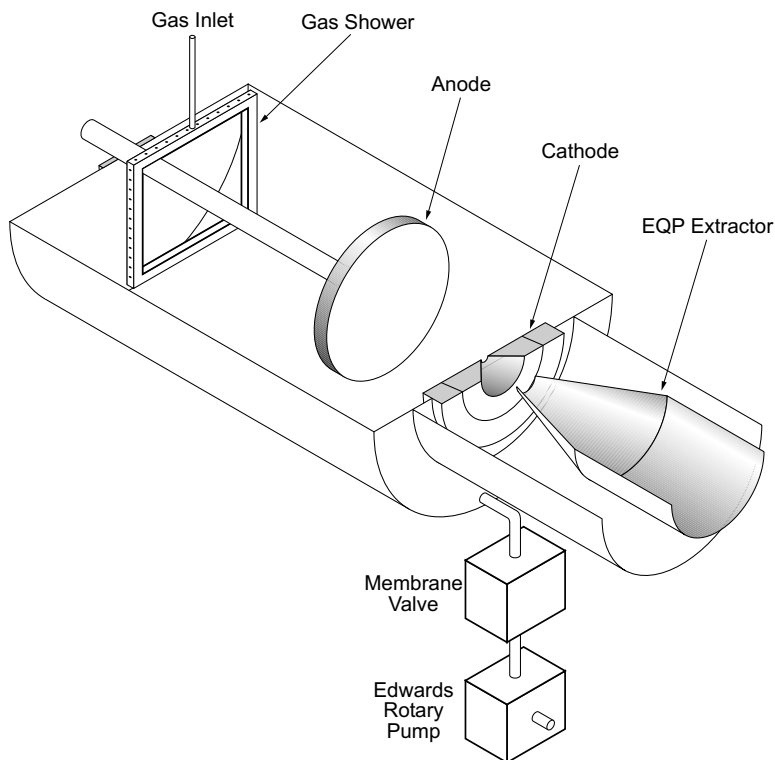


**Figure 2.2** The plasma chamber and the Hidden EQP (partly shown).

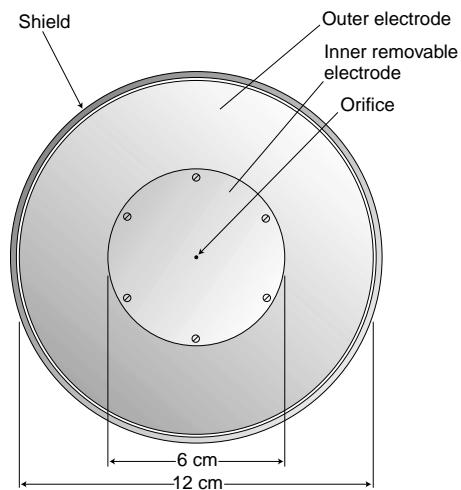


**Figure 2.3** Front view image of the fixed electrode. The inner electrode, containing the orifice, can be changed. In this way, orifices of 30, 100, 200 and 300  $\mu\text{m}$  could be used. This also gives one the possibility to change part of the cathode material, by evaporating a metallic film (e.g., aluminium) onto it.

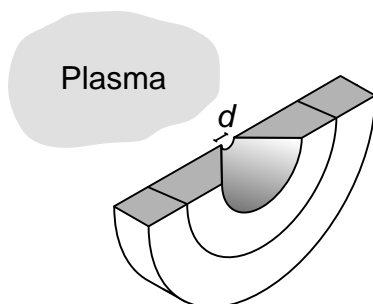


**Figure 2.4** Cross-sectional view of the orifice. Not to scale.

are available). Furthermore, this gives one the possibility to easily change (part of) the electrode material by evaporating a metal film onto the inner electrode. Some of the experiments reported in this thesis were performed with an inner electrode containing a 5000-Å thick aluminium layer (see Sect. 4.6). Changing the movable electrode (i.e., the “Anode”) material can be done by attaching a metallic plate of equal dimension (i.e., circular with a diameter of 12 cm) to it, containing a film of the desired electrode material on one side. This was successfully done with both aluminium and gold films using stainless steel plates (see Sect. A.2 for a more detailed description of how to do this).

## The orifice

The orifice, as already mentioned, is located at the center of the inner electrode. A cross-sectional view a typical orifice can be seen in Fig. 2.4. Orifices of 30, 100, 200 and 300  $\mu\text{m}$  could be fitted by changing the inner part of the fixed electrode. However, care has to be taken in choosing the orifice size. A large orifice naturally increases the number of particles that will enter into the Hidden EQP, hence improving the sampling efficiency and final counting rate of the SEM, thus yielding better statistics of the final spectra. However, there are a number of criteria which must be met, all of which dictate a maximum orifice diameter:

1. The orifice must be small enough to allow pressures in the mbar-range in the plasma chamber, while maintaining the working pressure of  $10^{-6}$  mbar within the Hidden EQP.
2. The presence of the orifice itself may not interfere notably with the plasma itself (e.g., by alteration of the discharge because of the small perturbation the orifice imposes to the geometry of the electrode or through field penetration from the Hidden EQP).

3. The orifice must fulfil the *efusive source criteria*, to ensure that the composition of the gas is maintained when passing through the orifice (only of importance when sampling neutral atoms).

The first two criteria are easily met or tested. Firstly, the pressure within the Hidden EQP is constantly monitored during operation. The 200  $\mu\text{m}$  orifice was the largest one used in the experiments, and did not result in any pressure problems. Secondly, as we saw in Chap. 1, typical sheath thicknesses, are of the order of  $s \sim 1$  cm. Hence, since all the dimensions of the orifice, which have values of about  $d \leq 300 \mu\text{m}$ , are significantly smaller than the sheath thickness,  $s$ , the presence of the orifice will only have very little influence on the plasma itself [26].

The third criteria, however, is much more restrictive although it can be relaxed when only *ion*-extraction is considered. If the composition of the sampled neutral gas is to be the same as in the plasma chamber, the orifice should act as an efusive source [26, 27]. For the orifice to be efusive, it is necessary to ensure that a molecule/atom can leave the plasma chamber and enter the extraction segment without making any collisions. This means that the dimensions of the orifice, notably the diameter,  $d$ , should be smaller than the mean-free-path (mfp) for elastic collisions between neutrals,  $\lambda_{\text{el}}$ , i.e.,

$$d \lesssim \lambda_{\text{el}}. \quad (2.1)$$

This mean-free-path is given by [28]:

$$\lambda_{\text{el}} = \frac{1}{4\sqrt{2}nr^2}, \quad (2.2)$$

where  $n = 2.4 \times 10^{16} \text{ cm}^{-3}$  is the ideal gas density at a pressure of 1 mbar at room temperature, and  $r$  is the radius of the neutral atom. The resulting mean free paths for a number of typical discharge gases are shown in Tab. 2.1, and their values thus estimate the maximum orifice diameters allowed.

In most of the experiments an orifice of 100  $\mu\text{m}$  was used, which showed in all cases to be the optimal choice. 200  $\mu\text{m}$  is also usable, but the 300  $\mu\text{m}$  cannot

GAS	AT. RADIUS ( $\text{\AA}$ )	$\sigma$ ( $10^{-15} \text{ cm}^2$ )	mfp ( $\mu\text{m}$ )
Ar	1.43	2.57	114
H <sub>2</sub>	1.38	2.39	122
N <sub>2</sub>	1.57	3.10	96

**Table 2.1** Atomic radius, elastic collision cross-section and mean-free-path (mfp) for typical discharges gases at a pressure of 1 mbar at room temperature. See Ref. 28 for details.

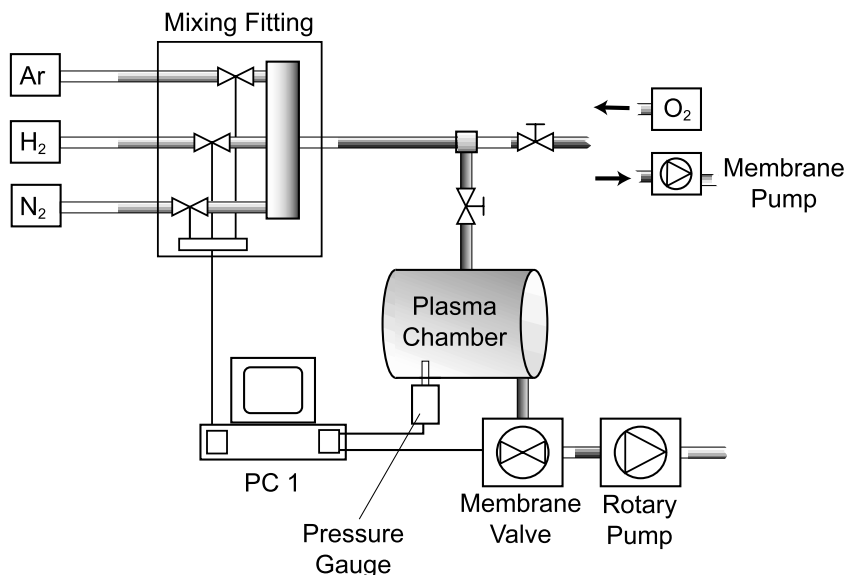


Figure 2.5 Schematic diagram of the gas supply and control system.

be recommended. Naturally, the 30  $\mu\text{m}$  orifice does not pose any problems in fulfilling the above mentioned criteria, but the statistics of the resulting spectra are not very good. Again, it should be noted that Eq. (2.1) does not need to be fulfilled in ion-extraction mode, which, by far, is the one most relevant to this work.

## The gas supply system

As mentioned earlier, the Hiden set-up is located at the Tribology Centre at the Danish Technological Institute in Århus. This allows us to use some of the gas supply and high-voltage facilities present there. Fig. 2.5 shows a schematic diagram of the gas supply and control system used with the Hiden set-up. Basically the system consists of two independent parts: a gas supply system, which provides the discharge gas at a predefined gas mixture and flow rate, and a pressure control system which stabilizes the pressure in the plasma chamber at a predefined value.

The argon, hydrogen and nitrogen gases<sup>2</sup> are led into a PC-controlled *mixing fitting*, allowing the flow-rate of each individual gas to be adjusted between 5–

<sup>2</sup>TiCl<sub>4</sub> was also available.

PARAMETER	RANGE	
Ar flow	5–150 slh	<sup>a</sup> The minimum achievable base pressure, with full pump and no gas flow (gas valve closed), was $2 \times 10^{-3}$ mbar. <sup>b</sup> Negative bias. The discharge current should be kept below 300 mA. <sup>c</sup> The rise and fall times of the pulses are around 1 $\mu$ s.
H <sub>2</sub> flow	5–400 slh	
N <sub>2</sub> flow	5–20 slh	
Pressure	0.05–5.00 mbar <sup>(a)</sup>	
Cathode voltage	100–1 000 V <sup>(b)</sup>	
Pulse on time	4–1 000 $\mu$ s <sup>(c)</sup>	
Pulse off time	10–1 000 $\mu$ s <sup>(c)</sup>	

**Table 2.2** Possible ranges of the main discharge parameters.

400 slh depending on gas (see Tab. 2.2). Hereafter the (mixed) gas flows through stainless-steel tubes ( $\varnothing$  6 mm) to a junction with two paths. One leads to the plasma chamber itself while the other was used for either adding additional gases (e.g., oxygen) or for decreasing the mixed gas flow-rate with a membrane pump. The latter was necessary, for example, when using multi-component gas mixtures where one component had a very low concentration ( $< 5\%$ ), which was only achievable with a high flow-rate of the other gases. Finally, the gas is fed into the plasma chamber through a *gas shower*, which consists of 4 interconnected stainless-steel tubes with small holes for gas exhaust (see Fig. 2.2).

The pressure in the plasma chamber was measured with a Tylan General cold-cathode pressure gauge and feedback stabilized at a pre-set value via a PC-controlled membrane valve which leads to an Edwards 80 two-stage rotary pump (80 m<sup>3</sup>/h). In this way, the gas pressure could be stabilized between 0.05–5.00 mbar. The base pressure of the plasma chamber was typically around  $2 \times 10^{-3}$  mbar, which was achieved with the gas valve closed and full pumping speed.

## Voltage control and data acquisition

Fig. 2.6 shows a schematic diagram of the voltage supply system and data acquisition set-up, each of which is controlled by a separate PC. The high-voltage (HV) supply used with the Hiden set-up is part of a commercial *Rübig* (Wels, Austria) PACVD plant, used at the Tribology Centre for the deposition of TiN coatings. When not in use for this, the power supply, together with the gas-supply facility, could be used with the Hiden set-up.

The on- and off-pulse times, and voltage of the high-voltage pulses are controlled via a computer (PC 1, which also controls the gas-supply) which is connected to the *Rübig* power supply. In Tab. 2.2 the possible ranges of the voltage parameters are shown. The HV-signal is fed through a *voltage divider* with a 1:100 output which is used for triggering and monitoring purposes, while the HV-signal itself is connected to one of the electrodes of the plasma chamber (in

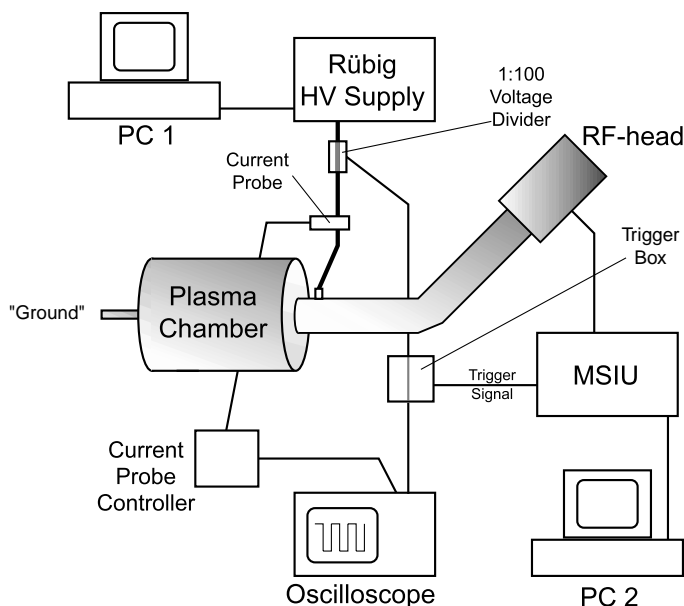


**Figure 2.6** Schematic diagram of the voltage supply and data acquisition system.

the figure, it is connected to the fixed electrode). In most cases, the other electrode would be grounded by short-circuiting it with the plasma chamber itself. The HV-current was measured with a Tektronix A6303 *current probe* which, via a control box, was connected to a Hewlett Packard HP-54600B digital *oscilloscope*. Also connected to the oscilloscope, is the monitoring signal originating from the 1:100 voltage divider. In this way, time resolved measurement of the discharge current and voltage could be performed.

The Hiden EQP, consisting of an energy and a mass analyser, and a SEM for ion detection, is fully controlled by the MSIU interface (*Mass Spectrometer Interface Unit*). This unit was in turn connected with a computer (PC 2), serving as a user interface and control center. The details of the EQP will be described in the following section. For now, it should merely be noted that the HV monitoring signal is led through a *trigger box*, which converts the voltage profile into a standard 0/+5 V TTL signal, which subsequently is fed into the MSIU. Hence, knowing the instantaneous state of the cathode voltage, the SEM could be configured to sample within a specified time-window (4–999  $\mu\text{s}$ ) with respect to the voltage profile. In this way, time-resolved measurement was possible.

## 2.3 The Hiden EQP

### Main characteristics

In short, the Hiden EQP (*Electrostatic Quadrupole Probe*) is a 45° sector field ion energy analyser combined with a quadrupole mass spectrometer. The probe is capable of acquiring mass spectra, energy spectra and appearance potential profiles,<sup>3</sup> allowing detailed analysis of positive ions, negative ions, radicals and neutrals. The probe head is mounted at a distance of 4.4 mm from the orifice of the fixed electrode of the plasma chamber. The EQP has a mass range of 300 amu and an energy range of 1 100 eV, the later of which is achieved by mounting the electrodes of the EQP on an adjustable high-voltage (0 to ±1 000 V) reference potential (the energy range of the EQP itself is ±100 eV). The ion detection sensitivity of the EQP is more than 6 decades. This is achieved by mounting the EQP within a two-stage differentially pumped system (driven by two Pfeiffer turbo pumps), which keeps the operating pressure within the EQP below 10<sup>-6</sup> mbar, while allowing pressures within the plasma chamber in the mbar-range.

A diagram of the EQP is shown in Fig. 2.7. The EQP has two fundamental modes of operation: *RGA mode*, which is used for rest gas analysis and radical detection, and *SIMS mode*, which is used for positive and negative ion analysis. The two modes differ only in the extraction segment, in as much as an *ionization source* is used in RGA mode to ionize neutrals entering the EQP and for performing appearance potential profiling. The main sections of the EQP are:

- **Extraction section** (Extractor, Lens1). This part consists of a pencil shaped extractor head (see Fig. 2.2), situated at a distance of 4.4 mm from the orifice. It has a circular entrance with a diameter of 700 μm. The extractor head is followed by a focusing lens.
- **Ionization Source**. In RGA mode, this is where the neutral gas atoms are ionized. The ionization potential is adjustable, thus allowing appearance potential profiling of neutrals and radicals.
- **Decelerating section** (Axis, Lens2, Quadrupole Lens). Here the ion-beam is decelerated and focused prior to entering the energy filter.
- **Energy analysis section** (Energy Filter, Focus2). Only ions with an energy of ~ 40 eV will be able to pass the 45° electrostatic field bend of the EQP.
- **Mass filter** (QMS). Here, rapid mass separation is performed with a radio-frequency mass-to-charge ratio spectrometer.

<sup>3</sup>The appearance potential is the electron energy at which electron impact ionization occurs.

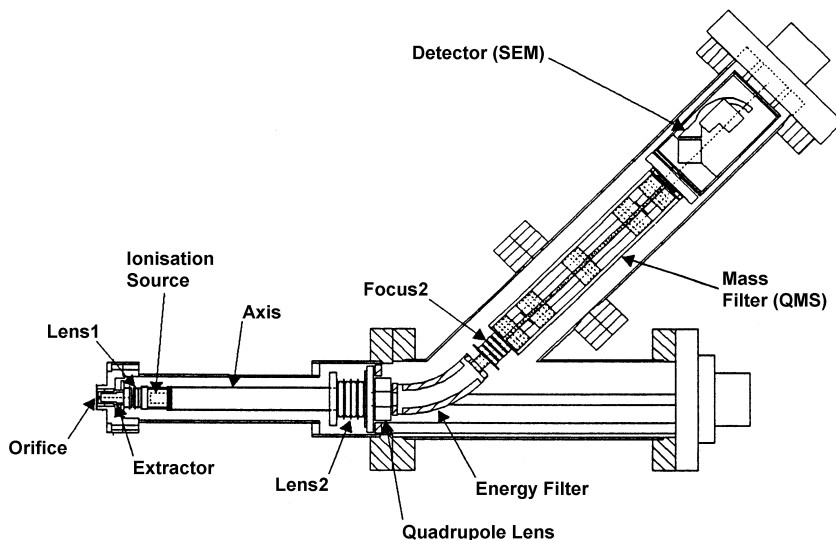


Figure 2.7 Diagram of the Hidden EQP.

- **Detector (SEM).** Finally, the ions that make it all the way, and hence have a well defined kinetic energy and mass, are detected by a conventional secondary electron multiplier.

The first four sections are completely electrostatic, and mainly consist of a more or less complicated configuration of electrodes constituting the *beam-optics* section. The purpose of this section is to extract, focus, and energy-analyze the ions traveling through it.

In the following, a short theoretical and practical description will be given of the different parts of the EQP.

### *The extraction section*

The first thing to do is to get the particles that enter the Hidden probe through the orifice of the fixed electrode successfully on the way on their quest through the beam-optics section. In RGA mode, the particles that are to be analyzed have no charge, and hence there is not much one can do, at this point, to electrostatically redirect astray particles towards the extractor head. Hence, one must rely on diffusion of the neutral particles from the (high-pressure) plasma chamber to the (low-pressure) ionization source of the EQP. Of course, when looking at neutrals, the density of particles in the plasma chamber is quite large and they will all have a room temperature thermal energy-distribution (i.e., they

all have an energy of  $\sim 0.026$  eV and the same angular distribution). Hence, in this case, representative sampling is merely a question of acquiring a sufficient amount of particles for the SEM to detect, which is not a problem. For the case of ion sampling, however, the situation is a bit more complicated. As was shown in Sect. 1.6, these particles must be assumed to have both a wide energy-distribution, ranging from 0–1 000 eV depending on the cathode voltage, and some angular distribution, which in turn depends on the ion energy (see Fig. 1.11). To achieve representative sampling of the ions leaving the orifice opening, it is imperative that as all these ions find their way into the EQP with equal — or at least similar — ease. To achieve this the potential of the extractor head must be at least some 20 volts<sup>4</sup> below the potential of the cathode (considering positive ions), so that astray ions (i.e., ions with a large incident angle) are attracted towards the extractor head opening.

### *The ionization section*

To make the neutral particles, which one wants to analyze when in RGA mode, sensitive to the beam-optics and mass analysis sections of the EQP, it is necessary to ionize them. This is done with a dual-filament electron-impact ionization source, which forms the ions at a preset potential energy. Furthermore, by scanning the ionization energy, appearance potential profiling is possible.

### *The decelerating section*

As already mentioned, the purpose of this section is to focus and, most importantly, decelerate ions of a particular initial kinetic energy to an energy of  $\sim 40$  eV, which they need to pass the 45° bend of the electrostatic energy analyser.

The electrostatic beam-optics section, starting with the extractor head, and ending with the energy filter, consists of 8 separate electrodes (7 in RGA mode), each with an individual voltage setting. The exact values of these settings determine which ions, i.e., which “kinetic energies”, will make it passed the energy filter. Hence, an energy scan of an ion with a particular mass is made by varying the voltage of some of these electrodes. In doing this, there are two criteria which must be fulfilled:

1. Naturally, the variation in electrode voltages must result in an actual scan of the ion energies between 0 eV and the maximum ion energy;
2. this, however, must be done while sustaining the focus and acceptance of the EQP. Or — at least keeping it at an optimum.

---

<sup>4</sup>Determined experimentally.

Finding out how to do this properly turned out to be somewhat time-consuming. Initially, referring to the Hiden EQP manual, we used the  $\pm 100$  eV scan functionality of the EQP, by breaking up an energy scan in 200 eV bits through a sequential shifting of the reference potential by 200 V. The results were, although usable, quite unsatisfactory, as this procedure resulted in inhomogeneous energy spectra with clearly unphysical characteristics (e.g., see Figs. 4.11 and 4.12 on p. 97). The reason for this was that it was not possible to sustain a uniform or optimal acceptance of the EQP over the total energy range using this scan method. Apparently, the  $\pm 100$  eV energy scan functionality of the EQP does not comply fully with the two criteria stated above. The right thing to do, as it turned out, was to simply scan the “reference” voltage, keeping the “energy” parameter of the EQP constant. More on this on p. 46ff.

### *The energy filter*

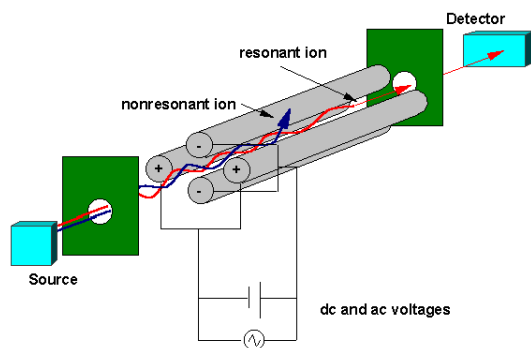
The energy filter is a  $45^\circ$  sector field energy analyzer. Ions entering the sector field are deflected according to their kinetic energy, so that only ions which have a transfer energy of  $\sim 40$  eV pass the bend. An energy resolution of  $\pm 0.75$  eV is provided by the manufacturers.

If we choose the input ion velocity in the  $x$ -direction then, upon transversing the sector field, the ion will deflect a distance  $s_y$  in the  $y$ -direction, given by:

$$s_y = \frac{1}{4} l^2 E_y \sqrt{\frac{q}{\mathcal{E}}}. \quad (2.3)$$

where  $l$  denotes the length of the sector field section,  $E_y$  denotes the sector field size,  $q$  the ion charge and  $\mathcal{E}$  the input ion energy. The first thing one notices is that  $s_y$  does not depend on the ion mass; large masses deflect more slowly but have an equally longer transfer time and, hence, these two mass dependencies cancel. Secondly, it should be noted that the sector field analyzer separates the *energy-to-charge* ratio ( $\mathcal{E}/q$ ). The choice of using a fixed input energy is also apparent from Eq. (2.3). As can be seen, the ion deflection is proportional to the inverse of  $\sqrt{\mathcal{E}}$ . Since the window of the sector field must have a finite size  $\Delta s_y$ , which defines the energy resolution, a variable input ion energy (in which case one would perform energy separation by scanning  $E_y$ ) would result in an energy resolution having some inverse dependence of the ion energy itself, which is inconvenient, and would furthermore lead to poor resolution at low energies. To avoid this, a fixed input ion energy is chosen, using the beam-optics section to decelerate/accelerate ions of a particular EQP-entrance energy to the pass-energy of the sector field. Since this is merely a shift in the kinetic energies of the ions, and no “windowing” is applied, a fixed and satisfactory energy resolution is achieved in this way.

**Figure 2.8** Schematic diagram of a quadrupole mass spectrometer (QMS). Ions with a charge-to-mass ratio which resonates with the settings of the QMS will pass, while non-resonant ions will collide with the electrodes.



### *The mass filter*

The mass filter section consists of a standard quadrupole mass spectrometer, a schematic diagram of which is shown in Fig. 2.8. It consists of four parallel metal rods which generate an electrical quadrupole field, driven by a superposition of a DC voltage and a radio-frequency AC voltage; two opposing rods are connected electrically and have a potential  $\Theta(t) = U + V \cos(\omega t)$ , while the same potential of opposite sign,  $-\Theta(t)$ , is applied to the other pair. This time-varying electric field affects the trajectories of the ions traveling through it in such a way, that only ions of a certain mass-to-charge ratio  $m/q$  travel all the way through the mass filter, while all other ions are thrown out of their path. The low-mass ions are removed by the RF field, while the high-mass are removed by the DC field. By varying the voltages,  $U$  and  $V$ , and/or the frequency,  $\omega$ , of the oscillating component a mass spectrum can be obtained.

### **Angular acceptance**

A large part of the initial work with the Hiden EQP was concentrated on gaining an idea of its sensitivity. That is, how well the measured energy spectra of the ions passing through the cathode orifice reflect the actual energy-distribution of the ions impinging on the cathode surface. As was shown in Sect. 1.6, these ions have an energy-dependent angular distribution, some of them hitting the cathode with angles of up to several tens of degrees. The question is, whether or not these ions are able to transverse the entire EQP. And might this ability be energy-dependent, thereby complicating matters even more?

To answer these questions, and to get some general information on the dependencies of the electrode voltages of the EQP, the beam-optics section was simulated using the *SIMION* ion optics simulation software [29]. This software is a professional beam-optics simulation tool that is able to calculate the potential of an arbitrary matrix of electrodes and to simulate the kinetics of charged particles in these potentials. Fig. 2.9 shows an image of the electrode configura-

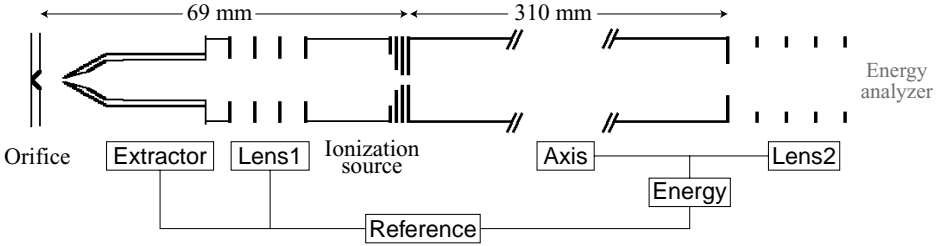


**Figure 2.9** The electrode configuration of the Hidden EQP beam-optics section as it was simulated with the SIMION software (except for the gap in the “Axis” section, needless to say).

tion which was used for these simulations, consisting of the cathode orifice and the beam-optics section of the EQP. To determine the acceptance angle of a specific electrode configuration, ion trajectories with different initial ion incident-angles were calculated, noting the maximum angle with which the ion could reach the energy analyser without hitting one of the electrodes. A small program was written for *SIMION*, automating this process, so that the angular acceptance for different ion-energies could be determined, whilst scanning the electrode voltages in such a way that an actual energy-scan was simulated. Fig. 2.11 shows the acceptance-angle curves determined in this way, for a number of different energy-scanning methods which were investigated. Before looking at the acceptance-angle profiles of Fig. 2.11, however, some comments should be made on the various scan methods used.

### Scan methods

There is a big degree of freedom in choosing the absolute and relative values of the electrode voltages (there are actually several more electrodes than shown in Fig. 2.9, but these are not of importance to the acceptance-angle). Hence, it is necessary to optimize the voltage of these electrodes to get the maximum yield. In particular, it was noted that Lens1 was very sensitive to the ion energy, when making ion energy scans by scanning the Energy parameter (see Fig. 2.9) as proposed by Hidden. This is equivalent to a simultaneous scan of the Axis and Lens2 electrodes (as illustrated in the figure). Fig. 2.10 shows *measured* Lens1-scans (solid lines) for a number of fixed ion-energies, equivalent to a number of fixed Energy parameter settings. As can be seen, the optimum (negative) Lens1 voltage increases numerically with increasing ion energy or Energy value. Hence, whilst making an Energy-scan, the Lens1 voltage has to be scanned simultaneously in such a way that its voltage follows the Energy parameter. In other words, to make an optimal energy scan, the Energy parameter *should* be scan-

ning the Lens1 voltage as well. One way of doing this is by making a *covariant* scan of the Lens1 voltage with the Energy parameter. Another way of doing it, as is clear from Fig. 2.9, is by scanning the Reference parameter instead, *if-and-so* the Extractor electrode may also be varied. As it turned out, doing this does not present any problems, as long as the voltage difference between the cathode and the extractor head does not exceed the breakdown voltage between the two. At the low pressures of the 1. pumping stage ( $\sim 10^{-4}$  mbar) this will not occur within any practical voltage range,<sup>5</sup> which is readily verified by inspection of the Paschen curve in Fig. 1.3 (page 12), where here we have

$$pd = 10^{-4} \text{ mbar} \times 0.44 \text{ cm} = 4.4 \times 10^{-5} \text{ mbar}\cdot\text{cm}.$$

The *major* advantage of performing Reference-scans, however, is that this parameter is not limited to a 200-V range like the Energy parameter is, so that ion energy measurements performed by Reference-scanning do not have to be broken into 200-eV parts (the benefit of which is clearly seen by comparing Figs. 4.11 and 4.12 on p. 97 with Figs. 4.7 and 4.8 on pp. 88–89).

The dashed curves in Fig. 2.10 show the square<sup>6</sup> of the acceptance angles of simulated Lens1-scans as derived using *SIMION*. Clearly, these curves follow the general trend of the measured curves, thereby giving some credit to the simulations. It can also be seen that the Lens1-profile widens with increasing ion energy, reflecting the fact that high-energy ions are less sensitive to the beam-optics in general.

### *The low-energy angular acceptance problem*

Now to the Hidden EQP acceptance-angle profiles of Fig. 2.11. As these simulated curves reveal, the angular-acceptance is quite narrow for ion-energies above  $\sim 50$  eV and increases towards lower energies, reflecting the fact that low-energy ions which are astray are easier to deflect. However, despite the superior acceptance at low energies, it is in this region that acceptance problems will occur, since it is here the wide angular-distribution exists. The figure shows simulated curves for the three scan methods discussed in the previous paragraph. As can be seen, both covariant scans and reference scans have a far better overall acceptance in the low-energy region. The peak structure of the fixed-Lens1 scan reflects the actual value of the Lens1 voltage during the scan.<sup>7</sup> The fact that the fixed-Lens1 curve has a somewhat better acceptance at *high*

<sup>5</sup>If it, for some reason, *does* occur, it would immediately be observed as an “unphysical” increase of the ion intensity at *low* energies during measurement.

<sup>6</sup>Since the measured intensity is proportional to the *area* of the orifice.

<sup>7</sup>The reason that the “fixed Lens1” scan exceeds the covariant and reference scans at this point is that the Lens1 and Reference voltages can only be scanned in integral values, so that optimal scans are not possible for these scan methods. This is a restriction of the Hidden EQP, not *SIMION*.

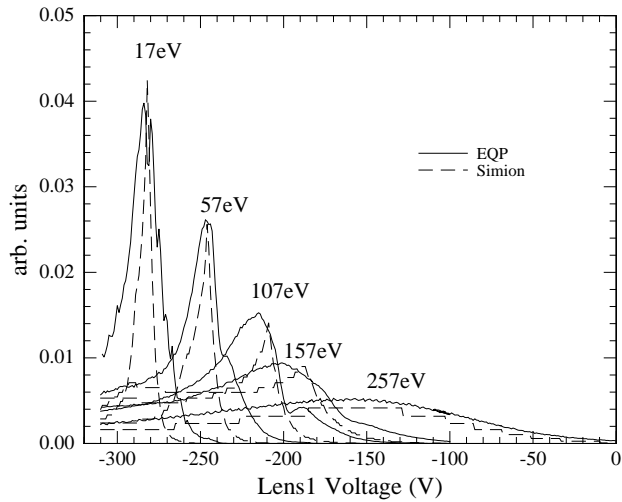


**Figure 2.10** Measured ion-intensity (solid lines) and the square of the acceptance-angle profiles (dashed lines) for a number of fixed ion-energies.

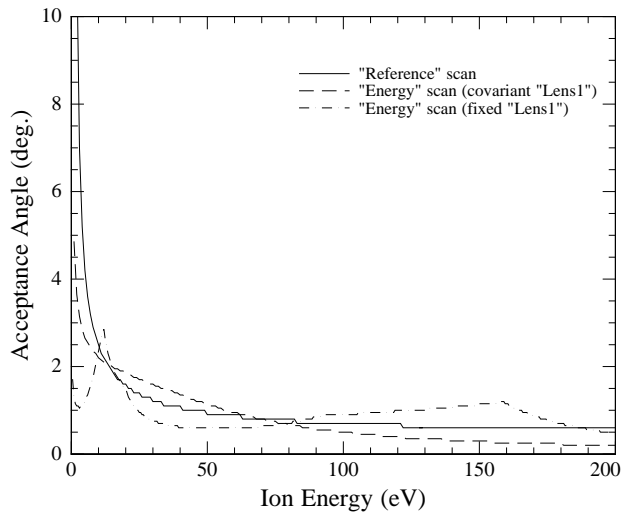


**Figure 2.11** Simulated Hidden EQP acceptance-angle profiles for three different scanning-methods.

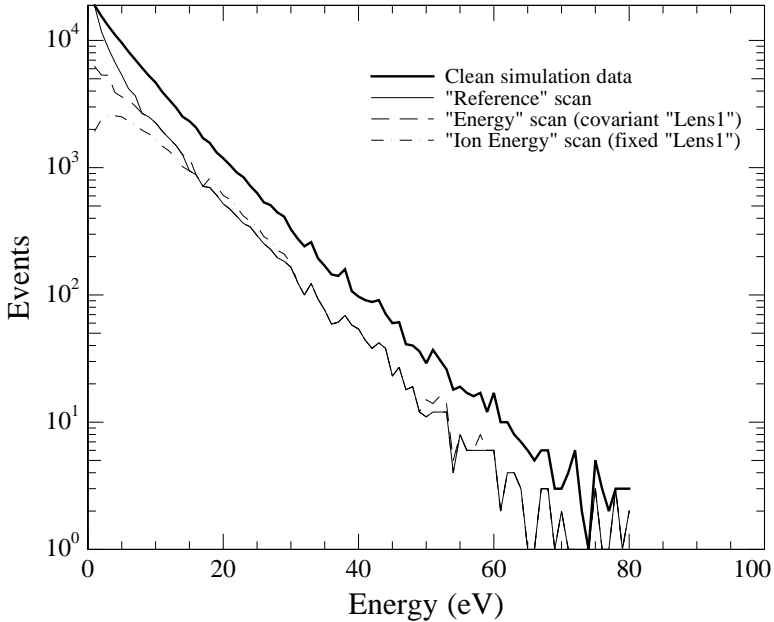


**Figure 2.12** The simulated ion energy-distribution of Figs. 1.11 and 1.12 (thick solid curve) and what their appearance after passing the beam-optics section (thin curves).

ion-energies is irrelevant, since the high-energy ions will have a next-to-zero incident angle.

This is also clear from Fig. 2.12, which shows the simulated ion energy-distribution of Fig. 1.12 on p. 30 (thick solid curve) and what this ion energy would look like after passing through the beam-optics of the Hiden EQP (thin curves). These three *appearance* profiles were made by taking the simulated ion-event data of Fig. 1.11 (p. 29) and using the acceptance curves of Fig. 2.11 to decide whether or not each individual ion-event would pass the beam-optics section or not. As the figure shows, all three scan methods yield the same appearance profiles in the high-energy region. In the low-energy region the covariant scan method seems to be the one which best reflects the actual ion energy curve, although the reference scan method has a better yield. The fixed-Lens1 method is clearly the worst of the three.

However, the appearance profiles of Fig. 2.12 only reflect the case of the mono-atomic Ar discharge. For other discharges the situation in the *low-energy* region might change, making the reference scan more reflective of the actual

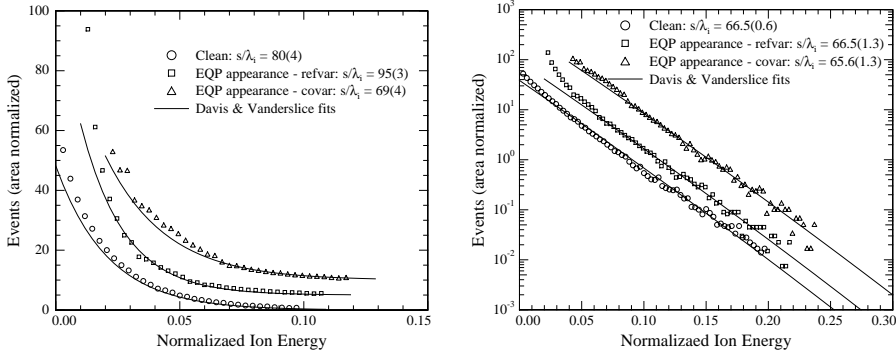


**Figure 2.13** Simulated ion energy-distributions ( $\circ$ ) and their appearance after passing through the beam-optics section of the EQP using the reference ( $\square$ ) and covariant ( $\triangle$ ) scan methods. **Left:** linear resolution and **right:** logarithmic resolution.

distribution than the covariant scan. Or both equally bad. The bottom line is, that for ion-energies below  $\sim 20$  eV, we do not know how well the measured ion energy-distributions reflect the actual ones. In most cases however, for example when considering physical sputtering, it is the *high-energy* ions which are of most interest, so this is not really a problem. The only situation where an equally good knowledge of the low-energy ions is important is when comparing *total* ion-intensities (i.e., the integrated ion energy-distribution curves) with, for example, the discharge current. In this case, every ion counts, irrespective of energy or incident angle. I shall address these issues when they arise (Chap. 4).

### Sensitivity of the Hidden EQP

Fig. 2.13 shows the curves of Fig. 2.12 on a linear (left) and a logarithmic scale (right). Also shown in the plots are the best fits of the Davis and Vanderslice distribution to these data (—). A comparison of these two plots immediately establishes the importance of the logarithmic sensitivity of the Hidden EQP. If only a linear sensitivity (equivalent to around 2 decades) is available, no consistent  $s/\lambda_i$ -values can be extracted from the data, since in this case we are confined to the very low-energy part of the spectra. Because of the angular distribution of the low-energy ions, the EQP acceptance is very sensitive to the choice of scan method in this region. On a logarithmic scale however, where more than 6 decades are available, this very low-energy part may be ignored. And as the right-hand-side plot reveals, the extracted  $s/\lambda_i$ -values for both scan methods agree with the “clean” simulated data within their statistical errors.

The plots of Fig. 2.13 show that the limited angular acceptance of the EQP

is adequately compensated by its high measuring sensitivity. Since the simulated data used here constitute a worst-case scenario for the EQP: very low ion energies and poor statistics, the performance for discharges with a higher fraction of high-energy ions is expected to be even better.

## 2.4 Rutherford Backscattering Spectrometry

In this work, Rutherford backscattering spectrometry (RBS) was used to measure the thickness of thin films prior to and after being subjected to a glow-discharge sputtering process. The theory of RBS is well-covered in textbooks, e.g., Feldman and Mayer [30]. Here, only the main theoretical aspects of the technique and characteristics of the RBS facility at Århus University will be given.

### Theory

RBS is a non-destructive spectrometric technique, in which the backscattered ions of a light particle (typically H or He) primary MeV-ion beam impinging on the measured sample are detected. The backscattered ions consist of primary ions which have undergone elastic scattering with the atomic nuclei of the sample. An ion with an initial energy  $E_1$  and mass  $M_i$  will after elastic scattering have an energy  $E_2$  given by [30]:

$$E_2 = \left( \frac{\sqrt{M_t^2 - M_i^2 \sin^2 \theta} + M_i \cos \theta}{M_t + M_i} \right)^2 E_1 \quad (2.4)$$

$$\equiv K(\theta)E_1, \quad (2.5)$$

where  $M_t$  is the target atom mass,  $\theta$  the scattering angle and  $K(\theta)$  denotes the kinematic factor. The cross-section for such an elastic scattering process is for the case of Coulomb scattering given by the Rutherford expression:

$$\sigma(\theta) = \left( \frac{Z_i Z_t e^2}{4E_i} \right)^2 \frac{1}{\sin^4(\theta/2)}, \quad (2.6)$$

where  $Z_{i,t}$  is the atomic number of the incident and target atom and  $E_i$  the incident ion energy. Hence, both the intensity of backscattered ions (Eq. (2.6)) and their energy angular-distribution (Eq. (2.4)) contains information about the identity of the target atoms.

Through knowledge of the rate of energy loss,  $dE/dx$ , of an ion traveling through a solid, the energy spread of the detected ions can be used to determine the thickness and composition of the sample. This energy loss is a result

of the numerous discrete inelastic collisions (excitation and ionization) the ions undergo with the neutral-atom electrons of the solid, leading in effect to a continuous attenuation of the ions. Although a complete formula for the energy loss (or *stopping power*),  $dE/dx$ , may be calculated (often referred to as the Bethe formula), tabulated values are preferably used in practical applications. An ion entering the target with an energy  $E_0$  and which undergoes elastic scattering at a depth  $t$  in the target, will prior to scattering have experienced an energy loss  $\Delta E_{\text{in}}$  given by:

$$\Delta E_{\text{in}} = \int_0^t \frac{dE}{dx} dx \quad (2.7)$$

$$\approx t \left. \frac{dE}{dx} \right|_{\text{in}}, \quad (2.8)$$

and thus have an energy of:

$$E(t) = E_0 - t \left. \frac{dE}{dx} \right|_{\text{in}}. \quad (2.9)$$

The approximation made from Eq. (2.7) to Eq. (2.8) greatly facilitates the practical computations necessary and does not induce any significant errors. Upon elastic scattering, the ion energy is altered by the kinematic factor according to Eq. (2.5), and subsequently loses energy along the outward path of length  $t/|\cos \theta|$  through the target, and thus emerges from it with a total energy given by:

$$E_1(t) = K(\theta) \left( E_0 - t \left. \frac{dE}{dx} \right|_{\text{in}} \right) - \frac{t}{|\cos \theta|} \left. \frac{dE}{dx} \right|_{\text{out}}. \quad (2.10)$$

Hence, the energy width  $\Delta E$  of a signal from a film of thickness  $d$  is given by:

$$\Delta E = E_1(0) - E_1(d) \quad (2.11)$$

$$= d \left( K(\theta) \left. \frac{dE}{dx} \right|_{\text{in}} + \frac{1}{|\cos \theta|} \left. \frac{dE}{dx} \right|_{\text{out}} \right). \quad (2.12)$$

Thus, knowing the stopping power  $dE/dx$  for a given material, the film thickness may be deduced from the energy-spread of the backscattered ions.

## Apparatus

At the RBS facility at Aarhus University the incident ion beam, usually 2-MeV  $^4\text{He}^+$ , is supplied by a Van de Graaff accelerator. The sample holder, capable of carrying  $20 \sim 1 \text{ cm}^2$  samples, is mounted on a double-axis goniometer. To acquire random, non-channeled spectra, the sample slowly processes around the

beam axis during measurement (typically  $2^\circ$  off-axis). The backscattered ions are measured simultaneously by two Si semiconductor detectors with an energy resolution of about 20 keV. One detector is positioned near glancing-angle ( $\theta = 110^\circ$ ), which assures high depth resolution and the other detector is positioned as close as possible ( $\theta = 161^\circ$ ) to full backscattering (i.e.,  $180^\circ$  scattering angle) without blocking the incident beam, giving the optimal mass resolution (see Eq. (2.4)). The interpretation of a measured RBS-spectra is performed with the *RUMP* [31, 32] computer code, and it is checked that the spectra obtained via the two Si detectors are in agreement. The depth resolution is usually reliable to within 50 Å.

# 3

---

## THE ARGON DISCHARGE

*some fundamental studies*

---

[The experimental results presented in this chapter are contained in **Article II**: “Energy Spectra of Particles Bombarding the Cathode in glow discharges”. C. V. Budtz-Jørgensen, J. Böttiger, and P. Kringhøj, *Vacuum*, **56**, 2000, p. 9. Presented at the E-MRS<sup>1</sup> '99 conference in Strasbourg, France.]

*The argon discharge is amongst the simplest of glow-discharges, argon being a mono-atomic, inert gas. Fundamental studies of the basic physics of discharges are hence often concerned with this case. In this chapter some of these studies, most of which use the pioneering work of Davis and Vanderslice [15] as their basis, will be briefly reviewed. This review is also intended as a more thorough discussion of the various aspects of the particle bombardment of the cathode, than was given in Chap. 1. For example, the importance of energetic neutrals will be discussed. Also presented in this chapter is my contribution to this, still ongoing saga, of the fundamentals of the glow-discharge. These results have been published in **Article II**.*

### 3.1 Introduction

In 1963 Davis and Vanderslice [15] made the first extensive experimental and theoretical investigation of the ion energy-distributions of a DC glow-discharge. Measurements of ion energy-distributions were performed on Ar, Ne and H<sub>2</sub> discharges within a pressure-range of 0.05–1.5 torr<sup>2</sup> and a discharge voltage-

---

<sup>1</sup>European Materials Research Society.

<sup>2</sup>1 torr  $\sim$  4/3 mbar. Hence, in practice *torr* and *mbar* may be considered equivalent.

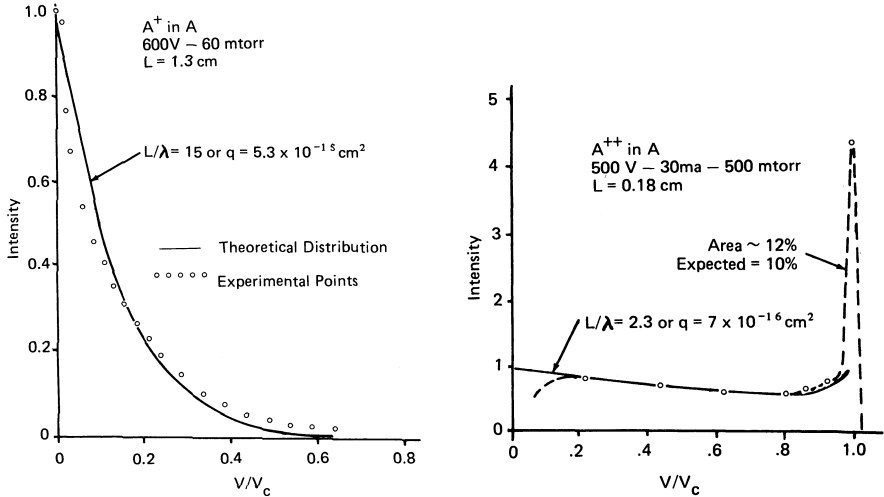


**Figure 3.1** Davis and Vanderslice's measured  $\text{Ar}^+$  and  $\text{Ar}^{2+}$  energy-distributions ( $\circ$ ) and a fit to their theory ( $—$ ). Taken from Ref. 15.

range of 440–660 V. They proposed a simple ion-neutral collision model, which was shown to describe measured energy spectra to a reasonable extent. This is the model which was described in Sect. 1.5, and the basic assumptions of which are restated here:

- all the ions originate from the bulk plasma (i.e., no ionization in the sheath);
- an ion that undergoes a collision loses all its kinetic energy (i.e., symmetrical charge transfer);
- the cross-section for ion-neutral collisions,  $\sigma$ , is energy independent;
- the electric field in the sheath is linear.

Under these four assumptions the ion energy-distribution function,  $f(E)$ , of the mono-atomic discharge takes the form:

$$f(E) = \frac{1}{m} \frac{s}{\lambda_i} (1 - E)^{(1/m)-1} \exp \left[ -\frac{s}{\lambda_i} (1 - [1 - E]^{1/m}) \right], \quad (1.36)$$

(cathode ion energy-distribution)

with, assuming a linear electric field in the sheath,  $m = 2$  in their case.

Fig. 3.1 shows their measured ion energy-distributions for the  $\text{Ar}^+$  ions of a 0.06 torr, 600-V argon discharge ( $\circ$ , left-hand side) and the  $\text{Ar}^{2+}$  ions of a 0.5 torr, 500-V discharge ( $\circ$ , right-hand side). Also shown in the figure are fits of their model to the experimental data (—). These two cases represent two relative “extremes”, with a large and a small  $s/\lambda$ -value respectively ( $L/\lambda$  in their notation). Just like the  $\text{Ar}^+$  ions,  $\text{Ar}^{2+}$  ions will undergo (two-electron) symmetric charge-transfer with Ar atoms, although the cross-section for this process is significantly smaller (at least for energies above  $\sim 0.1$  eV, see Phelps [10]), leading to smaller values of  $s/\lambda$  (since the mean-free-path,  $\lambda$ , is larger). The agreement between experiment and theory is seen to be reasonable in both cases, although not quite as convincing for the  $\text{Ar}^+$  spectra. To test the extracted  $s/\lambda$ -values, the sheath thickness,  $s$ , was estimated in each case, so that the mean-free-path for charge exchange,  $\lambda$ , and hence the cross-sections for this process could be calculated. The resulting values of  $\sigma[\text{Ar}^+] = 5.3 \times 10^{-15} \text{ cm}^2$  and  $\sigma[\text{Ar}^{2+}] = 7 \times 10^{-16} \text{ cm}^2$  are in good agreement with known values.

The reason for the less successful fit of the  $\text{Ar}^+$  spectra could be the poor resolution of their measurements, which is confined to a linear resolution of the ion-intensities. As was discussed in Sect. 2.3 p. 46ff, the angular distribution of the ions at very low energies will obscure the measured ion energy-distributions in this region, thus requiring a high-resolution measurement to acquire a greater proportion of the energy spectra (see Fig. 2.13, p. 51). Although this might explain the somewhat poorer fit of the  $\text{Ar}^+$  spectrum, an explanation could also be sought in some of the weaknesses of the Davis and Vanderslice model.

## Attacking the Davis and Vanderslice model

Although the assumptions a)–d) may seem plausible, they have been attacked by various groups over the years. Let us have a look at the points made in some of these studies.

- ad. a) As was apparent from the plasma simulations described in Sect. 1.6, ionization *does* in fact take place in the cathode sheath, giving rise to regions of increased ion density (the *cathode glow* and *negative glow* regions). Although this, as was also noted in Sect. 1.6, does not significantly alter the potential profile of the sheath, some contribution to the cathode ion energy-distribution from the ions created in this way must be expected. The fact that the potential distribution,  $\Phi(x)$ , is adequately described by a power-law, does not mean that the electrical field is equally well described by its derivative, and, even more so, that the charge density is at all well described by its second derivative (which was clearly seen in Fig. 1.10). The Davis and Vanderslice model has been criticized for neglecting sheath ionization (e.g., by Chapman [12]), and a number of authors have improved on the model, taking

this into account, e.g., Wroński *et al.* [33]. The results of these theoretical investigations, however, were that sheath ionization does *not* change the cathode ion energy-distribution significantly [34], mainly, because the cross-sections for both electron- and ion-impact ionization are so small compared to that of the symmetrical charge transfer process.

- ad. b) The assumption of zero initial energy of the ion after a charge transfer process holds for as far as the thermal energy of the Ar atom can be ignored. With gas-temperatures of the order  $T_g \sim 0.026$  eV (room-temperature) this will not be an issue for the discharges of interest here. Implicitly in this assumption, however, lies the assumption that the *initial* parent ions, originating from the bulk plasma, also have zero velocity. This can of course not be true, since they must have some finite velocity to pass the bulk plasma-sheath interface at all. To solve this apparent contradiction it is necessary to introduce a so-called *pre-sheath* region (see for example [9, Chap. 6]), having a small finite electric field where the ions can gain an initial velocity before entering the sheath (since the bulk plasma itself is field-free). It is this region that, so to speak, connects the sheath and the bulk plasma regions. The theoretical treatment of this region is not an easy matter and still a subject of some controversy. However, an estimate of the ion energy upon entering the sheath is given by the *Bohm sheath criterion* [9, p. 158]:

$$u_s \geq u_B = \left( \frac{T_e}{M} \right)^{1/2}, \quad (3.1)$$

where  $u_s$  is the initial ion velocity and  $u_B$  is the *Bohm velocity* which is given in terms of the electron temperature,  $T_e$ , and the ion mass,  $M$ . Hence, according to Eq. (3.1), the initial ion energy will be of the order  $T_e/2 \sim 1$  eV. Clearly, any such initial contribution to the ion energy-distribution function *at the cathode* will be insignificant.

- ad. c) The symmetrical charge transfer cross-section,  $\sigma_i$ , is obviously not energy independent, as can be seen by inspection of Fig. 1.2 (p. 10) — especially not in the, in our case, relevant region between 1 and 100 eV. The energy dependence could very well be important for the ion energy-distribution at the cathode. Moreno-Marín [35] report of a model taking into account both sheath ionization and the energy dependence of the symmetrical charge transfer cross section. The resulting ion energy-distributions are shown in Fig. 3.5 on page 63, for an argon discharge driven at a 1 000 V and pressures of 0.01–0.2 torr. Although a direct comparison with the Davis and Vanderslice model

was not made, a comparison with the distribution functions of Fig. 1.9 (p. 23) shows these distributions to be similar.

- ad. d) As the simulations in Sect. 1.6 revealed, the plasma potential, at least in the case studied there, has a  $x^{5/3}$ -dependence, leading to a  $x^{2/3}$ -dependence of the electric field in the sheath. Although Davis and Vanderslice assume a linear field, a simple generalization of their model to allow an arbitrary  $x^m$ -dependence is quite straightforward [16]. It should be noted, however, that the resulting energy-distribution, given by Eq. (1.36), leads to singularities at the sheath-bulk plasma interface. This is also the case for the linear electric field case ( $m = 2$ ) of Davis and Vanderslice. Again, this is a consequence of not taking into account the existence of the pre-sheath region. However, although inclusion of the pre-sheath leads to theoretically more solid models, it does not significantly alter the cathode ion energy-distribution function [33, 34].

It seems, that despite the various attempts to improve on the Davis and Vanderslice model, the four assumptions a)–d) and the ion energy-distribution function, given by Eq. (1.36), that follows from them have stood their ground. The reason for the success of this simple model, could be sought in the devastating properties of the symmetrical charge transfer process. An ion that undergoes such a charge exchange is effectively “reborn” — loosing all its knowledge of where and how it was originally created, and what the local characteristics of the discharge were at this point. For example, only the fraction of ions,  $e^{-s/\lambda}$ , that transverse the entire sheath without any collision contain any information of the pre-sheath region. For the vast majority of the ions, this “knowledge” has been lost to the neutrals via charge exchange — it only takes a single collision for this to happen. And since charge exchange dominates most other processes which are taking place in the sheath, such as ionization, the importance of these processes in defining the cathode ion energy-distribution is in general negligible.

## Comparison with experiments in the literature

There do not exist many reports of comparisons between the Davis and Vanderslice model and measured ion energy-distributions in the literature,<sup>3</sup> apart from those of Davis and Vanderslice themselves. In 1983 Houston and Uhl [36] report on measurements of an argon discharge driven at discharge voltages of 0.8–2 kV and pressures of 0.04–0.13 mbar (Fig. 3.2). Excellent agreement with the Davis

<sup>3</sup>Nor many accounts of ion energy-distribution measurements of glow-discharges on their own. Most measurements of ion energy-distributions have been performed on RF-discharges [38, and refs. herein].

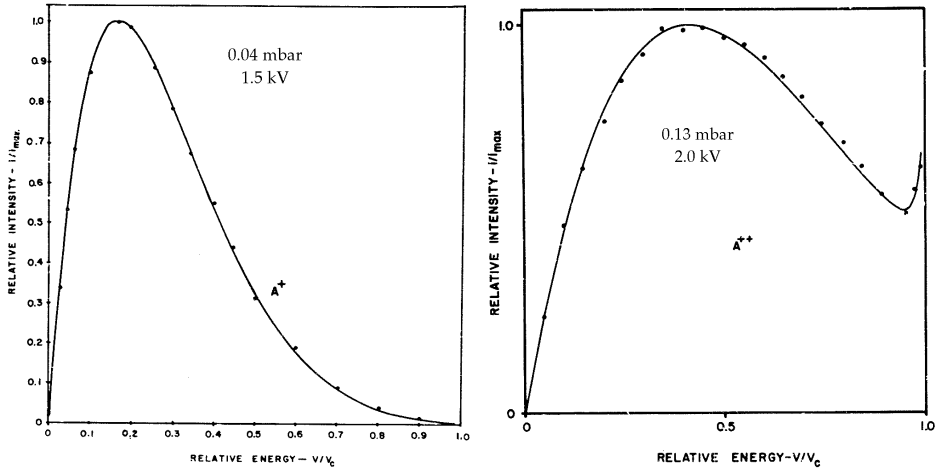
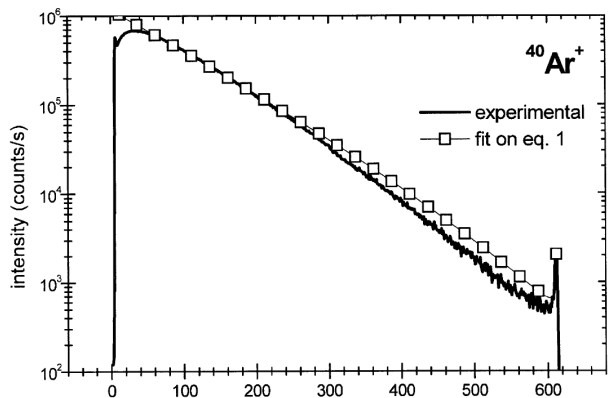


**Figure 3.2** Measured ion energy-distributions ( $\bullet$ ) and fit with the Davis and Vanderslice model ( $—$ ). **Left:**  $\text{Ar}^+$  energy-distribution of an argon discharge driven at 1.5 kV, 0.04 mbar.  $s/\lambda = 12$ . **Right:**  $\text{Ar}^{2+}$  energy-distribution of an argon discharge driven at 2.0 kV and 0.13 mbar.  $s/\lambda = 4.8$ . The suppression of the ion-intensity at low energies is a result of the energy-dependency of the experimental resolution, which has been taken into account in the theoretical curves. Taken from Houston and Uhl [36].

**Figure 3.3** Measured  $\text{Ar}^+$  energy-distribution of an argon discharge driven at 600 V and 0.2 mbar ( $—$ ) and a fit of the Davis and Vanderslice model ( $\square$ ) yielding  $s/\lambda = 8.9$ . Taken from Quast *et al.* [37].

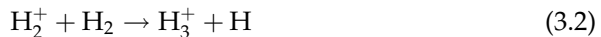


GAS	ION	VOLTAGE (V)	PRESSURE (MBAR)	$s/\lambda$	REF.
Argon	Ar <sup>+</sup>	600	0.08	15	15
	Ar <sup>+</sup>	600	0.20	8.9	37
	Ar <sup>+</sup>	1 500	0.04	12	36
	Ar <sup>2+</sup>	500	0.67	2.3	15
	Ar <sup>2+</sup>	800	0.13	4.8	36
Neon	Ne <sup>+</sup>	660	0.63	25	15
	Ne <sup>2+</sup>	650	0.80	5.6	
Hydrogen	H <sub>2</sub> <sup>+</sup>	650	1.20	23	15

**Table 3.1** Reported comparisons between measured ion energy-distributions at the cathode and the Davis and Vanderslice model for various discharge gasses as reported by Davis and Vanderslice [15], Houston and Uhl [36] and Quast *et al.* [37].

and Vanderslice model was reported for both Ar<sup>+</sup> and Ar<sup>2+</sup> ions, with  $s/\lambda$ -values of 12 and 4.8 respectively. They also performed angular-distribution measurements, but only for high-energy ions. For example, the incident angle of the 600-eV ions of a 2-kV discharge did not exceed  $\sim 1^\circ$ . Recently, Quast *et al.* [37] performed a comparison, also for an argon discharge, at a discharge voltage of 600 V and a pressure of 0.2 mbar (Fig. 3.3). The ion energy measurements were performed with an energy and mass analyser from *Hiden Analytical Ltd.* similar to ours. A fit to the Davis and Vanderslice model produced a  $s/\lambda$ -value of 8.9, with a reasonable agreement between experiment and theory.

In the Davis and Vanderslice article a comparison was also made with Ne and H<sub>2</sub> discharges. Neon is, as argon, a mono-atomic inert gas, and the assumptions of the model are valid for this case also. The agreement with experiments of the energy-distributions of Ne<sup>+</sup> and Ne<sup>2+</sup> was very good, better than for argon. The hydrogen discharge is somewhat more subtle, since both H<sup>+</sup>, H<sub>2</sub><sup>+</sup> and H<sub>3</sub><sup>+</sup> ions are present, and the various collisions which can occur between these ions and the H<sub>2</sub> molecules complicate the picture. For example, besides the symmetrical charge transfer process between H<sub>2</sub><sup>+</sup> and H<sub>2</sub> which has a cross-section of about  $10^{-15}$  cm<sup>2</sup> at 10 eV [39], the proton transfer process:

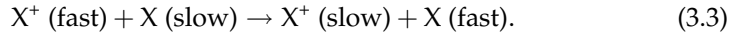


also has a large cross-section at low energies ( $\sim 8 \times 10^{-16}$  cm<sup>2</sup> at 0.1 eV;  $\sim 4 \times 10^{-17}$  cm<sup>2</sup> at 10 eV [39]), and thus acts as a *sink* for the H<sub>2</sub><sup>+</sup> ions. This must be expected to be of importance in defining the H<sub>2</sub><sup>+</sup> energy-distribution at the cathode. Nonetheless, Davis and Vanderslice performed a fit to the measured ion energy-distributions of H<sub>2</sub><sup>+</sup> with their model. The agreement was good, although clearly the physical interpretation of the result is somewhat obscured.

Tab. 3.1 summarizes the  $s/\lambda$ -values obtained by the various authors mentioned.

## Energetic neutrals

The symmetrical charge transfer process will always be a dominating process for any discharge because of its resonant character, and because it involves the abundant neutral gas atoms, X, and the primary ions of the discharge, X<sup>+</sup>:



As a result, the cathode of a glow-discharge must be expected to be bombarded with fast neutral atoms created via this process. A number of authors have reported on models estimating the amount of fast neutrals and their energy-distribution [33, 35, 40, 41]. The main processes for defining the neutral energy-distribution are charge exchange (Eq. (3.3)), which determines the initial energy of the neutrals created,<sup>4</sup> and elastic scattering between neutrals, which is the main attenuator of these fast neutrals. Mason and Allot [40], who devise a model within the formalism of the Davis and Vanderslice model, find the neutral atom flux to be considerably *higher* than the ion flux, for a discharge driven at a voltage of 800 V, a pressure of 1 torr and a sheath thickness of 0.2 cm. Depending on the ratio between the charge-exchange and the elastic scattering cross-sections, the neutral atom flux is seen to be a factor of 10 higher than the total ion flux at the cathode (Fig. 3.4). Also shown in the figure is the relative fast atom energy, which can be seen to be a fraction of the mean ion energy.

These findings are in good qualitative agreement with the calculations of Moreno-Marín *et al.* [35], shown in Fig. 3.5, who also devise an analytical model for the ion and neutral energy-distributions of a glow-discharge. The left-hand side figure shows calculated energy-distribution curves for (a) ions and (b) neutrals of a discharge driven at a voltage of 1 000 V, a discharge current of 10 A/m<sup>2</sup> and pressures of 0.01–0.2 torr. The total neutral flux is again seen to be significantly larger than the total ion flux. It can also be noted that the neutral energy-distribution curves are similar to those of the ions, but with a larger fraction towards low energies. This tendency is also supported by the findings of Wroński *et al.* [33]. The right-hand side of Fig. 3.5 shows the dependency on gas pressure of the total flux (a) and total energy (b) of the particles impinging on the cathode. Since the discharge current is kept constant, the ion flux of course does not change with pressure. In reality, changing the discharge pressure without changing the discharge current is not possible, which makes the plot presented in the figure somewhat odd (from an experimentalists point of view). Nevertheless — as the pressure increases, the total ion energy decreases since the ions undergo more collisions. This then, in turn, results in an increase of the total (fast) neutral flux since every charge exchange process creates a fast neutral, thus leading to an increase of the total energy of the neutrals impinging on the cathode.

<sup>4</sup>The initial energy of a neutral is equal to the energy of the fast ion prior to charge exchange. The distribution of these ions is in turn defined by Eq. (3.3).

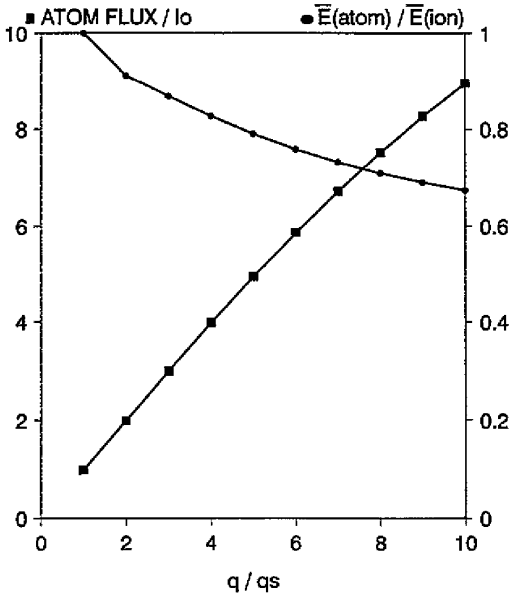


**Figure 3.4** Variation of relative total fast neutral (i.e., neutrals which were created via charge exchange) flux (●) and relative fast atom energy (■) with the ratio,  $q/q_s$ , between the charge transfer cross-section and the elastic scattering cross-section. Taken from Mason and Allot *et al.* [40].

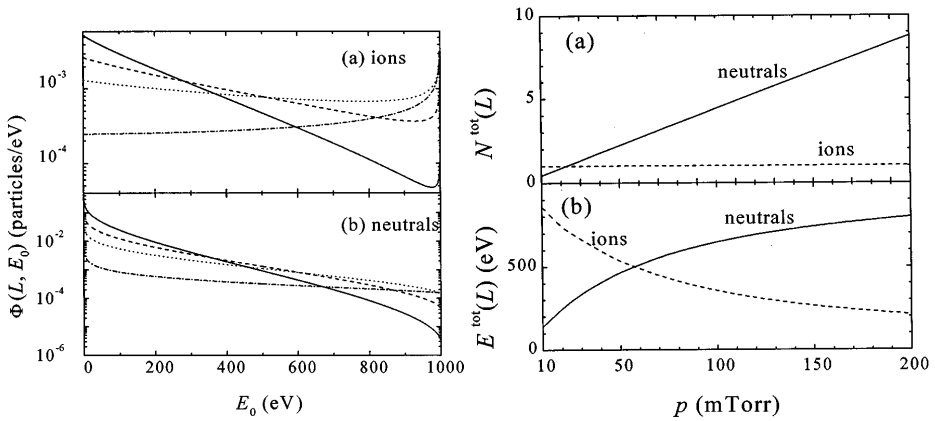


**Figure 3.5 Left:** Theoretical (a) ion- and (b) neutral-energy distributions at the cathode for an argon discharge with a discharge voltage of 1 000 V, a discharge current of 10 A/m<sup>2</sup> and pressures of 0.2 torr (solid line), 0.1 torr (dashed line), 0.05 torr (dotted line) and 0.01 torr (dash-dotted line). **Right:** Total neutral- (solid line) and ion- (dashed line) particles that bombard the cathode, as a function of discharge pressure, shown in terms of (a) number of particles and (b) total energy. Taken from Moreno-Marín *et al.* [35].

All in all, the general picture regarding the creation of fast neutrals seems clear. When considering particle bombardment of the cathode, the major energy-flux at the cathode is actually due to fast neutrals, and not ions! However, it has also been shown that the neutral energy-distribution does resemble that of the ions, although with a somewhat lower average energy. This is because it is the *ion* energy-distribution in the sheath, which defines the energy that a neutral will have right after charge exchange. The suppression of the high-energy region of the neutral energy-distribution, as compared with the ion energy-distribution, is caused by elastic scattering between neutrals and, of course, the fact the neutrals created are not accelerated further by the electric field in the sheath. Hence, knowing the ion energy-distribution, one also has a good idea of the neutral energy-distribution.

## 3.2 Ar<sup>+</sup> Ion Energy-Distribution Measurements

To test the Davis and Vanderslice model with our experimental set-up, a series of measurements were performed on an argon discharge using a pressure range of 0.14–1.0 mbar and a voltage range of 240–350 V, resulting in discharge currents of  $4 \times 10^{-3}$ –0.26 mA/cm<sup>2</sup>. The measured ion energy-distribution curves were fitted with the Davis and Vanderslice model yielding  $s/\lambda$ -values of 26–72. These are rather large values, meaning that the mean ion-energies are very low. The measurement and subsequent interpretation of these low-energy distributions serves as a good opportunity for evaluating the high sensitivity of the Hiden EQP. Furthermore, these measurements also give us the possibility to verify the adequacy of the Davis and Vanderslice distribution for higher values of  $s/\lambda$  than have been examined so far.

### Experimental

For the experiments reported here, the 30  $\mu\text{m}$  orifice was used, resulting in slightly longer sampling rates than are achieved with 100  $\mu\text{m}$  or 200  $\mu\text{m}$  orifices. However, as discussed in Sect. 2.2 p. 37ff, a small orifice will be less intrusive on the plasma and result in more representative ion sampling. Both the cathode and the anode material was stainless steel, and the distance between them was 5 cm (a schematic diagram of the plasma chamber is shown in Fig. 2.2 on p. 36). The voltage of the argon discharge was pulsed with an on-time of 900  $\mu\text{s}$  and an off-time of 100  $\mu\text{s}$ . Using the trigger facility of the EQP, ion sampling was performed only during a time window well within the on-pulse of the discharge voltage, so that no transient effects are expected to modify the measured energy distributions. As already mentioned, the discharge voltage,  $V_c$ , was varied between 240 V and 350 V, and the pressure,  $p$ , was varied between 0.14 mbar and 1.0 mbar. For each pressure-voltage pair ( $p, V_c$ ), an ion energy-distribution

curve,  $f(E)_{\text{exp}}$ , and the discharge-current,  $j$ , was measured (the discharge voltage was, in fact, also measured). Two series were performed; one keeping a constant pressure of  $p = 0.53$  mbar while varying the voltage (14 steps), and another set keeping a constant voltage of  $V_c = -350$  V and varying the pressure (12 steps).

### Theoretical model

The ion energy-distributions that were obtained were fitted with the Davis and Vanderslice distribution, which is restated here yet once more:

$$f(E) = \frac{1}{m} \frac{s}{\lambda} (1-E)^{(1/m)-1} \exp \left[ -\frac{s}{\lambda} (1-[1-E]^{1/m}) \right] \quad (1.36)$$

(cathode ion energy-distribution)

where, on the basis of the discussion in Sect. 1.6, we choose  $m = 5/3$ . As mentioned, the  $s/\lambda$ -values extracted are rather large, which means that the average energy of the ions must be expected to be quite small, i.e.,  $E \ll 1$ . In this case Eq. (1.36) can be approximated by the exponential expression:

$$f(E) \approx \frac{s}{m\lambda} \exp \left[ -\frac{s}{m\lambda} E \right]. \quad (E \ll 1) \quad (3.4)$$

However, as we shall see later, although the measured ion energy-distributions do have a seemingly simple exponential dependence, the more subtle functionality of Eq. (1.36) is still evident.

The sheath thickness,  $s$ , cannot be estimated to a sufficiently high degree of precision with our experimental set-up, and hence, the mean-free-path and cross-section for charge exchange cannot be extracted directly from the  $s/\lambda$ -values. However, knowing the voltage,  $V_c$ , and current-density,  $j$ , of the discharge, we may learn something from the collisional Child law which was derived in Sect. 1.4 and restated here:

$$j = \left(\frac{2}{3}\right) \left(\frac{5}{3}\right)^{3/2} \varepsilon_0 \left(\frac{2e\lambda}{\pi M}\right)^{1/2} \frac{V_c^{3/2}}{s^{5/2}}, \quad (1.27)$$

(collisional Child law)

where  $\varepsilon_0$  denotes the vacuum permittivity,  $e$  the unit charge and  $M$  the ion mass. Using the relations

$$\lambda = \frac{1}{n\sigma} \quad \text{and} \quad p = nkT, \quad (3.5)$$

where  $n$  is the neutral gas density,  $\sigma$  is the symmetrical charge transfer cross-section,  $p$  is the neutral-gas pressure,  $k$  is Boltzmann's constant and  $T = 300$  K is

the gas temperature, Eq. (1.27) can be written in terms of measurable quantities ( $j$ ,  $V_c$ ,  $p$  and  $s/\lambda$ ):

$$j = \left(\frac{2}{3}\right) \left(\frac{5}{3}\right)^{3/2} \epsilon_0 \left(\frac{2e}{\pi M}\right)^{1/2} \left(\frac{\sigma}{kT}\right)^2 \frac{V_c^{3/2} p^2}{(s/\lambda)^{5/2}}. \quad (3.6)$$

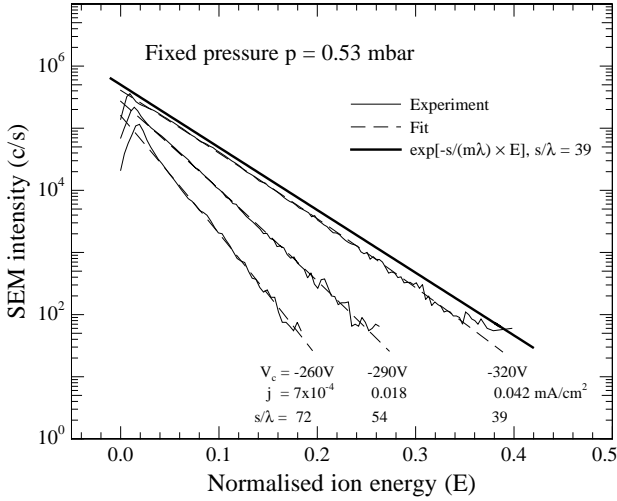
Since all the quantities and variables of Eq. (3.6) except (in principle) the cross-section for symmetrical charge transfer,  $\sigma$ , are known, its value can be extracted from these data through a fit with Eq. (3.6). Furthermore, this serves as a good test of how well the collisional Child law actually describes the argon discharge in this case.

### 3.3 Results

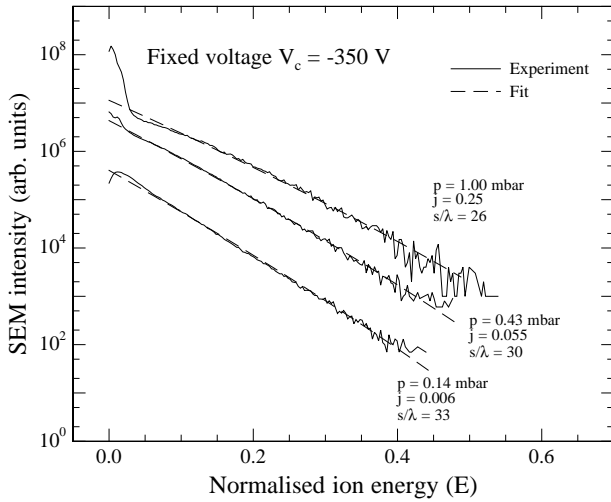
#### Dependence on discharge voltage

Fig. 3.6 shows the measured  $\text{Ar}^+$  energy spectra (solid lines) for an argon discharge at three selected discharge voltages and a pressure of 0.53 mbar. Note that the ion-energies have been normalized to the discharge voltage in each case. The measured curves were fitted with the theoretical energy-distribution given by Eq. (1.36) (dashed lines) so that the  $s/\lambda$ -values could be extracted from the data (shown in figure). The experimental data can be seen to be excellently described by the theoretical curves except at very low energies, where the angular acceptance profile of the EQP becomes of importance (see Sect. 2.3 page 46). The figure also clearly shows that the effect of increasing the discharge voltage is not merely a question of *scaling* the energy-distribution. As  $s/\lambda$  (and therefore effectively  $s$ ) decreases with increasing voltage and current, the number of ion-neutral collisions per ion in the sheath is reduced, thereby effectively shifting the ion energy-distribution towards higher values. Hence the effect of increasing the discharge voltage is twofold, both through the *scaling* of the ion energies and by increasing the *fraction* of high-energy ions.

One could argue, that the excellent fits revealed in the figure do not by themselves give credit to the Davis and Vanderslice distribution, but merely the approximate expression of Eq. (3.4). Also shown in the figure, however, is this simple exponential curve (slightly shifted upward), evaluated for  $s/\lambda = 39$  (thick solid line). The deviance of the Davis and Vanderslice distribution from the simple exponential is clearly seen, with increasing strength towards higher energies. Comparing these two curves, one also sees how well the measured data obey the subtle functionality of the full Davis and Vanderslice distribution. Therefore, we may conclude that the ion energy-distributions measured here are in fact excellently described by the Davis and Vanderslice distribution.



**Figure 3.6** Measured  $\text{Ar}^+$  energy spectra for different discharge voltages (thin solid lines) and best fits to the theoretical model given by Eq. (1.36) (dashed lines).



**Figure 3.7** Measured  $\text{Ar}^+$  energy spectra for different neutral gas pressures (thin solid lines) and best fits to the theoretical model given by Eq. (1.36) (dashed lines). For clarity the curves have been sequentially shifted upward by one decade.

## Dependence on pressure

Fig. 3.7 shows  $\text{Ar}^+$  spectra measured at a fixed discharge voltage of  $-350$  V for three different pressures. For clarity, the curves have been sequentially shifted upward by one decade. Again the spectra were fitted with the distribution function given by Eq (1.36), and again the agreement between experiment and theory is excellent. However, in this case there is no major change in  $s/\lambda$ , and hence in the ion energy-distribution, with varying pressure. Since  $s/\lambda$  is proportional to  $s \times p$  (see Eq. (3.5)), where  $p$  is the pressure, this is in accordance with the (approximate) thumb rule of  $s \times p \sim \text{const}$  which holds for DC discharges. The change in pressure (or mean-free-path,  $\lambda$ ) must therefore be counterbalanced by a change in the sheath thickness,  $s$ . It is this balance which is described by the Child law (Eqs. (1.27) and (3.6)).

As already mentioned, a series of measurements of  $\text{Ar}^+$  energy distributions were performed for different voltages and pressures within the ranges shown in Figs. 3.6 and 3.7. For each measurement,  $s/\lambda$  was extracted from the energy-distribution and the voltage ( $V_c$ ), current-density ( $j$ ) and pressure ( $p$ ) was measured. As suggested by Eq. (3.6), these data were plotted as  $j$  vs.  $(V_c^{3/2} p^2)/(s/\lambda)^{5/2}$ . The results are shown in Fig. 3.8 for varying voltage and Fig. 3.9 for varying pressure (the data points are illustrated by their experimental error-bars only). Also shown are the best linear fits (solid line) to the data, and the effective cross-section,  $\sigma$ , for  $\text{Ar}^+$  symmetric charge transfer which could be deduced from the slope through use of Eq. (3.6).

## 3.4 Discussion

It is clear from Figs. 3.6 and 3.7 that the simple ion-neutral model proposed by Davis and Vanderslice is in excellent agreement with the measured energy spectra for all energies. However, it should be noted that the measurements reported here have relatively large values of  $s/\lambda$  and hence the fits are not very sensitive to the full complexity of Eq. (1.36), but mainly the approximation given by Eq. (3.4), which is insensitive to the value of  $m$ . The choice of  $m = 5/3$  for the sheath potential dependence can therefore not be justified solely on the basis of the measured energy spectra.

The Child law for a collisional sheath is seen to be in qualitative agreement with the measured data. However, it is clear from Figs. 3.8 and 3.9 that there is a systematic deviation from the expected linearity, which can not be ascribed to measuring errors. The collisional Child law given by Eq. (1.27) may therefore not be telling the whole story. However, the effective cross-sections for symmetric charge transfer that were deduced from the fits,  $\sigma_v = 4.9(1) \times 10^{-15} \text{ cm}^2$  for varying voltage and  $\sigma_p = 3.7(1) \times 10^{-15} \text{ cm}^2$  for varying pressure, are well within the range of reported values. A. V. Phelps [11] reports of a SCT cross-

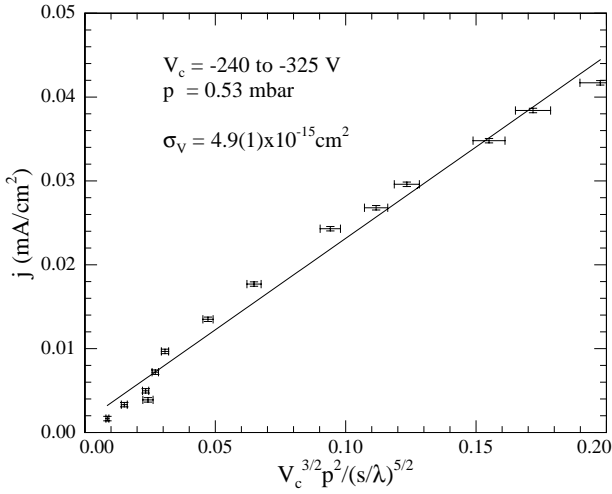


**Figure 3.8** The collisional Child law for varying voltage (see Eq. 5). The measured current-density is shown as a function of the discharge voltage ( $V_c$ ), neutral gas pressure ( $p$ ) and the  $s/\lambda$ -values obtained from the measured energy spectra.

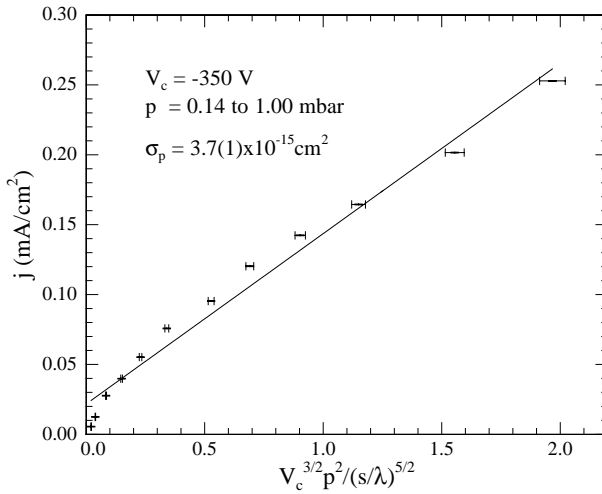
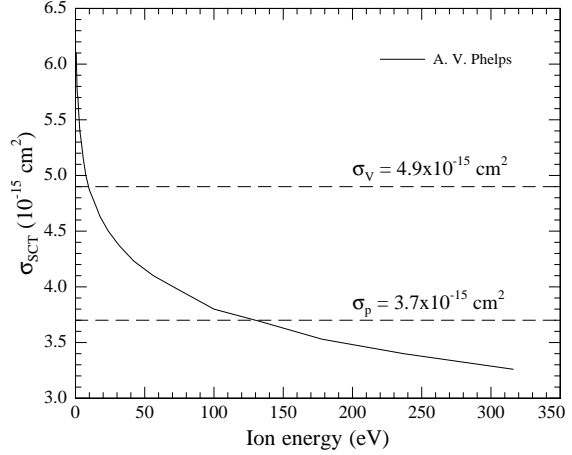


**Figure 3.9** The collisional Child law for varying pressure (see Eq. (3.6)). See Fig. 3.8 for details.

**Figure 3.10** The  $\text{Ar}^+$  symmetrical charge transfer cross-sections derived from the experiments and the energy-dependent values,  $\sigma_{\text{SCT}}$ , as reported by Phelps [11].



section for  $\text{Ar}^+$  of  $5.9 \times 10^{-15} \text{ cm}^2$  at 1 eV,  $4.9 \times 10^{-15} \text{ cm}^2$  at 10 eV, falling to  $3.1 \times 10^{-15} \text{ cm}^2$  at 422 eV. These data are shown in Fig. 3.10 together with  $\sigma_V$  and  $\sigma_p$ . The models we have used all assume constant cross-sections, so the values extracted here must be considered *effective* cross-sections. As the  $s/\lambda$ -values are high, the energy of the ions before their last charge-exchange must be expected to be quite low:

$$s/\lambda \sim 30 \quad \rightarrow \quad \langle E \rangle_{\text{ion}} \sim eV_c/30 \sim 10 \text{ eV}. \quad (3.7)$$

This is in good agreement with the value of  $\sigma_V$  (see figure). The discrepancy between  $\sigma_V$  and  $\sigma_p$ , we believe, must be sought in the failure of the collisional Child law (Eq. (1.27)) to adequately describe the data over the full current-density range covered.

### 3.5 Conclusions and Summary

The first part of this chapter served as a more elaborate discussion of the Davis and Vanderslice model, reports of its verification in the literature and the creation of fast neutrals. The four basic assumptions on which the model is founded, and by which its weaknesses are defined, have shown to stand their ground. The more elaborate models which have been developed since the Davis and Vanderslice model was presented have not significantly altered the ion energy-distribution function at the cathode.

The experimental verifications of the Davis and Vanderslice distribution function which have been reported in the literature so far have been for discharges with relatively low  $s/\lambda$ -values, i.e., high ion-energies. The reason, one

should think, is that representative sampling of the very low-energy ions is problematic due to the high incident angles of these ions. The measurements reported here have been performed with a high-sensitivity mass and energy analyser, thus allowing measurement of the few energetic ions that will always be present even at high  $s/\lambda$ -values — the measured energy-distributions presented here span almost 5 decades. It was shown that the Davis and Vanderslice distribution described the measured data excellently. Even though the functionality of the full Davis and Vanderslice distribution is very subtle at high values of  $s/\lambda$ , it was both clearly visible and perfectly mimicked by the measured distributions. This serves both as a further justification of the Davis and Vanderslice model and a verification of the high sensitivity of the Hiden EQP. Furthermore, the symmetrical charge transfer cross-section for  $\text{Ar}^+$  was extracted from the data by using the collisional Child law (i.e., intermediate pressures). Although some systematic deviation was observed, the extracted values were in good agreement with known values. This also gives quantitative credit to the Davis and Vanderslice model and the applicability of the Child law in this respect.

### Practical applications

When the voltage of an abnormal glow discharge is increased the current-density also increases, which in turn results in a narrowing of the cathode sheath. It is this balance which the Child law describes. This decrease in sheath thickness leads to a decrease of the mean number of ion-neutral charge exchange collisions,  $s/\lambda$ , thus shifting the ion energy-distribution towards higher energies. Hence, the effect of increasing the voltage is two-fold: it increases both the maximum energy attainable by the ions *and* the fraction of ions which gain high energies. Since, as mentioned in the introduction to this thesis, the energy of the particles which bombard the cathode play an important role for the processes taking place at the surface, one has to bare this sensitivity of the “voltage-knob” in mind. For example, most industrial plasma-assisted processes are power-controlled, thus allowing continuous readjustment of the discharge voltage. Keeping the *power* constant, however, doesn’t mean that you keep the average *energy* of the particles (ions and neutrals) bombarding the cathode constant!<sup>5</sup>

The treatment of the measurements presented here had the following flow:

1. The ion energy-distribution was measured;
2. this distribution was interpreted using the Davis and Vanderslice model,

---

<sup>5</sup>Although the discussion presented here is based on a pure argon discharge, it applies for all *abnormal* discharges, which are characterized by a mutual increase/decrease of the discharge voltage and current-density. All collisional processes in the sheath, irrespective of their nature, have the effect of attenuating the ions — or, as a minimum leave their energy unchanged. Hence, a decrease of the sheath thickness, leading to fewer collisions, will always increase the average particle energy.

thus allowing the  $s/\lambda$ -value, which is the defining parameter for this distribution, to be extracted;

3. several of these  $s/\lambda$ -values, in conjunction with the easily measurable discharge parameters: voltage ( $V_c$ ), current-density ( $j$ ) and pressure ( $p$ ), were inserted into to the collisional Child law and the symmetric charge transfer cross-section for  $\text{Ar}^+$  was successfully extracted from the data.

For practical applications the opposite flow could with equal success be used. Knowing the charge exchange cross-section and the basic parameters of a discharge, the Child law could be used to estimate  $s/\lambda$ , with which the ion energy-distribution can be determined using the Davis and Vanderslice model. This practical applicability of these two models was also noted by Fancey and Matthews [42]. Alternatively, if the sheath thickness,  $s$ , can be measured independently, one can avoid using the Child law at all. Of course, it should be mentioned that this can only be done in such a straightforward manner with single gas, mono-atomic discharges like Ar, which comply with the assumptions of the Davis and Vanderslice model and the collisional Child law. Nevertheless, if one can gain *some* information on the most prevalent species of a discharge and some idea of what type of collision defines their energy-distribution, this method could be used to predict these same energy distributions — at least to an extent which would be sufficient for most practical applications. For example, in the final chapter of this thesis (Chap. 6), ion energy-distribution measurements of  $\text{N}_2$  and  $\text{N}_2\text{-H}_2$  discharges will be presented. The most abundant ionic species of the  $\text{N}_2$  discharge will be shown to be  $\text{N}^+$  and  $\text{N}_2^+$ . Although these ions, just like the case was for the Davis and Vanderslice measurements of a  $\text{H}_2$  discharge, cannot be described simply by charge exchange, an *effective*  $s/\lambda$ -value can be extracted from these measurements. Using the Child law, these data could in turn be translated into an *effective* charge transfer cross-section. A clear physical interpretation of these values might well be difficult, but this does not undermine their practical usability.

# 4

---

## THE AR-H<sub>2</sub> DISCHARGE

*sputtering of Au and Al<sub>2</sub>O<sub>3</sub>*

---

*The Ar-H<sub>2</sub> discharge is an interesting case in its own right, being somewhat more complicated than the pure argon case; the addition of hydrogen has some drastic effects on both the plasma intensity and the energy-distribution of the ions at the cathode. This discharge is also used for practical surface processing applications such as surface cleaning. The efficiency of the Ar-H<sub>2</sub> discharge in this respect is partly due to the very high energies which are obtained by, mainly, the abundant ArH<sup>+</sup> ions of this discharge, thus giving rise to large physical sputtering rates. However, the presence of reactive hydrogen-related species also has a positive effect, since these give rise to chemical sputtering. The experimental results of this chapter are contained in **Articles I, III and VI.***

### **4.1 Introduction and Basic Concepts**

The Ar-H<sub>2</sub> glow-discharge is widely used in the industry as a surface-cleaning process, usually preceding chemical or plasma-assisted surface processing and deposition techniques such as plasma-assisted chemical vapor deposition (PACVD) or as *in situ* cleaning of surfaces for microelectronics processing applications. The effect of hydrogen in this respect is, however, not clear.

#### **Findings in the literature**

In most cases the Ar-H<sub>2</sub> plasma has been shown to increase the sputtering efficiency compared to a pure argon plasma. This, for example, is the case for silicon

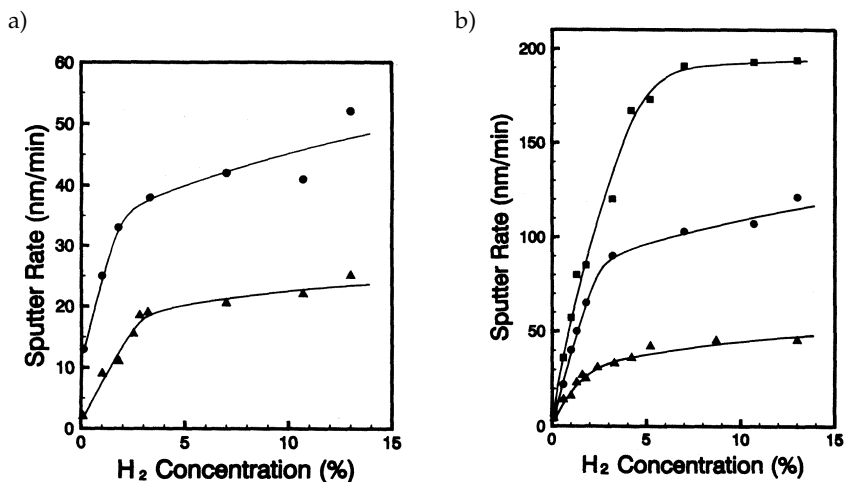


**Figure 4.1** Sputtering rate as a function of hydrogen concentration for (a) silicon and (b) carbon cathodes at operating currents of 20 mA ( $\blacktriangle$ ), 35 mA ( $\bullet$ ) and 50 mA ( $\blacksquare$ ). The partial argon pressure was fixed at 4 torr, and the voltage varied between 260 V and 470 V depending on current and time of measurement. Taken from Tsuji and Hirokawa [43].

and carbon sputtering, as has been reported by Tsuji and Hirokawa [43]. They report of sputtering experiments of silicon and carbon performed with Ar-H<sub>2</sub> discharges with a fixed partial argon pressure of 4 torr and a varying H<sub>2</sub> content of 0.9–13% (equivalent to a partial hydrogen pressure of 0.04–0.6 torr). The sputtering rates were determined by measuring the weight of the substrates before and after sputtering. Their results are shown in Fig. 4.1 for (a) silicon and (b) carbon. As the curves clearly reveal, the addition of very small amounts (1–2%) of hydrogen drastically increases the sputtering rates. The discharges they used were current-controlled, meaning that the current was kept constant during the experiments. As can also be seen from the figure, the sputtering rate scales more or less linearly with the current of the discharge — at least in the silicon case. From a practical point of view, the interesting sputtering parameter to measure is obviously the sputtering *rate*, i.e., the amount of sputtered material per minute. However, if one is interested in trying to understand what is going on, on a microscopic level, it is the sputtering *yield*, i.e., the number of sputtered substrate atoms per incident sputter-particle, which is the most informative. In other words, the *sputtering per particle*-efficiency of a discharge as opposed to the *sputtering per unit time*-efficiency. Since the measurements shown in Fig. 4.1 were current-normalized, sputtering rates and yields are of course the same in their case. However, the fact that the experiments *are* current-controlled

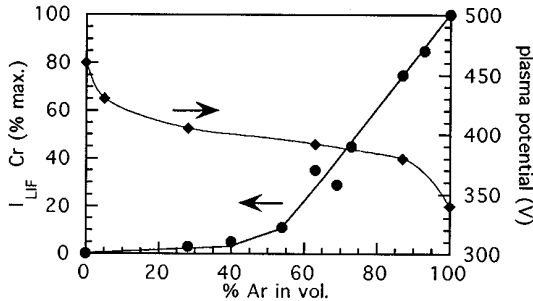


**Figure 4.2** Normalized intensity of the LIF signal of sputtered Cr atoms (●) vs. the relative gas composition in Ar-H<sub>2</sub> glow discharges (Ar content) at a constant pressure of 10<sup>-2</sup> torr and a total current of 250 mA. The evolution of the discharge voltage is also shown (◆). Taken from Tabarés and Tafalla [45].

poses some other fundamental problems which impede a deeper understanding of what is going on. To keep the current constant, the discharge voltage has to be varied during the measurement. As was evident from the discussions of Chap. 3, changing the voltage has a major influence on the energy-distribution of the particles, both ions and neutrals, that bombard to cathodic surfaces of a discharge. Also, the Tsuji and Hirokawa experiments were not performed with constant total discharge pressure when varying the H<sub>2</sub> content which, might, also be of importance for the energy-distribution. These variations of voltage and pressure during the experiments complicate a clear physical interpretation of the results in Fig. 4.1. Hence, the fact that the sputtering rates seem to increase linearly with discharge current in the silicon case is by no means obvious, since the energy-distribution of the sputtering particles will also be changing. This is also the case when considering the change in sputtering rate as a function of H<sub>2</sub> content.

Despite all this, however, the curves of Fig. 4.1 do show, without any doubt, that the addition of hydrogen does in fact increase the carbon and silicon sputtering efficiency as compared to a pure argon discharge. Tsuji and Hirokawa also mention that they performed sputtering experiments on silver and titanium (although no data was presented), and that no improvement of the sputtering rate was observed for these metals. Since hydrogenic particles have a very small mass, these do of course not contribute to any physical sputtering, and hence, the increase in sputtering rate was ascribed to chemical sputtering. Since chemical sputtering is strongly selective as to the type of material [44], this can also explain the lack of sputtering rate improvement in the silver and titanium cases.

Tabarés and Tafalla [45] report of sputtering experiments of the stainless steel walls of a glow-discharge chamber. They used laser induced fluorescence (LIF) measurements of chromium atoms as an indicator of the instantaneous sputtering rate. According to these measurements, which are shown in Fig. 4.2, a decrease in sputtering rate was observed upon the addition of hydrogen to an argon discharge.

Clearly, the effect of hydrogen for the sputtering efficiency of Ar-H<sub>2</sub> discharges is a complicated matter, an cannot solely be explained by a purely phys-

ical sputtering mechanism — chemical sputtering must be of importance. The term “chemical sputtering” can, however, cover a range of different sputtering mechanisms [44], such as purely *thermal desorption* of molecules created on the surface between incident and target particles, and *chemically enhanced* or *chemically decreased physical sputtering* through implantation and subsequent change of the surface binding energy. Alternatively, in *physically enhanced chemical sputtering* a certain degree of high energy particle bombardment is necessary for thermal desorption to take place. Clearly, the wide range of sputtering mechanisms that exist between purely physical and purely chemical (i.e., thermal) sputtering complicates the interpretation of sputtering experiments, in the cases where chemical effects are observed.

## Physical sputtering

In this section the basic aspects of physical sputtering are very briefly described. The main objective here is to define the quantities which we will be using to characterize physical sputtering. For a more detailed analysis see for example Behrisch [46].

When a particle impinges on a substrate, surface atoms may be ejected from the substrate because of momentum transfer if the energy of the incident particle is higher than some threshold energy,  $E_{\text{th}}$ . This process is called *physical sputtering* or *knock-on sputtering*. Although physical sputtering can be characterized in such a simple way, the physical processes which are actually taking place on a microscopic scale can be very complicated. For our purposes, it will by far be sufficient to concentrate on the main identity which is used to quantify sputtering, namely the sputtering *yield*,  $Y$ , defined as:

$$Y = \frac{\text{substrate atoms removed}}{\text{incident particle}}. \quad (4.1)$$

Besides the type of incident particle and substrate atoms, the most important parameter of the sputtering yield is the energy of the incident particle. Hence, the sputtering is usually characterized by the sputtering yield curve:

$$Y(E) = \frac{\text{substrate atoms removed}}{\text{incident particle with energy } E}. \quad (4.2)$$

In Fig. 4.3 the sputtering yield curves for various combinations of incident and substrate atoms are shown. Since physical sputtering is essentially a question of momentum transfer,  $Y$  increases with both energy and incident particle mass, as is clearly seen in the figure. The dependency on the type of substrate atom is not as simple, since, apart from its mass, the binding energy of a surface atom,  $U_s$ , (shown in the legend) will vary from element to element. This is clearly seen by noting the threshold energy for sputtering,  $E_{\text{th}}$ , since its value is essentially

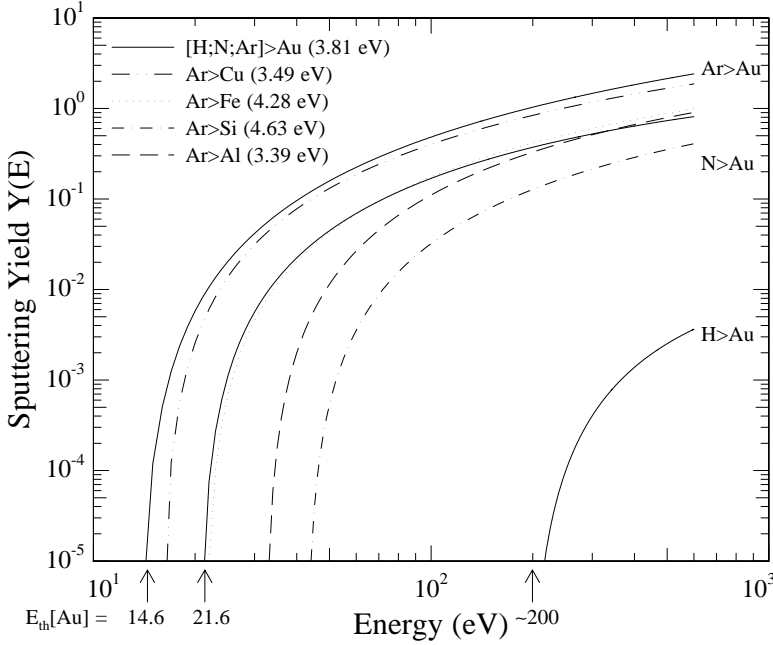


**Figure 4.3** Sputtering yields at normal incidence for  $X>Y$ , where  $X$  denotes the incident particle and  $Y$  denotes the substrate material. The energies in the legend denote the surface binding energy,  $U_s$ , of a surface atom while the energies near the x-axis denote the threshold energies for  $[H;N;Ar]>Au$ . The curves were calculated on the basis of an analytical model which was fitted to existing experimental data for sputtering yields (Yamamura and Tawara [47]).

determined by  $U_s$  and the energy transfer factor,  $\gamma = 4M_iM_s/(M_s + M_i)$ , which play an equally important role [47]:

$$E_{th} = \begin{cases} 6.7U_s/\gamma & (M_i \geq M_s) \\ (1 + 5.7[M_i/M_s])U_s/\gamma & (M_i \leq M_s) \end{cases} \quad (4.3)$$

where  $M_{i,s}$  is the incident and substrate atom mass. Hence, for fixed incident atom mass, heavy surface atoms actually *favor* sputtering, since they are able to absorb a larger fraction of the incident atom energy (Eq. (4.3) is a monotonically decreasing function with increasing  $M_s$ ). For heavy substrate atoms like Au, Cu and Fe which differ significantly in mass, the threshold energies can be seen to decrease with increasing mass. Oppositely, for Si and Al, which differ in mass by only one amu in favor of Si, the smaller binding energy for Al favors Al in terms

of sputtering yield. For a given substrate material (e.g., gold, see figure), the threshold naturally decreases with increasing incident atom mass. The curves shown in Fig. 4.3 are for normal incident particles. Although the sputtering yield is known to increase with incident angle [30, Chap. 4], this will not really be an issue in our case, since the ions which do have an incident angle, will not have the energy necessary to cause any significant sputtering.

Usually the incident particles considered do not have a single well defined energy but rather some energy-distribution, which can be described by an energy-distribution function,  $f(E)$ . In this case it is useful to define an *energy-averaged sputtering yield* for the group of particles which are defined by  $f(E)$ :

$$Y_f = \frac{\int f(E) \times Y(E) dE}{\int f(E) dE}. \quad (4.4)$$

The energy-distribution function,  $f(E)$ , could for instance be the measured Ar<sup>+</sup> ion energy-distribution for an argon glow-discharge. Now, considering a discharge, there will mostly be different types of ions,  $i$ , impinging on the cathode, each with a different energy-distribution function,  $f_i(E)$ , and sputtering yield curve,  $Y_i(E)$ . To describe the sputtering of such a group, let us define the *physical sputtering efficiency* by:

$$S_{\text{phy}} = \frac{\int \sum_i f_i(E) \times Y_i(E) dE}{\int \sum_i f_i(E) dE} \quad (4.5)$$

Hence,  $S_{\text{phy}}$  signifies the physical sputtering efficiency of, for example, a glow-discharge, by averaging the sputtering yield over all energies and species.  $S_{\text{phy}}$  can as such be considered to be a *property* of the discharge, describing how efficient it is with respect to physical sputtering of this or that substrate material (note that  $S_{\text{phy}}$  depends on the substrate material). As opposed to the sputtering *rate*, which is time normalized, the sputtering efficiency is normalized to the number of particles which are included in  $f_i(E)$ .

The problem now arises, of course, that we do not have this information for all the sputtering species of a discharge, since in our case we can only measure the ions. And as was discussed in Chap. 3, the total neutral flux can be several times larger than the total ion flux, thus leading to a substantial fraction of neutral-particle sputtering. Although it was also shown that the neutral energy-distributions are similar to the ion energy-distributions (at least for an argon discharge), this does of course present some uncertainties into comparisons made between sputtering efficiencies which are determined on the basis of Eq. (4.5) and the ones which are directly measured (e.g., by measuring the

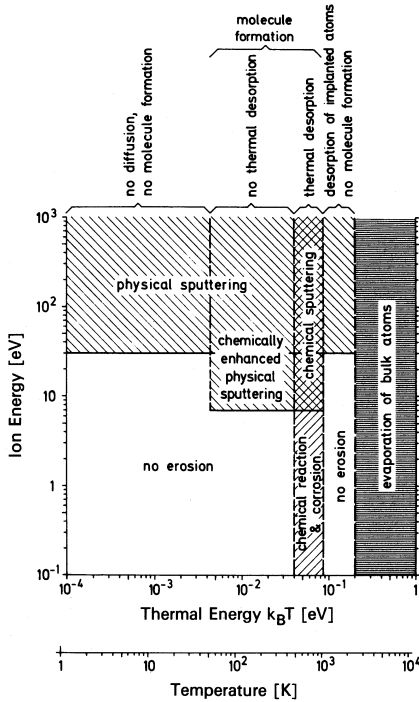


Figure 4.4 Limits in ion energy and surface temperature for erosion processes like physical sputtering, chemical sputtering and evaporation. Taken from Roth [44].

amount of removed substrate material). I shall address this issue again when it arises.

## Chemical sputtering

The “problem” with chemical sputtering, at least from this physicists point of view, is that it is not possible to describe it quantitatively by such simple identities as is the case for physical sputtering, while maintaining a qualitative picture of what is actually going on. Since we are dealing with chemical effects, the substrate temperature will naturally be of great importance, just like the ion energy is important for physical sputtering. In the work presented in this thesis, however, no attempt was made to examine the influence of substrate temperature (e.g., by measuring sputtering efficiencies as a function of temperature). This makes it rather difficult to assess the type of chemical sputtering which might be taking place. Nevertheless, since we can quantify the physical sputtering efficiency *and* measure the actual amount of sputtering (chemical and/or physical) which has happened during a sputtering process, we are at least in a position to say whether or not chemical sputtering *has* occurred. It is within this scope that chemical effects are considered in this thesis.

Fig. 4.4 summarizes the limits in ion energy and substrate temperature for both physical and chemical sputtering. A detailed description of the various chemical sputtering mechanisms presented in the figure is, partly because of the reasons stated above, beyond the scope of this thesis — see for example Roth [44] for such a review.

### *Chemical sputtering*

Purely chemical sputtering is not unanimously definable. Usually, it is regarded as a thermally mediated desorption process of surface atoms or molecules by the reactive sputtering species. Hence it – again usually – increases with temperature, until a maximum is reached, after which a decrease in chemical sputtering is observed as the temperature is increased even further. This maximum arises because of the balance between the desorption of surface molecules, and the adsorption of reactant molecules which precedes desorption; at high temperatures, the desorption rate exceeds the adsorption rate, thus effectively leading to a “suffocation” of the chemical sputtering process.

One way to define chemical sputtering is by inferring its existence from different experimental observations. Let us take this approach, quoting some of possible observations summarized by Roth [44]:

- i)* The sputtering yield should show strong variations with surface temperature;
- ii)* compared to physical sputtering, no sharp threshold energy should be observable;
- iii)* chemical sputtering should be strongly selective for different combinations of target atoms and sputtering ions.

Now, the observations mentioned in *i)* and *ii)* cannot be made in our case. It is, however, possible to observe the selectivity (*iii)* by determining whether or not such selectivity can be explained by physical sputtering. If not, chemical sputtering must be taking place. We could thus add a more customized version of *iii)*:

- iv)* a change in the *measured* amount of sputtering (e.g., caused by varying the parameters of a glow-discharge), should be inconsistent with the change of the physical sputtering efficiency,  $S_{\text{phy}}$ , inflicted by these variations.

It is on this basis, that we shall be inferring the existence of chemical sputtering in this work.

### *Chemically enhanced or decreased physical sputtering*

As its name suggests, this is not chemical sputtering but a chemical effect on the physical sputtering yield. For example, as was shown earlier, the surface binding energy of the outermost substrate atoms,  $U_s$ , enters inversely in the threshold energy for physical sputtering — this is also the case for the physical sputtering yield curve,  $Y(E)$ , itself (see for example Yamamura and Tawara [47]). Hence, any chemical effects which change the surface binding energy will lead to a change in the physical sputtering efficiency. These types of alteration of the surface properties may be initiated by either reactive ions or by the reactivity of the atmosphere in which the sputtering is taking place.

- **Reactive ions.** During physical sputtering, a fraction of the incident particles will be implanted into the surface layer of the sputtered substrate. Depending on the reactivity of these particles, their presence in the outermost part of the substrate will decrease the physical sputtering yield, because of the build-up of a solid layer of collected ions. For example, if one plots the sputtering yield of a Cu substrate as a function of the atomic number of the incident particle this effect is clearly seen (if the flux is sufficiently high) as *valleys* in the curve for reactant atoms such as H, C, and Ca, while strong *peaks* are seen for the inert atoms (Ne, Ar, Kr, Xe). Although H in this case decreases the physical sputtering yield, its presence may in other situations enhance it, for example, by removing oxides from the sputtered surface. An example of this effect will be shown in Sect. 4.6.
- **Reactive atmosphere.** Chemical reactions between the sputtered surface and the atmosphere in which sputtering is taking place may have equal effects on the sputtering yield. A typical example of this is oxidation of metals in oxygen-containing atmospheres. This, for example, is the case of Al and Fe, which is known to form  $Al_2O_3$  and  $Fe_2O_3$  layers if exposed to oxygen. The increased surface binding energy for these oxides results in a decrease of the sputtering yield.<sup>1</sup> In Sect. 4.5 we shall have a closer look at these two cases.

### *Physically enhanced chemical sputtering*

In some cases chemical sputtering is enhanced if the substrate is bombarded with high-energy particles such as ions. An example of this is silicon etching by  $XeF_2$  [49], which is widely used in the semiconductor industry. The  $XeF_2$  molecules will chemically sputter (or *etch*) Si by themselves, but a significant

<sup>1</sup>Metal(-oxides) like  $Mo(O_3)$ ,  $Nb_2(O_5)$  and  $W(O_3)$  actually have lower surface binding energies than their corresponding clean metals, but the fact that only a fraction of the sputtered atoms are metal atoms, effectively lowers the *metal* sputtering yield. An exception to this is  $V_2(O_5)$  for which an increase in metal sputtering rate is observed for the oxide [48].

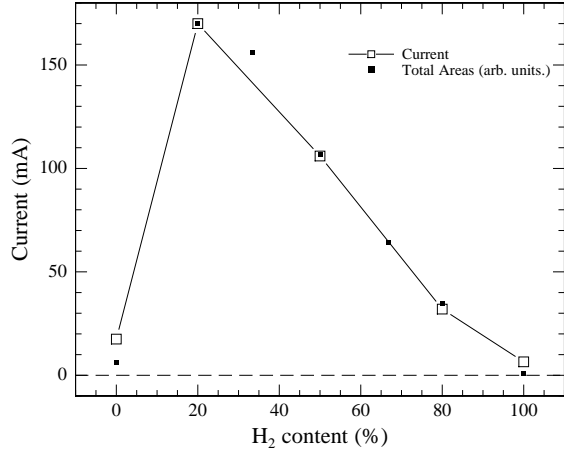


**Figure 4.5** Measured discharge current during on pulse as a function of hydrogen content (—□—) and summed charge weighted area of the ion energy-distributions (■).

increase in the etch rate is achieved if the Si substrate is simultaneously bombardment with 1 keV Ne<sup>+</sup> ions.

## 4.2 Measurements of the Ar-H<sub>2</sub> Discharge

Before looking at the sputtering properties of the Ar-H<sub>2</sub> discharge, let us examine what happens to the argon discharge when hydrogen is added to it, and establish which ions are present at the cathode and what their energy-distributions are. To do this, I will present some ion energy-distributions measured with the Hiden EQP of an Ar-H<sub>2</sub> discharge driven at discharge voltage of  $-300$  V and a pressure of 0.2 mbar with varying H<sub>2</sub> content. The measurements presented here were performed with an Al-coated inner electrode (see Sect. 2.2 p. 35).

### Plasma intensity

Fig. 4.5 shows the measured current of the discharge (—□—), and the total summed areas of the energy-distributions of all the ions which were measured by the Hiden EQP (■), both as a function of H<sub>2</sub> content. As the curve clearly reveals, the plasma intensity increases drastically upon the addition of even very small amounts of hydrogen — actually the current is even larger at 5% H<sub>2</sub> (not shown in the figure, see Fig. 4.13 p. 98, which is for a stainless steel cathode). It is, however, somewhat puzzling that hydrogen has this effect. Let us look at some possible reasons for this increase in intensity.

SOLID	Ar <sup>+</sup>	H <sub>2</sub> <sup>+</sup>	REF.
Al	0.12	0.095	Chapman [12]
Fe	0.058	0.061	
Cu	0.058	0.050	
W	0.095	0.029	Konuma [28]
Al	0.38	0.19	Böhm and Perrin [50]
Cu	0.26	0.08	
SS	0.29	0.07	
<i>a</i> -Si:H	0.28	0.14	

**Table 4.1** Secondary electron emission coefficients,  $\gamma_{se}$ , for Ar<sup>+</sup> and H<sub>2</sub><sup>+</sup> ions impinging on various materials. “SS” denotes stainless steel.

1. **Ionization and secondary electron emission rates of Ar and H<sub>2</sub>.** It is well known that H<sub>2</sub> has a higher breakdown voltage than Ar (see Fig. 1.3 p. 12). Also, Fig. 4.5 clearly shows the current of the pure H<sub>2</sub> discharge to be lower than that of the pure Ar discharge. This means

- that the secondary electron emission coefficient,  $\gamma_{se}$ , for H<sub>2</sub> is lower than that for argon, and/or
- that the electron-impact ionization cross-section is smaller for H<sub>2</sub> than for Ar.

Point (a) is supported by measurements of  $\gamma_{se}$  performed by Böhm and Perrin [50] yielding  $\gamma_{se}[\text{H}_2^+ > \text{Al}] = 0.19$  and  $\gamma_{se}[\text{Ar}^+ > \text{Al}] = 0.38$ , using 0.18-torr RF discharges. A lower  $\gamma_{se}[\text{H}_2^+]$ -value was also observed for all other cathode materials used (*a*-Si:H, stainless steel and Cu), resulting in even larger differences. Tab. 4.1 summarizes the values of  $\gamma_{se}$  for Ar<sup>+</sup> and H<sub>2</sub><sup>+</sup> found in literature for various materials. Although the actual value of  $\gamma_{se}$  will depend on ion energy and material dirtiness [25], thus maybe explaining some of the conflicting values in the table, a general tendency of  $\gamma_{se}[\text{Ar}^+] > \gamma_{se}[\text{H}_2^+]$  seems to be the case (maybe apart from Fe).

As for (b), the maximum cross-sections for electron-impact ionization are  $\sigma[\text{Ar}] \sim 2.8 \times 10^{-16} \text{ cm}^2$  (at 100 eV, see Fig. 1.2) and  $\sigma[\text{H}_2] \sim 10^{-16} \text{ cm}^2$  [51] (at 60–70 eV). Hence, the increase in plasma intensity upon addition of hydrogen cannot be ascribed to an increased secondary electron emission or ionization rate for H<sub>2</sub> as compared to Ar.

2. **Change in surface properties.** At the residual pressure of the plasma chamber ( $\sim 10^{-3}$  mbar) the aluminium surface oxidizes, thus leading to the build-up of an Al<sub>2</sub>O<sub>3</sub> surface layer (see Sect. 4.5). As we shall see in Sect. 4.6, the addition of hydrogen to an argon discharge drastically increases the sputtering of such a surface because of chemically enhanced

PROCESS		CROSS SECTION (CM <sup>2</sup> )
a)	$e^- + H_2 \rightarrow 2e^- + H_2^+$	$10^{-16}$ (40–70 eV)
b)	$e^- + H \rightarrow 2e^- + H^+$	$7 \times 10^{-17}$ (40 eV)
c)	$e^- + H(2s) \rightarrow 2e^- + H^+$	$10^{-15}$ (10–20 eV)
d)	$e^- + Ar \rightarrow 2e^- + Ar^+$	$2.8 \times 10^{-16}$ (100 eV)
e)	$e^- + Ar \rightarrow e^- + Ar^*$	$1.5 \times 10^{-16}$ (30 eV)
f)	$e^- + ArH^+ \rightarrow Ar + H^*$	$k \sim 10^{-7} \text{ cm}^3/\text{s}$
g)	$H_2^+ + H_2 \rightarrow H_2 + H_2^+$	$10^{-15}$ (10 eV)
h)	$H_2^+ + H_2 \rightarrow H_3^+ + H$	$8 \times 10^{-15}$ – $4 \times 10^{-17}$ (0.1–10 eV)
i)	$Ar^+ + Ar \rightarrow Ar + Ar^+$	$5 \times 10^{-15}$ (1–10 eV)
j)	$Ar^+ + H_2 \rightarrow ArH^+ + H$	$10^{-14}$ – $2 \times 10^{-15}$ (0.1–10 eV)
k)	$Ar + H_2^+ \rightarrow ArH^+ + H$	$6 \times 10^{-15}$ – $3 \times 10^{-16}$ (0.1–10 eV)
l)	$Ar^+ + H_2 \rightarrow Ar + H_2^+$	$10^{-15}$ (1–1 000 eV)
m)	$Ar + H_2^+ \rightarrow Ar^+ + H_2$	$3 \times 10^{-16}$ – $5 \times 10^{-16}$ (1–10 eV)

**Table 4.2** Some important processes which can occur between the major species of an Ar-H<sub>2</sub> discharge. Only processes involving at least one abundant species and with an appreciative cross-section are shown. Taken from Bogaerts and Gijbels [39], where also a more comprehensive list can be found.

sputtering, thus changing the cathode properties and hence the secondary electron emission coefficient. However, the secondary electron emission coefficient is known to increase with surface oxidation of Al. For example, Tucek *et al.* [52] report of a strong increase of  $\gamma_{se}[\text{Na}^+ > \text{Al}]$  as the oxygen surface coverage of Al increases. Hence, it does not seem likely that it is the sputtering of an Al<sub>2</sub>O<sub>3</sub> surface layer that causes the dramatic increase in plasma intensity.

3. **The “synergy” effect.** As is clear from Fig. 4.5, revealing that both the Ar and the H<sub>2</sub> discharge has a lower current than the Ar-H<sub>2</sub> discharge, it must be the *combination* of Ar and H<sub>2</sub> that seems to be increasing the plasma intensity. Obviously, the number of collisions which can occur between the species of such a discharge is enormous. Bogaerts and Gijbels [39] have made a comprehensive list of all these collisions, including ionization, excitation, charge transfer, and so on. In Tab. 4.2 the most important of these processes are shown. The first thing to notice is the very large cross sections of processes j) and k), leading to a high degree of “conversion” of Ar<sup>+</sup> and, to a somewhat lesser extent, H<sub>2</sub><sup>+</sup> ions into ArH<sup>+</sup>. As we shall see in a moment, ArH<sup>+</sup> is actually one of the dominant ions of the Ar-H<sub>2</sub> discharge, in good agreement with this. However, the ArH<sup>+</sup> ions generated by this process will quickly undergo electron recombination via process

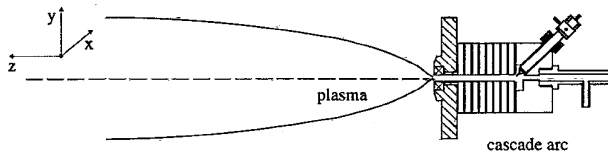


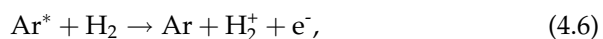
**Figure 4.6** Schematic diagram of the cascaded arc experiment performed by Meulenbroeks *et al.* [53].

f). On this basis, Bogaerts and Gijbels conclude that a *decrease* in Ar<sup>+</sup> and possibly electron density must be expected upon the addition of hydrogen to an argon discharge.

These conclusions are seemingly supported by the experiments of Meulenbroeks *et al.* [53] and Mason *et al.* [54]. Meulenbroeks *et al.* perform Thomas-Rayleigh scattering and optical emission spectroscopy experiments on an Ar-H<sub>2</sub> plasma jet with H<sub>2</sub> contents of 0–1.4 vol-% H<sub>2</sub>. Fig. 4.6 shows a schematic diagram of their experiment. Hydrogen is added to the argon flow before it enters the cascaded arc. The Thomas-Rayleigh scattering measurements were performed on a number of points on the z-axis, and showed a “severe” reduction of the electron density upon the addition of hydrogen, which they ascribe to the recombination channel j) + f). Mason *et al.* [54] perform fast flow glow discharge spectroscopy of an Ar discharge with H<sub>2</sub> added in the positive column. Hence, this is *essentially* not really an Ar-H<sub>2</sub> discharge, since the hydrogen is added to the *flow* of plasma ions from the discharge, i.e., *after* the plasma is formed. Nevertheless, it can be concluded from their experiments that an effective quenching of the Ar<sup>+</sup> ions occurs when H<sub>2</sub> is added.

It should be noted that the recombination of ArH<sup>+</sup> will result in the generation of excited H atoms, which have a large cross-section for electron impact ionization for the  $n = 2$  state (process c). Although this channel has been reported to re-increase the electron density of a pulsed Ar-H<sub>2</sub> discharge after ArH<sup>+</sup> recombination [55], it still requires an ArH<sup>+</sup> ion and hence, initially, an Ar<sup>+</sup> and H<sub>2</sub><sup>+</sup> ion to take place. Hence, despite the high cross-section for H(2s) ionization, the ionization rate of the discharge is still limited by cross-sections for Ar and H<sub>2</sub> ionization. The only effect of process c) in this respect would be to partly eliminate the discharge neutralization taking place by the channels j) + f) and k) + f).

One alternative possibility in explaining the increase of ionization could be sought in the *Penning ionization process* for excited Ar [56]:



which is possible for excited levels in argon which have an energy equal to or slightly larger than the H<sub>2</sub>-ionization energy of 15.43 eV. Argon has metastable (i.e., long-lived) levels at 11.55 eV and 11.72 eV, which clearly

cannot Penning ionize H<sub>2</sub>. However, within the discharge itself there will be a constant excitation of Ar atoms taking place, meaning that some finite amount of short-lived excited Ar atoms should always be present in the plasma. Hence, since argon has a vast amount of short-lived excited states around and above the ionization energy of H<sub>2</sub>, these excited states could be contributing to ionization in the discharge when of H<sub>2</sub> is added. Since the measurements of Meulenbroeks *et al.* and Mason *et al.* were made *after* the ionization region, were only the metastable levels can be expected to prevail, Penning ionization would not play any part in their cases.

The conclusion to all this, however, still seems to be that there is no major “synergy” effect by combination of Ar and H<sub>2</sub>. From an analytical point of view (Bogaerts and Gijbels) and the two experiments mentioned (Meulenbroeks *et al.* and Mason *et al.*), the addition of H<sub>2</sub> ought to be *decreasing* the plasma intensity. Not the opposite!!

4. **Secondary electron emission of ArH<sup>+</sup>?** So what possibilities do we have left? Well, since the bulk plasma by itself – apparently – cannot account for the increase in intensity, it must be its interaction with the cathode that does it. As already mentioned, ArH<sup>+</sup> is a very dominant ion in the Ar-H<sub>2</sub> discharge, for all H<sub>2</sub> concentrations, and with huge quantities of it bombarding the cathode (which we shall see in the next section). Maybe the secondary electron emission coefficient for the ArH<sup>+</sup> ions is significantly greater than that for Ar<sup>+</sup> and H<sub>2</sub><sup>+</sup>? If this is the case, maybe it could explain why the plasma “explodes” when H<sub>2</sub> is added. I, at least, cannot at present see any other explanation for the observed.

Concluding the discussion above, there is only to say that no conclusive evidence can be found, explaining why the plasma intensity behaves the way as shown in Fig. 4.5. The measurements shown there were performed with an Al cathode. The behaviour of the stainless steel cathode is exactly the same (see Fig. 4.13 p. 98). The most reasonable explanation at this point seems to lie in the properties of the ArH<sup>+</sup> ion — most notably its secondary electron emission coefficient. And as we shall see in the remainder of this chapter, when it comes to sputtering, ArH<sup>+</sup> will also prove to be playing the dominant role in the observed effects.

## Ion energy-distributions

Figs. 4.7 and 4.8 show the measured energy distributions for Ar-H<sub>2</sub> discharges at 0%, 50% and 100% H<sub>2</sub> content. The most abundant ions at the cathode are Ar<sup>+</sup>, Ar<sup>2+</sup>, ArH<sup>+</sup>, H<sub>2</sub><sup>+</sup> and H<sub>3</sub><sup>+</sup>. Because of the complexity of the Ar-H<sub>2</sub> discharges, these energy-distribution cannot be explained by such simple means as for the

pure argon discharge. However, with the collision processes of Tab. 4.2 in mind, a qualitative justification of the observed will not prove too difficult.

The first thing to notice, however, is the general increase in the fraction of high-energy ions that occurs when H<sub>2</sub> is added. The main reason for this is the decrease in sheath thickness which must be expected as a result of the increase in discharge current. Although the Child law (Eq. (1.27)) is only valid for a mono-atomic discharge, its qualitative features should also be applicable for the Ar-H<sub>2</sub> discharge. These features dictate, that for fixed voltage and pressure, an increase in current-density will result in a decrease of the sheath thickness. This can also easily be understood if one considers the mechanisms behind sheath formation; the higher the ion density in the sheath is, the smaller is the amount of space needed to sustain the discharge voltage. Hence, although we cannot really explain *why* the current increases, the fact that it does increase and thus leads to a thinning of the sheath, can be used to explain the general behaviour of the ion energy-distributions: when the sheath thickness decreases, the ions that transverse the sheath undergo fewer collisions and hence have higher energies.

### Ar<sup>+</sup>

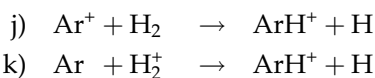
The discussion above could very in itself well explain the increase in average energy of the Ar<sup>+</sup> ions, which can be observed by comparison of Figs. 4.7a and 4.7b. As we know, the symmetrical charge transfer (SCT) process:



is an effective attenuator of Ar<sup>+</sup> ions accelerating in the sheath. In the pure argon case, the Ar<sup>+</sup> energy-distribution function resulting from this process is governed by the mean number of charge exchanges per Ar<sup>+</sup> ion,  $s/\lambda$ , where  $s$  is the sheath thickness and  $\lambda$  the mean-free-path for SCT. Since  $s$  has decreased, the Davis and Vanderslice distribution (Eq.(1.36)) leads to an increase of the high-energy fraction. Although the situation in the Ar-H<sub>2</sub> discharge is somewhat more complicated, the SCT process will still be the dominant attenuator of the Ar<sup>+</sup> ions, so that a comparison with the pure Ar discharge may be made.

### ArH<sup>+</sup>

Fig. 4.7b shows the energy-distributions of the ArH<sup>+</sup>, Ar<sup>+</sup> and Ar<sup>2+</sup> ions. As already mentioned in the previous section, the processes:



which both have relatively large cross sections (see Tab. 4.2) will result in a large amount of ArH<sup>+</sup> ions in the discharge. Since electron recombination (f) will of

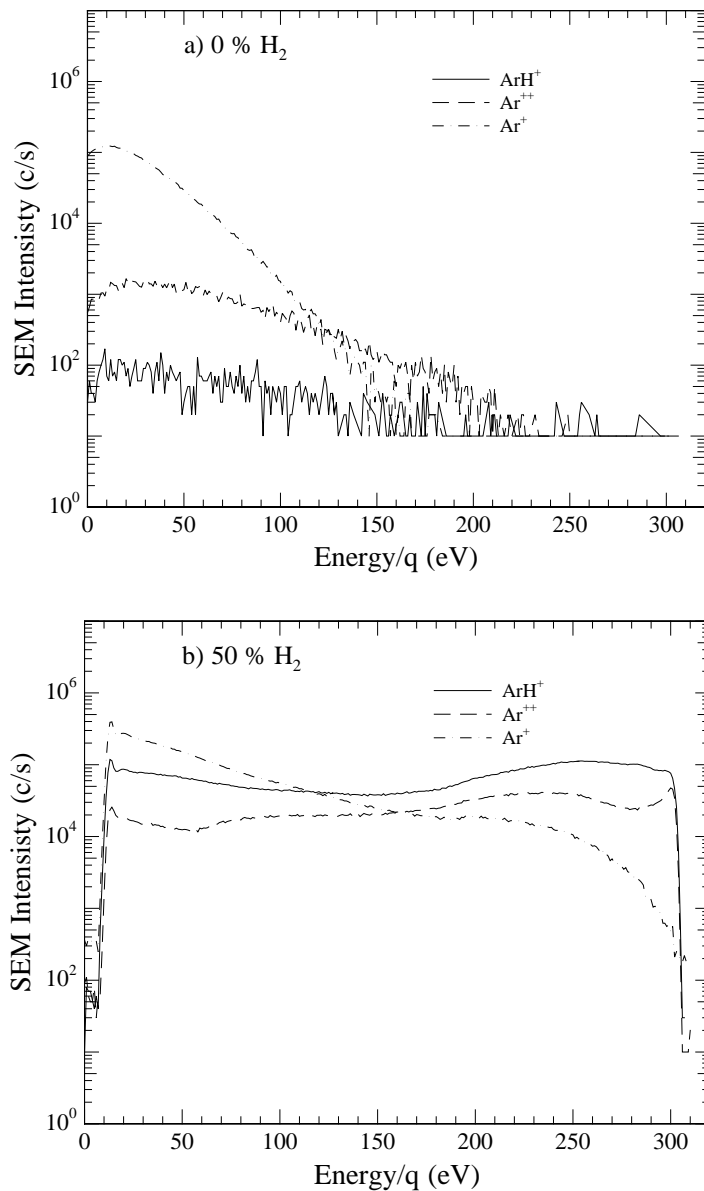


**Figure 4.7** ion energy-distributions of the most prevalent ions for an Ar-H<sub>2</sub> discharge (−300 V, 0.2 mbar) with a H<sub>2</sub> content of a) 0% and b) 50%. Note that for the Ar<sup>2+</sup> spectra the energy scale must be doubled, since Ar<sup>2+</sup> has charge number  $q = 2$ .

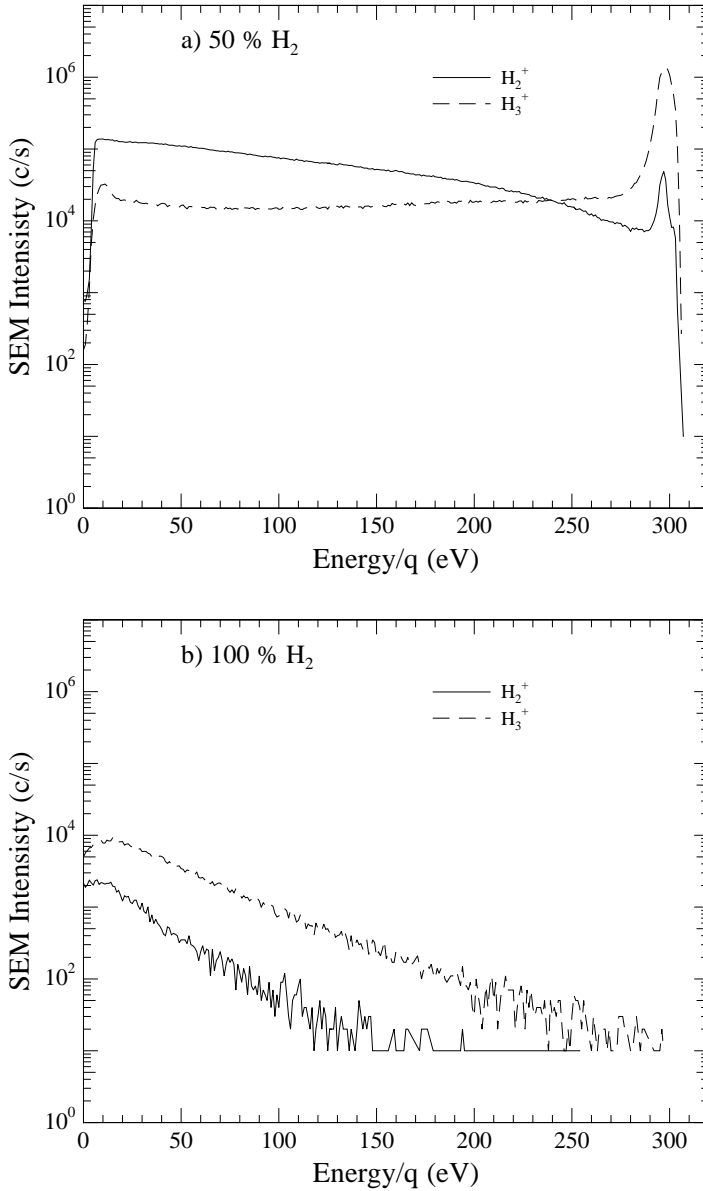


**Figure 4.8** ion energy-distributions of the most prevalent ions for an Ar-H<sub>2</sub> discharge (−300 V, 0.2 mbar) with a H<sub>2</sub> content of a) 50% and b) 100%. Note that for the Ar<sup>2+</sup> spectra the energy scale must be doubled, since Ar<sup>2+</sup> has charge number  $q = 2$ .

course neutralize these ions to some extent, it is difficult to assess how dominant the ion is in the bulk plasma itself. Since there are no electrons in the sheath, ArH<sup>+</sup> ions created here will not recombine to the same extent as those in the bulk plasma, which would increase the ArH<sup>+</sup> fraction at the cathode as compared to the bulk plasma.

Comparing the ArH<sup>+</sup> energy-distribution to that of the Ar<sup>+</sup> ions, it can be seen that the ArH<sup>+</sup> distribution has a much higher fraction of energetic ions (note the logarithmic scale). Since ArH<sup>+</sup> of course has no neutral counterpart, the ArH<sup>+</sup> ions are not as effectively slowed down on their way through the sheath as the Ar<sup>+</sup> ions are, thus leading to a relatively higher high-energy fraction.

### Ar<sup>2+</sup>

As is evident from Fig. 4.7b there are large quantities of Ar<sup>2+</sup> ions present at the cathode. Because of its doubly charged status,  $q = 2$ , the energy-distribution of these ions ranges from 0–600 eV. As for Ar<sup>+</sup>, Ar<sup>2+</sup> undergoes (two-electron) symmetrical charge exchange with the neutral Ar atoms, although the cross section is lower by roughly a factor of 10 [10]. As a result, just as in the pure argon case, the Ar<sup>2+</sup> ions are more energetic than the Ar<sup>+</sup> ions, as is also clear from the figure.

Now the question arises why Ar<sup>2+</sup> is so abundant. Naturally, electron impact ionization of Ar will significantly favor Ar<sup>+</sup> creation compared to Ar<sup>2+</sup>. Nevertheless, the abundance of Ar<sup>2+</sup> in this case is comparable to Ar<sup>+</sup>. Hence, it seems likely that there exist other routes to the creation of Ar<sup>2+</sup>, possibly via the ArH<sup>+</sup> ion, which can be seen to have a similar energy-distribution but with higher fluxes.

### H<sub>2</sub><sup>+</sup> and H<sub>3</sub><sup>+</sup>

Just like Ar<sup>+</sup>, H<sub>2</sub><sup>+</sup> is one of the primary ions of the Ar-H<sub>2</sub> discharge, created through electron impact ionization of H<sub>2</sub>. Although these ions will also undergo symmetrical charge exchange:



Fig. 4.8a shows them to have a higher average energy than Ar<sup>+</sup>. This can be explained by the fact the the SCT cross-section for H<sub>2</sub><sup>+</sup> is slightly lower than for Ar<sup>+</sup> (see Tab. 4.2). Furthermore, the end point peak, signifying the non-colliding ions, is very distinct for H<sub>2</sub><sup>+</sup>. Even more so is the case for the H<sub>3</sub><sup>+</sup> ion, which is probably created mainly via the process:



The very large fraction of non-colliding  $H_3^+$  indicates that this ion is very abundant in the bulk plasma, maybe even exceeding  $H_2^+$ . This is also clearly seen in Fig. 4.8b, showing the energy distributions of the ions of a pure  $H_2$  discharge.

### The neutrals

The energy-distributions shown here are for the ions impinging on the cathode. As mentioned several times earlier, fast neutrals are created via the various collision processes which these ions undergo in the sheath. Most notably the charge exchange processes. Now, of course neutrals are not accelerated in the sheath, so the fast neutrals which *do* exist must originate from an ion. Hence, although we cannot measure the energy-distribution of these neutrals, it seems safe to assume that they will in general be quite similar to the ion energy-distributions, but with a lower average energy (since they are not accelerated further upon creation).

## 4.3 Sputtering Experiments — Methods

The basic idea behind the sputtering experiments presented in this chapter is to perform a comparison between two sputtering efficiencies. The *measured* sputtering efficiency,  $S_{\text{tot}}$ , is determined by measuring how much substrate material was actually removed during a sputtering process. This was done using Rutherford backscattering spectrometry (RBS) to measure the thickness of the sputtered film before and after sputtering. The sputtered thickness,  $d$ , was then normalized to the total charge dose or integrated current,  $Q$ , the sample had received during sputtering:

$$S_{\text{tot}} = \frac{d\rho}{Q/(eA)}, \quad (4.7)$$

where  $\rho$  is the atomic density of the substrate material and  $A$  is the cathode area. The *expected* physical sputtering efficiency,  $S_{\text{phy}}$  was determined by inserting the measured ion energy-distributions of the sputter discharge,  $f_i$ , and the known physical sputtering yield curves,  $Y_i$ , into Eq. (4.5):

$$S_{\text{phy}} = \frac{\int \sum_i f_i(E) \times Y_i(E) dE}{\int \sum_i f_i(E) dE}. \quad (4.5)$$

$S_{\text{phy}}$  hence signifies the *physical* sputtering efficiency of the discharge while  $S_{\text{tot}}$  signifies the *total* (physical and/or chemical) sputtering efficiency.

Now, for a given discharge some care has to be taken when comparing these two quantities. Although both are ion-dose normalized,  $S_{\text{tot}}$  of course includes both the ion and neutral contributions through  $d$ , while  $S_{\text{phy}}$  only includes the ion contribution. However, it is not an absolute comparison between these two values which is important, but their variation *as a function of the H<sub>2</sub> content*. If we assume that the neutral contribution to physical sputtering is adequately described by the ions, as a function of H<sub>2</sub> content, this type of comparison may be made. We may do this if the change in energy-distribution of the neutrals as H<sub>2</sub> varies, mimics that of the ions. As was discussed at the end of the previous section, this assumption can readily be justified.

## 4.4 Gold — Physical Sputtering

[Article I (full-text): “The Critical Role of Hydrogen for Physical Sputtering with Ar-H<sub>2</sub> Glow Discharges”. C. V. Budtz-Jørgensen, P. Kringhøj, and J. Böttiger, *Surf. Coat. Tech.*, **116–119**, 1999, p. 938. Presented at the PSE<sup>2</sup> '98 conference in Garmish-Partenkirchen, Germany.]

### Abstract

The physical sputtering of gold surfaces by argon-hydrogen pulsed-DC glow discharges has been measured for various gas compositions, and an optimum has been found at 5-20% H<sub>2</sub>. Furthermore, the energy distributions of the ions hitting the cathodic surface have been measured and correlated to the sputtering rates using known sputtering-yield curves. It was found that the largest contribution to the ion sputtering originated from ArH<sup>+</sup>, the fluxes and energies of Ar<sup>+</sup> being significantly smaller than for ArH<sup>+</sup>.

### Introduction

For industrial surface processing such as Plasma Assisted Chemical Vapour Deposition (PACVD), the pulsed-DC argon-hydrogen glow discharge is frequently used as a pre-deposition cleaning plasma. The role of hydrogen for the erosion of the cathodic surfaces of these discharges is thought to be due to mainly its chemical sputtering. However, in general, little is known about the erosion processes taking place (both chemical and physical sputtering) and the fluxes and energies of the bombarding particles. The practical etching techniques using plasmas have to a large extent been developed on a trial-and-error basis. The bombarding particles hitting the cathode of a pure argon discharge consist of fast ions being accelerated in the cathode-sheath region [15] and fast neutral atoms created by symmetrical charge transfer (SCT) between Ar and Ar<sup>+</sup> [40]:



<sup>2</sup>Plasma Surface Engineering

Because of its resonant character, implying large cross-sections, the SCT process effectively limits the energies of ions and neutrals hitting the cathode, as ions accelerate only over small lengths before being neutralized (for pressures in the 0.1–1 torr range used here). These low bombardment energies limit the physical sputtering of the cathode.

In the present paper, investigations of the physical sputtering of Au cathodes by Ar-H<sub>2</sub> pulsed-DC glow discharges are reported. Especially, the role of hydrogen for the physical sputtering is investigated. We report on measurements of fluxes and energies of ions hitting the cathode of glow discharges. These measurements were performed in a small, cylindrical plasma chamber using the commercial *Hidden EQP (Electrostatic Quadrupole Probe)* energy analyser and mass spectrometer (*Hidden Analytical Ltd.*, Warrington, England). It was found that mainly energetic Ar<sup>+</sup> ions and ArH<sup>+</sup> ions hit the cathodic surface (disregarding neutrals), with a smaller fraction due to H<sub>3</sub><sup>+</sup> and H<sub>2</sub><sup>+</sup> (not discussed in the present paper). As opposed to Ar<sup>+</sup>, the ArH<sup>+</sup> energy distributions have a large high-energy tail, the origin of which can be explained by the lack of the SCT process for ArH<sup>+</sup>, as it has no neutral counterpart. Furthermore, it was observed that both the ion energy-distributions and the plasma current were very sensitive to the hydrogen content, with a strong peaking of the overall ion intensity at 5% H<sub>2</sub>.

In order to see if the change in the measured ion energy-distributions caused by varying the gas composition could be correlated to the actual sputtering process, a series of sputtering experiments were performed. Since this paper is concerned only with the *physical* sputtering due to the particles bombarding the cathode, chemical sputtering was eliminated by use of gold as the cathode material, gold being non-reactive. To determine the sputtered thickness, the thickness of the gold films was measured both before and after sputtering by use of Rutherford backscattering spectrometry (RBS).

Expected sputtering efficiencies were calculated from the measured ion energy-distributions using known sputtering yield curves. As will be shown in the following, the calculated sputtering efficiencies exhibit the same dependence on gas composition as the measured sputtering efficiencies. Furthermore, it was found that the largest contribution to the sputtering originated from ArH<sup>+</sup> ions.

## Experimental

Fig. 4.9 shows a schematic diagram of the experimental setup consisting of mainly two sections: the plasma chamber, where the pulsed-DC glow-discharge is formed, and the Hidden EQP (partly shown) used for mass and energy analysis. Ions are extracted from the plasma chamber into the EQP through a 100 μm orifice.

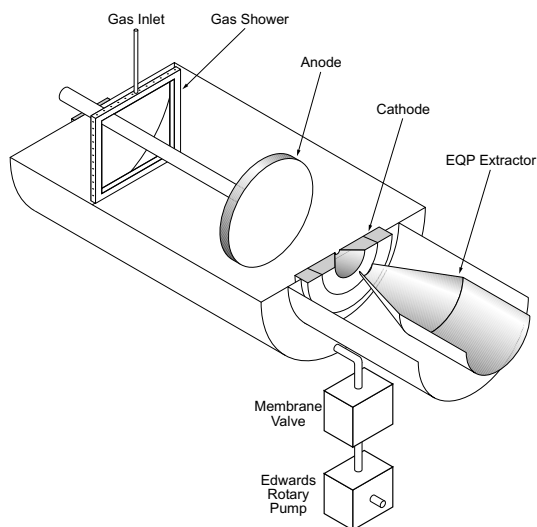


**Figure 4.9** Schematic diagram of the plasma chamber and the Hiden EQP (partly shown).

### *The plasma chamber*

The cylindrically shaped stainless steel vacuum chamber, which holds the plasma, has a diameter and length of 30 cm each. The discharge was formed between the stainless steel cathode and movable grounded anode (both circular with a diameter of 12 cm), using a cathode-anode spacing of 5 cm. The discharge voltage of  $-300$  V was supplied by a Rübige high-voltage power supply, which is part of a commercial Rübige PACVD plant. The voltage was pulsed with on- and off-times of  $100 \mu\text{s}$  each, with rise and fall times of the order of  $1 \mu\text{s}$ . The argon-hydrogen gas mixture was supplied through a gas shower, the gas flow and composition being externally controlled. The pressure was measured with a Tylan General cold-cathode pressure gauge and feedback-stabilized at a pre-set value via a computer-controlled membrane valve, which leads to a Edwards 80 two-stage rotary pump ( $80 \text{ m}^3/\text{h}$ ). An operating pressure of 0.44 torr was used with a base pressure of the order of  $10^{-4}$  torr. The  $100 \mu\text{m}$  orifice, through which the ions were extracted from the plasma chamber into the Hiden EQP, was situated at the center of the cathode (see Fig. 4.9). The pulsed-DC voltage was measured with a Hewlett-Packard digital oscilloscope through a 1:100 voltage divider, and the current was measured with a Tektronix current probe, allowing time-resolved measurement.

### *The Hiden EQP*

The Hiden EQP consists of a beam-optics section, a  $45^\circ$  sector field ion energy analyser and a quadrupole mass spectrometer. Ions passing through the orifice

are directed into the EQP by a pencil-shaped extractor head with a 700  $\mu\text{m}$  circular opening (shown in Fig. 4.9). The ions were detected by a secondary-electron multiplier (SEM).

In order to estimate the angular acceptance of the EQP, the beam-optics section was simulated using the beam-optics simulation software SIMION 3D [29]. These simulations showed an incident-angle acceptance of no more than  $\sim 2$  degrees. Computer simulations<sup>3</sup> of a pure argon plasma, taking into account both charge transfer and elastic scattering processes and driven under the same conditions as those used in our experiments, have shown that the low-energy (0–20 eV) ions can have incident angles of up to 40 degrees. Assuming similar incident angles for argon-hydrogen discharges, it is therefore to be expected that only a small fraction of the low-energy ions will actually be sampled by the EQP, resulting in suppression of the intensities of the energy spectra at low energies.

### Sputtering experiments

Between 1 000–3 000  $\text{\AA}$  of gold was e-gun evaporated on to silicon wafers in a vacuum of  $10^{-8}$  torr at 5  $\text{\AA}/\text{s}$ . A  $\sim 100\text{-\AA}$  Cr layer was used to enhance the adhesion between the Au layer and the Si wafer. To derive the sputtered thickness,  $d$ , the thickness of the Au layers on each sample was measured before and after sputtering by RBS using 2 MeV He (see Fig. 4.10). The  $\sim 1 \text{ cm}^2$ -cut samples were attached to the cathode of the plasma chamber using “silver paste” to ensure good electrical contact. The sputtering measurements were normalized to the integrated charge. A total ion-charge dose of  $Q = 3\,000\text{--}4\,000 \text{ mA} \times \text{min}$  was used, corresponding to sputtering times between 30 minutes and 20 hours, depending on the plasma current. The effective sputtering rate was calculated using the formula:

$$\text{Sputtering Rate} = \frac{\text{sputtered atoms/cm}^2}{\text{incident ions/cm}^2} = \frac{d \times \rho_{\text{Au}}}{Q/(e \times A)} \quad (4.9)$$

where  $\rho_{\text{Au}}$  is the atomic density of gold,  $e$  is the unit charge and  $A$  is the cathode area.

## Results

The measurements were performed with argon-hydrogen discharges of different gas compositions but with the same voltage profile (square wave, 0 V and  $-300$  V, with on- and off-times of 100  $\mu\text{s}$  each) and an operating pressure of 0.44 torr.

<sup>3</sup>Particle-In-Cell (PIC) and Monte Carlo computer simulations of an argon glow-discharge performed by the *xpdp1* plasma simulation software developed by the *Plasma Theory and Simulation Group* at Berkeley University.

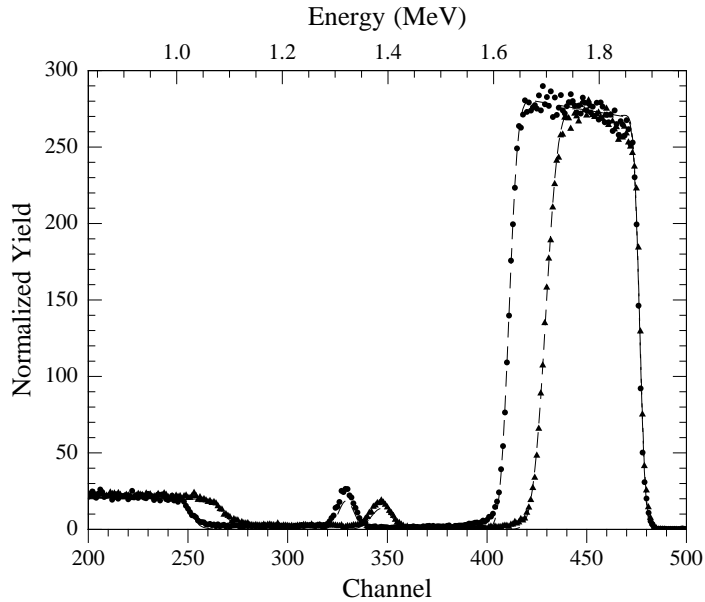


**Figure 4.10** Typical RBS spectrum of a thin gold film before and after sputtering (50% H<sub>2</sub>). Contributions can also be seen from the silicon substrate and the 100-Å Cr layer used to increase the adhesion between the silicon wafer and the gold film.

### Energy spectra

Figs. 4.11 and 4.12 show the measured energy spectra for Ar<sup>+</sup> and ArH<sup>+</sup> ions for various gas compositions (H<sub>2</sub> content shown). Time-resolved measurements have shown that the steady-state ion energy-distribution is established within the first few microseconds of the on pulse. A cut-off of the energy distributions can be seen at around 10 eV, which as mentioned is thought to be caused by the acceptance-angle profile of the EQP. The discontinuity of the spectra at 200 eV is also artificial, caused by the limited single-run energy-scan range of the EQP.

Upon addition of 5% hydrogen to the pure argon plasma, a drastic increase of the overall Ar<sup>+</sup> intensity is observed, most notably around the 80 eV region, where a peak structure develops (Fig. 4.11). A similar peak structure has previously been reported [57] for Ar<sup>+</sup> and H<sub>2</sub><sup>+</sup> ions in a N<sub>2</sub>-H<sub>2</sub>-Ar (5:5:1) glow-discharge at 1.5 torr. As the hydrogen content is increased further, the Ar<sup>+</sup>-ion intensity drops again although retaining the peak structure. Fig. 4.12 shows the energy spectra for ArH<sup>+</sup> ions, which are seen to be similar to the Ar<sup>+</sup> distribu-

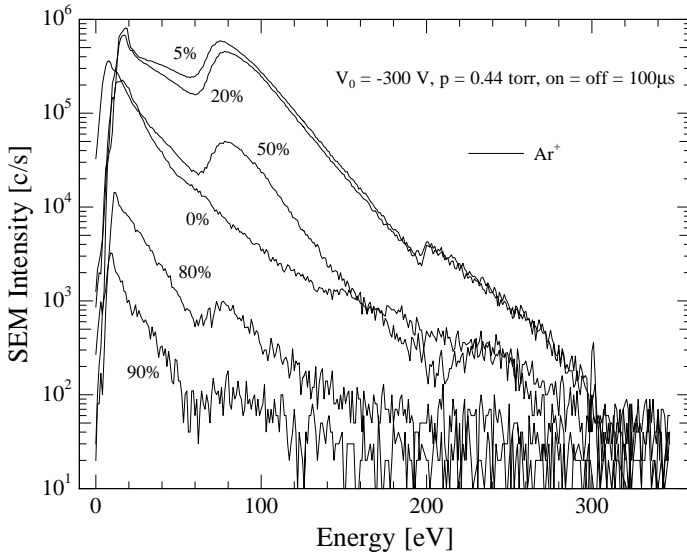


**Figure 4.11**  $\text{Ar}^+$  ion energy-distributions for different gas compositions ( $\text{H}_2$  content shown).

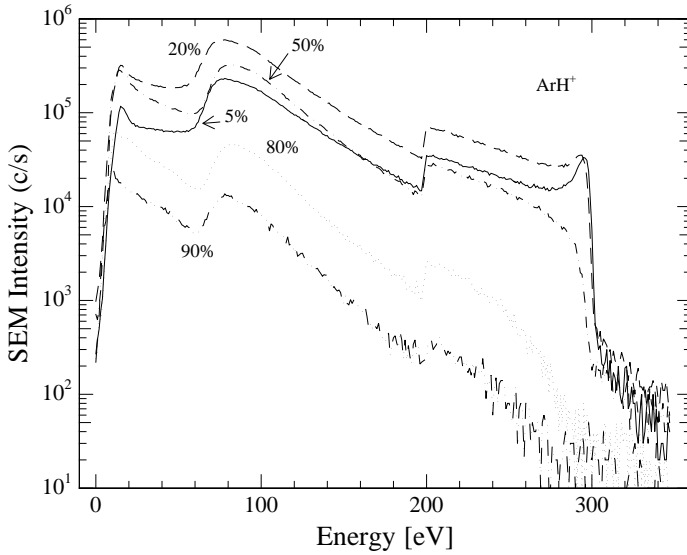


**Figure 4.12**  $\text{ArH}^+$  ion energy-distributions for different gas compositions ( $\text{H}_2$  content shown).

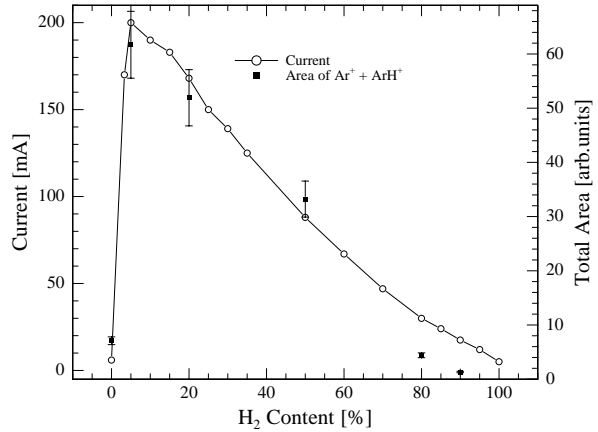


**Figure 4.13** Measured plasma current during voltage on pulse (—○—) in comparison with the total summed area of the Ar<sup>+</sup> and ArH<sup>+</sup> spectra (■).

tions at low energies, both in intensity and shape, although peaking in intensity at 20% H<sub>2</sub>. At high energies, however, the intensity of ArH<sup>+</sup> is significantly larger than that of Ar<sup>+</sup>, which can be explained by the lack of the SCT process for ArH<sup>+</sup> ions. Also, the 80 eV peak structure is seen to be more pronounced for the ArH<sup>+</sup> ions than for the Ar<sup>+</sup> ions, thereby suggesting its origin. Dissociation of energetic ArH<sup>+</sup> ions (e.g. via symmetric proton transfer with neutral Ar) may be a probable source for the energetic Ar<sup>+</sup> ions, causing the Ar<sup>+</sup>-ion energy-distribution to reflect that of the ArH<sup>+</sup> ions.

### *The plasma current*

Because of the energy-dependent detection efficiency of the EQP, the only real indication of the actual ion intensity on the cathode is the measured current (disregarding a small fraction due to secondary electrons). Fig. 4.13 shows the measured current as a function of gas composition (solid line), reflecting the plasma impedance, in comparison with the sum of the total areas of the Ar<sup>+</sup> and ArH<sup>+</sup> spectra (filled squares). Again the drastic effect of hydrogen is evident, the plasma current increasing a factor of 35 upon addition of 5% H<sub>2</sub>. Furthermore, the dependence of the areas of Ar<sup>+</sup>- and ArH<sup>+</sup>-spectra on gas composition can be seen to follow the measured current, in spite of the poor sampling efficiency at low energies. At high H<sub>2</sub>-contents the area curve can be seen to be somewhat lower than the measured current (taking into account the 10% error bars shown), suggesting that hydrogenic ions are contributing to the current. Even though hydrogenic ions were observed, the transmission efficiency of the EQP for these ions was observed to be different than for the heavier argon-related ions. The hydrogenic contribution is therefore neglected in the present paper.

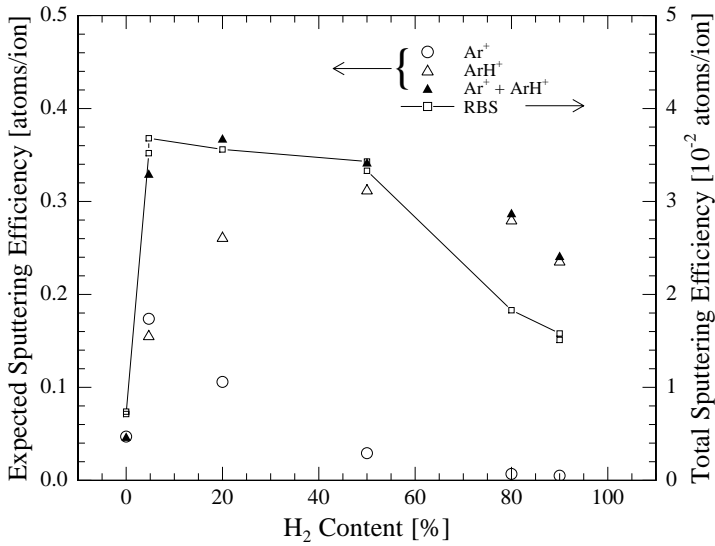


**Figure 4.14** Measured effective sputtering efficiencies on thin gold films ( $\square$ , right axis) and expected calculated sputtering efficiencies ( $\circ$ ,  $\triangle$ ,  $\blacktriangle$ , left axis).

### *Sputtering experiments*

Fig. 4.14 shows the measured sputtering efficiencies as a function of gas composition (solid line, right axis). The sputtering rate was determined for 0, 5, 20, 50, 80 and 90% H<sub>2</sub> content, and an optimum gas composition was found at around 5-20%. Error bars corresponding to 5-10% must be expected due to the RBS resolution, but for clarity these are not shown. In all cases, except for 20% and 80%, two separate samples were sputtered and measured for each gas composition (small squares in figure), and the resulting sputtering efficiencies are seen to be in good agreement. Another experimental factor to be considered is the importance of the gas flow used. All the efficiencies in Fig. 4.14 were measured using a total gas flow of 150 slh. Two samples were therefore sputtered at 50% H<sub>2</sub> content using a total gas flow of 75 slh at the same pressure, and no significant change in sputtering efficiencies was observed.

### *Sputtering efficiencies derived from the energy spectra*

In order to see if the H<sub>2</sub> dependence of the measured sputtering efficiencies could be correlated to the Ar<sup>+</sup> and ArH<sup>+</sup> energy spectra of Figs. 4.11 and 4.12,

the expected average sputtering efficiencies were derived from the spectra. This was done using the sputtering-yield curve for Ar on Au proposed by Y. Yamamura *et al.*[47] and the formula:<sup>4</sup>

$$\text{Average Sputtering Yield (atoms/ion)} = \frac{\int Y(E) \times g_E(E) dE}{\int g_E(E) dE} \quad (4.10)$$

where  $Y(E)$  denotes the yield curve and  $g_E(E)$  the total energy-distribution for both Ar<sup>+</sup> and ArH<sup>+</sup>. The total area of the distributions was used as the normalization factor. Some caution must be taken here in interpreting the results. Even though the low-energy region of the distributions does not contribute to the actual sputtering process, it plays its part in the normalization factor of Eq. (4.9), and therefore the values of the extracted average efficiencies. As only a small fraction of the low-energy ions are represented in the energy distributions of Figs. 4.11 and 4.12, this means that the calculated average efficiencies will be overestimated. One could argue here that this also would have consequences for the relative values of the calculated average efficiencies (i.e. the shape of the curve). However, it was shown in Fig. 4.13 that the number of ions sampled by the EQP represents the measured current. This means that even though the normalization factor of Eq. (4.9) is too low, it does represent the number of ions hitting the cathode *as a function of H<sub>2</sub> content*, and can therefore be used for normalization.

The sputtering efficiencies as calculated with Eq. (4.9) are also shown in Fig. 4.14 (left axis). The open symbols represent the contributions from Ar<sup>+</sup> (circles) and ArH<sup>+</sup> (triangles) and the full triangles show their sum.

## Discussion

From Fig. 4.14, it is seen that the shapes of the curves of the measured sputtering efficiencies and of the expected average sputtering efficiencies, calculated on the basis of the measured ion energy-distributions, are in good agreement. However, the absolute values of the calculated efficiencies are higher than the measured ones (by a factor of 10). Also it can be seen that the ArH<sup>+</sup> ions are the most important sputtering ions, even for plasmas with low hydrogen content. There are, however, a number of points to be considered when comparing the curves. First of all, neutral-atom sputtering was neglected. As mentioned above, because of the charge exchange process between Ar and Ar<sup>+</sup>, high-energy (neutral) Ar atoms directed towards the cathode are generated which also contribute to the measured sputtering efficiencies (and a similar contribution from ArH<sup>+</sup>). Theoretical calculations of a pure Ar plasma [40] have estimated that

<sup>4</sup>Disregarding the extra proton of the ArH<sup>+</sup> molecule. Upon hitting the surface, the ionic molecule is most likely split into its two components, the hydrogen atom receiving only 1/40 of the total energy.

the flux of fast neutrals will be significantly larger than that of the ions. It was also concluded that the fast-neutral energy-distribution would be similar though slightly lower than the ion energy-distribution, and that the proportion between the ion and atom fluxes is constant. The neutral contribution to the sputtering process will therefore reflect the ion contribution and will therefore not change the relative sputtering efficiencies as a function of H<sub>2</sub> content.

At the pressures used here, the back-diffusion and possible re-implantation of sputtered atoms has been estimated to be as large as 90% of the sputtered material [58], thereby underestimating the measured sputtering efficiencies to the actual sputtering yield *per ion*. Some preliminary measurements at different pressures have shown the measured sputtering rate to increase significantly at lower pressures, which is in agreement with back-diffusion effects.

The effect of pure hydrogen ions hitting the cathode has also not been considered. Because of their small mass they will not contribute significantly to the sputtering process, but only to the measured current. As the fraction of hydrogen ions must be expected to increase with the H<sub>2</sub> content of the discharge, the current normalization will cause the sputtering efficiencies to be underestimated at higher H<sub>2</sub> contents. As can be seen in Fig. 4.14, this is in fact the case for the 80% and 90% H<sub>2</sub> sputtering efficiencies.

Finally the secondary electron emission coefficient (SEC) for gold might be different than that for stainless steel, and show a dependence on gas composition, altering the discharge characteristics over the gold-film samples. Again, this is only important as far as the energy distributions of the ions are very sensitive to the SEC, which is not expected.

## Summary

In summary, we have shown that the physical sputtering is optimized for an Ar-H<sub>2</sub> erosion plasma with a hydrogen concentration of 5-20 vol-%. Due to the lack of a symmetrical charge transfer process in the case of ArH<sup>+</sup> ions, adding hydrogen to an Ar plasma results in a large increase in the number of energetic ions hitting the cathode, whereby the physical sputtering dramatically increases. The physical sputtering of gold surfaces by argon-hydrogen pulsed-DC glow discharges has been measured for various gas compositions, and an optimum has been found at 5-20% H<sub>2</sub>. Furthermore, the energy distributions of the ions hitting the cathodic surface have been measured and correlated to the sputtering efficiencies using known sputtering-yield curves. It was found that the largest contribution to the ion sputtering originated from ArH<sup>+</sup>, the fluxes and energies of Ar<sup>+</sup> being significantly smaller than for ArH<sup>+</sup>.

**Further notes (thesis only)**

The energy spectra presented in this article show an example of the problems which arise when using the Energy-scan method with fixed Lens1-value, as was discussed in Sect. 2.3. On the basis of the discussion presented there, the 80-eV peaks which are observed in the spectra can be explained as a reflection of the actual Lens1-value which was used during the scan. After changing to the Reference-scan method these peak structures were no longer observed, and, hence, they must in fact be considered an artifact.

Furthermore, the Hidden measurements presented here were performed with a stainless steel inner electrode. As mentioned in the article, the discharge characteristics over the Au samples might be different than that of the stainless steel electrode because of a difference in secondary emission coefficient. For example, as we shall see in Sect. 4.6, an Al cathode greatly enhances the plasma as compared to a stainless steel cathode. Nevertheless, we do not expect this to be the case for Au and stainless steel, since, by visual inspection, the plasma intensity was observed to be unaltered over the Au samples.

## 4.5 Oxidation of Metals — Al and Fe

[The experimental results presented in this section are contained in **Article VI**: “On Glow-Discharge Sputtering of Iron and Steels in a Commercial Deposition Plant”. P. Kringhøj, C. V. Budtz-Jørgensen, J. F. Nielsen, J. Böttiger, S. S. Eskildsen, and C. Mathiasen, to be published in *Surf. Coat. Tech.*, 2001]

Some metals are known to oxidize when they are subjected to an atmosphere containing oxygen. This, for instance, is the case for aluminium, on which an  $\text{Al}_2\text{O}_3$ -layer is easily formed on the surface, even at very low partial oxygen concentrations. A metal like Au, however, does not oxidize. In general, the surface binding energy,  $U_s$ , of metals and the corresponding metal-oxides do not differ very much, and depending on metal, both an increase and decrease of  $U_s$  can occur. In the case of Al oxidation has severe consequences for the surface properties. While Al has a surface binding energy of roughly 4 eV, the surface binding energy of  $\text{Al}_2\text{O}_3$  is about twice as high [48]. Hence, metal surface oxidation of Al will have some consequences on the physical sputtering yield; both because of the increase in surface binding energy, but also because only 2/5 of the sputtered atoms will actually be Al atoms. Thus, the sputtering rate of  $\text{Al}_2\text{O}_3$  will be considerably lower than the sputtering rate of Al. Just like aluminium, iron oxidizes in oxygen-containing atmospheres, forming a  $\text{Fe}_2\text{O}_3$  or  $\text{Fe}_3\text{O}_4$  layer on the surface with similar effects on the physical sputtering yield.

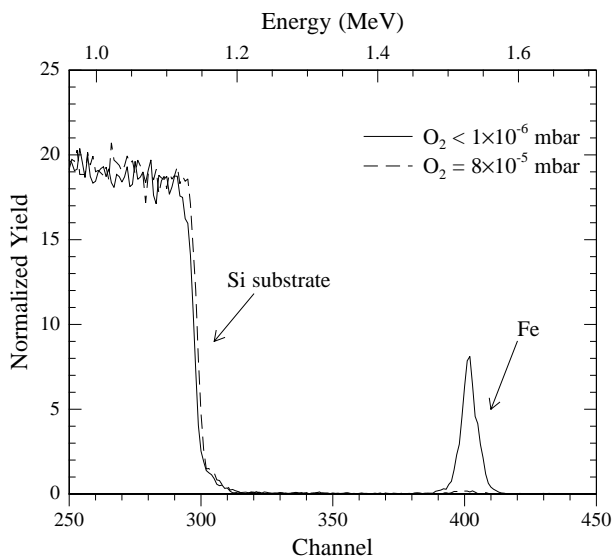
When sputtering metal surfaces such as aluminium or iron, the sputtering yield will thus depend on the partial oxygen pressure of the sputtering atmosphere. In 1973 Heller [59], who measured the sputtering rates of iron and cobalt targets in an oxygen-containing glow-discharge, proposed the following model: “Spontaneous oxide formation on the target surface and a sharp decrease of the sputtering can occur at a definite oxygen partial pressure  $p^*$  in the plasma. The pressure  $p^*$  is essentially a function of the oxidation rates of the target relative to the sputtering rate.” For low oxygen partial pressures, the sputtering rate corresponds to that of the clean metal, while for partial oxygen pressures  $p[\text{O}_2] > p^*$ , the sputtering rate corresponds to that of the oxide.

### Sputtering yield as a function of partial oxygen pressure

#### *The experiment*

To examine this effect, a number of sputtering experiments on Al and Fe foils were performed in an argon discharge (−600 V, 0.20–0.59 mbar) containing oxygen partial pressures ranging from below  $10^{-6}$  mbar to  $10^{-4}$  mbar. To achieve these low partial pressures, which are not obtainable in the plasma chamber to which the Hiden EQP is connected, these experiments were carried out in a turbo molecular pumped discharge chamber having a base pressure better than

**Figure 4.15** RBS spectra of the silicon catcher plates on which Fe was collected. The two cases are for a pure argon discharge (−600 V, 0.59 mbar) with an oxygen partial pressure of  $p[\text{O}_2] < 10^{-6}$  mbar (—) and  $p[\text{O}_2] = 8 \times 10^{-5}$  mbar (---).



$10^{-8}$  mbar. The argon gas used had a purity of 99.9999%. The experiments were performed as *catcher* experiments. The targets, which were functioning as the discharge cathode and thus exposed to Ar and Ar<sup>+</sup> bombardment, were Fe (99.98%) or Al (99.98%) foils. The catcher plate, functioning as the anode and placed at a distance of 34 mm from the cathode, was made of carbon (for Al) or silicon (for Fe). With this configuration, some of the material which was sputtered from the cathode during the experiment was collected on the catcher plates. The thickness of this layer was measured using Rutherford backscattering spectrometry (RBS) and normalized to the integrated current which was constantly monitored during the process. The value obtained in this way was taken as being proportional to the sputtering yield. Since these experiments were performed with a *pure* argon discharge, no chemical sputtering is expected to take place. Hence, in this case, we are considering purely *physical* sputtering, the yield of which is expected to be chemically decreased when the oxygen partial pressure exceeds some definite value,  $p^*$ .

### Results

Fig. 4.15 shows two examples of RBS spectra obtained in this way for Fe sputtering. In both cases the silicon substrate is clearly visible, while the RBS peak corresponding to Fe is only clearly visible for an oxygen partial pressure below  $10^{-6}$  mbar (—). At an oxygen partial pressure of  $p[\text{O}_2] = 8 \times 10^{-5}$  mbar the Fe peak is drastically diminished (---), indicating that the sputtering yield is significantly lower in this case. The reason for this is, as mentioned before, that

we in this case have  $p[\text{O}_2] > p^*$ , i.e., the oxidation rate of iron is larger than the sputtering rate.

For both the Fe and the Al foils, sputtering experiments were performed and RBS spectra like the ones in Fig. 4.15 taken, while only the oxygen partial pressure  $p[\text{O}_2]$  was varied. The sputtering yields obtained in this way are shown in Figs. 4.16 and 4.17 for iron and aluminium respectively, normalized to the highest sputtering yield which was achieved at the lowest oxygen partial pressure. The arrow in the figures marks the calculated ratio between the physical sputtering yield of the metal-oxide and the corresponding metal. These were calculated using sputtering yield values simulated with the *SRIM* computer code [60] for Fe and sputtering yield values taken from Chapman [12] for Al.

### Discussion

As the figures reveal, a *sharp* drop in sputtering yield does occur when the oxygen partial pressure exceeds a value of  $p^* \sim 4 \times 10^{-5}$  mbar for Fe and  $p^* \sim 10^{-5}$  mbar for Al. A drop of similar magnitude (close to a factor of 100 for Fe) was observed by Behrisch *et al.* [61] for *ion beam* sputtering of Fe by light particles (H, D, He). As the arrow indicates, the measured drop in sputtering yield for Fe is an order of magnitude lower than the calculated rate. This was also discussed by Behrisch *et al.* who, as we, suggest that these very low yields at high oxygen partial pressure arise from the fact that predominantly only atoms from the top surface layer are being removed. Because of the high oxygen partial pressure, both sputtered oxygen *and* iron atoms are quickly replaced by oxygen, thus leading to an increased oxygen atom concentration at the surface, which would lower the effective Fe sputtering yield even further. Assuming a target with only oxygen in the top surface layer, *SRIM* simulations indeed show a diminished sputtering yield in this case. The case for Al shows similar effects when oxygen is added to the sputtering atmosphere. The expected drop, indicated by the arrow, is based on sputtering yields given by Chapman [12]. In this case, the accordance between the expected and the measured drop is far better.

### Summary

The Au-sputtering experiments which were presented in Sect. 4.6 were performed in a plasma chamber which has a base pressure of  $\sim 10^{-3}$  mbar. For gold, which does not oxidize, this does not present a problem with respect to physical sputtering. As the experiments presented in this section reveal, however, the situation is quite different for aluminium. At the high base pressure of the plasma chamber to which the Hiden EQP is connected, Al-oxidation will certainly be taking place. Hence, sputtering experiments performed with Al samples will effectively be  $\text{Al}_2\text{O}_3$ -sputtering experiments. In a pure argon discharge, where only physical sputtering is occurring, we have seen that this phys-

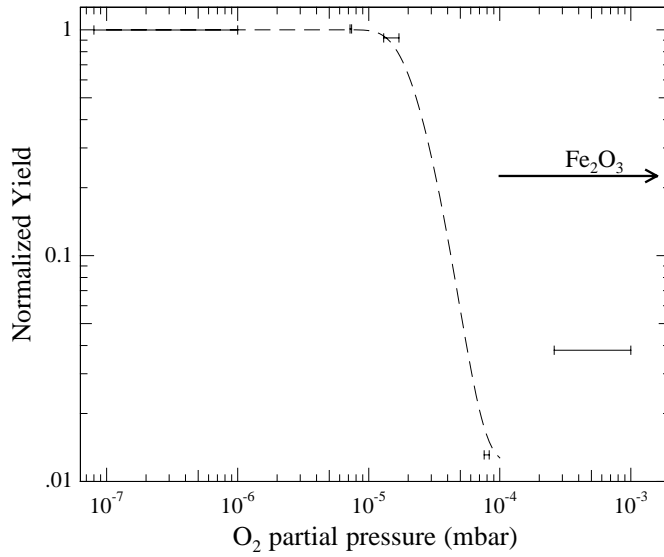


**Figure 4.16** Measured sputtering yield of iron in a pure argon discharge ( $-600$  V,  $0.59$  mbar) as a function of oxygen partial pressure.

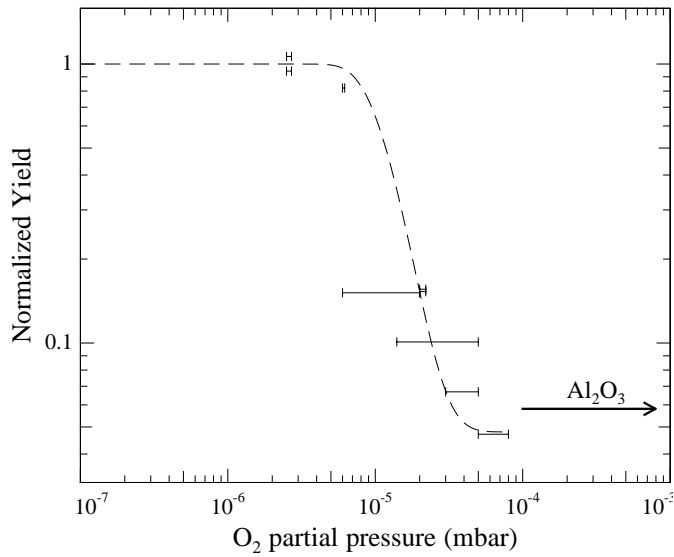


**Figure 4.17** Measured sputtering yield of aluminium in a pure argon discharge ( $-600$  V,  $0.20$  mbar) as a function of oxygen partial pressure.

ical sputtering is chemically reduced because of the presence of oxygen in the chamber, leading to a continuous re-formation of the sputtered  $\text{Al}_2\text{O}_3$ -layer and even a further reduction of the sputtering yield because of the high concentration of oxygen atoms at the surface. As we shall see in the next section, the addition of hydrogen to the discharge will effectively enhance the sputtering of these oxidized aluminium samples. Not just because of the increased average energy of the particles bombarding the cathode of such a discharge (as was discussed in Sect. 4.2), thus leading to higher physical sputtering efficiencies, but more so because of the chemical sputtering properties of the hydrogenic species themselves.

## 4.6 Alumina — Chemically Enhanced Sputtering

[Article III (full-text): “Chemical and Physical Sputtering of Aluminium and Gold Samples Using Ar-H<sub>2</sub> DC-Glow Discharges”. C. V. Budtz-Jørgensen, P. Kringhøj, J. F. Nielsen, and J. Böttiger, *Surf. Coat. Tech.*, **135**, 2000, p. 299]

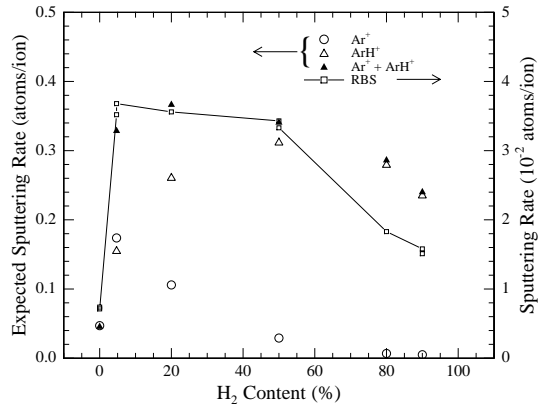
### Abstract

We present a series of sputtering experiments on aluminium samples performed with an Ar-H<sub>2</sub> DC-glow discharge at varying Ar-H<sub>2</sub> gas-composition, driven at a discharge voltage of  $-300$  V and a pressure of 0.2 mbar, in conjunction with measurements of the corresponding ion energy-distributions of the ions bombarding the discharge cathode ( $\text{Ar}^+$ ,  $\text{Ar}^{++}$ ,  $\text{ArH}^+$ ,  $\text{H}_2^+$  and  $\text{H}_2^+$ ). Similar measurements on gold samples, which have been published, have shown that the Au-sputtering efficiency of an Ar-H<sub>2</sub> glow discharge as a function of gas-composition could be adequately described by the corresponding change in the measured ion energy-distributions, under the assumption of a purely physical sputtering process. The experiments presented here show that this is not the case for aluminium (effectively  $\text{Al}_2\text{O}_3$ ). In this case, a measured optimal gas-composition of 80% H<sub>2</sub> was found for Al-sputtering, while the energy-distributions suggest an optimum at 20% (as for gold). This clearly suggests that hydrogen-enhanced chemical sputtering is taking place.

### Introduction

The Ar-H<sub>2</sub> DC-glow discharge is widely used in the industry as a surface cleaning process, preceding chemical or plasma-assisted surface processing and deposition techniques such as plasma-assisted chemical vapor deposition (PACVD) or as *in situ* cleaning of surfaces for microelectronics processing applications. The effect of hydrogen in this respect is, however, not clear. In most cases the Ar-H<sub>2</sub> plasma has been shown to increase the sputtering efficiency compared to pure argon plasma, as is the case for gold sputtering [62] as well as

**Figure 4.18** Measured effective sputtering rates on thin gold films ( $\square$ , right axis) and expected calculated sputtering yields ( $\circ$ ,  $\Delta$ ,  $\blacktriangle$ , left axis). Taken from Budtz-Jørgensen *et al.* [62].

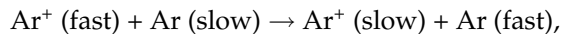


silicon and carbon sputtering [43]. However, a decrease in sputtering has been reported for stainless steel [45]. It should be noted that many of these sputtering experiments [43, 45] have been performed with power or current-controlled DC discharges. This complicates a clear physical interpretation because of the resulting variation of the discharge voltage with gas composition, which has a strong influence on the energy distributions of the impinging particles. Because of its small mass, hydrogen in itself will of course not be able to contribute significantly to physical sputtering. Hence, it is widely believed that the change in sputtering efficiency upon the addition of hydrogen to an argon discharge must be a chemical effect — i.e., chemical sputtering. The term “chemical sputtering” can, however, cover a range of different sputtering mechanisms [44], such as purely *thermal desorption* of molecules created on the surface between incident and target particles, and *chemically enhanced* or *chemically decreased physical sputtering* through implantation and subsequent change of the surface binding energy. Alternatively, in *physically enhanced chemical sputtering* a certain degree of high energy particle bombardment is necessary for thermal desorption to take place. Clearly, the wide range of sputtering mechanisms that exist between purely physical and purely chemical (i.e. thermal) sputtering complicates the interpretation of sputtering experiments, in the cases where chemical effects are observed.

### *Physical sputtering of gold*

Looking at the case of gold-sputtering, however, it has been shown [62] that the change in sputtering efficiency (here defined as the measured sputtering rate normalized to the discharge current) with varying hydrogen concentration in the discharge can be fully described by the measured ion energy-distributions

of the ions bombarding the gold surface, under the assumption of a purely *physical* sputtering process (i.e. by weighting the ion energy-distributions with the energy-dependent sputter-yield curve). This is shown in Fig. 4.18, where the filled triangles denote the calculated average sputtering rate based on the measured ion energy-distributions of  $\text{Ar}^+$  and  $\text{ArH}^+$  (left axis), and the connected squares denote the actual sputtering efficiency of the gold samples, as determined by Rutherford backscattering spectrometry (RBS) of the samples prior to and after sputtering (right axis). Clearly, the addition of hydrogen does in fact enhance the sputtering efficiency by a factor of over 30 compared to a pure argon discharge. However, this is not chemical sputtering but a result of the large amount of highly energetic  $\text{ArH}^+$ -ions, which are created upon the addition of hydrogen (open triangles). As these ions have no neutral counterpart, the symmetrical charge transfer (SCT) process, which is the dominant attenuator of fast  $\text{Ar}^+$  ions traversing the cathode sheath,



does not take place for the  $\text{ArH}^+$  ions. Hence, the cathode is bombarded by highly energetic  $\text{ArH}^+$  ions, effectively increasing the sputtering efficiency compared to the pure argon case. Moreover, as stated above, the agreement between the envelope of the measured sputtering efficiency curve and the calculated average sputtering rate curve clearly suggests that only physical sputtering is taking place. The discrepancy at 80% and 90%  $\text{H}_2$  content can be explained by the fact that hydrogenic ions were not considered in this case, resulting in an erroneous normalization of the expected sputtering rates at a high  $\text{H}_2$  content.

### *Sputtering of aluminium*

Of course, gold is known to be a chemically non-reactive material, so the purely physical nature of the sputtering process in this case is not surprising. In order to investigate a chemically more reactive material, the same set of experiments was performed using aluminium as the sputtered material.

A set of small aluminium samples were prepared and attached to the cathode of an experimental plasma chamber. The samples were sputtered with an  $\text{Ar-H}_2$  discharge with a discharge voltage of  $-300$  V and a gas pressure of 0.2 mbar at varying gas compositions. The sputtered thickness was determined by RBS measurements of the samples before and after sputtering. By normalizing to the integrated discharge current, the actual sputtering rate could be estimated. Ion energy-distributions of the ions hitting the aluminium cathode were measured using a commercial Hiden EQP (electrostatic quadrapole) energy analyser and mass spectrometer (Hiden Analytical Ltd., Warrington, UK). The most prevalent ion-species were found to be  $\text{Ar}^+$ ,  $\text{Ar}^{++}$ ,  $\text{ArH}^+$ ,  $\text{H}_2^+$  and  $\text{H}_3^+$ . The expected physical sputtering-rates were calculated by integrating these ion-distributions after they had been weighted with the sputtering-yield curves of Ar on aluminium (of

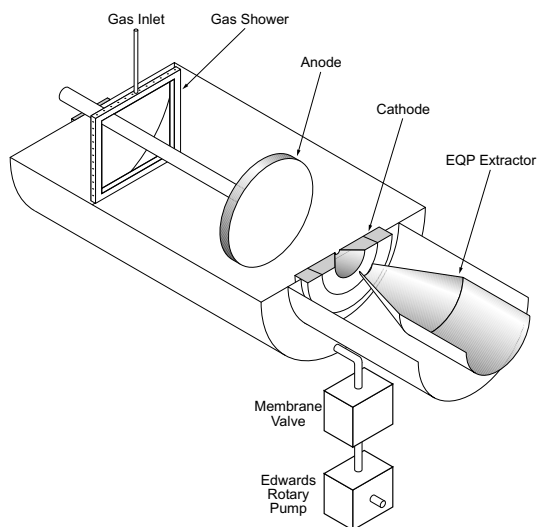


**Figure 4.19** The discharge chamber and the Hidden EQP (partly shown).

course,  $H_2^+$  and  $H_3^+$  do not contribute to the actual physical sputtering, but are merely used for normalization).

## Experimental

### *The plasma chamber and Hidden EQP*

Fig. 4.19 shows a schematic diagram of the experimental set-up, consisting of mainly two sections: the plasma chamber, where the DC glow-discharge is formed, and the Hidden EQP (partly shown) used for mass and energy analysis. Ions are extracted from the plasma chamber into the EQP through a  $100\ \mu\text{m}$  orifice.

The cylindrical stainless steel vacuum chamber, which contains the plasma, has a diameter and length of 30 cm each. The discharge was formed between the stainless steel cathode and movable grounded anode (both circular with a diameter of 12 cm), using a cathode-anode spacing of 5 cm. For these experiments, the inner part of the cathode, which holds the orifice and has a diameter of 6 cm (see Fig. 4.19), was coated with a  $\sim 5000\ \text{\AA}$  aluminium layer. The discharge voltage of  $-300\ \text{V}$  was supplied by a high-voltage power supply, which is part of a commercial Rübige (Wels, Austria) PACVD plant. The voltage was pulsed with on- and off-times of  $100\ \mu\text{s}$ , with rise and fall times of the order of  $1\ \mu\text{s}$ . The argon and hydrogen gas was supplied through a gas shower, the gas flow being externally controlled. The pressure was measured with a Tylan General cold-cathode pressure gauge and feedback-stabilized at a pre-set value via a computer-controlled membrane valve, which leads to a Edwards 80 two-stage

rotary pump (80 m<sup>3</sup>/h). An operating pressure of 0.20 mbar was used with a base pressure of 10<sup>-3</sup> mbar. The 100 μm orifice, through which the ions were extracted from the plasma chamber into the Hiden EQP, was situated at the center of the cathode (see Fig. 4.19). The pulsed-DC voltage was measured with a Hewlett-Packard digital oscilloscope through a 1:100 voltage divider, and the current was measured with a Tektronix current probe, allowing time-resolved measurement.

The Hiden EQP consists of a beam-optics section, a 45° sector field ion energy analyser and a quadrupole mass spectrometer. It is mounted within a differentially pumped system, keeping the pressure below 10<sup>-6</sup> mbar while having pressures in the plasma chamber in the mbar-range. Ions passing through the orifice are directed into the EQP by a pencil-shaped extractor head with a 700 μm circular opening (shown in Fig. 4.19). The ions were detected by a secondary-electron multiplier (SEM).

### *Sputtering experiments*

Aluminium samples were prepared by e-gun evaporating ~ 500 Å of Al onto ~ 1 cm<sup>2</sup> circular carbon samples, in a vacuum of 10<sup>-8</sup> mbar. The sputtering experiments themselves were performed using the “anode”-part as discharge cathode (i.e. grounding the cathode and applying the negative voltage to the anode of Fig. 4.19). The stainless steel “anode” was covered with a circular aluminium plate of equal dimension, so as to obtain an Al cathode. It was observed that the plasma was greatly enhanced when using aluminium compared to stainless steel, resulting in a more than 10-fold increase in discharge-current and plasma intensity under the same plasma conditions (voltage, pressure etc.). The samples were attached to the aluminium plate using a combination of bi-sticking tape (for good adhesion) and silver paste (for good electrical contact) and sputtered with a total ion-charge dose of  $Q \sim 13\,500$  mA·min on the total cathode area, corresponding to sputtering times between 3 and 40 hours (depending on the plasma current).

To determine the sputtered thickness, the Al layer on each sample was measured before and after sputtering by RBS using 2 MeV He ions (see Fig. 4.20). The area of the Al peak was in each case normalized to the C-substrate peak, and the change in area was used to calculate the actual sputtered thickness. Normalizing these values to the measured total ion dose  $Q$  (the time-integrated discharge current) in each case, gives the actual current-normalized sputtering rate. Also seen on Fig. 4.20 are peaks corresponding to a thin oxygen layer present between the carbon and aluminium layers and on the aluminium surface. The latter can be seen to have increased after plasma treatment. This surface layer is in fact due to Al<sub>2</sub>O<sub>3</sub>, which will naturally build up on the Al samples. This is also the case at 10<sup>-4</sup> mbar, which is the residue oxygen pressure of the plasma chamber. Therefore, it is actually the much more tightly bound Al<sub>2</sub>O<sub>3</sub> that is sputtered and not Al.

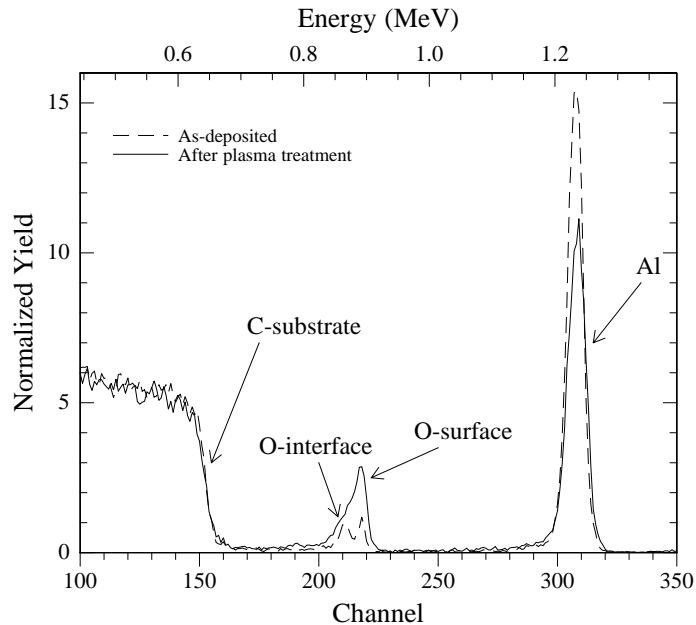


**Figure 4.20** Typical RBS spectrum of a 500 Å aluminium film on a carbon sample, before (dashed line) and after (full line) sputtering. The oxygen contributions stem from both the Al-C interface and from the Al surface, as an Al<sub>2</sub>O<sub>3</sub> layer will naturally build up.

### Energy measurements

As mentioned earlier, the DC discharges used in these experiments were pulsed, as the Rübige power supply did not allow clean DC-voltage profiles. During the ion-distribution measurements presented here, the off-time of the profile was 100 μs, while the on-time was 900 μs (100 μs for the sputtering experiments), and the EQP was set to sample in a time window well within the on-pulse. This results in cleaner and more presentable ion energy-distributions than can be achieved with non-windowed EQP measurements of a discharge with on- and off-times of 100 μs, as were used in the sputtering experiments. The qualitative conclusions are however not affected by this.

## Results

The results presented here consist of two separate experiments. First, measurements of the energy distributions of ions hitting the Al cathode of an Ar-H<sub>2</sub>

discharge at varying hydrogen content, which are used to determine the expected average physical sputtering rate of the bombarding ions. Secondly, a set of sputtering experiments of Al samples used to estimate the actual sputtering rate. Although these two experiments were performed in the same chamber and with the same plasma parameters, they were done at different times. All measurements were performed at a gas pressure of 0.20 mbar and a discharge voltage of  $-300$  V.

### *Energy spectra*

Figs. 4.7 and 4.8 (p. 88–89) show the measured ion energy-distributions of the most prevalent ions hitting the cathode in an Ar-H<sub>2</sub> discharge with a hydrogen content of 0%, 50% and 100% (Ar<sup>+</sup>, Ar<sup>++</sup>, ArH<sup>+</sup>, H<sub>2</sub><sup>+</sup> and H<sub>3</sub><sup>+</sup>). Ion energy-distributions were also measured for 20%, 33%, 66% and 80% H<sub>2</sub> content (not shown). Note that the Ar<sup>++</sup> energies have been divided by two in order to display the spectra on the figure ( $q = 2$ ). As mentioned before, Al-cathode discharges have high ion current-densities compared to, e.g. stainless steel cathodes. As high current-densities result in thin cathode-sheaths (Child's law) and hence few collisions, the overall ion-energies for all species are relatively high, and a high degree of non-colliding ions are seen (the end-point-peaks in the distributions). At 0% H<sub>2</sub> the distributions are naturally dominated by pure argon ions (Fig. 4.7a), with relatively low mean ion energies, as a consequence of the SCT process between Ar<sup>+</sup> and Ar. Ar<sup>++</sup> does not undergo SCT and hence has higher mean energies. Addition of hydrogen to the discharge greatly increases the discharge current-density (see Fig. 4.5), whereby the cathode sheath decreases, resulting in an overall increase of the mean ion energies for all species [63]. Moreover, a significant amount of high-energy ArH<sup>+</sup> ions are created (Fig. 4.7b). Also, the Ar<sup>++</sup> contribution is seen to increase drastically. The energy distributions of hydrogen-related ions can be seen in Fig. 4.8a to consist of H<sub>2</sub><sup>+</sup> and a large amount of non-colliding H<sub>3</sub><sup>+</sup>. As for argon, the SCT process is expected to be an attenuating factor for H<sub>2</sub><sup>+</sup> because of the large abundance of neutral H<sub>2</sub>. Finally, Fig. 4.8b shows the pure hydrogen case; consisting of only H<sub>2</sub><sup>+</sup> and H<sub>3</sub><sup>+</sup>, being low in both intensity and mean energy.

### *The plasma current and normalization*

Computer simulations<sup>5</sup> of a pure argon plasma, taking into account both the SCT process and elastic scattering, have shown that low energy (0–20 eV) ions have a relatively wide angular spread, of up to several tens of degrees. This

<sup>5</sup>Particle-in-cell (PIC) and Monte-Carlo computer simulations of an argon glow discharge performed with the *xpdp1* plasma simulation software developed by the Plasma Theory Group at Berkeley University.

of course poses a problem for the Hidden EQP, which has a much smaller angular acceptance, in providing the correct ion intensities at low energies, resulting in an artificial cut-off of ion energy-distributions around 0 eV. Although these ions do not contribute to sputtering, this could result in normalization problems when comparing the area-normalized calculated sputtering rate derived from the ion energy-distributions with the current-normalized measured sputtering rates of the Al samples. Fig. 4.5 (p. 82), however, shows the total area (filled squares) of the ion energy-distributions weighted with the charge number  $q$  of each individual ion (i.e. 2 for Ar<sup>++</sup> and 1 for the rest) together with the measured discharge current (connected open squares) as a function of H<sub>2</sub> content. Clearly, the areas of the ion energy-distributions excellently reflect the actual ion currents (disregarding a small contribution due to secondary electrons) and, therefore, the total ion-dose hitting the samples. This justifies comparing the calculated sputtering rates to the measured sputtering rates *as a function of H<sub>2</sub> content*.

#### *Sputtering rates derived from the energy spectra*

On the basis of the ion energy-distributions for Ar<sup>+</sup>, ArH<sup>+</sup> and Ar<sup>++</sup>, we calculated the expected average sputtering rate by weighting the distributions with the sputtering-yield curve for Ar on Al<sub>2</sub>O<sub>3</sub>.<sup>6</sup> The Al yield when sputtering Al<sub>2</sub>O<sub>3</sub> with Ar was estimated using the SRIM<sup>7</sup> software [60], utilizing a surface binding energy of 10 eV for Al<sub>2</sub>O<sub>3</sub> [48] for both Al and O. This was done for a number of Ar energies between 75 eV (yield = 0.0017) and 650 eV (yield = 0.098), and the results were approximated with a polynomial. The sputtering yield for energies below 75 eV was set to zero. The sputtering yield curve is, as for Ar on Au, essentially given by a slightly sub-linear form. With this curve, the expected average sputtering rates were then calculated using the formula:

$$\text{Average Sputtering Rate [atoms/ion]} = \frac{\int Y(E) \times g_{E,\text{sput}}(E) dE}{\int g_{E,\text{total}}(E) dE} \quad (4.11)$$

where  $Y(E)$  denotes the sputtering-yield curve,  $g_{E,\text{sput}}(E)$  the summed energy distributions of the sputtering ions (Ar<sup>+</sup>, ArH<sup>+</sup> and Ar<sup>++</sup>) and  $g_{E,\text{total}}(E)$  the summed energy distributions of all species (Ar<sup>+</sup>, ArH<sup>+</sup>, Ar<sup>++</sup>, H<sub>2</sub><sup>+</sup> and H<sub>3</sub><sup>+</sup>). Hence, Eq. (4.11) gives the sputtering rate per bombarding ion of the discharge (and not per sputtering ion). The rates calculated in this way are shown in Fig. 4.21 (open squares, left axis). Also shown in the figure (dashed lines, left

<sup>6</sup>Disregarding the extra proton in the case of the ArH<sup>+</sup> molecule. Upon hitting the surface, the ionic molecule is most likely split into its two components, the hydrogen atom receiving only 1/40 of the total energy.

<sup>7</sup>Formerly known as TRIM.

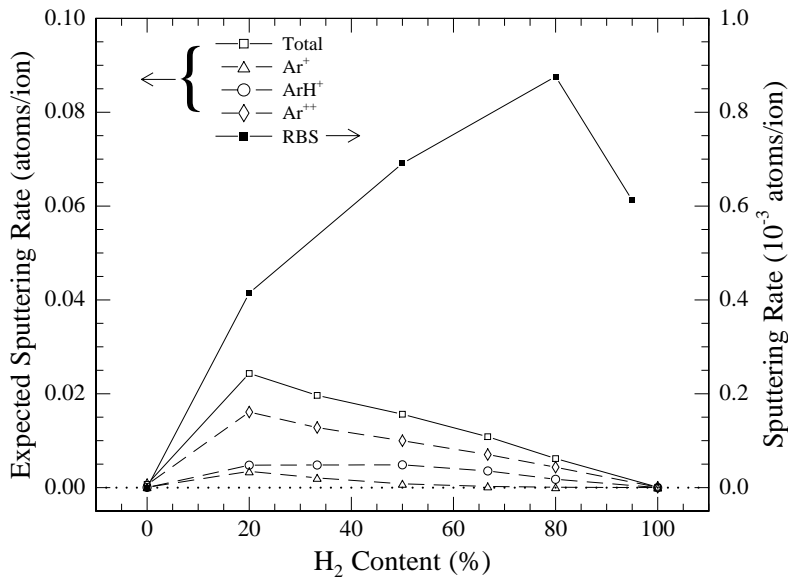


**Figure 4.21** Effective sputtering rate based on RBS measurements of sputtered Al samples (filled squares, right axis) and expected average physical sputtering rate calculated from the ion energy-distributions (open squares, left axis). The contribution to the expected rate of each of the sputtering species is also shown (open symbols, dashed line).

axis) are the contributions of each of the sputtering ions. A distinct optimum for the expected physical sputtering can be seen at 20% H<sub>2</sub>.

### Sputtering experiments

Also shown on Fig. 4.21 are the measured sputtering rates (filled squares, right axis) determined from the sputtering experiments of the Al samples. For each gas composition (0%, 20%, 50%, 80% and 95% H<sub>2</sub>), two samples were sputtered, and the mean was taken. Error bars corresponding to 5-10% must be expected due to statistical errors, but for clarity these are not shown. The actual observed optimum for sputtering of the Al samples can be found at around 80% H<sub>2</sub>.

### Discussion

Comparing Fig. 4.21 with Fig. 4.18, one clearly sees the difference of the effect of hydrogen in the Al and Au cases. Whereas physical sputtering, described by

the calculated sputtering rates, adequately predicts the hydrogen dependence of the sputtering rates for the gold case, it cannot be used to explain the sputtering of the aluminium samples. In the latter case, the optimal gas composition for sputtering has much higher hydrogen content than the estimated sputtering rate curve proposes. This clearly suggests that chemical sputtering is dominating the sputter mechanism for aluminium.

Although the hydrogenic species in themselves are seen to be very important to sputtering, the 95% H<sub>2</sub> plasma has a lower sputtering rate than discharges with 50% and 80% H<sub>2</sub>. This poses the question of how hydrogen in fact enhances the sputtering process. If sputtering was mainly due to purely hydrogenic species, via some chemical reaction with surface atoms and subsequent thermal desorption, one would expect the 95% H<sub>2</sub> case to be the most effective. This indicates that synergy effects between the high-energy ion bombardment (i.e. physical sputtering) and chemical reactions with the hydrogenic species are taking place. The main effect of hydrogen could be to lower the effective surface binding energy of Al<sub>2</sub>O<sub>3</sub> through their presence in the near surface region. SRIM calculations show that halving the surface binding energy of Al<sub>2</sub>O<sub>3</sub> will more than double the physical sputtering rate of the argon species. This, however, does not comply all that well with the relatively high sputtering rate at 95% H<sub>2</sub>, as the physical sputtering rate for the argon species is very low in this case. Also, the presence of ArH<sup>+</sup> might be of importance. As this ionic molecule is expected to break up into its components upon impact, it combines locally the properties of the energetic Ar particles and the chemically reactive hydrogenic particles.

The typical measured sputtering rates of Fig. 4.21 can be seen to be a factor of 100 lower than the calculated sputtering rates (note the different scales on the left and right axes of the graph). However, much care should be taken when trying to make an absolute comparison between the two curves. We believe that the sputtering process, irrespective of its physical or/and chemical nature, is controlled by an equilibrium between the sputtering of Al and O atoms from the Al<sub>2</sub>O<sub>3</sub> surface and the constant rebuild of the Al<sub>2</sub>O<sub>3</sub> layer that will be taking place at the residual oxygen pressure of 10<sup>-4</sup>–10<sup>-3</sup> mbar of our experiments. The net effect of this process is the removal of Al from “underneath” the Al<sub>2</sub>O<sub>3</sub> layer, as is also clearly seen from the RBS spectrum in Fig. 4.20. Intermingling with this process, however, is back diffusion and possible re-implantation of sputtered atoms, which has been estimated to be as large as 90% at the pressures used here [58]. This will clearly diminish the effective sputtering rate, in good agreement with what is observed in Fig. 4.21. On the other hand, high-energy neutral atoms, which are not considered here, will also be playing an important role, at least as regards physical sputtering, as their fraction might be significantly higher than that of the ions [40], thereby increasing the effective sputtering rate. Although the energy-distribution of these high-energy neutrals

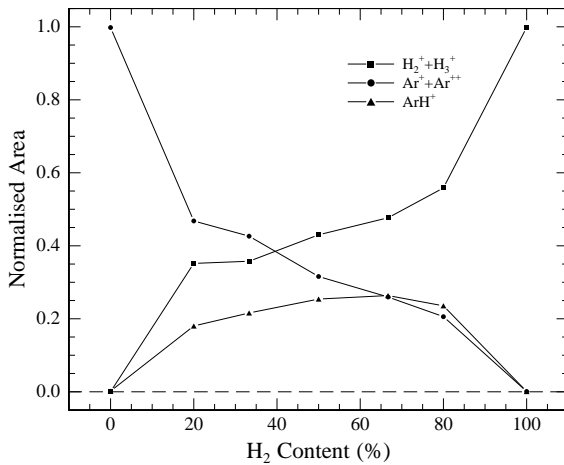


**Figure 4.22** Ion-distribution areas normalized to the total area for the hydrogenic ions (—■—), the argon ions (—●—) and for the ArH<sup>+</sup> ion (—▲—).

are expected to reflect that of the ions, and hence will not change the envelope of the expected sputtering-rate curve in Fig. 4.21, they will cause the measured current-normalized sputtering rate to be overestimated. Hence, with quantitatively important effects pushing the measured sputtering rate in either way, an absolute comparison between the expected sputtering rates and the measured sputtering rates is not possible.

As was also the case for gold sputtering, it should be noted that the addition of hydrogen to an argon glow discharge, keeping both the discharge pressure and voltage constant, drastically increases the physical sputtering of the cathode. Obviously, because of their small mass, the hydrogen ions do not sputter. The increase in physical sputtering is primarily due to the creation of energetic ArH<sup>+</sup> ions (see Fig. 4.22), which do not undergo SCT and hence have high mean energies. Secondly, the increased plasma current-density results in a narrower cathode sheath, which will further increase the mean energies as a result of the fewer collisions they undergo. Notably, in the case of an Al cathode, also the Ar<sup>++</sup> ions are seen to be dominant physical sputter ions, due to their very high energies. This was not observed for the Au case. We expect this increase of particle momentum upon the addition of hydrogen to an argon glow discharge to be qualitatively independent of cathode material. Hence, any observed decrease in sputtering efficiency must be explained by chemical effects.

## Conclusions

Sputtering experiments on Al (Al<sub>2</sub>O<sub>3</sub>) samples have shown that the addition of hydrogen to an argon glow-discharge effectively increases the sputtering rate.

Furthermore, energy measurements of the sputtering ions were used to calculate the expected physical sputtering rates at varying hydrogen content, equally showing an increase upon the addition of hydrogen. However, as opposed to the case of gold sputtering, the calculated physical sputtering rates do not adequately describe the dependence on hydrogen content. Hence, Al sputtering cannot be described by a purely physical or knock-on sputtering process. This clearly shows that some kind of chemically enhanced sputtering process must be taking place.

## 4.7 Sputtering Experiments — Summary

The treatment of the sputtering experiments presented in this chapter is based upon performing a comparison between

1. the actual measured sputtering efficiencies (chemical and/or physical), as determined using Rutherford backscattering spectrometry on the sputtered samples, and
2. the expected physical sputtering efficiencies, calculated on the basis of measured ion energy-distributions.

This was done for gold (Sect. 4.4) and aluminium (Sect. 4.6) samples. For the gold samples, the dependence of the measured sputtering efficiency on the H<sub>2</sub> content of the discharge was shown to be adequately described by the purely physical sputtering process which is considered when calculating the physical sputtering efficiency  $S_{\text{phy}}$ . Although the ions, which are the only species considered in evaluating  $S_{\text{phy}}$ , might well only constitute a fraction of the sputtering species (cf. the importance of neutrals), this does not undermine the agreements achieved, since the fast neutral atom energy-distribution is expected to reflect that of the ions — ions are the only source of fast neutrals in the discharge. This assumption also holds when varying the H<sub>2</sub> content of the discharge. Hence, it may be concluded that gold sputtering by Ar-H<sub>2</sub> glow-discharges is governed by a purely physical sputtering process.

This was clearly not the case for the aluminium – or more precisely – Al<sub>2</sub>O<sub>3</sub> samples. As was discussed in Sect. 4.5, with the relatively high base pressure of the plasma chamber to which the Hiden EQP is connected (and in which the sputtering experiments were performed), an oxide layer in the form of Al<sub>2</sub>O<sub>3</sub> builds up on the Al surface, effectively decreasing the physical sputtering yield of the Al samples (for example, by comparing Figs. 4.14 and 4.21, the sputtering efficiency of the gold samples can be seen to a factor of 100 higher than that for the aluminium samples, clearly indicating how resistant Al<sub>2</sub>O<sub>3</sub> is towards sputtering). The generation of the Al<sub>2</sub>O<sub>3</sub> layer, and its effect on the physical sputtering efficiency, was verified by sputtering experiments performed with a

pure argon discharge, which does not contain any chemically reactive species, at varying partial oxygen pressure.

The importance of chemical or chemically enhanced sputtering of the Al samples at high oxygen base pressures was clearly observed when hydrogen was added to the argon discharge. In all respects, a hydrogen content of 5-20% seems to maximize the properties of the Ar-H<sub>2</sub> discharge in terms of current, intensity (i.e., light emission), sputtering efficiency and so on. It is the most physically “aggressive” composition. The optimal H<sub>2</sub> content for the sputtering efficiency of the Al samples, however, was 80% — far above the maximum of the expected physical sputtering efficiency,  $S_{\text{phy}}$ , which occurs at a H<sub>2</sub> content of 20%. Hence, one can conclude that in the case of Al sputtering with an Ar-H<sub>2</sub> discharge, the sputtering mechanisms are dominated by chemical processes. What kind of chemical processes which are taking place at the surface are, however, difficult to assess. This is partly due to the fact that these processes must be expected to be (at least to some extent) thermally activated, a parameter the importance of which is not investigated in this work. Nevertheless, some points could be made on the basis of the H<sub>2</sub>-content dependence of the measured sputtering efficiency. First of all, since it exhibits a maximum, it may be inferred that both physical sputtering (i.e., high-energy particle bombardment) and chemical sputtering is of importance. As was discussed in the article, hydrogen atom implantation in the Al<sub>2</sub>O<sub>3</sub> surface could lower the effective surface binding energy, thus giving rise to an increase in physical sputtering (i.e., chemically enhanced physical sputtering). Furthermore, as was mentioned in Sect. 4.5, the decrease in the Al:O atom ratio at the surface could be expected to severely diminish the Al atom sputtering yield. This effect could be reduced by the presence of reactive hydrogenic species at the surface, which would be effective in removing oxygen (i.e., chemical sputtering of O), thus re-increasing the Al:O ratio and hence the Al physical sputtering yield. The physical sputtering of Al (and O), and the crucial chemical sputtering of O would thus give rise to an optimal sputtering efficiency for some composition.



# 5

---

## ENERGETIC ION BOMBARDMENT OF THE ANODE

*an effect of discharge pulsing*

---

[**Article IV** (full-text): “Energetic Ion Bombardment of the Grounded Anode in Pulsed DC-Glow Discharges”. C. V. Budtz-Jørgensen, J. Bøttiger, and P. Kringhøj, *Surf. Coat. Tech.*, **137**, 2001, p. 104]

*Most glow-discharges which are used for practical surface coating or processing applications are pulsed — typically using pulse times of some hundred microseconds. The only reason for doing this is, that this gives one the opportunity to control the power of the discharge without changing its basic parameters, such as pressure and voltage. Some investigations, consisting of both energy-distribution measurements and plasma simulations, were performed to see what effect this pulsing has on the anode. These showed that, upon collapse of the discharge during the onset of the off-pulse, the anode is bombarded with energetic ions of up to several hundred eV. Furthermore, the importance of anode material sputtering because of these ions was assessed. These findings were recently reported in **Article IV**, the contents of which is presented in its full-text form in this chapter.*

### **Abstract**

We present measurements of ion energy-distributions of the ions impinging on the grounded anode of a pulsed argon DC-glow discharge (cathode voltages of  $-300$  to

–450 V, and a gas pressure of 0.5 mbar) with on- and off-pulse times of 100–900  $\mu\text{s}$ . During the on pulses of the discharge, as expected, low energy ions ( $< 10$  eV) were observed, originating from the potential difference between the plasma (i.e., the plasma potential) and the grounded anode. However, during the initial tens of microseconds of the off pulse, ions were detected with energies of the order of the cathode potential (i.e., several hundred eV). Furthermore, voltage measurements of a floating anode show that the plasma potential has a high positive voltage peak during the onset of the off pulse. The explanation of the observed phenomena must be sought in the sudden change in the boundary conditions of the discharge and the subsequent redistribution of charged particles, leading ultimately to the collapse of the discharge. This has been confirmed by Monte-Carlo simulations of the discharge.

## 5.1 Introduction

In many industrial plasma-processing techniques using DC-glow discharges, the DC voltage is pulsed in order to control the substrate heating while simultaneously allowing a fixed high DC voltage. We have examined what effect this pulsing of the discharge has on the grounded anode and the ions that bombard it. A pulsed-DC argon discharge was formed in a small cylindrical stainless steel discharge chamber, with an anode-cathode spacing of 5 cm. Discharge voltages from –300 to –450 V were used with on- and off-pulse times of 100–900  $\mu\text{s}$ . An argon gas pressure of 0.5 mbar was used. Using a time-resolved, high sensitivity Hiden EQP (electrostatic quadrupole) energy analyser and mass spectrometer (Hiden Analytical Ltd., Warrington, UK), the ions hitting the anode were detected throughout the voltage cycle. During the on pulse, low energy ions ( $< 10$  eV) were detected, originating from the potential drop between the plasma (i.e., the plasma potential) and the grounded anode. During the first tens of microseconds of the off pulse, however, ions with energies of the order of the cathode potential were observed to bombard the anode. Measurements of the energy distributions of these high-energy anode ions and their dependence on basic plasma parameters will be presented. These ions are ascribed to the collapse of the plasma which occurs when the cathode is suddenly grounded, resulting in a spatially inhomogeneous increase of the plasma potential, which is dictated by the sudden change in the boundary conditions of the discharge. This explanation is supported by floating anode measurements, showing that the plasma potential does in fact attain high positive values at the onset of the off pulse. Furthermore some results of Monte-Carlo simulations of the discharge will be shown, which can be used to explain the basic physics of the process. Finally, the effect of anode material sputtering due to this process, and its relative importance for practical process contamination will be discussed.

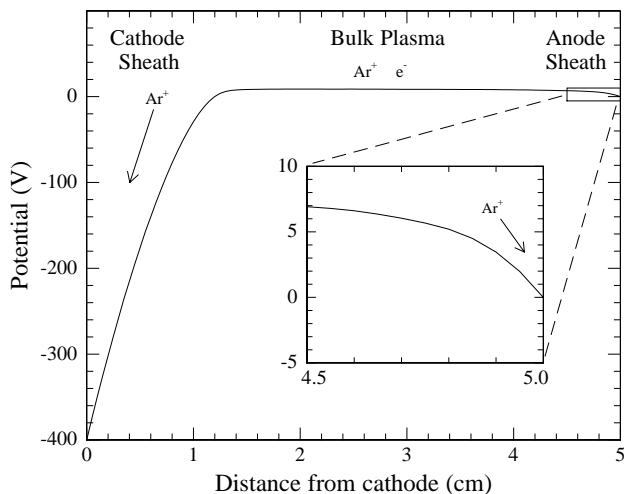


**Figure 5.1** The plasma potential of a DC-glow discharge. The main characteristics are the positively charged cathode sheath (left-hand side), the quasi-neutral bulk plasma and the anode sheath (right-hand side and subplot).

## 5.2 The DC Discharge

Here, a brief outline of the DC-glow discharge will be given. Fig. 5.1 shows a typical distribution of the potential of a DC-glow discharge. The curve stems from a Monte-Carlo simulation (see Sect. 5.5 for more information) of a DC argon discharge with a cathode voltage of  $-400$  V, a gas pressure of 0.5 mbar and a cathode-anode spacing of 5 cm (the cathode is on the left-hand side and the anode on the right-hand side). The well-known major characteristics of the glow-discharge are clearly seen. The full discharge voltage is carried over a  $\sim 1$  cm region adjacent to the cathode, called the *cathode sheath*. This region is depleted of free electrons and it is here that the positive ions entering from the *bulk plasma* region are accelerated towards the cathode, bombarding it with high energies. The quasi-neutral bulk plasma region has a slightly elevated potential of 5–10 eV. This is clearly seen in the subplot of Fig. 5.1, showing the *anode sheath* region. As on the cathode side, positive ions entering the anode sheath region are accelerated towards the anode, thereby gaining a kinetic energy of some eV. It should be noted that because of collisions with the neutral background gas (in this case dominated by symmetrical charge transfer with neutral argon atoms), the argon ions impinging on the cathode or anode do not have an energy corresponding

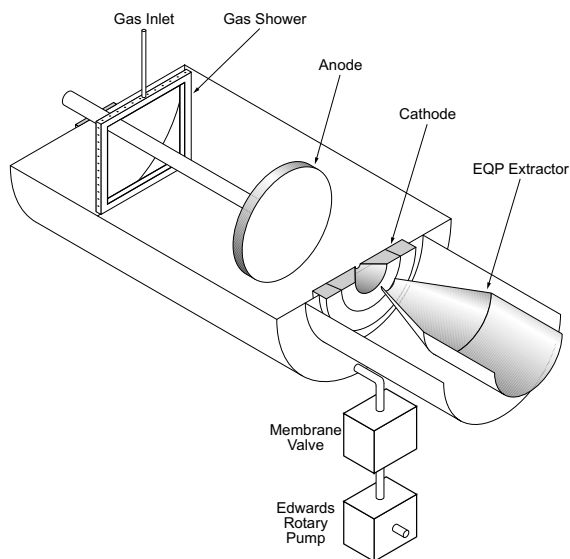


**Figure 5.2** Schematic diagram of the plasma chamber and Hiden EQP (partly shown).

to the full potential drop, but end up with some energy-distribution [15, 63].

The topic of this paper is an investigation of the effect on the equilibrium state shown in Fig. 5.1, when the cathode voltage is suddenly changed from  $-400$  V to ground (0 V).

### 5.3 Experimental

Fig. 5.2 shows a schematic diagram of the experimental set-up, consisting of mainly two sections: the plasma chamber, where the pulsed DC glow-discharge is formed, and the Hiden EQP (partly shown) used for mass and energy analysis. Ions are extracted from the plasma chamber into the EQP through a  $100\ \mu\text{m}$  orifice.

The cylindrical stainless steel vacuum chamber, which holds the plasma, has a diameter and length of 30 cm each. The discharge was formed between the stainless steel movable cathode and grounded anode (both circular with a diameter of 12 cm), using a cathode-anode spacing of 5 cm. The discharge voltage was supplied by a Rübzig high-voltage power supply, which is part of a commercial Rübzig PACVD plant (Wels, Austria). The voltage was pulsed with on- and off-times of 100-900  $\mu\text{s}$ , with rise and fall times of the order of 1  $\mu\text{s}$ . The discharge gas was supplied through a gas shower, the gas flow being externally controlled. The pressure was measured with a Tylan General cold-cathode pressure gauge and feedback-stabilized at a pre-set value via a computer-controlled

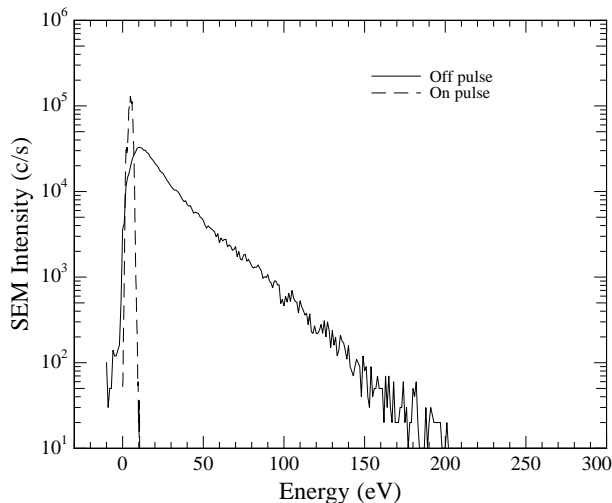


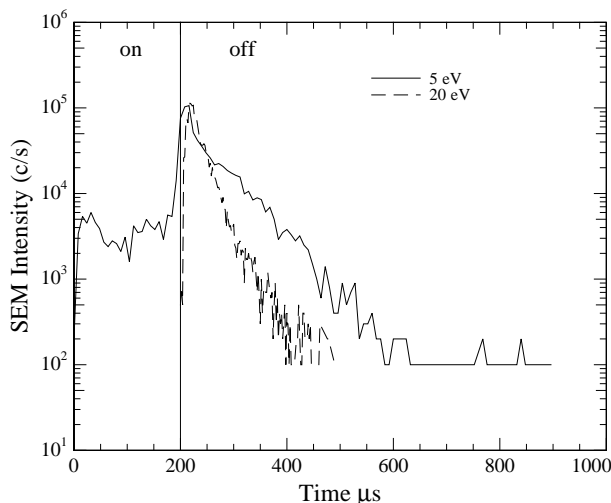
**Figure 5.3** Measured energy-distribution of the  $\text{Ar}^+$  ions hitting the grounded anode during the off-pulse (—) and on-pulse (---) of the voltage cycle.

membrane valve, which leads to a Edwards 80 two-stage rotary pump ( $80 \text{ m}^3/\text{h}$ ). An operating pressure of 0.50 mbar was used with a base pressure of  $10^{-4}$ – $10^{-3}$  mbar. The  $100 \mu\text{m}$  orifice, through which the ions were extracted from the plasma chamber into the Hidden EQP, was situated at the center of the anode (see Fig. 5.2). The pulsed-DC voltage was measured with a Hewlett-Packard digital oscilloscope through a 1:100 voltage divider, and the current was measured with a Tektronix current probe, allowing time-resolved measurement. During the floating anode measurements, the anode potential was measured with the oscilloscope using a 1:10 voltage probe.

The Hidden EQP consists of a beam-optics section, a  $45^\circ$  electrostatic sector field ion energy analyser and a quadrupole mass spectrometer. It is mounted within a differentially pumped system, keeping the pressure below  $10^{-6}$  mbar while having pressures in the plasma chamber in the mbar-range. Ions passing through the orifice are directed into the EQP by a pencil-shaped extractor head with a  $700 \mu\text{m}$  circular opening (shown in Fig. 5.2). The ions were detected by a secondary-electron multiplier (SEM), which could be triggered and windowed relative to the measured discharge voltage, thus allowing time-resolved measurement of the ion-energies.

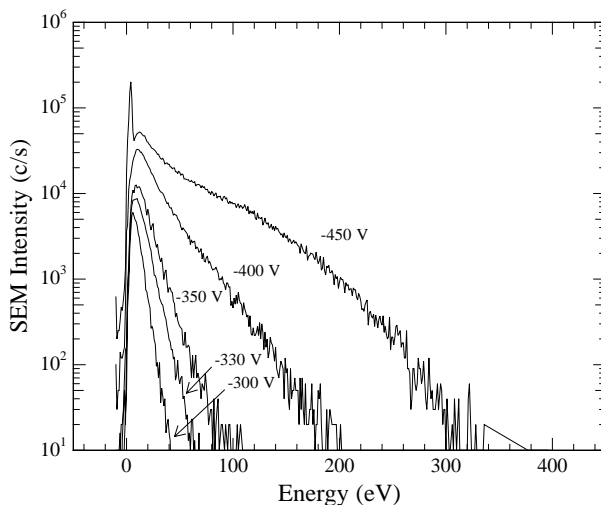
## 5.4 Experimental Results

Fig. 5.3 shows the measured ion energy-distribution of  $\text{Ar}^+$  ions hitting the anode during the  $200 \mu\text{s}$  on pulse (dashed line) and  $200 \mu\text{s}$  off pulse (solid line),



**Figure 5.4** Time-scan of the 5 eV (—) and 20 eV (---) ions hitting the discharge anode of a pulsed-DC argon discharge with an on pulse of 200  $\mu\text{s}$  and an off pulse of 900  $\mu\text{s}$ .

for an argon discharge with a cathode on-pulse voltage of  $-400$  V. The spectra represent the ions sampled during the full extent of the on- and off-pulse, respectively. During the on pulse, the observed ions have an energy no higher than  $\sim 10$  eV, in good agreement with typical plasma potentials (see Fig. 5.1). During the off pulse, however, ions with energies up to 200 eV are observed. The existence of high-energy ions (i.e., higher than the on pulse plasma potential) during the off pulse is also clear from Fig. 5.4, which shows the temporal evolution of the 5 eV ions (solid line) and the 20 eV ions (dashed line) (i.e.,  $\text{Ar}^+$  ions with energies below and above the plasma potential, respectively). These time-scans were taken by measuring the intensity of the 5 and 20 eV  $\text{Ar}^+$  ions while scanning the trigger-time of the Hiden EQP with respect to the discharge-voltage profile and utilizing a detection time-window of 2  $\mu\text{s}$ . To observe the full extent of the evolution of the off pulse ions, an off pulse of 900  $\mu\text{s}$  was used. Again, one sees the existence of low energy ions both throughout the on-pulse and the off-pulse. At the onset of the off pulse, a sharp increase in the 5 eV ion signal is observed, followed by a more or less exponential decay lasting 400  $\mu\text{s}$  into the off pulse. Moreover, 20 eV ions are observed during the first 200  $\mu\text{s}$  of the off pulse. This temporal behaviour of the anode ions suggests that the existence of high-energy ions and the increased intensity of low-energy ions at the anode are closely connected with the collapse of the plasma.



**Figure 5.5** Measured energy distributions of the ions hitting the anode during the off pulse of the discharge voltage, measured at different cathode voltages (shown in figure).

Fig. 5.5 shows the measured energy spectra of the anode ions in the off pulse at a number of different cathode voltages between  $-300$  V and  $-450$  V. As can be seen from the figure, an increase of the cathode voltage results in an increase of the maximum energy achieved by anode ions, ranging from  $50$  eV to  $300$  eV for cathode voltages varying from  $-300$  V to  $-450$  V, respectively. As the anode was always at ground potential during these measurements, these energetic positively charged ions must originate from a region of high positive potential within the discharge, which is created at the onset of the off pulse (i.e., grounding of the cathode). As is evident from Fig. 5.5, the value of this positive potential is directly connected with the (negative) value of the on-pulse voltage of the cathode. In order to confirm the existence of this positive potential, we performed a series of experiments using a floating anode. This was done by connecting the anode to a digital oscilloscope. The high input resistivity of the oscilloscope effectively keeps the anode at floating potential. In this way, the temporal evolution of the floating potential of the anode, and hence the plasma potential near the anode, could be measured. It should be noted, however, that these measurements are only indicative of what goes on in the case of a grounded anode, as the boundary conditions of course differ in the two cases. The results are shown in Fig. 5.6 for the cases of a cathode voltage of  $-300$  V (dashed line) and  $-400$  V (solid line). During the on pulse, the floating

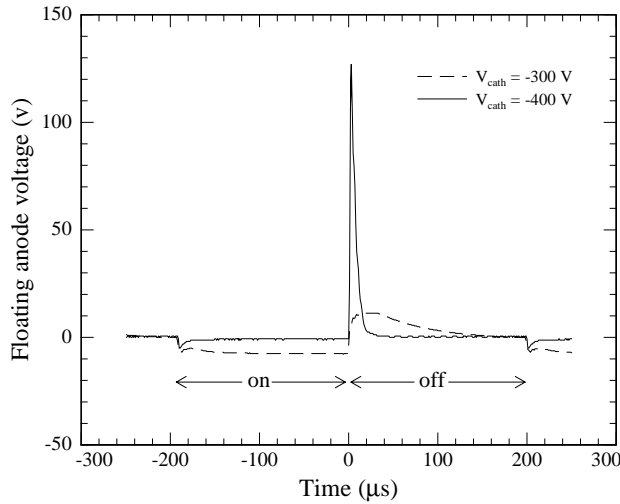


**Figure 5.6** Temporal evolution of the floating anode voltage during one voltage cycle, measured with a digital oscilloscope, using a cathode on-pulse voltage,  $V_{\text{cath}}$ , of  $-300$  V (---) and  $-400$  V (—). The on- and off- times of the discharge voltage profile was  $200 \mu\text{s}$ .

anode potential is slightly negative, in accordance with what is known to be the case with the floating-wall potential of a glow-discharge [9]. At the onset of the off-pulse a drastic increase of the floating anode potential to  $130$  V can be seen in the case of a cathode voltage of  $-400$  V, dropping to ground potential within  $\sim 20 \mu\text{s}$ . For the slightly lower cathode voltage of  $-300$  V the floating anode potential rises to only  $\sim 10$  V, dropping with a longer decay time of  $\sim 100 \mu\text{s}$ . Although, as mentioned, these measurements can only be taken as indicative of what takes place in the case of a grounded anode, they clearly show that when the cathode of the discharge is grounded, the potential within the discharge does in fact rise to a high positive value, where after it decays within the first  $10$ - $100 \mu\text{s}$  of the off pulse, depending on the cathode voltage. Again, what one sees here are the effects of the collapse of the discharge.

A comparison between the measurements depicted in Fig. 5.5 and Fig. 5.6 are seen in Fig. 5.7, showing the peak values of the floating anode potentials (squares) and the maximum ion-energies measured at a grounded anode (triangles), as a function of cathode voltage. As can be seen, there is consistency between the two experiments.

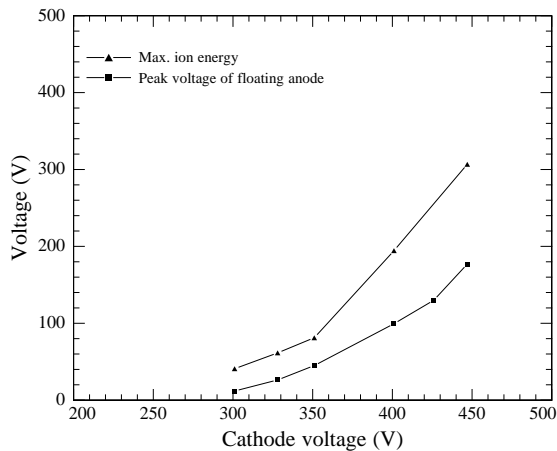


**Figure 5.7** The maximum ion energy deduced from the measured energy distributions shown in Fig. 5.5 of the ions hitting the anode ( $\blacktriangle$ ) and the peak voltage of the floating anode voltage measurements shown in Fig. 5.6 ( $\blacksquare$ ), depicted as a function of cathode voltage.

## 5.5 Plasma Simulations

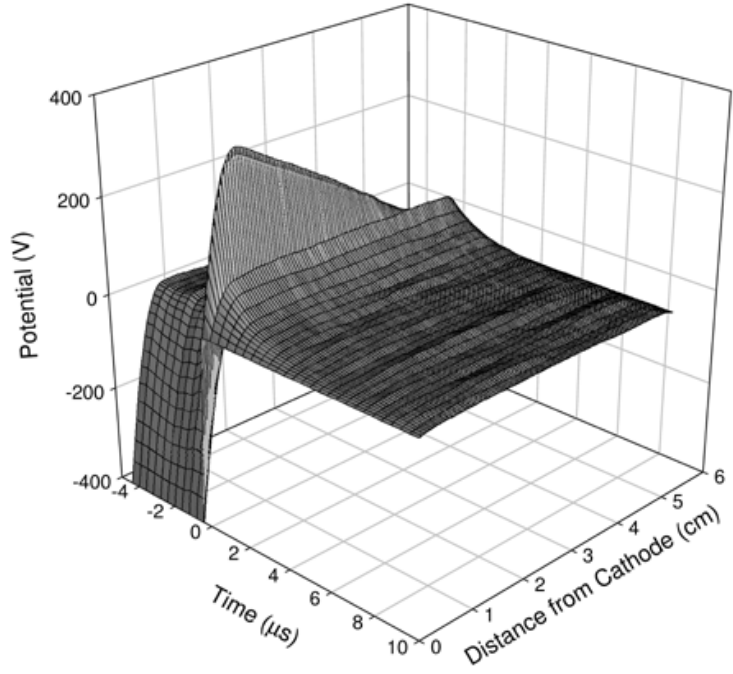
On the basis of the results described in the previous section, it is reasonable to conclude that the sudden grounding of the negatively biased cathode of a glow-discharge leads to a temporary and high positive plasma potential, causing the anode to be bombarded with energetic particles. To further validate the existence of this potential, and to shed more light on the dynamics and physics of this effect, plasma simulations of a pulsed-DC argon glow-discharge were performed. This was done using the *xpdp1* plasma simulation software developed by the Plasma Theory and Simulation Group at Berkeley University [64]. The computer code is based on the *Particle-in-Cell* (PIC) and *Monte-Carlo* methods, for particle dynamics and particle collision simulation, respectively.

Some results of these simulations are seen in Figs. 5.8 and 5.9. The surface plots show the evolution of the plasma potential and the electron and ion current-densities around the time of the onset of the off-pulse (defined at the time,  $t = 0$ ). The data shown is for at pulsed-DC argon glow-discharge with a cathode voltage of  $-400$  V, on- and off-pulse times of  $200 \mu\text{s}$ , an argon gas

*Caption to Figs. 5.8 and 5.9 (following two pages)*

Plasma simulation of an argon pulsed-DC glow-discharge with a gas pressure of  $0.5$  mbar, a cathode on pulse voltage of  $-400$  V and a cathode-anode spacing of  $5$  cm. The figures show the temporal evolution of (5.8a) the plasma potential and (5.8b) the ion current-density on a  $\mu\text{s}$  timescale, and (5.9a) the plasma potential and (5.9b) the electron current-density on a ns timescale, in the region around the grounding of the cathode (time,  $t = 0$ ). See Fig. 5.10 for a two-dimensional representation.

- a) Potential  
( $\mu\text{s}$ -timescale)



- b) Ion-current density  
( $\mu\text{s}$ -timescale)

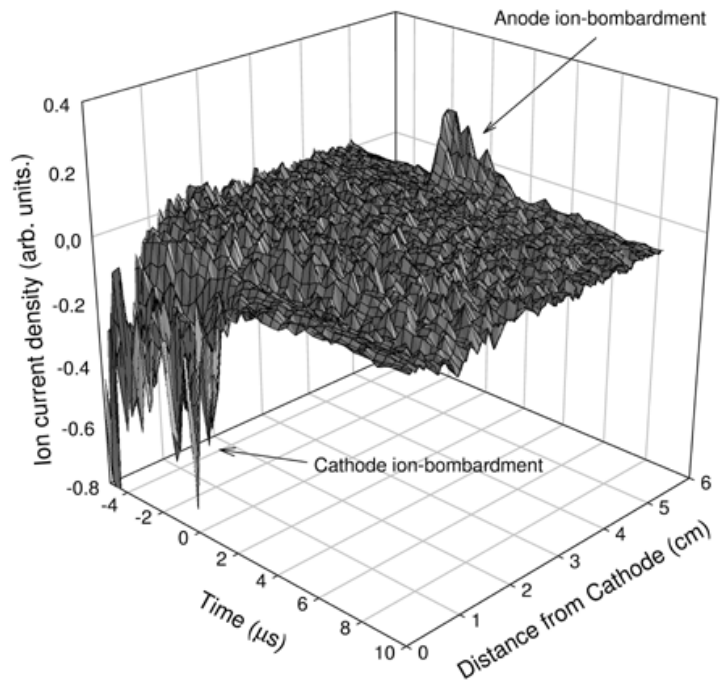


Figure 5.8  
(caption on p. 129)

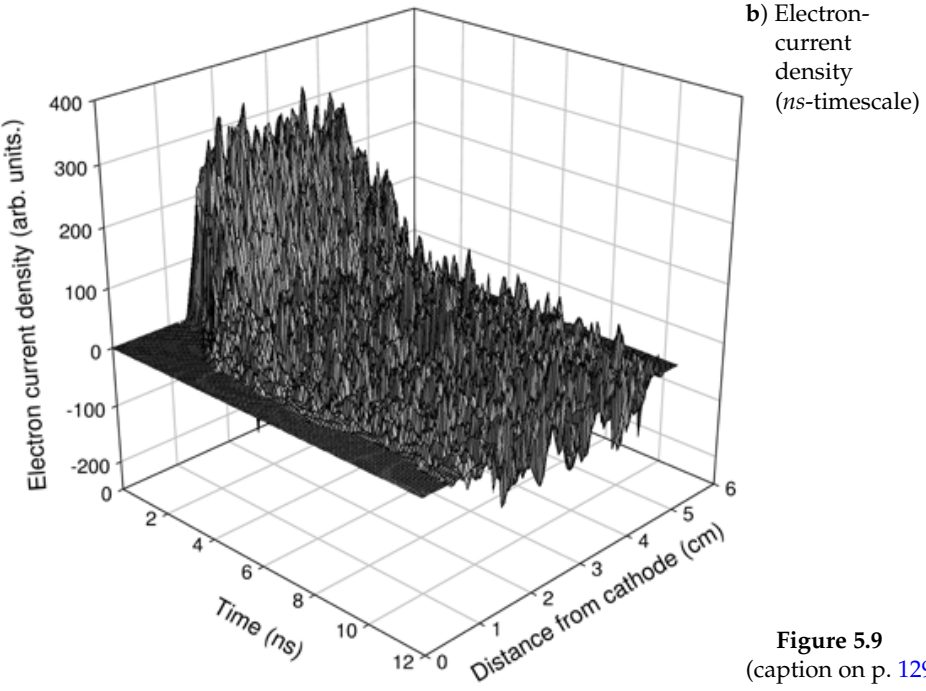
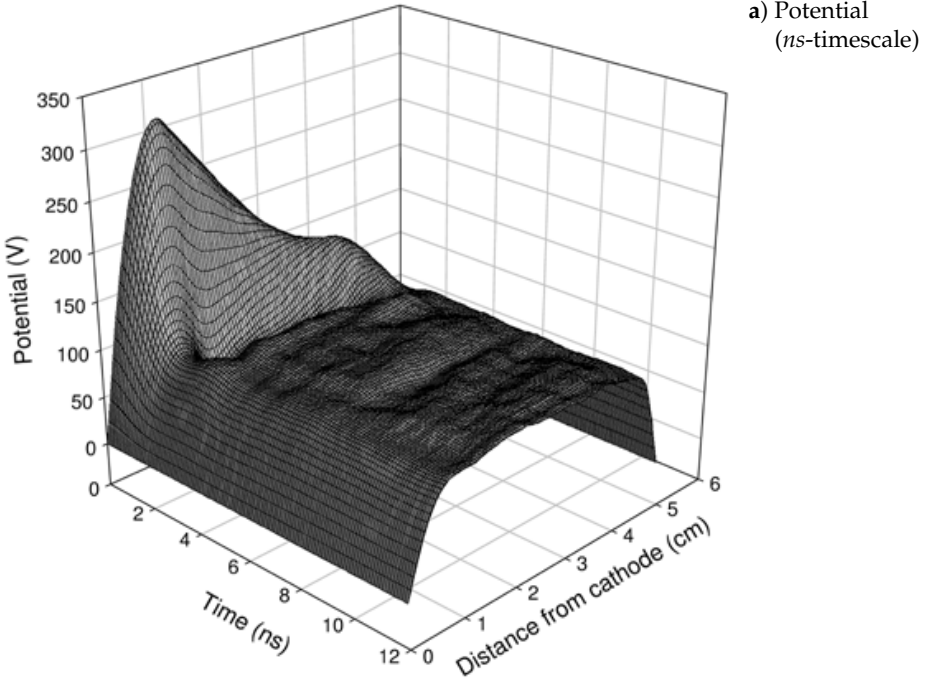
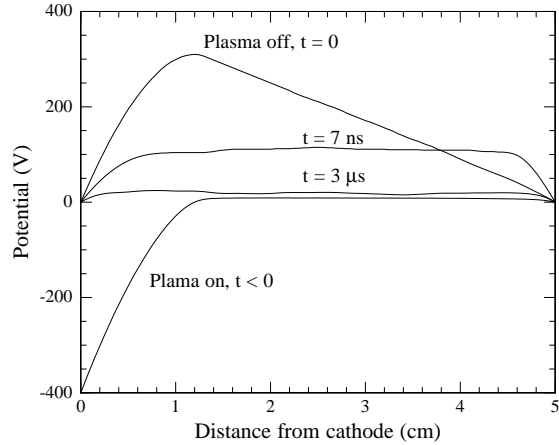


Figure 5.9  
(caption on p. 129)

**Figure 5.10** Plots of the plasma potential distributions between the cathode and anode of the pulsed-DC glow-discharge simulation shown in Figs. 5.8 and 5.9, at different times surrounding the grounding of the cathode.



pressure of 0.5 mbar and a cathode-anode spacing of 5 cm, i.e., the same conditions as for the experiments described in the previous section. To ensure that an equilibrium state of the pulsed-DC glow-discharge was achieved, 13 ms in discharge-time, equivalent to 32 voltage cycles was simulated before extracting the data shown. In Fig. 5.8, the temporal evolution of the plasma potential between cathode and anode of the glow-discharge and the corresponding ion current-densities are shown on a microsecond timescale. Before the onset of the off-pulse ( $t < 0$ ), part of the potential distribution, which is characteristic of a steady-state negative biased glow-discharge (also shown in Fig. 5.1), can be seen. This is the cathode sheath region that, as mentioned in Sect. 5.2, is the origin of the energetic ions bombarding the cathode. These fast ions can be seen in Fig. 5.8b as high negative values of the ion current-density in the near-cathode region (denoted in the figure as "Cathode ion-bombardment"). Returning to Fig. 5.8a, at the onset of the off pulse ( $t = 0$ ), one sees the instantaneous effect of grounding the cathode, as a drastic increase of the plasma potential to voltages comparable in size with the negative cathode voltage ( $\sim 350$  V at peak-value). To help the reader, a two-dimensional representation of the transition is shown in Fig. 5.10.

The reason for this drastic change in the plasma potential must be sought in the abrupt change of the glow-discharge boundary conditions and the inertia of the charged particles. The potential distribution before the onset of the off pulse is, of course, a result of a well-defined charge-distribution (i.e., electron- and ion-distribution) throughout the discharge. These charged particles cannot redistribute themselves instantaneously when the cathode is grounded, and hence the plasma potential must attain high positive values in order to comply with

both the existing charge distribution from the on pulse and the new boundary conditions of the grounded cathode. The potential distribution at  $t = 0$  is, of course, highly unstable, hence it quickly relaxes to a more spatially homogeneous distribution (shown in Fig. 5.10,  $t = 7$  ns), with a potential of  $\sim 100$  V.

This fast redistribution can be understood from Fig. 5.9, showing the temporal evolution of the plasma potential and the electron-current distribution on a nanosecond timescale, which is the timescale of electron motion in this case. Here one sees the transition from the  $t = 0$  to the homogeneous  $t = 7$  ns potential distribution (Fig. 5.9a). The mechanism here is the fast redistribution of electrons, which is evident from Fig. 5.9b, where a net electron motion towards the cathode region is seen as high positive values of the electron-current distribution (note that in terms of *particle* current Figs. 5.8b and 5.9b have opposite signs). This takes about 4 ns, after which the electron-current distribution takes a form that is characteristic of thermal electrons. Returning again to Fig. 5.8, showing the evolution on a timescale characteristic of ion motion, the ultimate decay of the plasma can be seen to take place during subsequent  $\sim 4$   $\mu$ s (see also Fig. 5.10). In Fig. 5.8b one also sees how this positive and relatively long-lived plasma potential results in bombardment of the glow-discharge anode (denoted in the figure as "Anode ion-bombardment"). These are the ions that are observed by the Hidden EQP during the off pulse of the discharge.

From the simulations described above, it can be concluded that the collapse of the plasma can be described by two transitions; one on a timescale for electron motion (ns) and a subsequent transition occurring on the timescale for ion motion ( $\mu$ s). However, in practical application pulsed-DC glow-discharges, the grounding of the cathode does usually not take place on a nanosecond timescale, e.g., the rise- and fall-time of the experimental voltage-profiles described in this paper was of the order of 1  $\mu$ s. Hence, the highly unstable potential distribution of the simulations at  $t = 0$  will probably never build up, as the electrons have sufficient time to redistribute themselves during the grounding process itself. However, the homogenous plasma potential distribution that is seen at  $t = 7$  ns and decays on a microsecond timescale, will have time to build up — at least to some extent — in the present experiments, and hence result in the observed high-energy ion bombardment of the anode.

## 5.6 Anode Sputtering

As typical thresholds for physical sputtering are some 10–20 eV, it is clear that the high-energy ions bombarding the anode are capable of sputtering anode material. An estimate of the relative importance of anode sputtering compared to cathode sputtering is seen in Fig. 5.11. The figure shows the expected amount of anode ( $\blacksquare$ , left axis) and cathode ( $\blacktriangle$ , left axis) sputtering as a function of cathode voltage. The curves were calculated by integrating the product of the

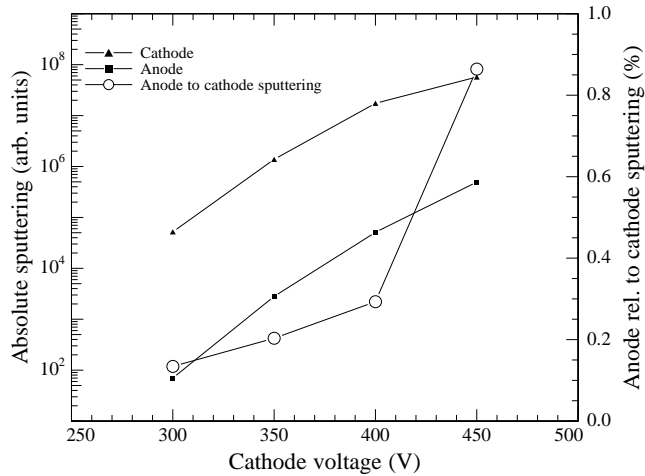


**Figure 5.11** The amount of sputtering expected in the case of gold sputtering at the cathode ( $\blacktriangle$ , left axis) and anode ( $\blacksquare$ , left axis) as a function on cathode voltage, calculated on the basis of the measured ion energy-distributions in each case, and the relative amount of anode sputtering compared to cathode sputtering ( $\circ$ , right axis).

measured ion energy-distributions and the sputter-yield curve for gold sputtering by argon ions [47] (i.e., the yield of sputtered gold atoms per incident argon atom, as a function of argon atom energy). The sputter-yield curve for gold is taken as representative of typical physical sputter-yield curves. This was done using the anode ion energy-distributions of Fig. 5.5 and a set of measured ion energy-distributions of ions impinging on the cathode (not shown). See Ref. 63 for examples of typical cathode ion energy-distributions. Also shown in the figure is the ratio between the anode and cathode sputtering values ( $\circ$ , right axis). For the plasma conditions used here, the expected degree of anode sputtering can be seen to lie between 0.1% to 1% of the sputtering occurring on the cathode. Moreover, the relative importance of anode sputtering can be seen to increase with increasing cathode voltage.

A note should be added to the comparison just made. In comparing the absolute expected sputtering of the anode and the cathode, one has to assume that the measured ion energy-distributions for the cathode and anode are equally representative of the actual ones. As low energy ( $< 20$  eV) ions have a large angular distribution, due to the collisions they have undergone, this could present a problem in the low-energy region of the energy distributions, as the angular acceptance of the Hidden EQP is quite narrow. However, at the energies where

sputtering is dominant ( $> 100$  eV) it is safe to assume that all ions entering the orifice will actually be detected by the EQP, as these ions do not have high incident angles.

## 5.7 Discussion and Concluding Remarks

As was evident from the ion energy measurements shown in Sect. 5.4, the anode is bombarded with high-energy ions during the off pulses of a pulsed-DC glow discharge. The origin of these high-energy ions is the creation of a temporary high and positive plasma potential when cathode is grounded. The existence of this potential was directly verified by floating anode measurements, showing plasma potentials of more than 100 V. Moreover, plasma simulations have also confirmed the existence of this potential, attaining values and decay times in good qualitative agreement with the experiments. Furthermore, they gave a good understanding of the physics of the process: it is a result of the instantaneous or fast grounding of the cathode combined with the inertia of the charged particles that form the plasma. Note, that the ion energy and temporal evolution measurements were performed with logarithmic sensitivity, as opposed to the floating anode experiments and the plasma simulations, which only had linear sensitivity.

The degree of anode sputtering was estimated for the case of sputtering of gold, and was shown to lie between 0.1 and 1% of cathode sputtering. Whether or not this is of importance depends, of course, on the specific application of the pulsed glow-discharge. Especially when using high-purity environments, the degree of anode sputtering that occurs as a result of discharge pulsing should be considered. In the present set-up it was not possible to attain negative cathode voltages of over 450 V, but as Fig. 5.11 indicates, the relative importance does seem to increase with increasing voltage, making anode material sputtering an issue even in lower-purity environments. For example, in typical industrial PACVD processes, cathode voltages of up to 1 000 V are used.

One rather straightforward way of avoiding high-energy ion bombardment of the anode would be to ramp the grounding of the cathode on the timescale of ion motion, i.e., between 10-100  $\mu\text{s}$  depending on circumstances. This would allow the ions to redistribute themselves during the grounding process itself, so that the build-up of the high and positive plasma potential is avoided.

## 5.8 Summary (thesis only)

The results presented in this article are a good example of the use of plasma simulations to give a deeper understanding of the physics of glow-discharges and a qualitative explanation of a measured effect. Obviously, the *grounded anode* re-

gion during the *plasma off* period of a pulsed DC glow-discharge is probably that last place one would expect the existence of energetic ions! Nevertheless, the Hidden EQP measurements of the ions impinging on the anode of such a discharge clearly showed this to be the case. Considering the dynamics of the collapse of a glow-discharge upon the grounding of the cathode, clearly illustrated by the plasma simulations presented here, the origin of these energetic ions could be established and their existence readily verified. The creation of a high-voltage plasma potential (with respect to the grounded electrodes) during the onset of the off-pulse results in an acceleration of the ions which exist near the anode, thus leading to an energetic ion bombardment of the anode. Of course, the flux of these ions cannot compare in size with the ion-flux at the cathode during the on-pulse. Nevertheless, this anode-ion flux – in conjunction with the energies they obtain – is high enough for anode material sputtering to occur. Compared to the total amount of cathode material sputtering, the amount of anode material was estimated to 0.1–1%.<sup>1</sup> Depending on the purity requirements of a practical application utilizing pulsed-DC glow-discharges, the importance of this effect should hence be considered.

---

<sup>1</sup>This comparison, which is depicted in Fig. 5.11, was made on the basis of the measured ion energy-distributions, and the total integrated ion-fluxes at the cathode and anode (including both the on and the off pulse), as obtained from the simulations.

# 6

---

## THE $N_2$ AND $N_2$ - $H_2$ DISCHARGES

*characterization and nitriding*

---

*Like the Ar- $H_2$  discharge, the  $N_2$ - $H_2$  discharge has a well-established practical surface processing application, namely nitriding. Metals which are exposed to a  $N_2$ - $H_2$  discharge at high temperatures ( $\sim 500^\circ\text{C}$ ), experience a degree of nitrogen intake of the surface, which effectively enhances the tribological properties of the metal. In this chapter, measured ion energy-distributions of the  $N_2$  and  $N_2$ - $H_2$  discharges will be presented. We will try and explain the energy-distributions of the  $N_2$  discharge within the formalism of the Davis and Vanderslice model. Finally, a series of nitriding experiments will be presented, and viewed upon in the light of the measured ion energy-distributions of this discharge.*

### 6.1 Introduction

Just like the  $H_2$  discharge studied by Davis and Vanderslice, the  $N_2$  discharge is fundamentally different from the Ar discharge because of its molecular nature; it has both  $N^+$  and  $N_2^+$  as primary ions. Charge exchange with the neutral background gas ( $N_2$ ) still dominates the sheath kinetics, but for  $N^+$  this collision is not resonant and thus has a significantly lower cross-section (the neutral N concentration is of the order of the degree of ionization [65]). Hence, the  $N^+$  ions bombarding the cathode are highly energetic, just like the  $ArH^+$  ions of an Ar- $H_2$  discharge, which also have no neutral counterpart. In this chapter we will

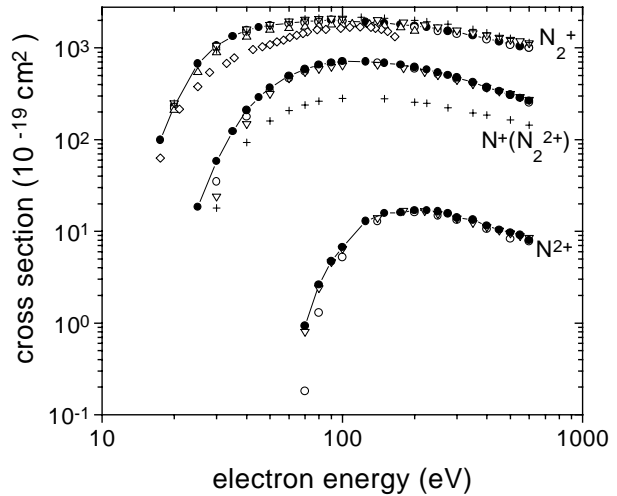


**Figure 6.1** Electron-impact ionization cross-section for  $N_2$ . Because of equal  $q/m$ ,  $N^+$  and  $N_2^{2+}$  are not discernable. The  $N_2^{2+}$ -contribution, which is created via a double-ionization process is however expected to be negligible. Taken from Tian and Vidal [68].

have a look at the energy-distribution of these two ions, and try to give a qualitative explanation of their main characteristics. Because of the slightly more complicated nature of the  $N_2$  discharge, the Davis and Vanderslice model is not directly usable. However, one can still learn something from the discrepancies which arise when applying this simple model.

Adding  $H_2$  to the discharge naturally complicates matters even more — 8 major ionic species are now present at the cathode. One of the major practical uses of the  $N_2$ - $H_2$  discharge (both DC and RF) is for the nitriding of steels, which is a well-established commercial surface-hardening process providing wear, fatigue and corrosion-resistant surfaces [66, 67]. When exposing steels to a  $N_2$ - $H_2$  discharge at high temperatures ( $\sim 500^\circ\text{C}$ ), N will penetrate the surface and diffuse into the steel, resulting in a hardening of the surface and diffusion zone. It is however not clear what is taking place during this process on a microscopic level. Some insight on this may be gained by correlating the hardening properties of various  $N_2$ - $H_2$  discharges with the measured ion energy-distributions of these same discharges, using a similar approach as in Chap. 4, where the physical and chemical sputtering properties of the Ar- $H_2$  discharge was studied.

## 6.2 The $N_2$ discharge

As already mentioned, the main ionic species of the  $N_2$  discharge are  $N^+$  and  $N_2^+$ . Fig. 6.1 shows the electron impact ionization cross-section for  $N_2$ , showing the main products to be  $N_2^+$  and  $N^+$ . There are several ionization channels leading to the production of these ions (Tian and Vidal [68]). One of these is double-ionization leading to the production of  $N_2^{2+}$ , which is not discernable from  $N^+$

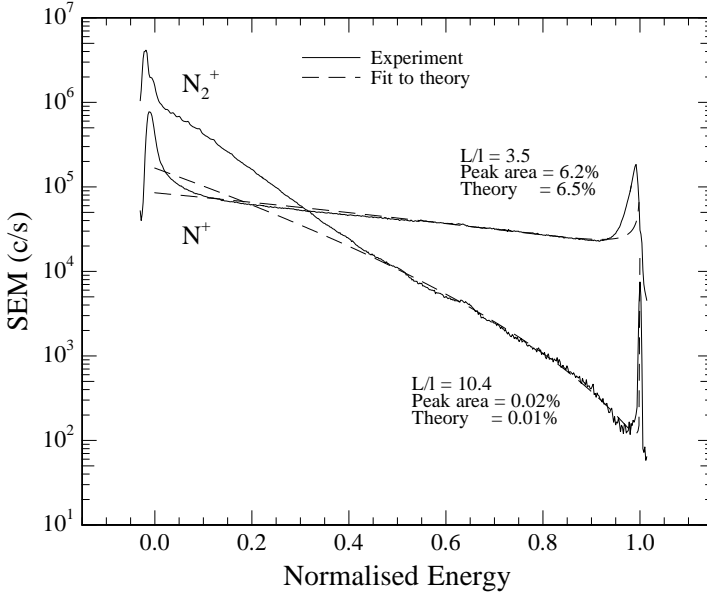


**Figure 6.2** Measured ion energy-distributions for the N<sup>+</sup> and N<sub>2</sub><sup>+</sup> ions (—) of a N<sub>2</sub> discharge (−500 V, 0.37 mbar). Also shown are the best fits to the data with the Davis and Vandarslice distribution (---).

since they have equal  $q/m$ . The authors, however, expect the N<sub>2</sub><sup>+</sup> contribution to be negligible. In Fig. 6.2 the measured energy-distribution of N<sup>+</sup> and N<sub>2</sub><sup>+</sup> are shown for a discharge driven at a (stainless steel) cathode voltage of −500 V and a N<sub>2</sub> pressure of 0.37 mbar. As expected, resonant charge transfer effectively attenuates N<sub>2</sub><sup>+</sup>, resulting in relatively low-energy ions. This is not the case for N<sup>+</sup>, which can be seen to have an almost homogeneous energy-distribution. These are also the qualitative findings of Wroński and Murlak-Stachura [69] and Quast *et al.* [37], who have also performed ion energy-distribution measurements of an N<sub>2</sub> discharge. Both for N<sup>+</sup> and N<sub>2</sub><sup>+</sup> an end-point peak, corresponding to the fraction  $e^{-s/\lambda}$  of ions which transverse the sheath without any collisions is clearly visible. The question now is, what processes determine the mean-free-path,  $\lambda$ ?

### N<sub>2</sub><sup>+</sup> (I)

If we start by looking at N<sub>2</sub><sup>+</sup> as an isolated ion, ignoring N<sup>+</sup> for the moment, the energy-distribution should be explainable by the Davis and Vandarslice model, since symmetric charge exchange is controlling its kinetics in the sheath. See

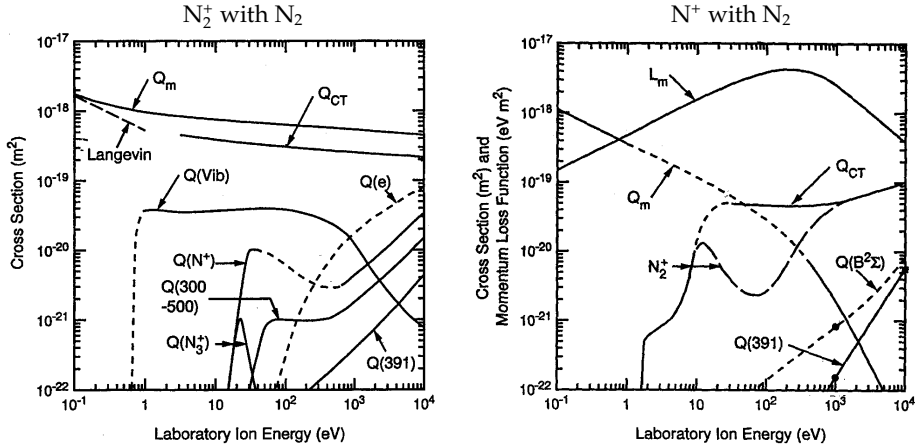


**Figure 6.3** Various collision cross-sections for  $N_2^+$  and  $N^+$  with  $N_2$ .  $Q_m$ : momentum transfer.  $Q_{CT}$ : charge transfer.  $L_m$ : momentum loss function. The “dip” in the charge transfer curve for  $N^+$  from 10–300 eV (the curve denoted  $N_2^+$ ) can be explained by the variable  $N_2^-$ -collection efficiency of measurements, and is therefore not necessarily real. Taken from Phelps [11].

Fig. 6.3 (left) for the main collision processes for  $N_2^+$  with  $N_2$ . The dashed line in Fig. 6.2 shows the best fit of the Davis and Vanderslice distribution. The agreement can be seen to be excellent in the high-energy region, which the fit was confined to, with a  $s/\lambda$ -value of 10.4.<sup>1</sup> Using a charge exchange cross-section of  $\sigma[N_2^+] \sim 3 \times 10^{-15} \text{ cm}^2$  (see Fig. 6.3) and a  $N_2$  gas density of  $n_g \sim 9 \times 10^{15} \text{ cm}^{-3}$  (0.37 mbar, 300 K) the sheath thickness can be estimated, yielding  $s \sim 4 \text{ mm}$ .

Also shown in the figure are the experimental and measured end-point peak fractions. For the measured curve, this fraction was obtained by integrating the full extent of the peak and normalizing to the total area of the distribution. This same procedure was used for the theoretical curve, whereafter the collision-less fraction,  $e^{-s/\lambda}$  was added. In this way, both the collision-less fraction *and* the high-energy peak structure of the theoretical distribution are taken into account (e.g., see Fig. 1.9 on p. 23). This also considers the effects of the finite energy resolution ( $\pm 0.75 \text{ eV}$ ) of the EQP. The peak-area fractions calculated in this way are in good agreement with each other, which in itself substantiates that the Davis and Vanderslice model appropriately describes the  $N_2^+$  ions entering the sheath.

In the low-energy region, however, the Davis and Vanderslice distribution clearly fails, underestimating the  $N_2^+$  intensities by almost a decade. Since the

<sup>1</sup>These fits were performed with  $m = 2$ .

high-energy region was clearly well-described by the charge exchange model, this means that some source of N<sub>2</sub><sup>+</sup> ions must exist, which predominantly generates low-energy ions which are then superimposed on the Davis and Vanderslice distribution. One such source could be the N<sup>+</sup> ions, which are seen to be readily available in the sheath.

### N<sup>+</sup>

Fig. 6.3 (right) shows the cross-sections for the dominant collision processes between N<sup>+</sup> and N<sub>2</sub>. By comparing the curves for momentum transfer ( $Q_m$ ) and charge transfer ( $Q_{CT}$ ) with those for N<sub>2</sub><sup>+</sup>, the fundamental difference between the kinetics of these two ions in the sheath is apparent. Furthermore, charge transfer between N<sup>+</sup> and N<sub>2</sub> does not act as an attenuator of N<sup>+</sup> but as a sink, since its product ion is N<sub>2</sub><sup>+</sup> and not N<sup>+</sup>:



Hence, if this were the only process taking place it would not, as is the case for N<sub>2</sub><sup>+</sup> or Ar<sup>+</sup>, give rise to a change in the energy-distribution, but merely reduce the intensity of N<sup>+</sup> at the cathode — all of which would have the full potential energy of the sheath. Although Fig. 6.2 shows that N<sup>+</sup> indeed has a large end-point peak, elastic scattering between N<sup>+</sup> and N<sub>2</sub> will of course result in some final energy-distribution at the cathode, which is also apparent from the figure.

Clearly, the Davis and Vanderslice model cannot be used to describe the energy-distribution of the N<sup>+</sup> ions, since the non-destructive collision process which N<sup>+</sup> undergoes (viz. elastic scattering) does not comply with the assumption of zero initial energy after a collision. Nevertheless, a fit of this model to the N<sup>+</sup> energy-distribution is shown in the figure (—). As can be seen, the agreement is quite good. Of course, just like the theoretical curve, the measured energy-distribution is quite “simple” or homogenous, meaning that the good agreement between the envelope of the two distributions (which is basically just a constant) does not by itself give too much credit to the theory. However, using the  $s/\lambda$ -value of 3.5 which results from the fit, the end-point peaks of the theoretical and measured distribution can be compared. These peak fractions are also shown in the figure, and are equally seen to be in good agreement with each other. Hence, it seems that the full functionality of the Davis and Vanderslice distribution is also adequate in describing the N<sup>+</sup> distribution. The question now arises, what the significance is of the mean-free-path value,  $\lambda$ , which can be deduced from the fit? From the N<sub>2</sub><sup>+</sup> distribution we extracted the sheath thickness  $s \sim 4$  mm. Using this value, the  $s/\lambda$ -value of 3.5 for can be converted into a cross-section of:

$$\sigma[\text{N}^+] = \frac{1}{n_g \lambda} = \frac{1}{n_g s} \frac{s}{\lambda} \sim 9 \times 10^{-16} \text{ cm}^2. \quad (6.2)$$

where we have used  $n_g \sim 9 \times 10^{15} \text{ cm}^3$  (0.37 mbar, 300 K). Let us for the moment accept the fact that the Davis and Vanderslice distribution is seemingly a good function also for the  $N^+$  ions. In this model, a collision is defined as a process under which the ion loses all its energy — namely charge exchange. The probability of this process is characterized by a mean-free-path, signifying the average distance an ion travels before it charge exchanges (or loses all its energy). The difference between elastic scattering and charge transfer is, that the ion does not lose all its energy when it undergoes the former process, but *some* of it. Hence, staying within the framework of the Davis and Vanderslice model, we could define an *effective* mean-free-path as *the distance an ion can travel before it has lost all its energy*. The pseudo-collision defined in this way, which will include several real elastic scattering collisions, complies with the assumptions of the Davis and Vanderslice model (if we may also assume that it is energy independent, which an inspection of the momentum transfer curve ( $Q_m$ ) in Fig. 6.3 does not exactly endorse — nevertheless we will assume this). The mean-free-path defined in this way must be longer than the mean-free-path for elastic scattering. With this mind, we may interpret the cross-section given by Eq. (6.2), and compare it with the elastic scattering cross-section for  $N^+$  shown in Fig. 6.3; the former value should be *smaller* than the latter (since its mean-free-path is larger). However, the curve for  $Q_m$  varies quite a lot in the energy range which is of relevance here, meaning that any cross-section derived from the spectra would merely be some appropriately energy-averaged value. It may thus only be concluded that the cross-section given by Eq. (6.2) is not in direct contradiction with the known values for elastic scattering.

Clearly, the interpretation of the Davis and Vanderslice fit given above is rather speculative, and is merely intended as a heuristic (or is it “heroic”?) attempt at explaining the apparent success of the Davis and Vanderslice model in this respect.

## $N_2^+$ (II)

We may now return to the  $N_2^+$  distribution, and try to explain the disagreement between the Davis and Vanderslice and the measured distributions at low energies. As already mentioned,  $N^+$  ions which undergo charge exchange with  $N_2$  (Eq. (6.1)) may act as a source of these  $N_2^+$  ions. The cross-section for this process is also shown in Fig. 6.3 ( $Q_{CT}$ ). Clearly, as opposed to what is the case of  $N_2^+$ ,  $N^+$  charge exchange strongly favors relatively high ion energies (note the two separate curves which make up the  $Q_{CT}$  curve; these stem from different experiments — the dip in the lower curve may be explained by experimental effects, and hence is not necessarily real). Since energetic  $N^+$  ions are favored, this implies that  $N^+$  charge exchange with  $N_2$  occurs between somewhere near the middle of the sheath (depending on the *exact* energy threshold of  $Q_{CT}$ ) and the cathode, since this is where energetic  $N^+$  exists. Hence, the  $N_2^+$  ions created here

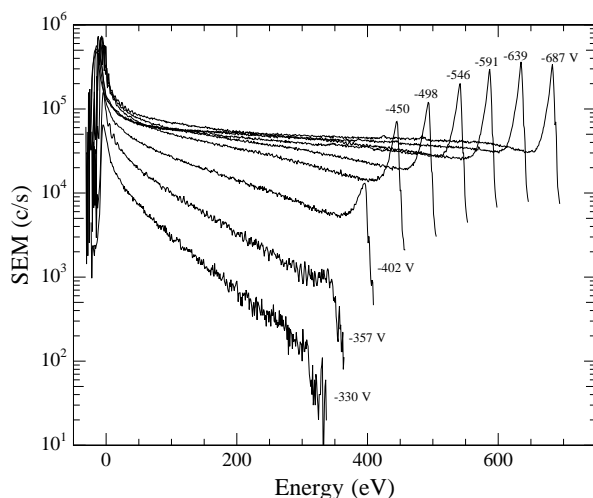


**Figure 6.4** Measured  $N^+$  energy-distributions of a 0.37-mbar  $N_2$  discharge at varying discharge voltage (shown in figure).

cannot gain high energies and will thus contribute only to the low-energy region of the energy-distribution, thus giving a possible explanation of the observed. It is however difficult to assess to what extent this is the complete story, since the threshold for charge exchange is not completely established. If, as Fig. 6.3 may indicate, it is around 10–30 eV, it does not seem likely that this model can fully explain the high fraction of low energy  $N_2^+$  ions. Since the discharge voltage was 500 V, a threshold of about 250 eV (i.e., the lower  $Q_{CT}$  curve), would agree more with the measured  $N_2^+$  distribution.

### Dependence on Voltage and Pressure

Fig. 6.4 shows a series of measured  $N^+$  energy-distributions of an 0.37-mbar  $N_2$  discharge with different discharge voltages. In this figure, the effect of increasing the discharge voltage as was discussed in Chap. 3 is clearly visible. The high-energy fraction can be seen to increase drastically with increasing voltage, as does the collision-less fraction. Clearly, a power controlled discharge which could easily be varying the voltage in say the 400–500 V range, would result in a very unsteady energy bombardment of the cathode. In Fig. 6.5, which shows the variation with pressure at a fixed voltage of 500 V, it can be seen that a change in pressure does not at all interfere with the ion energy-distribution (i.e., the  $s/\lambda$ -values) at the cathode. Clearly, in this case, the rule-of-thumb which states that  $s \times p \sim \text{const}$ , which implies  $(s/\lambda)_{\text{var } p} \sim \text{const}$ , is valid (remember,  $p \propto 1/\lambda$ ).

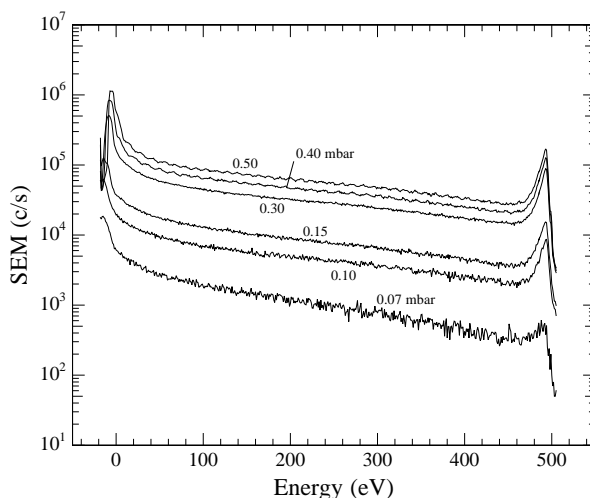


**Figure 6.5** Measured  $N^+$  energy-distributions of a 500-V  $N_2$  discharge at varying pressures (shown in figure).

### 6.3 The $N_2$ - $H_2$ discharge

In the present work, no attempt has been made to try and explain the energy-distributions of the  $N_2$ - $H_2$  discharge — at least not to the extent of, for example, the  $Ar$ - $H_2$  discharge. Here, I shall merely present the energy-distributions which were measured for an  $N_2$ - $H_2$  discharge driven at a voltage of  $-400$  V and a pressure of  $0.37$  mbar with a  $H_2$ -content of  $20\%$ . These are shown in Figs. 6.6–6.8.

The  $N_2$ - $H_2$  discharge, the neutral background gas of which consists of two molecular, reactive species, produces a large number of different ionic species at the cathode. I have divided these into three groups:

1. **Fig. 6.6:**  $N^+$ ,  $N_2^+$  and  $N_2H^+$
2. **Fig. 6.7:**  $NH^+$ ,  $NH_2^+$ ,  $NH_3^+$  and  $NH_4^+$
3. **Fig. 6.8:**  $H_2^+$  and  $H_3^+$

Tab. 6.1 presents the relative intensity and various kinetic properties of these ions, calculated on the basis of the measured energy-distributions. Although the hydrogen content of the discharge was only  $20\%$ , it can be deduced from the relative intensities shown in the table that hydrogen makes up  $33\%$  of the ionic molecules which impinge on the cathode. This could be explained by the

ION	MASS	REL (%)	$\langle E \rangle$ (eV)	REL $\langle E \rangle$ (%)	$\langle mv \rangle$	REL $\langle mv \rangle$ (%)
N <sub>2</sub> <sup>+</sup>	28	34.7	57	19.2	52	30.16
N <sub>2</sub> H <sup>+</sup>	29	35.7	106	36.7	72	42.70
N <sup>+</sup>	14	10.2	184	18.3	67	11.38
NH <sup>+</sup>	15	2.1	216	4.3	76	2.59
NH <sub>2</sub> <sup>+</sup>	16	2.8	194	5.3	73	3.40
NH <sub>3</sub> <sup>+</sup>	17	6.3	120	7.4	58	6.06
NH <sub>4</sub> <sup>+</sup>	18	1.0	342	3.3	109	1.77
H <sub>2</sub> <sup>+</sup>	2	7.2	78	5.5	16	1.92
H <sub>3</sub> <sup>+</sup>	3	0.1	62	0.1	16	0.03

**Table 6.1** The relative intensity and various kinetic properties of the main ions at the cathode of a N<sub>2</sub>-H<sub>2</sub> discharge. MASS: ion mass in amu,  $\langle E \rangle$ : mean energy, REL: the relative intensity (integrated energy-distributions, REL $\langle E \rangle$ : energy-weighted relative intensity,  $\langle mv \rangle$ : mean momentum (calculated using  $\sqrt{2mE}$ , with the ion mass,  $m$ , in amu and the energy,  $E$ , in eV) and REL $\langle mv \rangle$ : momentum-weighted relative intensity. The values have been calculated on the basis of the measured ion energy-distributions shown in Figs. 6.6–6.8.

fact that fast neutrals created via some ion-neutral collision process are not accounted for. The fraction of hydrogen amongst the fast neutrals could be equally smaller.

### N<sup>+</sup>, N<sub>2</sub><sup>+</sup> and N<sub>2</sub>H<sup>+</sup>

These ions by far constitute the majority (81%) of the ions at the cathode. Just as the case was for the N<sub>2</sub> discharge, the N<sup>+</sup> ions are much more energetic than the N<sub>2</sub><sup>+</sup> ions, which have plenty of N<sub>2</sub> to symmetrically charge transfer with. This is clearly seen in Fig. 6.6 and Tab. 6.1, which shows the mean energy of N<sup>+</sup> to be more than three times as larger than that for N<sub>2</sub><sup>+</sup>. Interestingly, the dominant ion of the discharge can be seen to be N<sub>2</sub>H<sup>+</sup>, both in intensity and relative energy and momentum. In this sense, the N<sub>2</sub>-H<sub>2</sub> discharge is similar to the Ar-H<sub>2</sub> discharge, which produces a large amount of energetic ArH<sup>+</sup>. The mean energy of N<sub>2</sub>H<sup>+</sup> is, however, still significantly lower than that of N<sup>+</sup>—N<sub>2</sub>H<sup>+</sup> is merely much more abundant.

### NH<sub>1-4</sub><sup>+</sup>

A N<sub>2</sub>-H<sub>2</sub> discharge produces large amounts of ammonia (NH<sub>3</sub>). This can, for example, easily be verified by the scent which fills the room when a plasma chamber is opened after holding such a discharge. Amorim *et al.* [70] have performed laser induced fluorescence (LIF) measurements on a N<sub>2</sub>-H<sub>2</sub> discharge, allowing

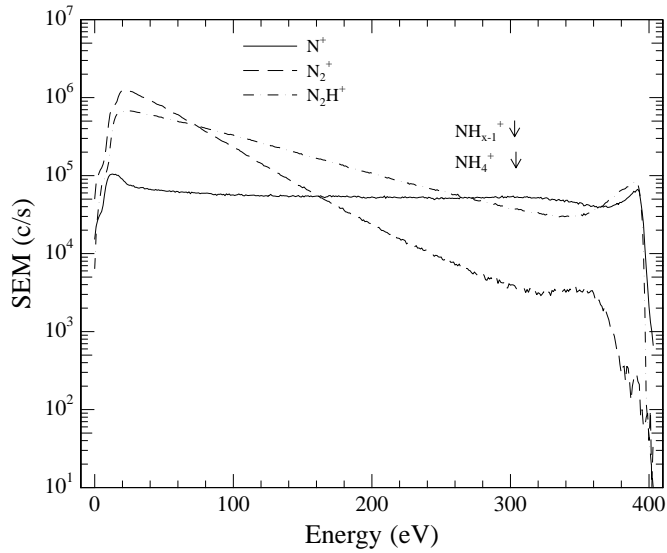


**Figure 6.6** Measured  $N^+$ ,  $N_2^+$  and  $N_2H^+$  energy-distributions of a  $N_2$ - $H_2$  discharge ( $-400$  V,  $0.37$  mbar,  $20\%$   $H_2$ ).

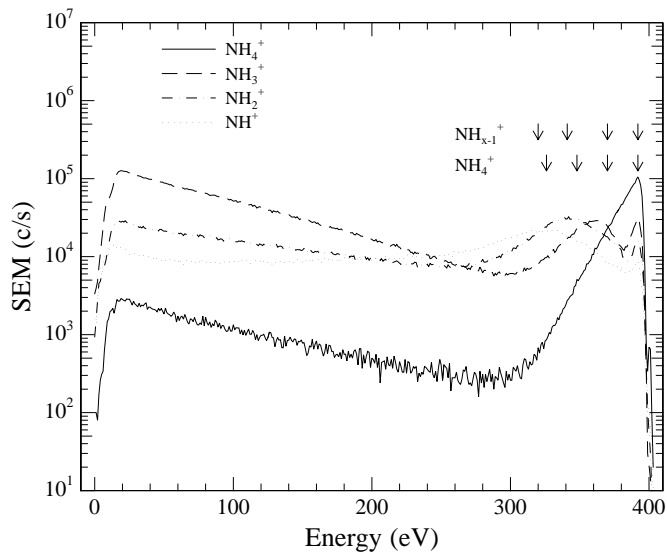


**Figure 6.7** Measured  $NH_{1-4}^+$  energy-distributions of a  $N_2$ - $H_2$  discharge ( $-400$  V,  $0.37$  mbar,  $20\%$   $H_2$ ).

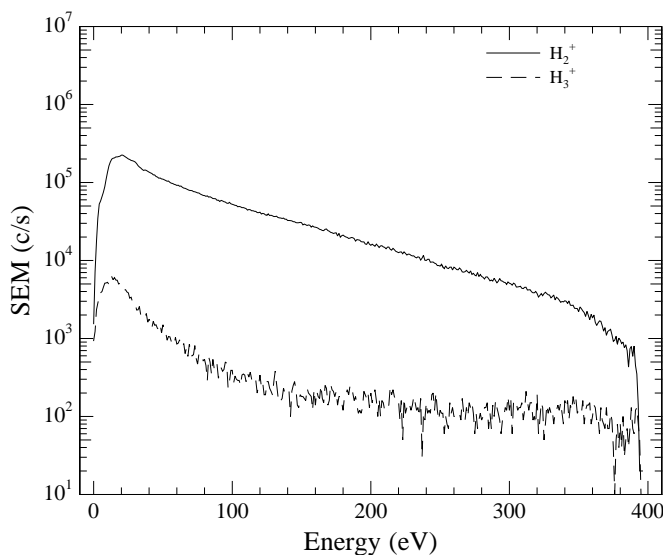
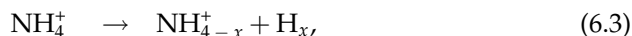


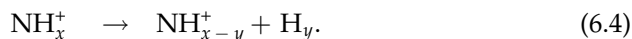
**Figure 6.8** Measured H<sub>2</sub><sup>+</sup> and H<sub>3</sub><sup>+</sup> energy-distributions of a N<sub>2</sub>-H<sub>2</sub> discharge (−400 V, 0.37 mbar, 20% H<sub>2</sub>).

an absolute determination of the NH<sub>3</sub> density. For a 2-torr discharge with a discharge current of 50 mA and H<sub>2</sub> content of 20%, i.e., a discharge similar to the one presented here, the NH<sub>3</sub> density was  $\sim 4 \times 10^{12} \text{ cm}^{-3}$  (the uncertainty was estimated to  $\pm 20\%$ ).

Amongst the NH<sub>*x*</sub><sup>+</sup> ions observed at the cathode, NH<sub>3</sub><sup>+</sup> is indeed seen to be the most abundant, in good agreement with the expected production of ammonia. Also present are relatively large amounts of NH<sub>2</sub><sup>+</sup> and NH<sup>+</sup>. The least abundant ion of the NH<sub>*x*</sub><sup>+</sup>-series is NH<sub>4</sub><sup>+</sup>, which however has a rather interesting energy-distribution. Obviously, since it has such a distinct end-point peak, with practically no ions below 350 eV, any non-destructive collision processes must have very low cross-sections — including elastic scattering. The energy-distributions of NH<sub>1-3</sub><sup>+</sup>, however, indicate that some fragmentation of NH<sub>4</sub><sup>+</sup> is taking place, leading directly to NH<sub>1-3</sub><sup>+</sup>:



and possibly a subsequent fragmentation of the ions generated in this way:



The ions generated in this way would be superimposed on the energy-distribution of the ions which originate from the bulk-plasma. Since the kinetic en-

ergy of the initial ion would be mass-ratio shared between the fragments, the high-energy hills of the  $NH_{1-3}^+$  energy-distributions could be explained if this process were to take place near the cathode. For example, an  $NH_4^+$  ion having an energy of 400 eV would split up into an  $NH_3^+$  ion with an energy of  $(17/18) \times 400 \text{ eV} = 378 \text{ eV}$  and a H atom with an energy of 22 eV. The arrows in Fig. 6.7 indicate the energies calculated in this way. The lower arrows were calculated by removing  $H_x$  from the  $\sim 400 \text{ eV } NH_4^+$  ion (i.e., process (6.3)), and the upper arrows were calculated by removing a  $H_1$  atom from a  $NH_x^+$  ion (i.e., process (6.4) with  $y = 1$ ), using the measured hill-top energy of the parent ion. Also,  $N^+$  could be generated via these processes, which is indicated by the arrows in Fig. 6.6. A hill-top can be very faintly observed in the  $N^+$  energy-distribution, if one really insists. As can be seen, the position of the arrows are in an overall good agreement with the hills in the distributions. Also, it can be noted that these hills widen with decreasing mass, which suggests that process (6.4) is important, since a sequential fragmentation would result in an increased spread in the energy of the product ions or hills. On the other hand, the hill-top of the  $NH_2^+$  energy-distribution is higher than that of the  $NH_3^+$  energy-distribution, even though  $NH_3^+$  is more abundant (giving its energy-distribution a larger background). This indicates that the process:



is more important than the fragmentation of  $NH_3^+$  for the creation of  $NH_2^+$ .

Although one could easily imagine that  $NH_x^+$  will fragmentate when hitting the cathode, this can of course not explain the measurements, since the ions which are sampled clearly do not hit the cathode! However, the fact that the hills in the energy-distributions of the  $NH_{1-3}^+$  ions are so relatively distinct, clearly does indicate that fragmentation dominates near the cathode. If it were to occur throughout the sheath, the product ions would receive a whole wide range of energies, depending on the energy of the  $NH_4^+$  ion just prior to fragmentation. Furthermore, the subsequent acceleration of the ions in the cathode sheath does not distinguish between the mass of the ions. Hence, the closer to the bulk-plasma interface fragmentation occurs, the less distinguished the energy of the different  $NH_{1-3}^+$  ions will be. Finally, it cannot be discarded that these fragmentation processes (also) take place within the Hiden EQP itself, which could equally explain the apparent systematics of the hill-tops. However, it seems unlikely that fragmentation would play a larger role in less hostile environment of the EQP than in the cathode sheath.

Though an interesting phenomena, we are not at the present able to give a clear explanation of the observed effects. Some insight, and a possible explanation, could maybe be obtained by initiating a more thorough investigation of the various processes which can occur with the species involved, and maybe some studies of what effect it has on the *measured* energy-distributions if these pro-

cesses were to take place within the Hiden EQP. The latter could, for example, be simulated with the *SIMION* code (see Sect. 2.3 p. 46).

### $H_2^+$ and $H_3^+$

Fig. 6.8 shows the energy-distributions of the  $H_2^+$  and  $H_3^+$  ions.  $H_2^+$  is clearly the most abundant, somewhat in contradiction to what was the case for the Ar- $H_2$  discharge. However, it should be mentioned that we did have some initial problems sampling the very low mass ions. It can therefore not be completely dismissed that the  $H_3^+$  fraction in reality is somewhat higher than the figure and Tab. 6.1 indicate.

## 6.4 Nitriding Experiments

[The experimental results presented in this section are contained in **Article V**: “On Nitriding of Steels”. M. Berg, C. V. Budtz-Jørgensen, H. Reitz, K. O. Schweitz, J. Chevallier, P. Kringhøj, and J. Böttiger, *Surf. Coat. Tech.*, **124**, 2000, p. 25]

### Introduction

As mentioned in the introduction to this chapter, the  $N_2$ - $H_2$  discharge is well-established as a nitriding process plasma, providing wear, fatigue and corrosion resistant surfaces. When a steel is exposed to a  $N_2$ - $H_2$  discharge at elevated temperatures ( $\sim 500^\circ\text{C}$ ), nitrogen may penetrate the surface and diffuse 20–200  $\mu\text{m}$  into the steel (diffusion zone). If the nitrogen content is sufficiently high a compound zone (3–10  $\mu\text{m}$ ) may form at the surface. For the case of a pure iron substrate, the compound zone consists of  $\gamma'$  ( $\text{Fe}_4\text{N}$ ) and  $\varepsilon$  ( $\text{Fe}_{2-3}\text{N}$ ) intermetallics as well as nitrides. It is this compound zone which enhances the various tribological properties of the nitrided steel.

In an attempt to shed some light on the atomistic processes which occur during nitriding, some experiments were performed on four different steels; construction steel (CS), stainless steel (SS), nitriding steel (NS) and a powder-metallurgical tool steel (TS). These steels differ in the type and amount of alloying (see Tab. 6.2 p. 152). The nitriding processes were performed using discharges with varying discharge parameters ( $H_2$  content, voltage, temperature and process time), and the effect of the process was in each case quantified by measuring the hardness depth-profile of the nitrided steel. From these profiles the depth of the diffusion zones could be extracted and their variation with one of the discharge parameters, namely the  $H_2$  content, could be explained on the basis of the ion energy-distributions of equivalent discharges which were measured with the Hiden EQP. It is this comparison, which constitutes my main contribution to this work, which will be presented in this section, as a relevant

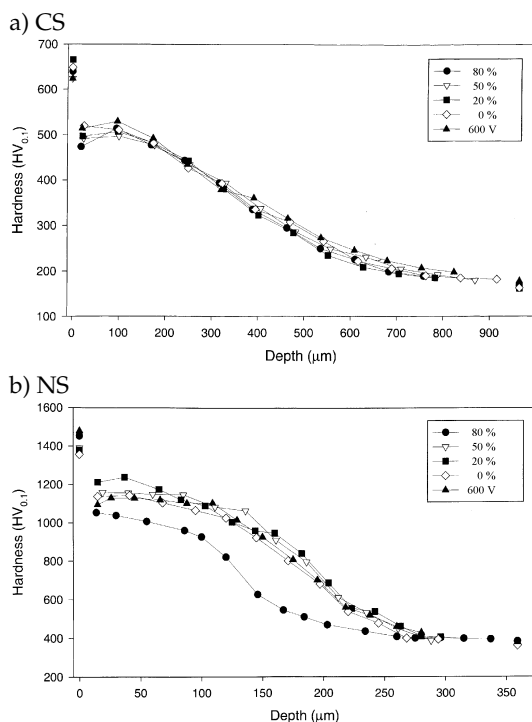


**Figure 6.9** Hardness depth-profiles for of the CS and NS steels for different  $H_2$  contents at 500 V. The 600-V curve is for a 80%  $H_2$  discharge.

example of the applicability of ion energy-distribution measurements of the  $N_2$ - $H_2$  discharge. For the full treatment of the experiments, I refer the reader to the published article.

## The nitriding process

The nitriding was performed in a commercial plasma-assisted vapour deposition (PACVD) plant made by Rübiger (Wels, Austria). See Ref. 71 for detailed description of the set-up. In the experiments presented here, a pulsed-DC voltage of  $-500$  V was used. The length of the on-pulse was kept constant at  $100 \mu s$ , while that of the off-pulse was continuously adjusted to keep the temperature constant. In addition to plasma heating, heaters were fitted to the walls of the chamber. The temperature of the substrates was monitored using a thermocouple and kept at  $525^\circ C$ . The pressure of the process gas ( $N_2$ - $H_2$ ) was kept constant at 1 mbar. For each steel, a nitriding process was performed with a different  $H_2$  content (0%, 20%, 50% and 80%). Before nitriding, the various steels were cut

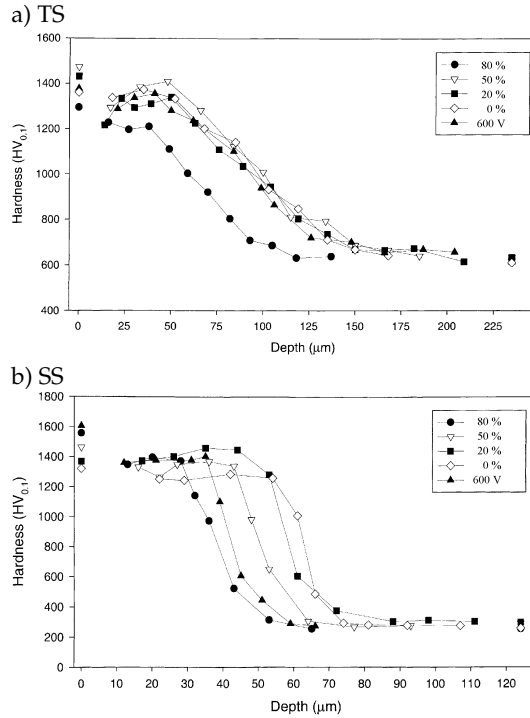


**Figure 6.10** Hardness depth-profiles for of the TS and SS steels for different H<sub>2</sub> contents at 500 V. The 600-V curve is for a 80% H<sub>2</sub> discharge.

into 3-mm thick discs with a diameter of 10 mm, after which they were polished to reflection. The steels were processed in the nitriding chamber for a period of 15 hours, during which the discharge current and the length of the off-pulse was constantly monitored, so that the total integrated current the samples had received could be determined.

### Hardness depth-profiles

After nitriding the hardness depth-profiles of the samples were measured with a commercial Vickers hardness micro-indenter, using cross-sectional nitrided steel samples. The Vickers hardness is defined as  $HV = P/M$  where  $P$  is the indent load and  $M$  is the area of the indentation created with the diamond square pyramid (136° apex angle) indentation head. Diamond, for example, has a Vickers hardness of  $HV = 10\,000$ . For these measurements an indent load of  $P = 0.1$  kg was used (hence, the notation  $HV_{0.1}$ ). The results are shown in Fig. 6.9 for the CS and NS steels and in Fig. 6.10 for the TS and SS steels. Also shown are the surface

STEEL	DEPTH ( $\mu\text{m}$ )	ALLOYS-%	ELEMENTS
CS	400	0.24	C, Al
NS	127	4.30–5.67	C, Cr, Mo, Ni, Al
TS	75	14.65	C, Cr, Mo, V
SS	40	29.5–35.0	C, Cr, Mo, Ni

**Table 6.2** Nitrogen penetration depth, the amount of alloying in weight-% and the alloying elements of the four nitrided steels.

hardnesses which, owing to the compound zones, are significantly higher than the hardnesses of the diffusion zones. It is the extent of the diffusion zones, however, which we shall be considering here. Independent Scanning Electron Microscopy (SEM) measurements [72] of the nitrogen concentration versus depth in the various steels have showed that the Vickers hardness in the diffusion zone was proportional to the nitrogen concentration. Hence, the hardness-depth profiles (in the diffusion zone) may also be viewed upon as nitrogen depth-profiles.

*The CS steel.* In Fig. 6.9a it is seen that the hardness profiles of the CS steels were insensitive to the  $H_2$  content of the discharge. As we shall see in a moment, the number of nitrogen atoms penetrating the surface must change with varying  $H_2$  content. Hence, this indicates that the nitrogen intake in this case is diffusion limited, and not limited by the supply of nitrogen through the surface. For all discharges, the nitrogen intake is saturated.

*The NS steel.* For the NS-steel case, shown in Fig. 6.9b, a suppression of the nitrogen intake is seen in the 80%- $H_2$  case, while the remaining profiles are seen to be saturated. Since both the nitrogen concentration (the hardness) and penetration depth are smaller in the 80%- $H_2$  case, this indicates that the nitrogen surface penetration has decreased in this case. Hence, in this case the nitrogen intake saturation level is located between a 50% and 80%  $H_2$  content of the discharge.

*The TS steel.* For the TS steel, the results of which are shown in Fig. 6.10a, a similar effect as for the NS steel is observed. All the hardness profiles are saturated except for the discharge with the highest  $H_2$  content (80%). As with the NS steel, nitrogen intake saturation is located between a 50% and 80%  $H_2$  content of the discharge.

*The SS steel.* In this case, shown in Fig. 6.10b, only the 0% and 20%  $H_2$  content discharges have saturated the nitrogen intake. The 50%  $H_2$  content discharge yields a limited nitrogen intake, and the 80%  $H_2$ -case even more so. Hence, for this steel the saturation level occurs between a 20% and 50%  $H_2$  content of the discharge.

The different behaviours of the steels can be understood from Tab. 6.2, which

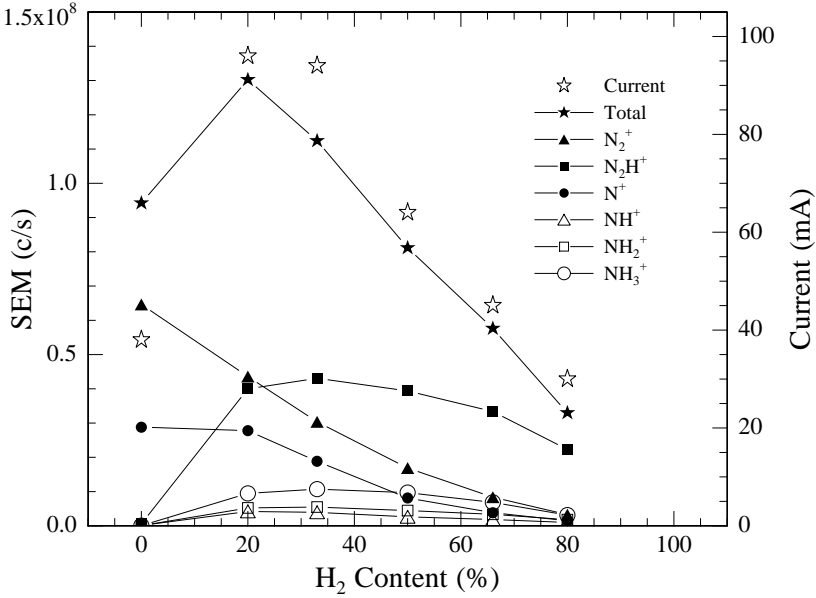


**Figure 6.11** Integrated ion energy-distributions (measured) of a N<sub>2</sub>-H<sub>2</sub> discharge driven at a voltage of -500 V and a pressure of 0.37 mbar as a function of H<sub>2</sub> content (—). Also shown is the measured discharge current (open stars).

shows the nitrogen penetration depth and the alloying constituents of the various steels. As can be seen, the penetration depth decreases with an increasing amount of alloying elements. This effect can be explained by the more efficient trapping of nitrogen diffusing into the steels by the alloy elements present in the steel.

**Hidden measurements — ion energy doses**

The N<sub>2</sub>-H<sub>2</sub> discharges which had been used for the nitriding experiments were investigated in the Hidden plasma chamber. Since only room-temperature is obtainable in the Hidden chamber, the gas pressure was adjusted so as to ensure an equal gas density as was used for the nitriding experiments; a pressure of 1.00 mbar at 525°C is (density-wise) equivalent to a pressure of 0.37 mbar at room-temperature.

Fig. 6.11 shows the areas of the energy-distributions of the various ions which impinge on the cathode, as a function of H<sub>2</sub> content. These were calculated by integrating the energy-distributions. From the figure it can be seen

that the addition of 20% H<sub>2</sub> has no effect on the N<sup>+</sup> intensity while the N<sub>2</sub><sup>+</sup> intensity drops significantly. This drop could be partly explained by vast amount of N<sub>2</sub>H<sup>+</sup> which is formed. As with the Ar-H<sub>2</sub> discharge, a H<sub>2</sub> content of 20% yields the optimum plasma intensity. For higher percentages the N<sup>+</sup> and N<sub>2</sub><sup>+</sup> intensity drops while the N<sub>2</sub>H<sup>+</sup> intensity remains comparatively constant. Also shown are the NH<sub>1-3</sub><sup>+</sup> ions, which are seen to constitute a small fraction of the total ion intensity. The NH<sub>4</sub><sup>+</sup>, H<sub>2</sub><sup>+</sup> and H<sub>3</sub><sup>+</sup> ions were not measured in these experiments.<sup>2</sup> The hydrogen ions do of course not contribute to the nitrogen intake, and the NH<sub>4</sub><sup>+</sup> ions do not contribute significantly to the total energy flux towards the cathode (see Tab. 6.1 for the 20%-H<sub>2</sub> case). Hence, it is justifiable that their presence may be neglected when considering the nitrogen-bombardment efficiency of the discharge. Also shown in the figure, however, is the measured discharge current. For the discharges with non-zero H<sub>2</sub> content the envelopes of the total ion intensity and the current are in good agreement with each other, while the total ion intensity of the pure discharge seems to be overestimated. Or, equivalently, the H<sub>2</sub>-containing intensities are underestimated, which (at least partly) can be explained by the deficiency of the previously mentioned ions (for the 20%-H<sub>2</sub> case, NH<sub>4</sub><sup>+</sup>, H<sub>2</sub><sup>+</sup> and H<sub>3</sub><sup>+</sup> constitute about 8% of the total ion intensity, which is clearly not enough to fully explain the discrepancy).

To compare the Hiden measurements with the nitriding experiments, it is necessary to obtain a measure of the energy deposited on the cathode by each individual nitrogen ion species, *i*. Hence, the following integral was calculated:

$$D_i = \int_{20 \text{ eV}}^{\infty} f_i(E) E \, dE, \quad (6.6)$$

where  $f_i(E)$  is the measured energy distribution of ion *i*. The contribution below 20 eV was omitted because of the problems with performing representative sampling at low energies. In any case, this part of the energy-distribution does obviously not contribute significantly to the integral. As a measure of the total deposited energy on the cathode *per ion*, DE, the  $D_i$  values were summed for all ions and normalized by dividing with the discharge current. The reason for not normalizing to the areas is that, as already mentioned, not all the ions of the discharge are represented by the energy-distribution measurements. Although these ions are not expected to be contributing to the nitrogen energy bombardment at the cathode, they do of course contribute to the total discharge current. Since the total ion bombardment of the steel samples in the nitriding experiments is quantified in terms of the integrated (Rübig) discharge current,  $\hat{Q}$ , the discharge current of the Hiden measurements is the most adequate normalization for DE. The  $D_i$  and DE-values calculated in this way are shown in Fig. 6.12 as a function of H<sub>2</sub> content. Now, the hardness-profiles of Figs. 6.9 and 6.10 can of course

<sup>2</sup>This does not, however, mean that they were not present.

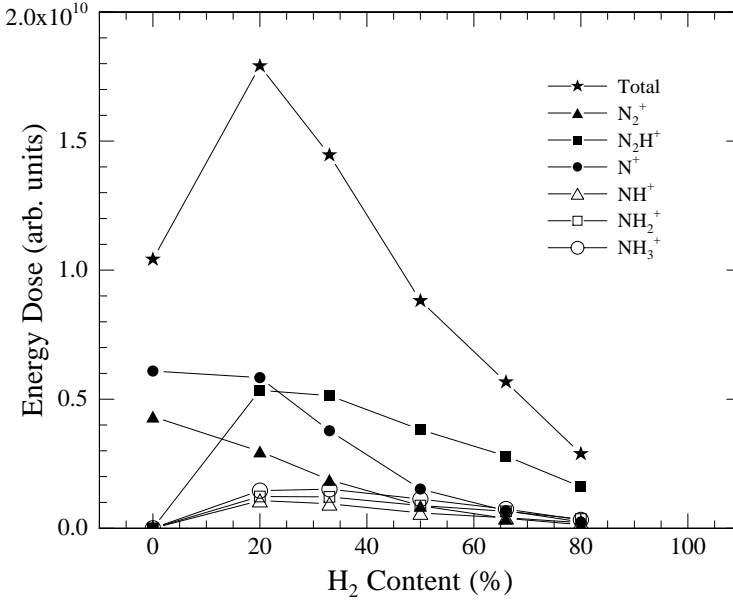


**Figure 6.12** The integrated energy-weighted ion energy-distributions,  $D_i$ , as calculated using Eq. (6.6) and their summed values, DE (—★—). See Fig. 6.11 for details.

not be normalized to (i.e., divided by) the integrated discharge current,  $\tilde{Q}$ . Instead, the DE-values were multiplied by  $\tilde{Q}$ , so that a measure of the total energy deposited *during the nitriding processes* was obtained. The effective deposited energy values obtained in this way are shown in Fig. 6.13 as a function of H<sub>2</sub> content. Note that the order of which the discharges have the highest total energy dose per ion is the same in Figs. 6.12 and 6.13. Hence, any conclusions made on the basis of Fig. 6.13 (which is specific to the actual nitriding experiments presented here) may be generalized.

## Discussion

From Fig. 6.13 it is seen that the total amount of energy deposited by nitrogen ions during the nitriding process increases with decreasing H<sub>2</sub> content of the discharge until a H<sub>2</sub> content of 20% is reached. After this optimum DE drops significantly at 0% H<sub>2</sub>. Also shown in the figure, is an indication of where the saturation level is located for the four nitrided steels. Below the saturation level, nitrogen surface-penetration is limiting the nitrogen intake while above the saturation level it is diffusion limited. For the CS steel all the discharges

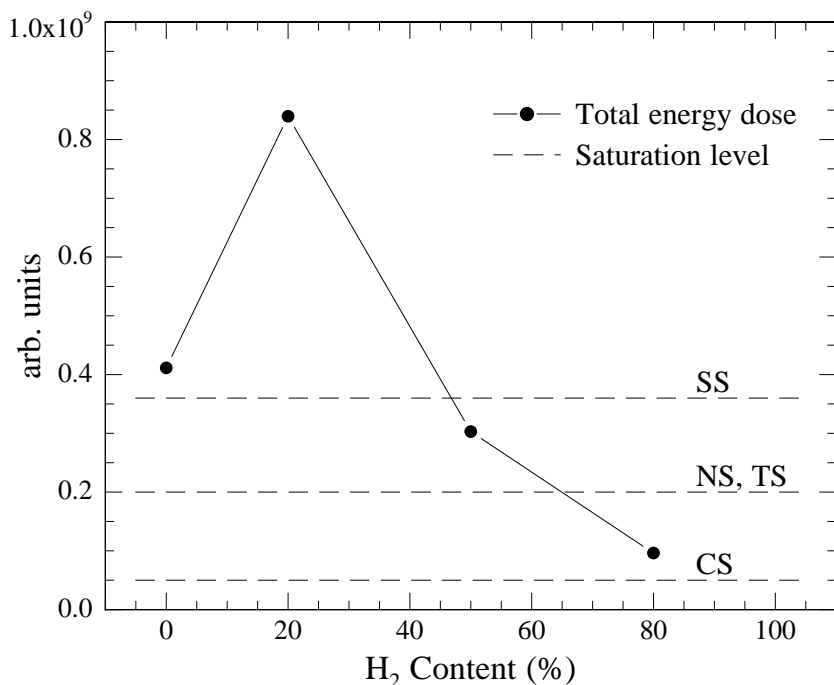


**Figure 6.13** Total ion energy dose as a function of  $H_2$  content (—●—) and an indication of the saturation level of the SS, NS, TS and CS steels (—).

saturated the nitrogen intake. For the NS and TS steels, however, the 80%  $H_2$  discharge did not saturate the nitrogen intake, which can be explained by the lower amount of deposited energy of this discharge. And for the SS steel, the 50%  $H_2$  discharge did also not lead to saturation of the nitrogen intake, which can be explained by the lower energy deposited by the 50%  $H_2$  discharge than the 0% and 20% discharges. Hence, since the DE-values depicted in the figure are a measure of the mean energy of the nitrogen ions impinging on the cathode, it can be concluded that the nitrogen intake correlates directly with the mean energy of the nitrogen ions of the discharge. Furthermore, the 20%- $H_2$  discharge can be seen to be the most efficient discharge for nitriding in general,<sup>3</sup> and for the four steels investigated here, a discharge with 0%  $H_2$  content is equally good. Hence, in these cases, hydrogen is essentially not necessary. In contrast to the correlation with mean ion energy, an increase in discharge current-density did

<sup>3</sup>Just like a  $Ar$ - $H_2$  discharge with 5–20%  $H_2$  content is the optimal discharge for physical sputtering (see Chap. 4).

not always result in a larger penetration depth (or saturation). For example, the current-density of the 0% H<sub>2</sub> discharge (0.35 mA/cm<sup>2</sup>) was lower than that of the 50% H<sub>2</sub> discharge (0.53 mA/cm<sup>2</sup>), although the penetration depth of the SS steel at 0% H<sub>2</sub> was larger than for the 50%-H<sub>2</sub> discharge.

## 6.5 Summary

In the first part of this chapter, ion energy-distribution measurements of N<sub>2</sub> and N<sub>2</sub>-H<sub>2</sub> discharges were presented. For the N<sub>2</sub> discharge, which is still comparatively simple, the N<sup>+</sup> and N<sub>2</sub><sup>+</sup> energy-distributions were sought qualitatively explained within the formalism of the Davis and Vanderslice model, although no final conclusions could be made. Ignoring the generation of N<sub>2</sub><sup>+</sup> in the sheath, these ions should be fully characterized by the Davis and Vanderslice energy-distribution function, which indeed seemed to be the case for the high-energy ions. The low-energy part of the energy-distribution was, however, clearly underestimated by the Davis and Vanderslice energy distribution, indicating that some source of N<sub>2</sub><sup>+</sup> ion generation exists. As discussed, a reasonable candidate for these are the N<sup>+</sup> ions, which produce N<sub>2</sub><sup>+</sup> via charge transfer with N<sub>2</sub>. The N<sub>2</sub>-H<sub>2</sub> discharge is a rather more complicated case, with 8 major ionic species at the cathode. Although no attempt was made to explain the energy-distributions of these ions, these energy-distribution were, in the latter part of this chapter, used to understand a series of nitriding experiments performed on four different steels using N<sub>2</sub>-H<sub>2</sub> discharges at varying H<sub>2</sub> content. By measuring the hardness depth-profiles, which are a direct indication of the nitrogen content, and interpreting these in the light of the measured ion energy-distributions, it could be concluded that the nitrogen intake may be directly correlated to the mean energy of the ions at the cathode.



---

# SUMMARY

---

The aim of the work which has been presented in this thesis, was to initiate an investigation of the basic physics of glow-discharges used for surface processing techniques, and to correlate this with the actual effects these discharges have on the surfaces which are exposed to them. This was done using an ion energy and mass analyzer to determine the ionic species at the cathode and their energy-distribution. As such, it is an attempt to combine the knowledge of the basic physics of plasmas with the knowledge of surface processes on an atomistic level, in a pursuit to deepen the understanding and contribute to the ongoing improvement of these surface enhancement techniques.

The thesis contains both investigations which are concerned with the basic physics of plasmas, and those which are more a direct measurement of the effects of samples exposed to specific glow-discharges. In all cases, however, both perspectives were sought to be combined. Either by estimating the practical implications or applications of an observed basic property of the plasma, or by discussing an observed plasma-surface interaction and its dependence on the process parameters in the light of the basic physics of the discharge.

## The argon discharge

This discharge is one of the simplest of glow-discharges, and hence served as a good subject for an investigation of the basic physics which was reviewed in Chap. 1. The main interest of this work is the energy-distribution of the particles at the cathode. These energy-distributions are, for the case of a simple mono-atomic discharge, adequately described by the Davis and Vanderslice model, despite the fact that not all the assumptions of the model are essentially valid. Nevertheless, as was discussed in Chap. 3, all attempts at improving the model reported in the literature, although yielding more solidly founded models, have not significantly altered the energy-distribution of the ions at the cathode. Using the high sensitivity of the Hiden EQP, this was verified to a high degree of precision (5 decades) for an argon discharge in a voltage range of 340–325 V and a pressure range of 0.14–1.00 mbar, despite the very low energies of the ions at the cathode (cf. the problem of representative sampling at low energies). From these energy-distribution measurements the defining parameter of the Davis and Vanderslice distribution,  $s/\lambda$ , where  $s$  is the cathode-sheath thickness and  $\lambda$  is the mean-free-path for ion-neutral collisions, could be extracted. Using the Child law for a collisional sheath in conjunction with the basic param-

eters of the discharge (voltage, pressure and current-density), the cross-section for  $\text{Ar}^+$  symmetrical charge-exchange could be extracted from a series of  $s/\lambda$ -values, yielding a value which was in good accordance with literature. This served both as a further quantitative justification of the Davis and Vanderslice model and the applicability of the Child law in this respect. Furthermore, the practical use of the Davis and Vanderslice distribution in combination with the Child law to predict the energy-distributions of a discharge with a given set of parameters was discussed.

### The Ar-H<sub>2</sub> discharge and sputtering

The Ar-H<sub>2</sub> discharge is widely used as an in-situ pre-deposition surface cleaning process. Measurements of the ion energy-distribution of the dominant ions at the cathode of this discharge were presented, and the effect of hydrogen for the physics of the discharge was discussed. Clearly, adding even small amounts of hydrogen drastically increases the plasma intensity and discharge current compared to a pure argon discharge. It is, however, not quite clear what the reason for this increase is. Most evidence from the literature points in the direction of a *decrease* in plasma intensity upon the addition of hydrogen to an argon discharge. Nevertheless, the observed effect was quite clear. This was also evident from the sputtering experiments performed on gold and aluminium samples. For the case of gold, a drastic increase in sputtering was observed upon the addition of hydrogen, mimicking the increase in overall plasma intensity. This increase in sputtering was mainly due to the vast amount of highly energetic  $\text{ArH}^+$  ions formed in this discharge. As opposed to  $\text{Ar}^+$ ,  $\text{ArH}^+$  does not have a neutral counterpart to symmetrically charge exchange with, thus resulting in a far lower mean number of collisions on its way towards the cathode. The optimal hydrogen content for sputtering in this case was a 5–20%. Furthermore, the dependency of the sputtering efficiency as a function of hydrogen content could be adequately described by the measured ion energy-distribution, assuming a purely physical sputtering process. Hence, it could be concluded that only physical sputtering is taking place during Ar-H<sub>2</sub> sputtering of gold. For the case of the aluminium samples, the addition of hydrogen also drastically increased the measured sputtering efficiency. However, the optimal hydrogen content in this case was 80%, while a purely physical sputtering model, based again on measured energy-distributions, predict an optimum at 20%, as for gold. Hence, it was concluded that chemical sputtering is dominating Ar-H<sub>2</sub> sputtering of aluminium, through direct chemical sputtering by reactive hydrogenic species and/or chemically enhanced physical sputtering. The observed effects can be understood from that fact that tightly bound oxides ( $\text{Al}_2\text{O}_3$ ) form on the Al samples because of the relatively high partial oxygen pressure of the sputtering atmosphere, thus drastically reducing the physical sputtering yield of Al atoms. It is suggested that these oxides are (preferentially) removed by the hydrogenic

species, thus explaining the observed importance of a high hydrogen content in the discharge.

### **Anode sputtering in pulsed plasmas**

Most DC glow-discharges used for practical surface processing techniques are pulsed. This allows one to control the power of the discharge by varying the pulse times, without changing the basic parameters of the discharge (e.g., the voltage). An investigation on what effect this pulsing has on the anode of the discharge was presented, showing that, during the onset of the off-pulse, the anode is bombarded by ions with energies of up to several hundred eV. This was directly verified by ion energy-distribution measurements performed at the anode. The origin of these ions was shown to be the creation of a high positive plasma potential when the boundary conditions of the discharge are suddenly changed (i.e., when the cathode is grounded). The reason for this is, that the inertia of the charged particles – both electrons and ions – constituting the plasma, prohibits an equally instantaneous redistribution of charge, thus forcing an increase of the plasma potential so as to comply with the boundary conditions of the off pulse. These findings were supported by floating anode potential measurements and computer simulations of a pulsed-DC glow-discharge. During the decay of this highly unstable potential, ions in the vicinity of the anode are attracted towards it, thus bombarding it with high energies. Although a small effect compared to the ion bombardment of the cathode during the on-pulse, the degree of anode material sputtering was estimated to be 0.1–1% of that of cathode material sputtering, and with an increasing fraction with increasing discharge voltage. Depending on the purity requirements of practical application pulsed-DC glow-discharges, this effect should be considered.

### **The N<sub>2</sub> and N<sub>2</sub>-H<sub>2</sub> discharges and nitriding**

Ion energy-distributions of the N<sub>2</sub> and N<sub>2</sub>-H<sub>2</sub> discharges were presented. For the relatively simple N<sub>2</sub> discharge, the measured ion energy-distributions of the N<sup>+</sup> and N<sub>2</sub><sup>+</sup> ions were sought interpreted within the formalism of the simple Davis and Vanderslice model. Although, essentially, this model is not adequate for describing the acceleration of the ions in the sheath of a N<sub>2</sub> discharge, the discrepancies between the model and the measured energy-distributions gave some further insight of what additional processes are important in defining these energy-distributions. The N<sub>2</sub>-H<sub>2</sub> discharge is even more complicated, with 8 major ionic species present at the cathode. This discharge is used in the industry for plasma-assisted nitriding of steels. A series of nitriding experiments using four different steels were presented. It was shown that, for these four steels, the addition of hydrogen was not necessary in order to achieve nitrogen intake

saturation. Furthermore, saturation was not achieved for all steels if the hydrogen content was too high. This could be explained using ion energy-distribution measurements of similar  $N_2$ - $H_2$  discharges as were used in the nitriding experiments, which showed the optimal hydrogen content for nitriding to be 20% (quantified in terms of the mean energy per bombarding ion). These data also showed the pure nitrogen discharge to have a higher mean energy per ion than the 50% and 80%  $H_2$  discharges. Thus, it could be concluded that the nitrogen intake of these steels during the nitriding process correlated directly with the mean energy of the bombarding ions.

---

# A

---

## EXPERIMENTAL NOTES

---

During my work here, some practical experience has been gained with using the Hiden EQP. In this appendix some of the essentials of this knowledge will be briefly reviewed, so as to ease the initial phases of the work a successor to me in this respect might have. This presentation is mainly concerned with what approach one should take when acquiring ion energy-distributions with the EQP. Also, some practical notes are given on changing the inner orifice, evaporating film on to it and how small samples are best attached to the electrodes of the discharge chamber.

### A.1 Hiden EQP Data Acquisition

This section assumes that the reader is familiar with the Hiden equipment and the Hiden manual.

Tuning the mass spectrometer only has to be done if the EQP has been out of use for a prolonged amount of time, or some major alterations have been made to the equipment itself. Most notably, the low mass area (1–10 amu) is quite sensitive to the mass tuning parameters; masses 2 and 3 require frequent tuning, at least just to make sure they are still there.

In practice, it is a good idea to tune the Lens1, Lens2, Horiz and Vert voltages (see Fig. A.2) of the Hiden EQP before every session (i.e., on a daily basis). This should be done for every single mass which is to be sampled. The tune parameters can be saved when a tuning is finished, and loaded into a given scan profile using the "File/Import" option in the menu. Thus, each mass has its own tune environment. The higher the mass, the less important it is to make separate tunes, i.e., for masses 40 and 41 (e.g., Ar<sup>+</sup> and ArH<sup>+</sup>) the same tuning environment may be used. Especially, however, the tunes for masses 2 and 3

differ strongly from each other and the higher masses (notably in the Horiz and Vert voltages). During tuning, and subsequently energy scanning, I propose the Extractor voltage to be set to about half the cathode voltage and the Energy voltage to be set to zero. The optimal choice of the Extractor voltage is however best decided upon on the basis of a couple of energy scans. Lens1 has two optima, and the one closest to 0 V should be chosen (usually  $-25$  to  $0$  V). The Lens2 optimum is typically around  $-110$  V. Also, the Focus2 voltage may be checked, but this one is usually quite insensitive (around  $-250$  V).

Finally, and rarely, the position of the EQP extractor head can be optimized upon via the three bolts near the  $45^\circ$  bend which hold the RF-head. This is best done while performing a MID-scan with Massoft of a specific ion at a specific energy. However, it should be noted, that in many cases the optimum position of the extractor head depends on the energy which is monitored. As opposed to the beam-optics of the EQP, it is the high-energy ions which are most sensitive to this positioning of the extractor, since the beam-optics section cannot redirect them to the same extent as the low energy ions. Hence, it is suggested that this type of extractor head optimization is performed with relatively high energy ions.

As mentioned in Sect. 2.3, it is not recommended to use the energy scan method which is proposed in the Hiden manual, which consists of breaking up an energy spectra in 200 eV bits by changing the Reference voltage (see Fig. A.1) and performing the actual energy scan by scanning the Energy parameter with Massoft. I propose that the Energy is kept fixed at, for example,  $0$  V (effectively taking it out of function), and that an energy-spectra is acquired by scanning the Reference voltage. As already mentioned, the optimal choice of for the Extractor voltage seems to be about half of the cathode voltage. If the Extractor value is too low, sampling problems arise in the high-energy part of the spectra, while the opposite is the case, although to a somewhat lesser extent, if the Extractor voltage is too high. The actual choice thus depends on what region of the energy-distribution of the ions sampled is dominant. In general, however, and from an experimental point of view, it is best to use the same Reference voltage value for a set of measurements having equal cathode voltage, if a comparison between these is to be made.

## A.2 Changing the Electrode Material

The inner part of the fixed electrode may be detached by unscrewing the 6 screws (see Fig. 2.3 on p. 36). This allows one to change the orifice size used. Also, by evaporating in thin film onto it, part of the cathode material may be changed, thus allowing ion energy-distribution measurement of discharges of arbitrary cathode material. Naturally, in doing this, one has to consider to what extent these energy-distributions are affected by the fact that the outer part of

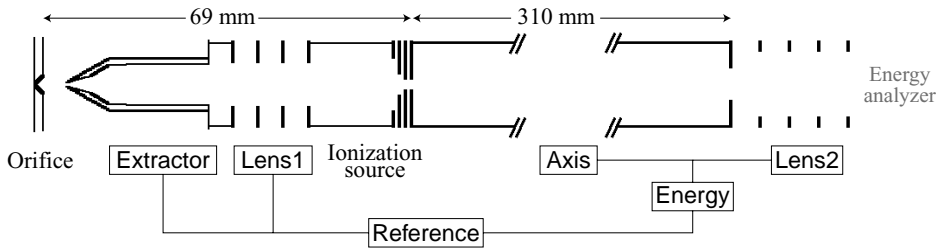


**Figure A.1** The electrode configuration of the Hidden EQP beam-optics section the voltages used when performing energy scans. More information in Chap. 2.3.

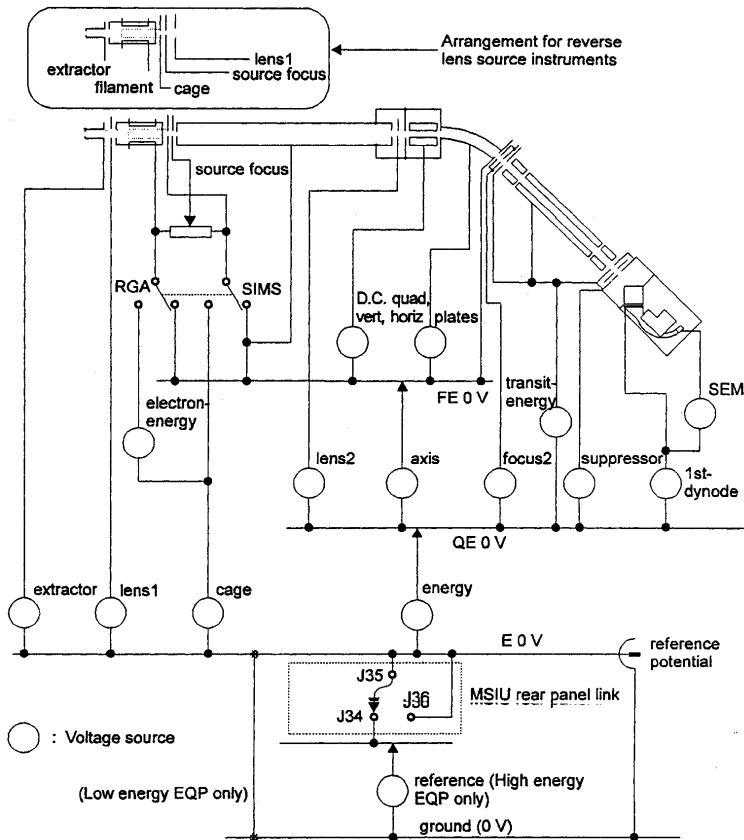


**Figure A.2** Diagram of the electrode connects within the Hidden EQP. Taken for the Hidden manual.

the cathode is still made of stainless steel. This can partly be done by visual inspection of the glow region, and determining how homogeneous its light emission is. However, because of the small size of the orifice, one would not expect this to have a major effect on the energy-distribution. It does, however, naturally have a major effect on the *discharge*, since, for example, the current-density of a dual-component cathode will not be the same as a single-component discharge. This in itself does of course alter the energy-distributions, since a change in current-density results in a change of the sheath thickness. Hence, although the measured energy-distributions are characteristic of the electrode material of the inner electrode, they are not the ones one would acquire if the entire cathode was made of the given material.

A way to investigate a discharge with an entirely different cathode material, thus being able to measure, e.g., the current-density and breakdown voltages characteristic of the material, is to attach a disc of the desired material to the movable electrode, and using the movable electrode as the discharge cathode. This was successfully done using stainless steel discs of equal dimension as the movable electrode (circular with a diameter of 12 cm), which had either Al or Au films evaporated on to them. To ensure good adhesion between the disc and the electrode, a number of small pieces of vacuum-resistant bi-sticking tape was used.<sup>1</sup> Good electrical contact can be assured by applying adequate amounts of silver-paste between the disc and the electrode.

### A.3 Sample Attachment

In a similar way small samples were attached to one of the electrodes. In this case, the silver-paste is usually adequate for good adhesion as well. It is however necessary to let the silver-paste dry out for several hours before pumping the plasma chamber down to operation pressure. If this is not done, the samples usually detach themselves — probably because of small air bubbles confined within the paste. The drying process can be speeded a bit by pumping out some of the air from the chamber (but not down to  $10^{-2}$  mbar!), thus increasing the evaporation rate of the silver-paste.

---

<sup>1</sup>The ones Jacques Chevallier uses with the SEM — confer with him about it if possible.

---

# REFERENCES

---

The last line of each entry refers to the page(s) of reference in the thesis.

- [1] J. E. Green.  
*Low-Energy Ion/Surface Interactions During Crystal Growth from the Vapor Phase: Effects on Nucleation and Growth, Defect Creation and Annihilation, Microstructure Evolution, and Synthesis of Metastable Phases.*  
In D. T. J. Hurle (editor), *Handbook of Crystal Growth (Vol. 1)*. Elsevier Science Publishers, Amsterdam, 1993.  
1, 2
- [2] W. Ensinger.  
*Low energy ion assist during deposition — an effective tool for controlling thin film microstructure.*  
*Nucl. Instr. Meth. B*, **127/128**, (1997), p. 796.  
1
- [3] W. Ensinger.  
*On the mechanism of crystal growth orientation of ion beam assisted deposited thin films.*  
*Nucl. Instr. Meth. B*, **142**, (1995), p. 796.  
1
- [4] K. O. Schweitz, J. Arnt, J. Böttiger, and J. Chevalier.  
*The dependence of stress in IBAD films on the ion-irradiation energy and flux.*  
*Nucl. Instr. Meth.*, **127/128**, (1997), p. 809.  
1
- [5] T. C. Huang, G. Lim, F. Parmigiani, and E. Kay.  
*Effect of ion bombardment during deposition on the X-ray microstructure of thin silver films.*  
*J. Vac. Sci. Tech. A*, **3** (6), (1985), pp. 2161–2166.  
1
- [6] L. Hultman, U. Helmersson, S. A. Barnett, J. E. Sundgren, and J. E. Greene.  
*Low-energy ion irradiation during film growth for reducing defect densities in epitaxial TiN(100) films deposited by reactive-magnetron sputtering.*  
*J. Appl. Phys.*, **61** (2), (1987), pp. 552–555.  
2
- [7] L. Hultman, S. A. Barnett, J. E. Sundgren, and J. E. Greene.  
*Growth of epitaxial TiN films deposited on MgO(100) by reactive magnetron sputtering: the role of low-energy ion irradiation during deposition.*  
*J. Cryst. Growth*, **92** (3–4), (1988), pp. 639–656.  
2
- [8] "plasma" *Encyclopædia Britannica Online*.  
<<http://www.eb.com:180/bol/topic?eu=119057&sctn=1>>.

- [Accessed October 9 2000].  
5
- [9] M. A. Lieberman and A. J. Lichtenberg.  
*Principles of Plasma Discharges and Materials Processing*.  
John Wiley & Sons, 1994.  
7, 8, 12, 13, 17, 19, 58, 128
- [10] A. V. Phelps.  
*The Application of Scattering Cross Sections to Ion Flux Models in Discharge Systems*.  
*J. Appl. Phys.*, **76** (2), (1994), pp. 747–753.  
10, 57, 90
- [11] A. V. Phelps.  
*Cross Sections and Swarm Coefficients for Nitrogen Ions in N<sub>2</sub> and Argon Ions and Neutrals in Ar for Energies from 0.1 eV to 10 keV*.  
*J. Phys. Chem. Ref. Data*, **20** (3), (1991), p. 557.  
10, 68, 70, 140
- [12] B. Chapman.  
*Glow Discharge Processes: Sputtering and Plasma Etching*.  
John Wiley & Sons, 1980.  
17, 57, 83, 105
- [13] V. Vahedi, M. A. Lieberman, M. V. Alves, J. P. Verboncoeur, and C. K. Birdsall.  
*A one-dimensional collisional model for plasma-immersion ion implantation*.  
*J. Appl. Phys.*, **69** (4), (1991), p. 2008.  
19
- [14] N. Jelić, R. Schrittwieser, and S. Kuhn.  
*Revised generalized Child-Langmuir law*.  
*Phys. Lett. A*, **246**, (1998), p. 318.  
19
- [15] W. D. Davis and T. A. Vanderslice.  
*Ion energies at the cathode of a glow discharge*.  
*Phys. Rev.*, **131**, (1963), p. 219.  
or *Proc. R. Soc. A*, **137**, 1963, p. 662.  
20, 55, 56, 61, 92, 124
- [16] K. Rickards.  
*Energies of particles at the cathode of a glow discharge*.  
*Vacuum*, **34** (5), (1984), p. 559.  
20, 59
- [17] Z. Wroński.  
*Ion energy distributions in a special glow-discharge source*.  
*Vacuum*, **36** (6), (1986), pp. 329–335.  
22
- [18] G. G. Lister.  
*Low-pressure gas discharge modelling*.  
*J. Phys. D*, **25** (12), (1992), pp. 1649–1680.  
24
- [19] J. P. Verboncoeur, M. V. Alves, V. Vahedi, and C. K. Birdsall.

- Simultaneous Potential and Circuit Solution for 1D Bounded Plasma Particle Simulation Codes.*  
*J. Comput. Phys.*, **104** (2), (1993), p. 321.  
[24](#)
- [20] V. Vahedi, R. W. Stewart, and M. A. Lieberman.  
*Analytic model of the ion angular distribution in a collisional sheath.*  
*J. Vac. Sci. Technol. A*, **11** (4), (1993), p. 1275.  
[24](#)
- [21] V. Vahedi and M. Suranda.  
*A Monte Carlo collision model for the particle-in-cell method: applications to argon and oxygen discharges.*  
*Comput. Phys. Comm.*, **87** (1–2), (1995), p. 179.  
[24](#), [25](#)
- [22] C. K. Birdsall and A. B. Langdon.  
*Plasma Physics via Computer Simulations.*  
Adam Hilger, IOP Publishing, Bristol, 1991.  
[24](#)
- [23] Plasma Theory and Simulation Group at University of California, Berkeley.  
*xpdp1 v. 3.5 plasma simulation software.*  
For more information see <<http://ptsg.eecs.berkeley.edu>>.  
[24](#)
- [24] K. S. Mogensen.  
*Deposition of TiN Coatings Using Pulsed DC PACVD — Plasma Investigations and Coating Characterization.*  
Ph.d. thesis, University of Aarhus, Institute of Physics and Astronomy, 1997.  
[24](#)
- [25] A. V. Phelps and Z. Lj. Petrović.  
*Cold-cathode discharges and breakdown in argon: surface gas phase production of secondary electrons.*  
*Plasma Sources Sci. Technol.*, **8**, (1999), pp. R21–R44.  
[27](#), [83](#)
- [26] Hiden Analytical Ltd., Warrington, England.  
*Handbook of Plasma Diagnostics.*  
[38](#)
- [27] J. D. Swift and H. J. R. Schwar.  
*Electrical Probes for Plasma Diagnostics.*  
Iliffe, London, 1970.  
[38](#)
- [28] M. Konuma.  
*Film Deposition by Plasma Techniques.*  
Springer-Verlag, Berlin, 1992.  
[38](#), [83](#)
- [29] D. A. Dahl.  
*SIMION 3D Version 6.0.*

- In *43rd ASMS Conference on Mass Spectrometry and Allied Topics*. Atlanta, Georgia, May 21–26 1995.  
For information on SIMION see <<http://www.sisweb.com>>.  
46, 95
- [30] L. C. Feldman and J. W. Mayer.  
*Fundamentals of Surface and Thin Film Analysis*.  
North-Holland, Elsevier Science, Amsterdam, 1986.  
52, 78
- [31] L. R. Doolittle.  
*Algorithms for the Rapid Simulation of Rutherford Backscattering Spectra*.  
*Nucl. Inst. Meth.*, **B9**, (1985), p. 344.  
For information and RUMP download service see <<http://www.genplot.com>>.  
54
- [32] L. R. Doolittle.  
*A Semiautomatic Algorithm for Rutherford Backscattering Analysis*.  
*Nucl. Inst. Meth.*, **B15**, (1986), p. 227.  
54
- [33] Z. Wroński, J. L. Sullivan, and S. O. Saied.  
*Energy distribution of heavy particles generated in the cathode fall of glow discharge*.  
*J. Phys. D*, **25**, (1992), pp. 1607–1615.  
58, 59, 62
- [34] Z. Wroński.  
*Private Communications*.  
58, 59
- [35] J. C. Moreno-Marín, I. Abril, and R. Garcia-Molina.  
*Radial profile of energetic particles bombarding the substrate in a glow discharge*.  
*J. Vac. Sci. Technol. A*, **17** (2), (1999), p. 528.  
58, 62, 63
- [36] J. E. Houston and J. E. Uhl.  
*A Characterization of the Ionic Species Incident on the Cathode of a Glow Discharge*.  
Sandia Research Report SC-RR-71-0122, Sandia Laboratories, Albuquerque (New Mexico, USA), 1971.  
59, 60, 61
- [37] M. Quast, P. Mayr, and H-R Stock.  
*Plasma monitoring of plasma-assisted nitriding of aluminium alloys*.  
*Surf. Coat. Tech.*, **120–121**, (1999), pp. 244–249.  
60, 61, 139
- [38] K. Riemann, U. Ehlmann, and K. Wiesemann.  
*The ion energy distribution in front of a negative wall*.  
*J. Phys. D*, **25**, (1992), pp. 620–633.  
59
- [39] A. Bogaerts and R. Gijbels.  
*Effects of adding hydrogen to an argon glow discharge: overview of relevant processes and some qualitative explanations*.  
*J. Anal. At. Spectrom.*, **15**, (2000), pp. 441–449.

- 61, 84
- [40] R. S. Mason and R. M. Allot.  
*The theory of cathodic bombardment in a glow discharge by fast neutrals.*  
*J. Phys. D*, **27**, (1994), p. 2372.  
62, 63, 92, 100, 116
- [41] I. Abril, A. Gras-Martin, and J. A. Valles-Abarca.  
*Energy distributions of particles striking the cathode in a glow discharge.*  
*Phys. Rev. A*, **28** (6), (1983), pp. 3677–8.  
62
- [42] K. S. Fancey and A. Matthews.  
*Some Fundamental Aspects of Glow Discharges in Plasma-Assisted Processes.*  
*Surf. Coat. Tech.*, **33**, (1987), pp. 17–29.  
72
- [43] K. Tsuji and K. Hirokawa.  
*Studies on chemical sputtering of silicon in Ar-H<sub>2</sub> glow discharge plasma by optical emission spectroscopy.*  
*Thin Sol. Film.*, **205**, (1991), p. 6.  
74, 108
- [44] J. Roth.  
*Chemical Sputtering.*  
In R. Behrisch (editor), *Topics in Applied Physics (Vol. 52): Sputtering by Particle Bombardment II.* Springer-Verlag, Berlin, 1983, pp. 91–141.  
75, 76, 79, 80, 108
- [45] F. L. Tabarés and D. Tafalla.  
*Sputtering of metallic walls in Ar/H<sub>2</sub> direct current glow discharges at room temperature.*  
*J. Vac. Sci. Technol. A*, **14** (6), (1996), p. 3087.  
75, 108
- [46] R. Behrisch (editor).  
*Topics in Applied Physics (Vol. 47): Sputtering by Particle Bombardment I.*  
Springer-Verlag, Berlin, 1981.  
76
- [47] Y. Yamamura and H. Tawara.  
*Energy Dependence of Ion-Induced Sputtering Yields from Monatomic Solids at Normal Incidence.*  
*Atom. Nucl. Dat. Tab.*, **62** (2), (1996), p. 149.  
77, 81, 100, 134
- [48] R. Kelly and N. Q. Lam.  
*The Sputtering of Oxides. Part I: Survey of the Experimental Results.*  
*Rad. Eff.*, **19**, (1973), p. 39.  
81, 103, 114
- [49] S. M. Sze.  
*Semiconductor Devices: Physics and Technology.*  
John Wiley & Sons, New York, 1985.  
81
- [50] C. Böhm and J. Perrin.

- Retarding-field analyzer for measurements of ion energy distributions and secondary electron emission coefficients in low-pressure radio frequency discharges.*  
*Rev. Sci. Instrum.*, **64** (1), (1992), p. 31.  
83
- [51] H. C. Straub, P. Renault, B. G. Lindsay, K. A. Smith, and R. F. Stebbings.  
*Absolute partial cross sections for electron-impact ionization of H<sub>2</sub>, N<sub>2</sub> and O<sub>2</sub> from threshold to 1000 eV.*  
*Phys. Rev. A*, **54** (3), (1996), p. 2146.  
83
- [52] J. C. Tucek, S. G. Walton, and R. L. Champion.  
*Secondary-electron and negative-ion emission from Al: Effect of oxygen coverage.*  
*Phys. Rev. B*, **53** (21), (1996), p. 14 127.  
84
- [53] R. F. G. Meulenbroeks, A. J. van Beek, A. J. G. van Helvoort, M. C. M. van der Sanden, and D. C. Schram.  
*Argon-hydrogen plasma jet investigated by active and passive spectroscopic means.*  
*Phys. Rev. E*, **49** (5), (1994), p. 4397.  
85
- [54] R. S. Mason, P. D. Miller, and I. P. Mortimer.  
*Anomalous loss of ionization in argon-hydrogen plasma studied by fast flow glow discharge mass spectrometry.*  
*Phys. Rev. E*, **55**, (1997), p. 7462.  
85
- [55] Y. Watanabe, M. Shiratani, S. Ogi, N. Kunihiro, and I. Ogawa.  
*Reincrease in electron density in the current-decaying phase of pulsed-discharge of argon-hydrogen mixture.*  
*Jap. J. Appl. Phys.*, **27** (8), (1988), pp. 1469–1476.  
85
- [56] H. S. Massey.  
*Electronic and Ionic Impact Phenomena (Vol III): Slow Collisions of Heavy Particles.*  
Oxford University Press, London, 1971.  
85
- [57] S. Peter, R. Pintaske, G. Hecht, and F. Richter.  
*Determination of mass and energy distribution of ions in glow discharges.*  
*Surf. Coat. Tech.*, **59**, (1993), p. 97.  
96
- [58] R. S. Mason and M. Pichiling.  
*Sputtering in a glow discharge source — pressure dependence: theory and experiment.*  
*J. Phys. D*, **27**, (1994), p. 2383.  
101, 116
- [59] J. Heller.  
*Reactive sputtering of metals in oxidizing atmospheres.*  
*Thin Solid Films*, **17** (2), (1973), pp. 163–176.  
103
- [60] J. F. Ziegler, J. P. Biersack, and U. Littmark.

- The Stopping and Range of Ions in Solids.*  
Pergamon Press, New York, 1985.  
See <<http://www.research.ibm.com/ionbeams>> for more information and download service.  
[105](#), [114](#)
- [61] R. Behrisch, J. Roth, J. Bohdansky, A. P. Matrinelly, B. Schweer, D. Rusbüldt, and E. Hintz.  
*Dependence of light-ion sputtering yields of iron on fluence and oxygen partial pressure.*  
*J Nucl. Mat.*, **93 & 94**, (1980), pp. 645–655.  
[105](#)
- [62] C. V. Budtz-Jørgensen, P. Kringhøj, and J. Böttiger.  
*The Critical Role of Hydrogen for Physical Sputtering with Ar-H<sub>2</sub> Glow Discharges.*  
*Surf. Coat. Tech.*, **116–119**, (1999), p. 938.  
**Article I** of this thesis (Sect. 4.4).  
[107](#), [108](#)
- [63] C. V. Budtz-Jørgensen, J. Böttiger, and P. Kringhøj.  
*Energy Spectra of Particles Bombarding the Cathode in Glow Discharges.*  
*Vacuum*, **56**, (2000), p. 9.  
**Article II** of this thesis (Chap. 3).  
[113](#), [124](#), [134](#)
- [64] C. K. Birdsall.  
*Particle-in-cell charged-particle simulations, plus Monte Carlo collisions with neutral atoms, PIC-MCC.*  
*IEEE Trans. Plasma Sci.*, **19** (2), (1991), p. 65.  
See <<http://ptsg.eecs.berkeley.edu>> for more information.  
[129](#)
- [65] H. Störi.  
*Private Communications.*  
[137](#)
- [66] M. J. Baldwin, M. P. Fewell, S. C. Haydon, S. Kumar, G. A. Collins, and K. T. Short.  
*Rf-plasma nitriding of stainless steel.*  
*Surf. Coat. Tech.*, **98** (1–3), (1998), p. 1187.  
[138](#)
- [67] F. Mahboubi, M. Samandi, D. Dunne, A. Bloyce, and T. Bell.  
*Plasma nitriding of microalloyed steel.*  
*Surf. Coat. Tech.*, **71** (2), (1995), p. 135.  
[138](#)
- [68] C. Tian and C. R. Vidal.  
*Electron impact ionization of N<sub>2</sub> and O<sub>2</sub>: contributions from different dissociation channels of multiply ionized molecules.*  
*J. Phys. B*, **31**, (1998), pp. 5369–5381.  
[138](#)
- [69] Z. Wroński and H. Murlak-Stachura.  
*The energy distributions of major ions in the cathode zone of a strongly abnormal nitrogen DC glow discharge.*

- Vacuum*, **49** (2), (1998), pp. 97–100.  
139
- [70] J. Amorim, G. Baravian, and G. Sultan.  
*Absolute density measurements of ammonia synthesized in N<sub>2</sub>-H<sub>2</sub> mixture discharges.*  
*Appl. Phys. Lett.*, **68** (14), (1996), pp. 1915–1917.  
145
- [71] K. S. Mogensen, N. B. Thomsen, S. S. Eskildsen, C. Mathiasen, and J. Böttiger.  
*A parametric study of the microstructural, mechanical and tribological properties of PACVD  
TiN coatings.*  
*Surf. Coat. Tech.*, **99**, (1998), pp. 140–146.  
150
- [72] M. Berg.  
*Plasma Nitriding.*  
Master's thesis, Institute of Physics and Astronomy, Aarhus University, Ny  
Munkegade, 8000 Århus C, Denmark, February 1999.  
152

**Comprehensive author index**

*The numbers refer to the entry in the list of references.*

- Abril, I. 35, 41  
Allot, R. M. 40  
Alves, M. V. 13, 19  
Amorim, J. 70  
Arnt, J. 4
- Baldwin, M. J. 66  
Baravian, G. 70  
Barnett, S. A. 6, 7  
Behrisch, R. 44, 46, 61  
Bell, T. 67  
Berg, M. 72  
Böhm, C. 50  
Biersack, J. P. 60  
Birdsall, C. K. 13, 19, 22, 64  
Bloyce, A. 67  
Bogaerts, A. 39  
Bohdansky, J. 61  
Böttiger, J. 4, 62, 63, 71  
Budtz-Jørgensen, C. V. 62, 63
- Champion, R. L. 52  
Chapman, B. 12  
Chevalier, J. 4  
Collins, G. A. 66
- Dahl, D. A. 29  
Davis, W. D. 15  
Doolittle, L. R. 31, 32  
Dunne, D. 67
- Ehlmann, U. 38  
Ensinger, W. 2, 3  
Eskildsen, S. S. 71
- Fancey, K. S. 42  
Feldman, L. C. 30  
Fewell, M. P. 66
- Garcia-Molina, R. 35  
Gijbels, R. 39  
Gras-Martin, A. 41  
Green, J. E. 1
- Greene, J. E. 6, 7
- Haydon, S. C. 66  
Hecht, G. 57  
Heller, J. 59  
Helmersson, U. 6  
Hintz, E. 61  
Hirokawa, K. 43  
Houston, J. E. 36  
H-R Stock 37  
Huang, T. C. 5  
Hultman, L. 6, 7  
Hurle, D. T. J. 1
- Jelić, N. 14
- Kay, E. 5  
Kelly, R. 48  
Konuma, M. 28  
Kringhøj, P. 62, 63  
Kuhn, S. 14  
Kumar, S. 66  
Kunihiro, N. 55
- Lam, N. Q. 48  
Langdon, A. B. 22  
Lichtenberg, A. J. 9  
Lieberman, M. A. 9, 13, 20  
Lim, G. 5  
Lindsay, B. G. 51  
Lister, G. G. 18  
Littmark, U. 60  
Lj. Petrović, Z. 25
- Mahboubi, F. 67  
Mason, R. S. 40, 54, 58  
Massey, H. S. 56  
Mathiasen, C. 71  
Matrinelly, A. P. 61  
Matthews, A. 42  
Mayer, J. W. 30  
Mayr, P. 37  
Meulenbroeks, R. F. G. 53  
Miller, P. D. 54  
Mogensen, K. S. 24, 71  
Moreno-Marín, J. C. 35  
Mortimer, I. P. 54

- Murlak-Stachura, H. 69
- Ogawa, I. 55  
Ogi, S. 55
- Parmigiani, F. 5  
Perrin, J. 50  
Peter, S. 57  
Phelps, A. V. 10, 11, 25  
Pichiling, M. 58  
Pintaske, R. 57
- Quast, M. 37
- Renault, P. 51  
Richter, F. 57  
Rickards, K. 16  
Rieman, K. 38  
Roth, J. 44, 61  
Rusbüldt, D. 61
- Saied, S. O. 33  
Samandi, M. 67  
Schram, D. C. 53  
Schrittwieser, R. 14  
Schwar, H. J. R. 27  
Schweer, B. 61  
Schweitz, K. O. 4  
Shiratani, M. 55  
Short, K. T. 66  
Smith, K. A. 51  
Stebbing, R. F. 51  
Stewart, R. W. 20  
Straub, H. C. 51  
Störi, H. 65  
Sullivan, J. L. 33  
Sultan, G. 70  
Sundgren, J. E. 6, 7  
Suranda, M. 21  
Swift, J. D. 27  
Sze, S. M. 49
- Tabarés, F. L. 45  
Tafalla, D. 45  
Tawara, H. 47  
Thomsen, N. B. 71  
Tian, C. 68
- Tsuji, K. 43  
Tucek, J. C. 52
- Uhl, J. E. 36
- Vahedi, V. 13, 19, 20, 21  
Valles-Abarca, J. A. 41  
van Beek, A. J. 53  
van der Sanden, M. C. M. 53  
van Helvoort, A. J. G. 53  
Vanderslice, T. A. 15  
Verboncoeur, J. P. 13, 19  
Vidal, C. R. 68
- Walton, S. G. 52  
Watanabe, Y. 55  
Wiesemann, K. 38  
Wroński, Z. 17, 33, 34, 69
- Yamamura, Y. 47
- Ziegler, J. F. 60

*fin.*